8-2006

Effect of Ionizing Radiation on the Crystalline Morphology of Ultra High Molecular Weight Polyethylene (UHMWPE)

Christopher Phillip Stephens
University of Tennessee - Knoxville

To the Graduate Council:

I am submitting herewith a thesis written by Christopher Phillip Stephens entitled "Effect of Ionizing Radiation on the Crystalline Morphology of Ultra High Molecular Weight Polyethylene (UHMWPE)." I have examined the final electronic copy of this thesis for form and content and recommend that it be accepted in partial fulfillment of the requirements for the degree of Master of Science, with a major in Polymer Engineering.

Roberto S. Benson, Major Professor

We have read this thesis and recommend its acceptance:

Bin Hu, Gajanan Bhat

Accepted for the Council:
Carolyn R. Hodges

Vice Provost and Dean of the Graduate School

(Original signatures are on file with official student records.)

To the Graduate Council:

I am submitting herewith a thesis written by Christopher Phillip Stephens entitled "Effect of Ionizing Radiation on the Crystalline Morphology of Ultra High Molecular Weight Polyethylene (UHMWPE)." I have examined the final electronic copy of this thesis for form and content and recommend that it be accepted in partial fulfillment of the requirements for the degree of Master of Science with a major in Polymer Engineering.

Roberto S. Benson
Major Professor

We have read this thesis
and recommend its acceptance:

Bin Hu

Gajanan Bhat

Accepted for the Council:

Anne Mayhew
Vice Chancellor and
Dean of Graduate Studies

(Original signatures are on file with official student records)

Effect of Ionizing Radiation on the Crystalline Morphology of Ultra High Molecular Weight Polyethylene (UHMWPE)

A Thesis Presented for

The Masters of Science Degree

The University of Tennessee, Knoxville

Christopher Phillip Stephens

August 2006

Acknowledgments

The author would like to express appreciation to his mentor and friend, Dr. Roberto S. Benson. He would also like to show appreciation for the other members of his committee, Drs. Bin Hu and Gajanan Bhat. The author would also like to thank Dr. J.S. Lin for use of the Small Angle X-Ray Scattering Facility in the Solid State Division of Oak Ridge National Laboratories. He would also like to show his appreciation to those people he supported him personally through the process of earning this degree including: his parents, Justin Hall, Sherry Lou, Tim Hughes, and David Cooper.

Abstract

The two main applications of ionizing radiation and Ultra High Molecular Weight Polyethylene (UHMWPE) are in space radiation shielding and articulating orthopedic implants (hips and knees). Samples are exposed to both proton and gamma irradiation. Proton irradiation doses are varied from 0-8.7 kGy. Proton Irradiation showed significant increases in crosslinking on the surface, which interferes with recrystallization of the polymer. Gamma Irradiation is conducted at a high (2.9 kGy/hr) and low (0.25 kGy/hr) dose rate at integral doses of 75 and 150 kGy. Gamma irradiation shows significant crosslinking and recrystallization in the center of the sample where oxygen diffusion is limited.

Table of Contents

List of Tables

List of Figures

1. Introduction

Ultra High Molecular Weight Polyethylene (UHMWPE) is the polymer of choice for many orthopedic prostheses and is known as the standard in radiation shielding material from space voyages.

UHMWPE Performance in Artificial Joints

UHMWPE is an excellent material for arthroplasties due to the combined desirable characteristics of high abrasion resistance and impact strength. This material also offers a low coefficient of friction, excellent biocompatibility with human tissue, a non-stick self-lubricating surface and good chemical resistance [1, 2]. Two of the main biomedical applications of UHMWPE involving exposure to ionizing radiation are hip and knee arthroplasties. UHMWPE is used in the acetabular cup component of the hip and tibial plateau component of the knee. Both components are major load bearing, articulating surfaces within the total joint replacement, and articulate against a metal counterface. The generated wear debris can result in many problems for the patient, including osteolysis (bone resorption), inflammatory and cytotoxic reactions. The wear debris rate fluctuates with a number of variables including but not limited to: UHMWPE fabrication methods, sterilization methods, surface roughness, and size of implant, biological environment, patient age, lifestyle, weight, and other medical conditions. The wear rates for UHMWPE is comparatively low, as seen in Figure 1, typically within the range of 0.05 - 0.20 mm/year [3]. However, the problem is not the rate of wear but the generation of wear debris.

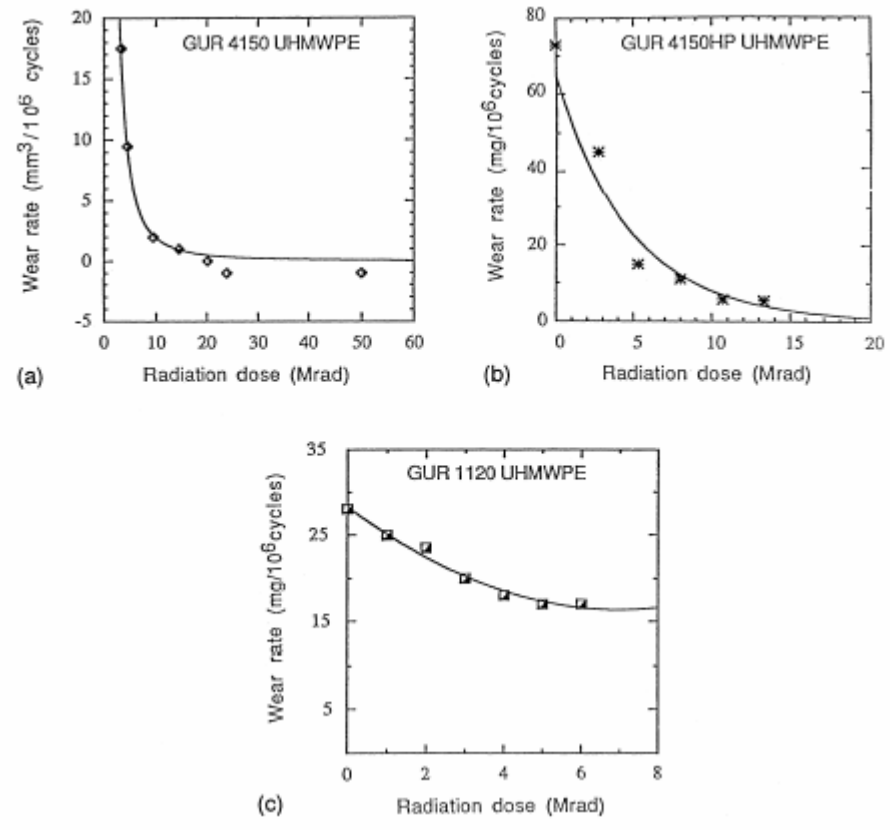

Figure 1: Effect of Radiation on the Wear Rate of UHMWPE in Hip Simulators [4]

The use of ionizing radiation to improve the overall wear rate of UHMWPE has been relatively successful, but a total understanding of the surface properties remains a necessity. The effect of ionizing radiation at high integral radiation doses leads to recombination of free radicals into inter-chain crosslinks; these crosslinks, as seen in Figure 1, lead to the improvement of wear resistance [4]. However, extensive crosslinking can lead to deleterious effects on fatigue, fatigue crack propagation, and fracture toughness [4]. In a semi-crystalline polymer free-radicals are preferentially in the interfacial and amorphous regions [4]. Since polyethylene is a semi-crystalline polymer, an inhomogeneous network is developed and free radicals have a long lifetime due to their slow diffusion out of the crystal, where they can react to form crosslinks or chain scissions [4].

UHMWPE in Space Radiation Shielding Applications

The use of human manned space vehicles requires that the construction materials be radiation shielding to reduce deleterious effects on the DNA of the human. The materials for radiation shielding are listed starting with the best: liquid hydrogen, liquid methane, lithium hydride, polyethylene, and then water [5]. Of the listed good radiation shielding materials polyethylene is chosen for cost saving and ease of use. Polyethylene is considered to be the benchmark material for radiation shielding [5]. This is primarily due to its high concentration of low Z materials, including hydrogen, carbon, and oxygen (if oxidized) [5]. UHMWPE is also an exceptional material for radiation shielding, due to its inherent tendency to cross-link upon irradiation, high hydrogen content, and high

molecular mass. Another concern with radiation shielding material is the effect of atomic oxygen on the degradation of the polymeric material; however, much of this concern has been alleviated by coating the shielding material with a very thin coat of metal [6]. Much of this atomic oxygen is found in the low earth orbit (LEO) and causes erosion per incident oxygen atom of 3.97 ± 0.23 cm3/atom [6].

Effect of Ionizing Radiation on Polymers

Types of Radiation

The ionizing radiations include gamma irradiation [4, 7, 8], energetic electrons and protons [9], X-ray irradiation, UV irradiation [10-12], and plasma treatment, or heavy ion beams of keV or MeV energy [13-16].

Irradiation

The absorbed radiation dose is dependent on depth from the surface due to kinetic energy transfer [17], as seen in Figure 2. Kinetic energy transfer takes place in two stages: 1) the high-energy photon (gamma irradiation) uniformly exciting the electrons in the UHMWPE 2) the excited electrons collide with neighboring molecules dispersing their energy [17]. Since energy is transferred by collision, the material near the surface does not have as many collisions with excited electrons as the material in the bulk and therefore has a lower absorbed dose, as seen in Figure 2 [17]. The R, build up region, value (Figure 2) typically observed is on the order of 1 mm [17]. Initial reactive species formed during radiation are alkyl free-radicals (metastable) and double bonds, which then become stable allyl free radicals [17]. At times greater than about 400 minutes there are only allyl free radicals remaining on the order of 10^{-25} $(allyl/cm^3)^{-1}/s$ [18].

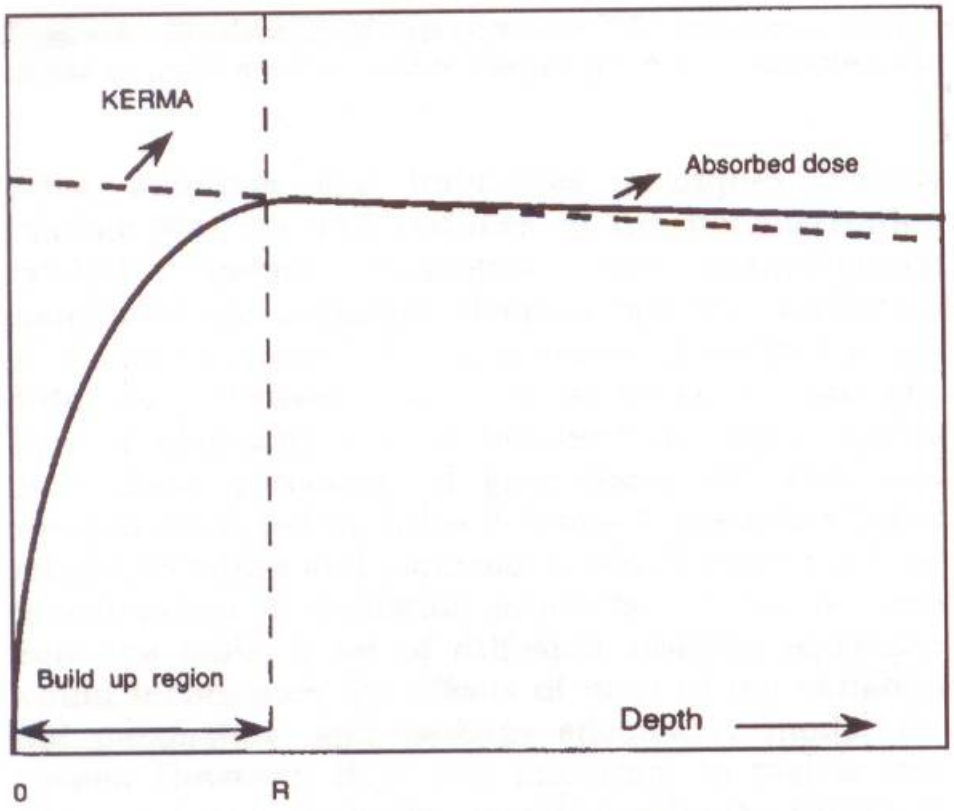

Figure 2: Absorbed Dose with Depth of Penetration [17]

Impurities from the polymerization (vinyl chain ends from Ziegler-Natta catalyzed polymerization and calcium stearate) of UHMWPE have also been known to generate reactive species upon irradiation [17].

Crosslinking and Chain Scissioning

The free radicals formed during radiation will react to form either crosslinks or chain scissions depending on access to oxygen. The presence of molecular oxygen may completely prevent the formation of cross-links by reacting with the radicals. Irradiation of polyethylene leads to the formation of free radicals, migration of free radicals, and reaction of free radicals into crosslinks or chain scissions, as seen in Figure 3. The presence of molecular oxygen (O_2) during irradiation leads to a higher degree of chain scission and deterioration of mechanical properties. In an inert environment, intermolecular cross-linking is the predominant process during ionizing radiation of polyethylene. Figure 4 displays typical free radical concentrations as a function of time and the subsequent concentration of oxidation products. It can be seen that there is a high concentration of oxidation products in the subsurface, due to the depth dependent absorbed dose and high concentration of oxygen near the surface of the material. Inversely, it is expected that the concentration of crosslinks will be high in the center of the sample as compared to the surfaces, since diffusion of oxygen to the center of the sample is slow enough to allow for crosslinking kinetics. These two effects are shown together in Figure 5, where chain scissioning is present in the subsurface and crosslinking is prevalent in the center of the sample [18].

(1) Irradiation causes generation of new species:

$-CH_2-CH_2- \longrightarrow -\dot{C}H-CH_2-$ (mobile alkyl radicals) + $\dot{H}$
$-CH_2-CH_2- \longrightarrow -CH=CH-$ (double bond) + H_2
$-(CH_2-CH_2)_n- \longrightarrow -(CH=CH)_n-$ (conjugated double bonds) + $n\ H_2$

and other radicals like methyl radical or those from additives and dissolved gases.

(2) Migration of mobile radicals and formation of relatively immobile allyl and polyenyl radicals:

$-\dot{C}H-CH_2- + \dot{H} \longrightarrow -CH=CH-$ (double bond) + H_2
$-(\dot{C}H-CH_2)_n- + \dot{H} \longrightarrow -(CH=CH)_n-$ (conjugated double bonds) + $n\ H_2$
$-\dot{C}H-CH_2- \longrightarrow -CH_2-\dot{C}H-$ (intrachain migration of alkyl radicals)
$-\dot{C}H-CH_2- + -CH_2-CH_2- \longrightarrow -CH_2-CH_2- + -\dot{C}H-CH_2-$ (interchain migration of alkyl radicals)
$-\dot{C}H-CH_2-(CH=CH)_n- \longrightarrow -CH_2-\dot{C}H-(CH=CH)_n-$ (allyl and polyenyl radicals by intrachain migration)
$-\dot{C}H-CH_2- + -CH_2-CH_2-(CH=CH)_n- \longrightarrow -CH_2-\dot{C}H-(CH=CH)_n- + -CH_2-CH_2-$ (allyl and polyenyl radicals by interchain migration)

(3) Reactions among alkyl radicals and with oxygen (alkyl radicals are represented by $\dot{R}$).
[Note: the following reactions are a chain and until all radicals are terminated they will continue.]

$\dot{R} + O_2 \longrightarrow R\dot{O}O$ (reversible step forming peroxy radicals)
$R\dot{O}O + RH \longrightarrow ROOH + \dot{R}$ (propagation)
$ROOH \longrightarrow R\dot{O} + H\dot{O}$ (hydroxyl radicals)
$R\dot{O} + RH \longrightarrow ROH + \dot{R}$ (propagation and formation of alcohol)
$H\dot{O} + RH \longrightarrow HOH + \dot{R}$ (propagation and formation of water)
$\dot{R} + \dot{R} \longrightarrow R-R$ (cross-linking and termination)
$R\dot{O}O + R\dot{O}O \longrightarrow O_2$ (cross-linking and termination)
$\dot{R} + R\dot{O}O \longrightarrow ROOR$ (cross-linking and termination)
$-CH_2-CH(OOH)-CH_2- \longrightarrow -CH_2-CHO + HO-CH_2-$ (scission and formation of aldehyde and alcohol)
$-CH_2-CH(OOH)-CH_2- \longrightarrow HOH + -CH_2-(C=O)-CH_2-$ (scission and formation of ketone and water)
$-CH_2CH(O\dot{O})CH_2- \longrightarrow CO_2 + -CH_3 + \dot{C}H_2-$ (scission and formation of CO_2)
Also, (1) other smaller radicals can also participate in termination; (2) smaller molecular weight hydrocarbons and CO can also be formed.

(4) Reactions of the allyl radical:

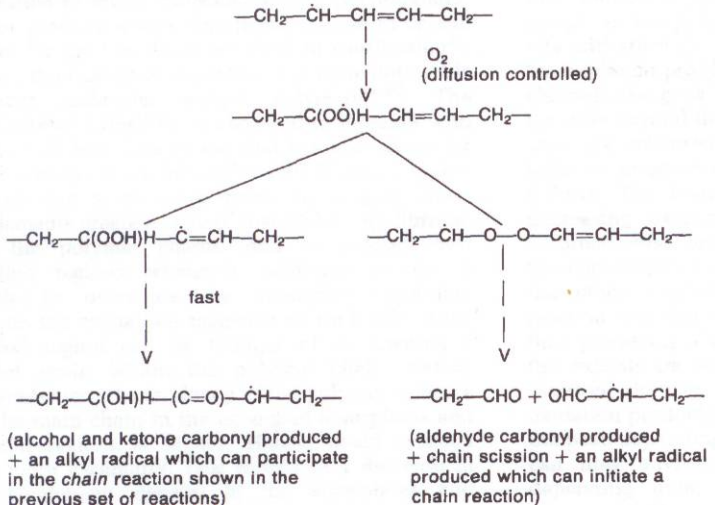

Figure 3: Irradiation Effects on Polyethylene [17]

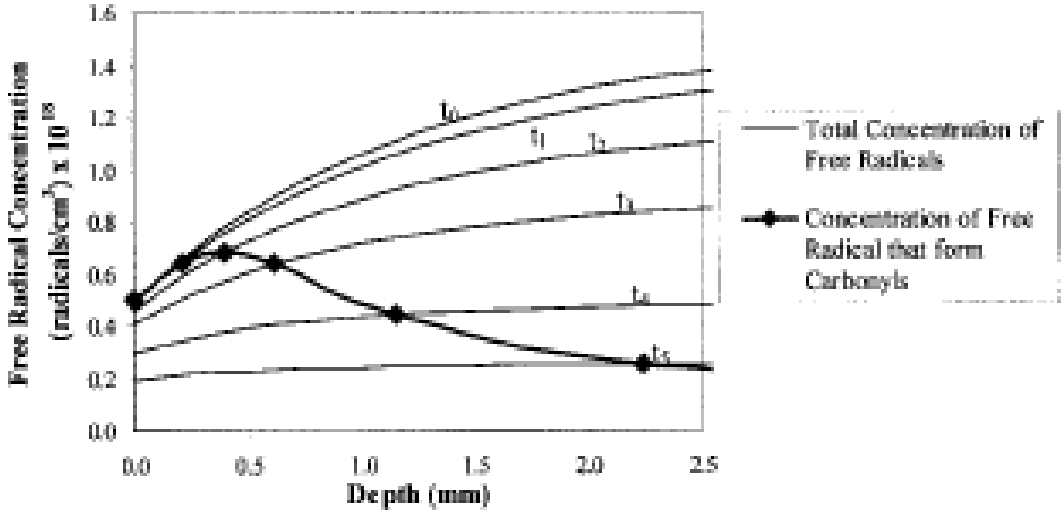

Figure 4: Concentration of Free-Radicals as a Function of Time and Subsequent Oxidative Product Concentration [18]

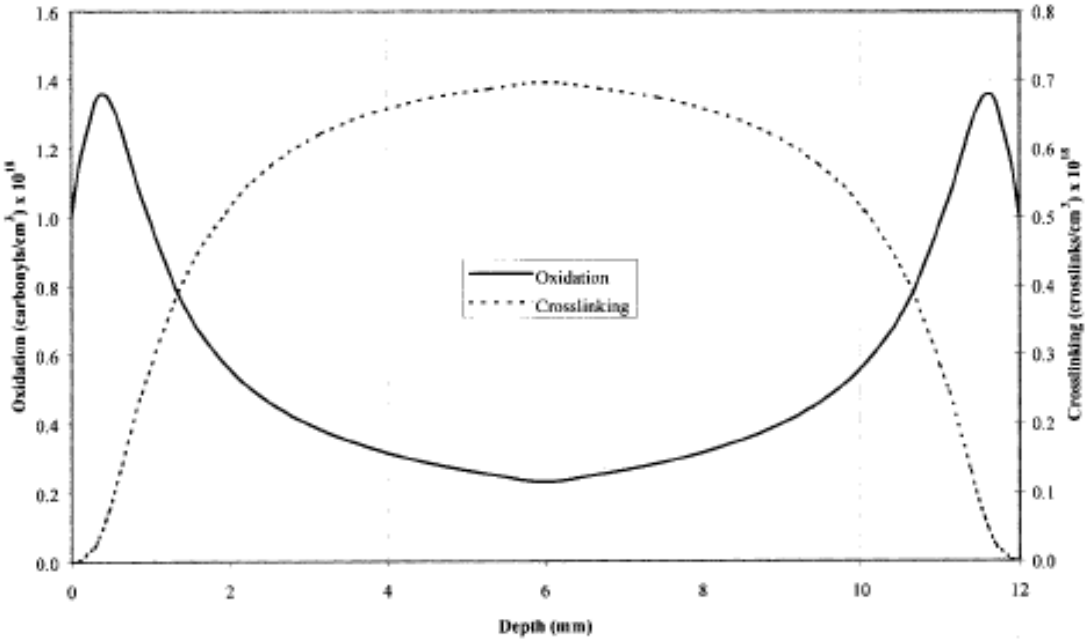

Figure 5: Depth Dependence of Crosslinking and Chain Scissioning [18]

G Factors

Basically, the irradiation of polymers involves two competing processes: chain scission and cross-linking. When dispropotionation is the predominant termination step, chain scission prevails. A preference for the recombination of radicals as the termination step leads to formation of intermolecular cross-links. The g-factors are defined as seen in equation 3 for chain scission and equation 6 for crosslinking [19]. Some G factors for polyethylene are G (H_2)=3-4, G (alkyl)=1.3-3.0, G (allyl)=0.2-0.4, G (dienyl)=0.015, G (V_t)=2.0±0.3, and G (X)=0.1-1.34, G (S)<0.1 [19]. These g-factors show that polyethylene has a strong tendency to cross-link.

$$\frac{\partial w(p,y)}{\partial y} = -pw(p,y) + 2p\int_p^\infty \frac{w(l,y)}{l}dl \qquad 1$$

$$y = \int_0^t r dt \qquad 2$$

$$G(S) = \frac{100N_A y}{D} \qquad 3$$

$$\frac{1}{p}\frac{\partial w(p,x)}{\partial x} = -2w(p,x)\int_0^\infty w(l,x)\,dl + \int_0^p w(l,x)\,w(p-1,x)\,dl \qquad 4$$

$$x = \int_0^t r dt \qquad 5$$

$$G(X) = \frac{100N_A x}{D} \qquad 6$$

Changes in mechanical properties, such as hardness and wear are generally associated with increased cross-linking.

2. Theory

Crystal Morphology

Polyethylene organizes into an orthorhombic crystal (Figure 6 and Figure 7) with lattice parameters of a=0.7417nm, b=0.4945nm, and c=0.2547nm [20]. UHMWPE can be described efficiently by using a three-phase crystallite model. The three-phase crystallite model is made up of amorphous, interfacial, and crystalline regions (Figure 8). The amorphous phase is a collection of entangled disordered chains. The crystalline region is a collection of chains that fold into organized orientations forming an orthorhombic crystal. The interfacial region of the polymer is composed of slightly ordered chains at the interface of the crystal and amorphous regions. The long period of the PE crystal is determined by SAXS. DSC is used to find the lamella thickness, purely crystalline portion. UHMWPE crystallizes in a lamellar structure. There are three main models for the description of the molecular chain reentry into the crystal, as seen by Figure 9. The lamella structure is the basic crystalline unit for both solution and bulk crystallized PE. In PE crystallized from the bulk, the amorphous regions include tie chains that participate in more than one lamella, as illustrated in Figure 10.

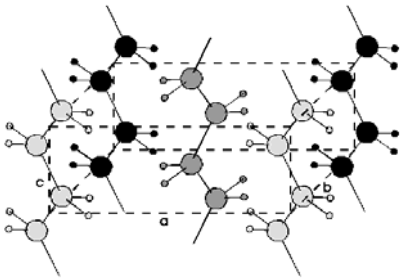

Figure 6: Polyethylene Unit Cell [21]

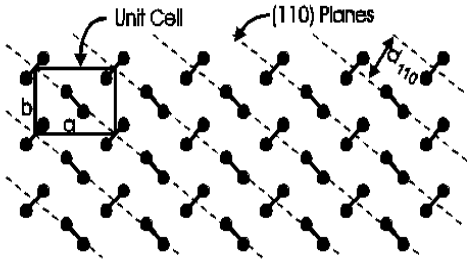

Figure 7: Polyethylene (110) Crystallographic Plane [21]

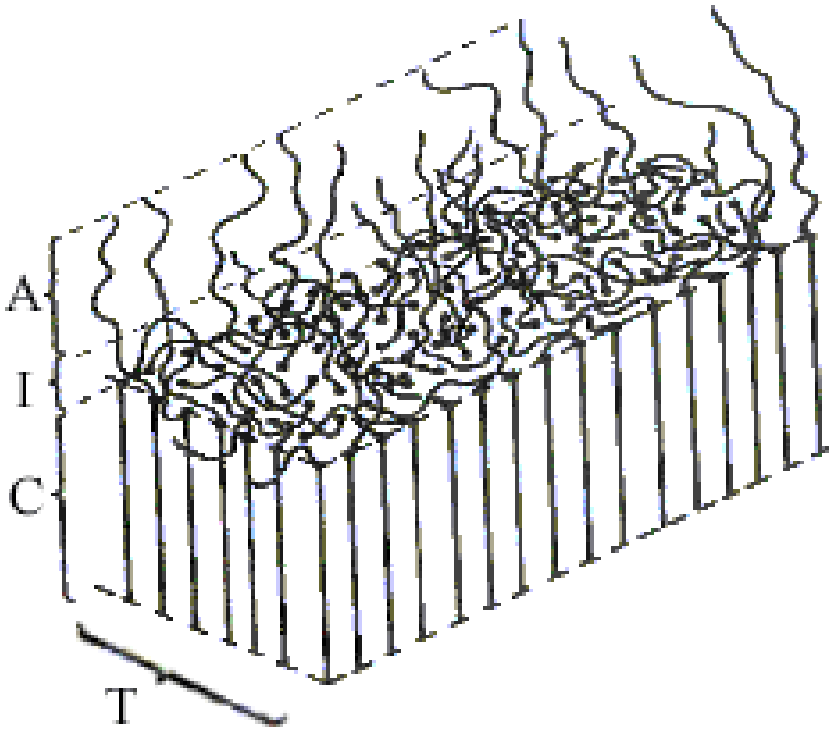

Figure 8: Three-Phase Crystallite Model

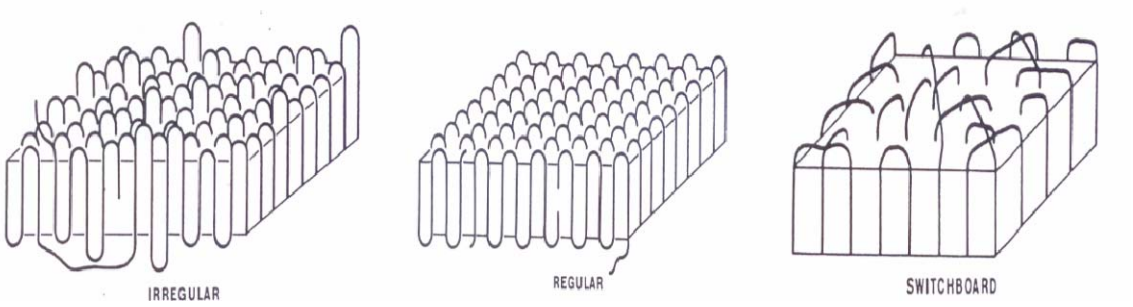

Figure 9:Models of Lamella Crystallization [22]

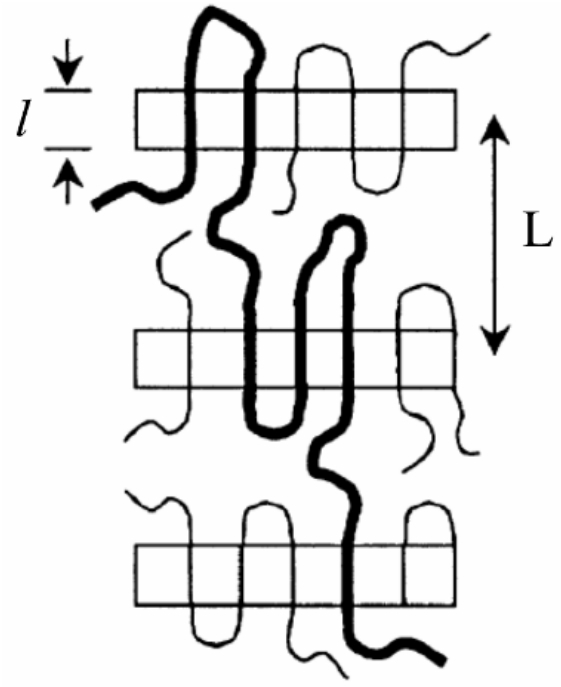

Figure 10: Tie Chains Between Lamella Crystals [23]

Effect of Radiation of Crystalline Morphology

Radiation energy is absorbed within the semicrystalline material uniformly. Which means that radical formation should be uniform throughout the material [24]. However, it has been shown that upon radiation there is no significant cross-linking or chain scission that occurs within the crystalline core, which means that the radicals produced within this crystalline region must migrate to the edge of the crystal in order to react [24]. This means that cross-linking and chain scission is limited to the interfacial and amorphous regions of the materials. This fact makes the entangled loops and tie chains very important in a radiation study, because they are located at the interfacial region where there is a high concentration of radicals diffusing from within the crystal. This means that the interface could be exposed to a higher concentration of reactive radicals than the amorphous region, due to the diffusion of radicals out of the crystal. This fact will affect both the melting behavior and mechanical properties of the bulk polymer due to the reduction of mobility of the chains, induced by crosslinking, that make up the reentry loops, tie chains, and amorphous region.

Differential Scanning Calorimeter (DSC) Space Transformation

The degree of crystallinity can be determined from DSC by using Equation 7, where the ΔH_{FUS} is the heat of fusion of the sample and ΔH_m is the heat of fusion for a sample of the same material with 100% crystalline material.

$$\alpha_m = \frac{\Delta H}{\Delta H_m} \qquad 7$$

In order to gain further insight regarding crystallite size and distribution from the DSC Endotherm, they must be transformed into probability distributions based on temperature (Equation 8) and crystallite thickness (Equations 9 and 10). Where ΔH_m is the heat of fusion per unit mass for the perfect crystal, P(T) is the DSC power output, ρ_c is the crystalline density, M is the sample mass, and α_m is the mass fraction crystallinity of the sample [25]. These thermal parameters are used to determine the probability density as a function of temperature is given by *f(T)*, Equation 8.

$$f(T)\,dT = \frac{1}{\alpha_m \Delta H_m} \frac{P(T)dT}{M\left(dT/dt\right)} \qquad 8$$

An apparent crystal thickness distribution is calculated from transferring f(T) into an equation dependent on the crystal thickness (*l*), Thompson equation (Equation 9 and Figure 11) and the weight distribution function of thickness, Equations 10 and 11, where σ_e is the basal surface energy, T_m^o is the melting temperature for an infinite crystal, and T_m is the melting temperature of the sample [25-27]. The transformation procedure is depicted graphically in Figure 11.

$$l = \frac{2\sigma_e 10^3}{\Delta H_m \rho_c \left(1 - \frac{T_m}{T_m^o}\right)} \quad , nm \qquad 9$$

$$g(l) = KP(T)\left(T_m^o - T\right)^2 \quad , nm^{-1} \qquad 10$$

$$K = \frac{\rho_c}{2\sigma_e T_m^o M \alpha_m 10^9 \left(dT/dt\right)} \qquad 11$$

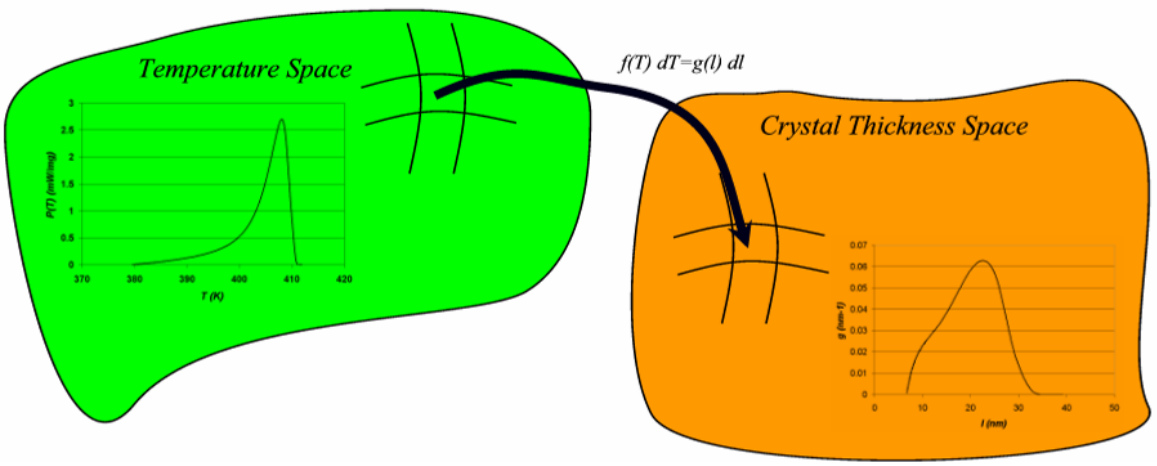

Figure 11: DSC Space Transformation

The constant parameters for polyethylene are T_m^o=418.7 K, ΔH_m=288 kJ/kg, σ_e=90 mJ/m^2, and ρ_c=967 kg/m^3 and sample dependent parameters are T_m in K, α_m, M in kg, dT/dt in K per second and P(T) in mW [25]. The crystallizable sequence length is determined by dividing the crystallite thickness by the value for the c-dimension (0.2547nm) of a UHMWPE crystal, which tells the number of repeat units in the crystal. Often the crystallizable segment length will be capped with cross-links or oxidation products that cannot be incorporated into the crystal, as seen in Figure 12 (this will especially show to be true in melting and recrystallization post-irradiation). The crystallizable fractions of the pristine and irradiated UHMWPE samples were determined using equation 12, where *x* is the mole fraction of crystallizable units, R (1.9873 cal/mol K) is the gas constant, and ΔH_u (960 cal/mol) is the molar heat of fusion of repeat units in the crystals. [28]

$$\frac{1}{T_m^c} = \frac{1}{T_m^o} - \frac{R}{\Delta H_u} \ln x \qquad 12$$

Wide Angle X-Ray Diffraction (WAXD)

WAXD allows for the determination of crystal structure by displaying the intensity of the x-ray beam reflected by specific crystalline planes.

Crystallinity

The crystallinity was calculated by using Equation 13, where I is the integrated intensity of the corresponding diffraction peak [25].

$$W_{C,X} = \frac{I_{110} + 1.42 * I_{200}}{I_{110} + 1.42 * I_{200} + 0.651 * I_A} \qquad 13$$

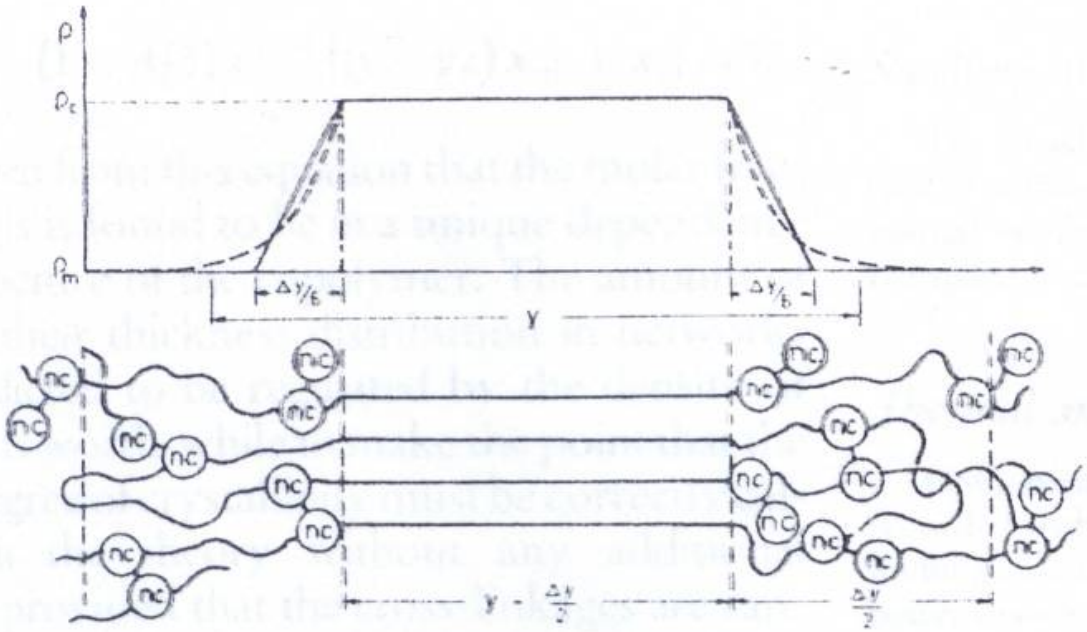

Figure 12: Effect of Non-Crystallizable Units on Crystallization

Small Angle X-Ray Scattering (SAXS)

SAXS is an analytical technique used to determine the long period of the polymer. The analysis used is based on Bragg's law stated in Equation 14, where D is the distance between crystallographic planes, λ is the radiation wavelength, 2θ is the angle of scatter, and n is the integer order of reflection [29]. Bragg's law is set equal to the momentum transfer, Q, in Equation 15 to determine the long period of the repeat unit of the polymer [29]. Since we are looking at the first order of the reflection n is set equal to 1. Long period can be determined from Equation 16, where q_{max} is the q at the maximum of the Lorenz plot [30, 31].

$$n\lambda = 2D\sin\theta \tag{14}$$

$$Q = 4\pi\,\lambda^{-1}\sin\theta \tag{15}$$

$$L = \frac{2\pi}{q_{MAX}} \tag{16}$$

By multiplying the DSC based crystallinity times the long period the size of the crystalline region can be determined. By multiplying the WAXD crystallinity by the long period the size of the crystalline region plus two interfacial regions can be determined. Therefore, using SAXS, DSC, and WAXD an approximation of the parts of the three-phase model can be determined.

Hardness Testing

Nanoindentation

Nano-indentation permits the determination of surface micro-properties such as hardness and modulus. This form of testing can provide better insight into surface morphology-

property relationships. Normally this technique is used with indentations on nano-scale lengths, however due to the three-phase nature of the material the indenter had to probe much deeper, ~5 μm, to get an average of the phases and a reasonable hardness and modulus value.

Hardness can be calculated by the ratio of maximum load over contact area, since during the experiment load, contact area, and displacement into the material were measured. The reduced modulus of the material can be calculated by using Equation 17, where S is the stiffness of the material and A is the contact area [32]:

$$E_r = \frac{\sqrt{\pi} S}{(2.068)\sqrt{A}} \qquad 17$$

The modulus of sample can be calculated by using Equation 18. Where v is the Poisson's ratio of the sample (UHMWPE), v_i is the Poisson's ratio for the indenter tip, E_i is the modulus of the indenter, and E modulus of the sample[32]:

$$\frac{1}{E_r} = \frac{\left(1-v^2\right)}{E} + \frac{\left(1-v_i^2\right)}{E_i} \qquad 18$$

Hardness Analysis

The modulus of semi-crystalline polymers is known to depend directly on the degree of crystallinity, ∝. The micro-hardness has been shown to depend directly on crystal thickness, l_c [33, 34]. The dependence of the hardness of the crystal, H_c, on the crystal thickness, l_c, is illustrated in equation 19, where H_c^{∞} is the hardness of an infinite size crystal [33, 34]. The parameter b is defined by equation 20, where σ_e is the surface free

energy and δh is the enthalpy of the crystal destruction [33, 34]. The yield stress is also able to estimated using the Tabor's relationship expressed in Equation 21 [33, 34]. From both the crystal hardness and yield stress relationships, it can be seen that both values are highly dependent on the lamella thickness, l_c.

$$H_c = \frac{H}{\alpha} = \frac{H_c^{\infty}}{\left(1 + b/l_c\right)} \tag{19}$$

$$b = \frac{2\sigma_e}{\delta h} \tag{20}$$

$$\sigma_y^o \approx \frac{H_c}{3} \tag{21}$$

3. Experimental

Sample Preparation

UHMWPE samples are machined into discs with a diameter of 35 mm and a thickness of 6.35 mm from a rod of Tivar® 1000 produced by Poly Hi Solidor (Fort Wayne, IN).

Proton Irradiation

Proton irradiation was conducted at the Indiana University Cyclotron Facility (IUCF). The samples were irradiated with protons at a fluence of $3.6x10^{17}$ protons/m^2 and a flux of $2x10^{14}$ protons/m^2s (low dose irradiation) and a fluence of about $2x10^{18}$ protons/m^2 (flux of about $3x10^{14}$ protons/m^2s) for the high dose irradiation. All irradiations were carried out in air, at room temperature. The incident energy and total dose for each sample is listed in Table 1. The Linear Energy Transfer (LET) was estimated by using the standard SRIM program, with a corrected density of 0.97 g/cm^3 for UHMWPE. The LET was estimated for incident and emergent faces of the sample and averaged. Both electronic and nuclear contributions were added. The energy deposited by the beam in each sample was calculated by multiplying the average LET by the thickness of the sample. PMMA spacers of different thickness were used between UHMWPE samples. The samples were stacked together for irradiation, see Figure 13.

Table 1: Proton Irradiation Parameters

Sample Description	Energy of Incidence (MeV)	Absorbed Dose (MRads)	L_{el} ($MeVcm^2/mg$)	L_{nucl} ($MeVcm^2/mg$)	L_{tot} ($MeVcm^2/mg$)
Control (4 Samples)	0	0	0	0	0
Low Dose (8 Samples)	198	0.094	0.00482	1.83e-6	0.00482
	186	0.096	0.00502	1.943e-6	0.00502
	160	0.103	0.00556	2.23e-6	0.00556
	120	0.123	0.00681	2.91e-6	0.00681
	27	0.37	0.02203	1.730e-5	0.02203
High Dose (3 Samples)	195	0.68	0.00487	1.86e-6	0.00487
	127	0.83	0.00654	2.76e-6	0.00654
	133	0.87	0.00633	2.65-6	0.00633

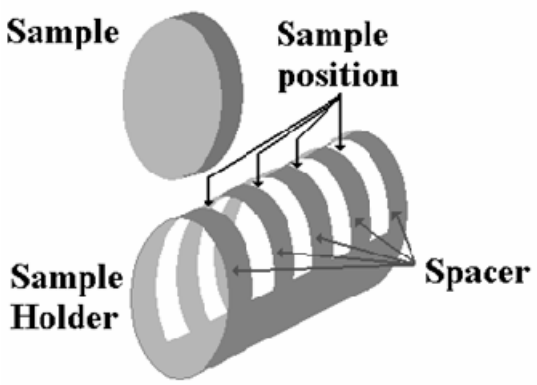

Figure 13: Sample Holder for Proton Irradiation

The sample holder was made of a PVC (Polyvinylchloride) tube. The spacer introduced a layer of air with a thickness of about 5 mm between samples in order to decrease heat accumulation during the irradiation. The energy deposited by the incident particle in the target is dominated by the electronic component, which is larger by about 2 orders of magnitude than the nuclear stopping power. The sample holder had about 40 positions for samples and it was calculated to allow for a total "sample length" longer by about 50% that the range of 200 MeV protons in polyethylene.

Gamma Irradiation

Gamma Irradiation was conducted at the National Institute for Nuclear Research in Mexico City. The samples were exposed to gamma irradiation from a ^{60}Co source in an inert argon atmosphere at a dose rate of 0.25 (low dose rate) or 2.9 kGy hr^{-1} (high dose rate) for a γ of 75 or 150 kGy.

Differential Scanning Calorimeter (DSC)

The basic principle of a DSC supplies enough energy to linearly increase the temperature of both a polymer sample and a reference sample, as seen in Figure 14. Following radiation, cores of 6.35 mm diameter are taken from the sample and sliced into 1 mm thick discs using a razor blade, to limit mechanical modification of the samples.

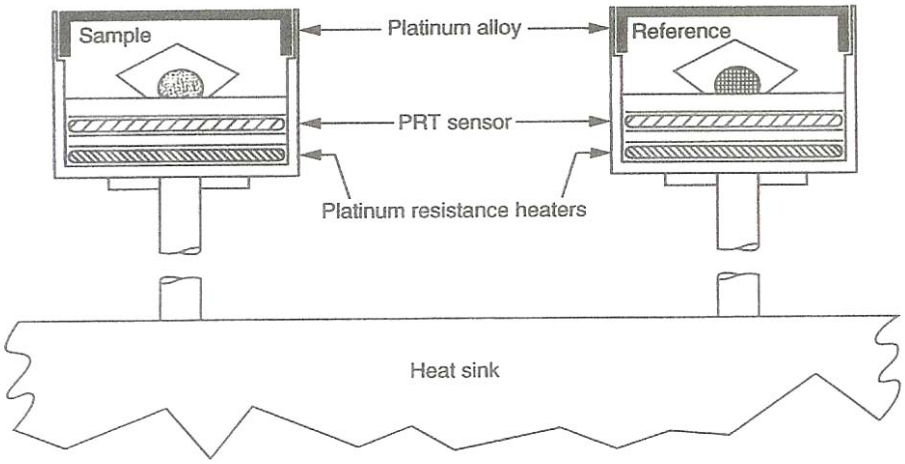

Figure 14: Schematic of a Typical DSC [35].

For the gamma irradiation experiments, a 1 mm thick sample is taken from the surface and center of the irradiated disc and held at 75^{o}C for 10 minutes followed by a heating segment from 75^{o}C to 180^{o}C at 1 ^{o}C/min. For the proton irradiation experiments, a 1 mm thick sample is taken from the surface of the sample and exposed to a three segment thermal test: 1) 75^{o}C to 180^{o}C at 1 ^{o}C/min (Run 1), 2) 180^{o}C to 75^{o}C at -1 ^{o}C/min, and 3) 75^{o}C to 180^{o}C at 1 ^{o}C/min (Run 2). These slow rate experiments avoid the artificial increase of the T_m, seen in 10 ^{o}C/min heating rate experiments, to values above the theoretical melting temperature of polyethylene assigned to infinite size crystals, T_m^{o}. Increase in melting temperature of UHMWPE has been cited by Zachariades and Logan [36, 37]. The anomaly is possibly due to the existence of crystals in a microenvironment consisting of high degree of chain entanglement and/or cross-linking found in these irradiated UHMWPE samples. Following each DSC run melting temperature corrections are conducted using an Indium standard. Following the experiment the endotherm is transformed into a probability distribution on crystalline lamella thickness, as discussed above. The median crystallite thickness, l_n, of this probability distribution is then determined by integrating the area under the curve and determining the middle of the area, as displayed in Appendix II and IV. The first moment of this probability distribution is then calculated and the median crystallite thickness, l_w, (Equation 22) of this distribution is determined by integrating the area under the curve to determine the median value.

$$l_w = \frac{\sum N_i l_i^2}{\sum N_i l_i} \qquad 22$$

The second moment of the probability function is determined and the median crystallite thickness, l_z, (Equation 23) of this new distribution is determined by integrating the area under the cure to determine the median value. A graphical depiction of the meaning of l_n, l_w, and l_z is depicted in Figure 16.

$$l_z = \frac{\sum N_i l_i^3}{\sum N_i l_i^2} \qquad 23$$

Wide Angle X-Ray Diffraction (WAXD)

The samples were scanned over a 2-Theta range from 8 to 44 degrees in step sizes of .01 degrees held for 1 second. The detector used was a 4x4 Programmable Receiving Slit (PRS), and the source was controlled using a 2x2 Cross-slit. The generator was kept at 45 kV and 40 mA at all times during testing. The experimental setup is shown in Figure 15.

Small Angle X-Ray Scattering (SAXS)

Following radiation 6.35 mm diameter cores are taken from the sample and sliced into 1 mm thick discs using a razor blade, to limit the introduction of stress induced morphological modification of the samples. The experiments were conducted using a 10-m SAXS camera within the Solid State Division at Oak Ridge National Laboratory. The 10-m SAXS camera consisted of x-ray source, a monochromator, a collimator, a specimen chamber, and a two dimensional position-sensitive detector. The detector is 20x20 cm^2 with an element spacing of 3 mm.

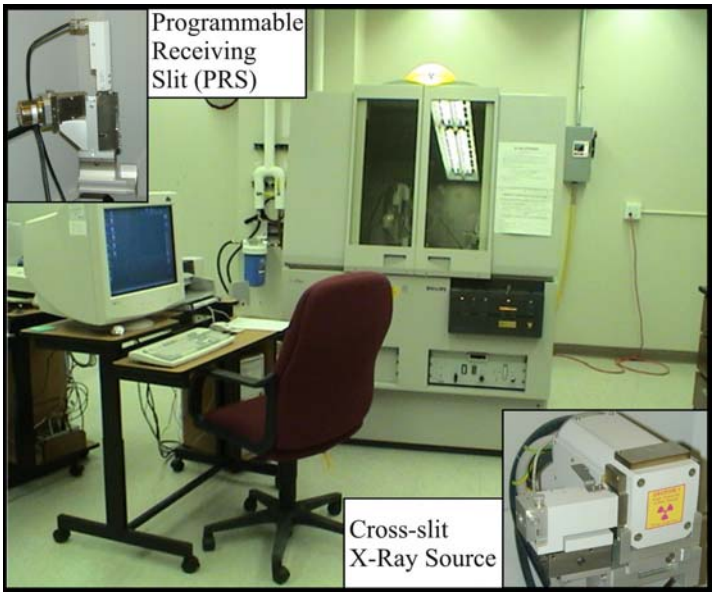

Figure 15: Wide-Angle X-ray Setup

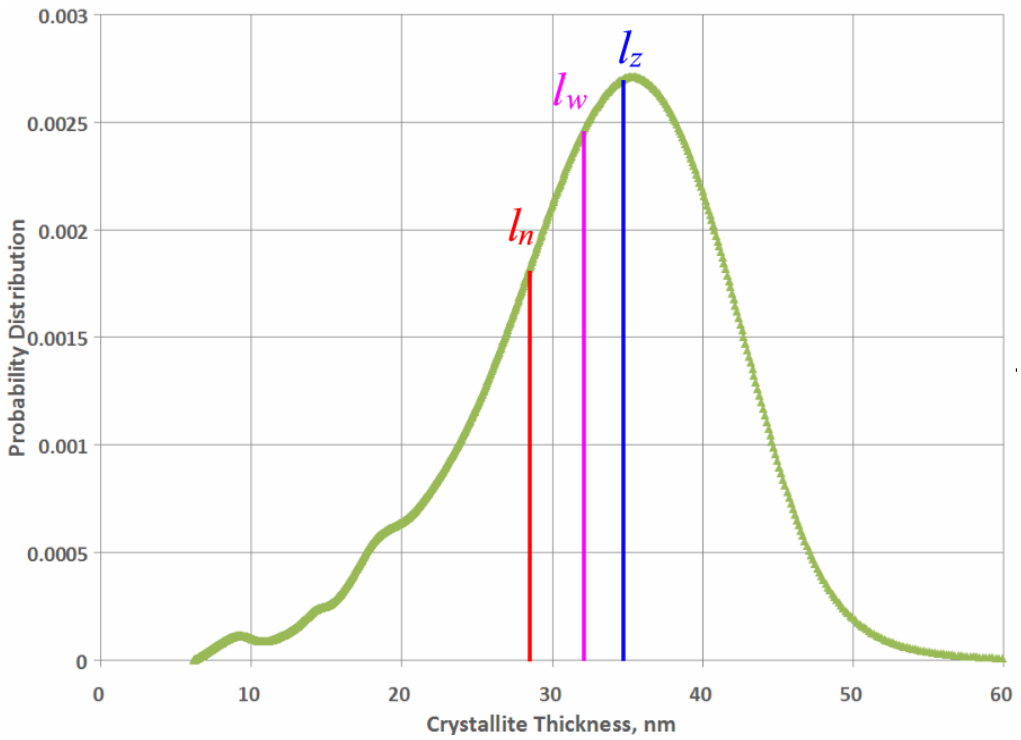

Figure 16: Graphical Depiction of the Number, Weight, and Z-Average Crystallite Thicknesses

The scattering vector (q) used was 0.0479nm^{-1} to 0.9812 nm^{-1}. The detector was held at 5.119 m from the sample. The machine was calibrated with a Fe^{55} radioactive isotope to remove background cosmic radiation and electronic noise. The power setting was maintained at 100 kV and 40 mA.

Nano-Indentation

A Nano-Indenter XP (Nano Instruments, Inc.) was used to determine the surface hardness and modulus. A three-sided pyramidal Berkovich indenter used in maximum load to penetrated the surface 17 to 22 μm depending on hardness of the sample. Indentation measurements were made in a Continuous Stiffness Measurement (CSM) mode. The load, displacement (h), and stiffness (S) data collected as a function of time was used to calculate the hardness (H) and elastic modulus (E) [38]. A total of four samples per treatment condition were studied. Each test specimen was indented 5 times at a temperature of 21.5 C. A Poisson ratio of 0.46 was assumed for the calculations [39]. The program settings for these tests included a strain rate of 0.003 sec^{-1} and a harmonic frequency of 45 Hz.

4. Results of Proton Irradiation

Differential Scanning Calorimeter (DSC)

The DSC endotherms for the proton irradiated samples are displayed in Appendix 1 (Figure 64 and Figure 65). The crystallite thickness probability distribution for all samples is presented in Appendix 1 (Figure 66 to Figure 95). The area calculations for the proton irradiated samples are displayed in Appendix 2 (Figure 96 to Figure 185).

Thermal Analysis of Post-Irradiated Samples (Run 1)

The effect of integral dose for run 1 of the proton irradiated samples is displayed in the percent crystallinity (Table 2), crystallite thickness distribution (Figure 17), the first moment of the distribution (Figure 18), and the second moment of the distribution (Figure 19). The percent crystallinity shows no significant changes (outside of standard deviation), as seen in Table 2. With increasing radiation dose there is an increase in the number average crystallite thickness, l_n, (Table 3 and Figure 20): 21.00 ± 3.78 nm, 24.97 ± 1.29 nm (3.97 nm increase from control), and 25.56 ± 1.88 nm (0.59 nm increase from 1.77 kGy) for 0 kGy, 1.77 kGy, and 5.89 kGy, respectively.

Table 2: Effect of Radiation for Run 1 of Proton Irradiated Samples

Dose (kGy)	Average	Standard Deviation
0	60%	9%
1.77	58%	3%
5.89	62%	5%

Table 3: Median Crystallite Thicknesses for Proton Irradiated Samples in the First DSC Run

Dose (kGy)	Crystallite Thickness Distribution, l_n		First Moment, l_w		Second Moment, l_z		l_w/l_n	l_z/l_n
	Average	StdDev	Average	StdDev	Average	StdDev		
0.00	21.00	3.78	24.93	3.33	25.24	2.72	1.19	1.20
1.77	24.97	1.29	27.03	1.18	28.41	1.38	1.08	1.14
5.89	25.56	1.88	28.78	2.35	30.81	2.67	1.13	1.21

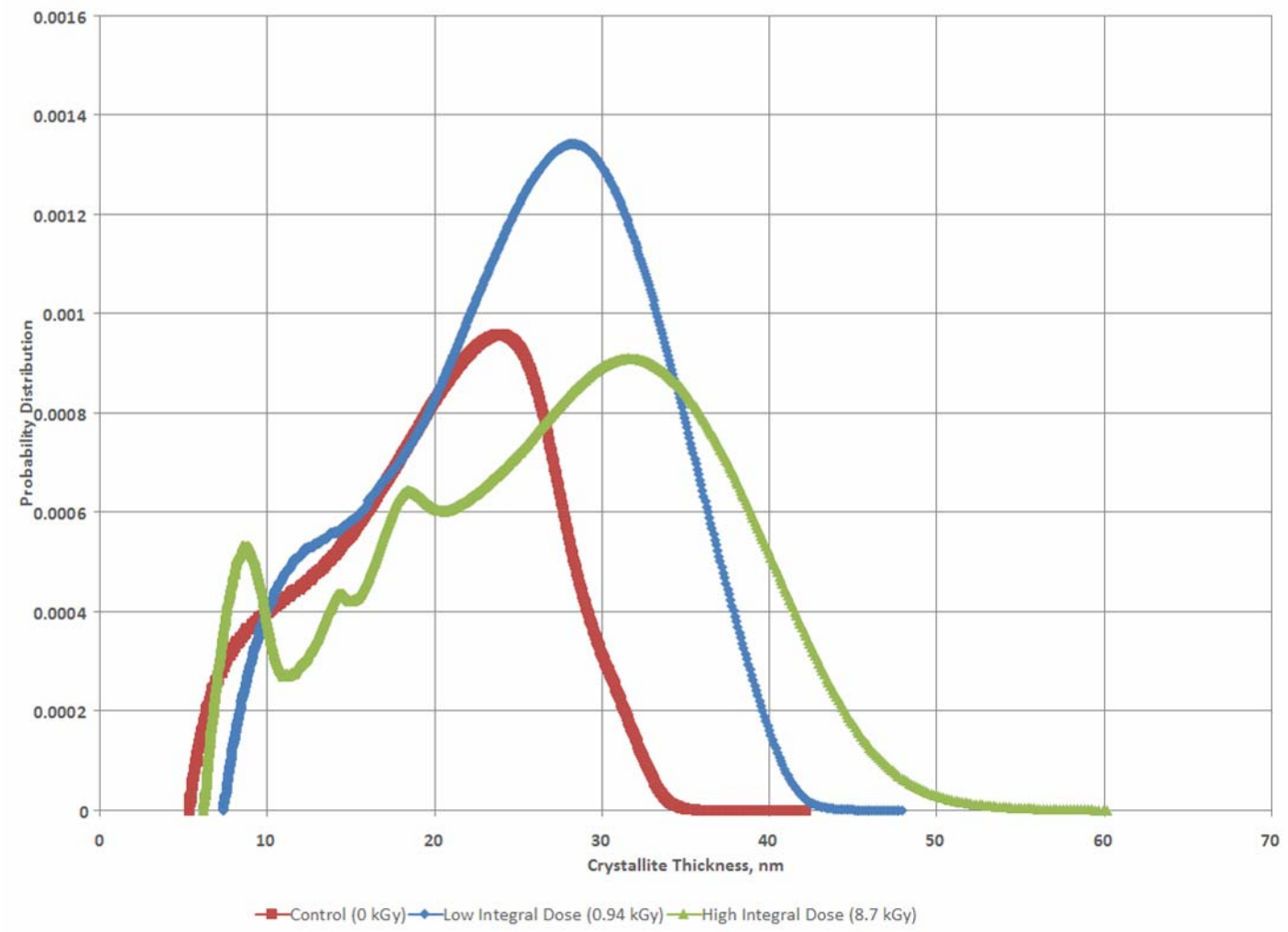

Figure 17: Crystallite Thickness Distribution of Run 1

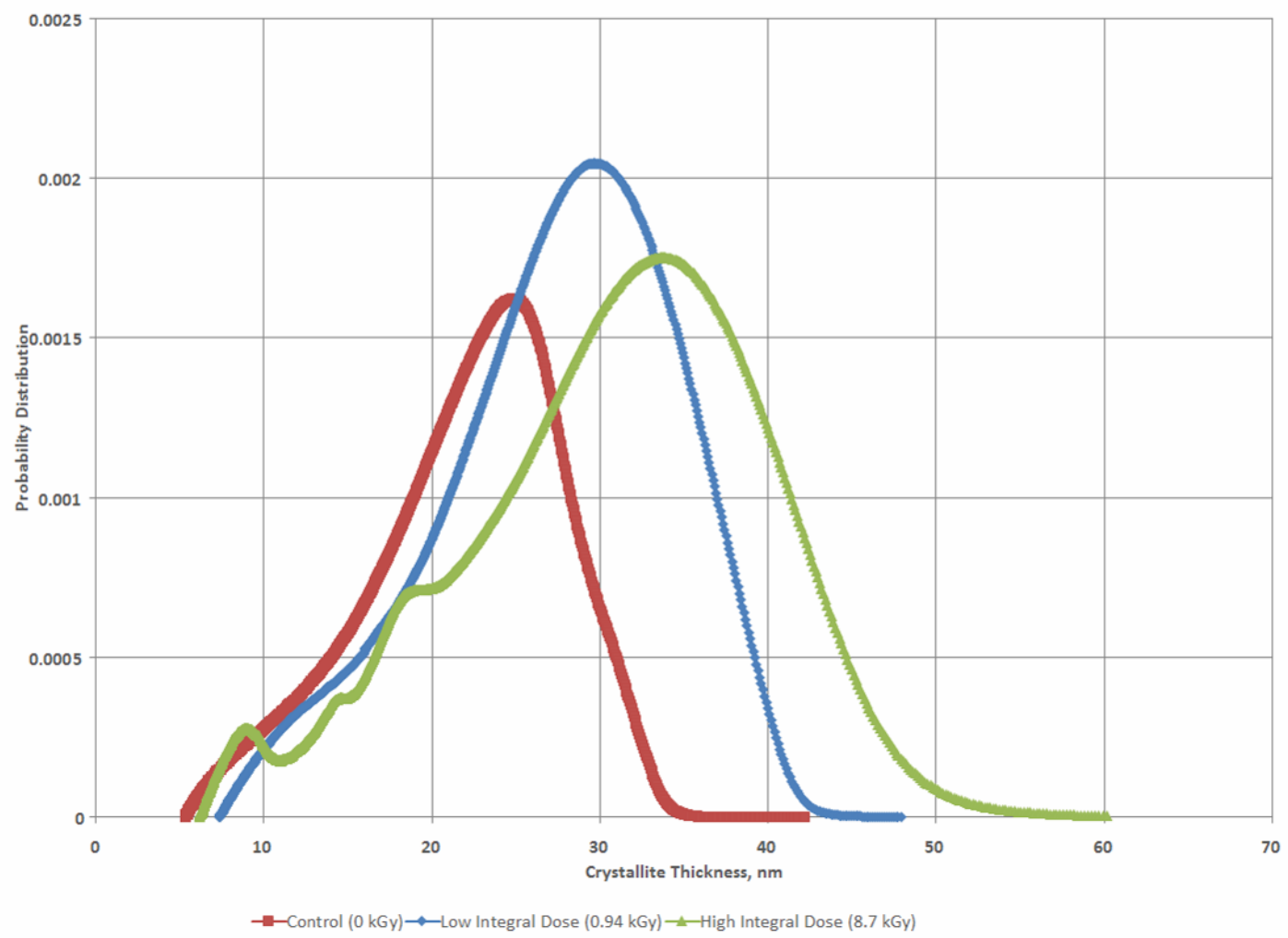

Figure 18: The First Moment of the Crystallite Thickness Distribution for Run 1

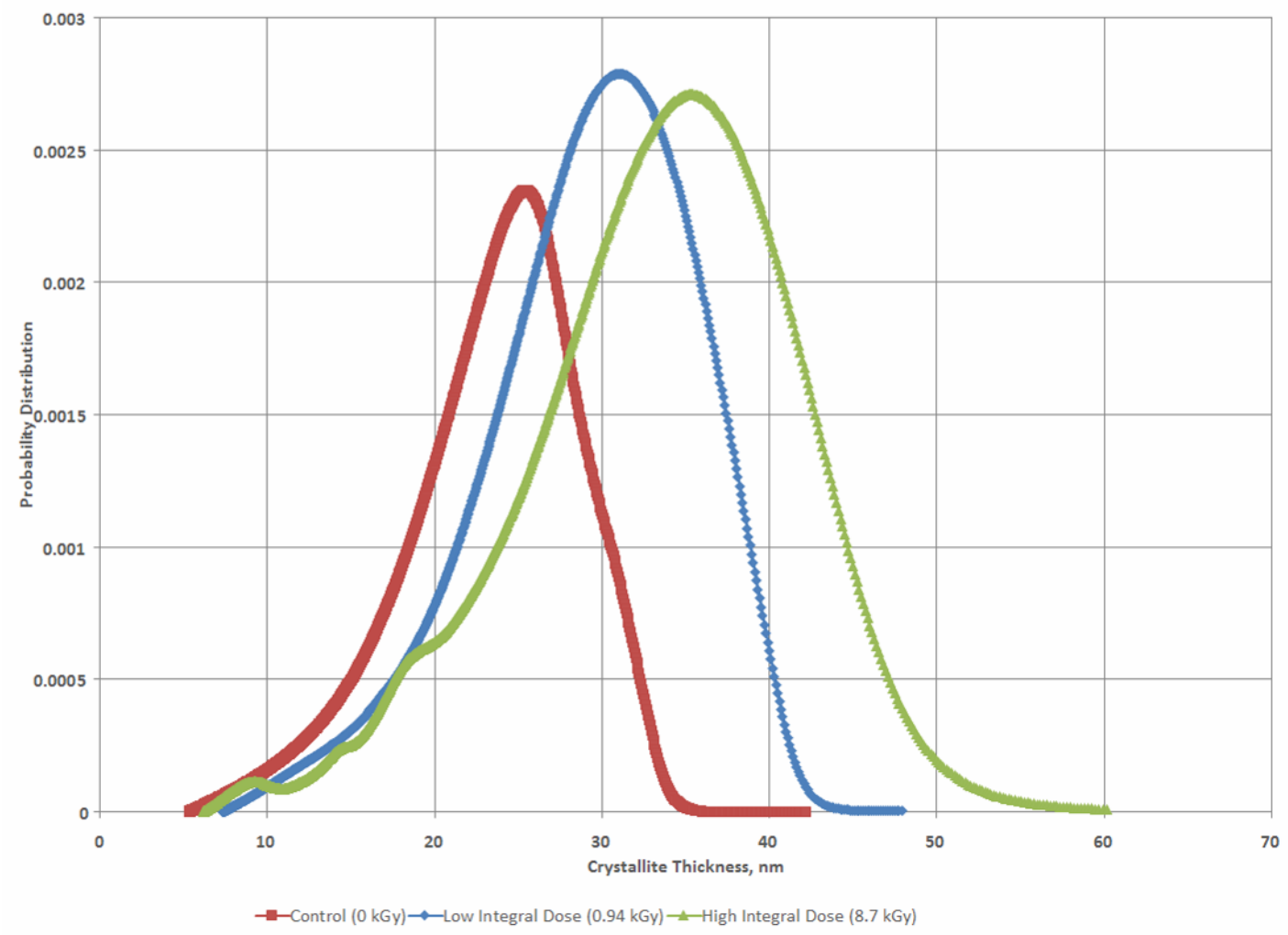

Figure 19: The Second Moment of the Crystallite Thickness Distribution for Run 1

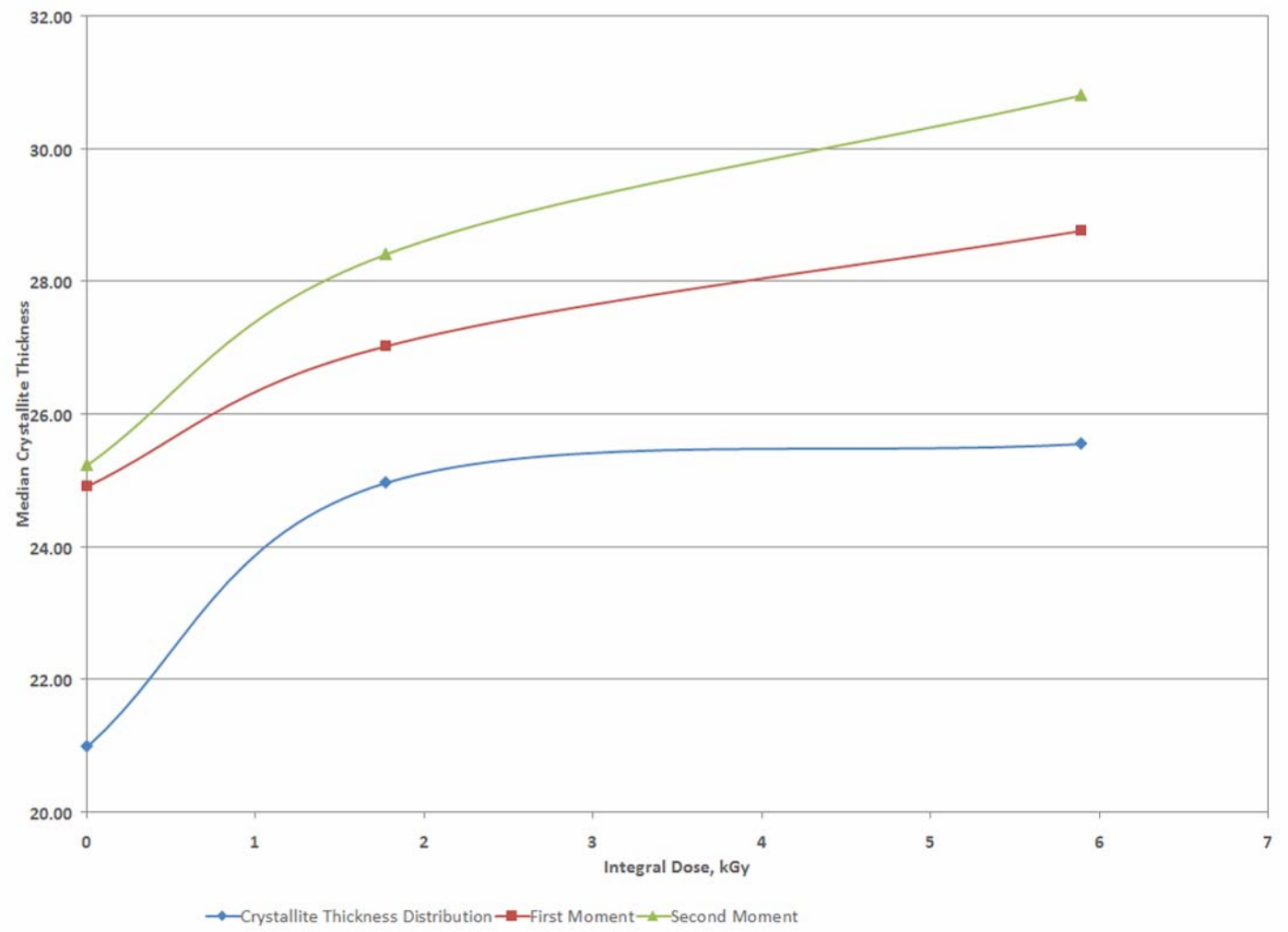

Figure 20: Median Crystallite Thicknesses for Proton Irradiated Samples in the First DSC Run

The weight average crystallite thickness, l_w, increases with increasing radiation (Table 3 and Figure 20): 24.93 ± 3.33 nm, 27.03 ± 1.18 nm (2.1 nm increase from control), and 28.78 ± 2.35 nm (1.75 nm increase from 1.77 kGy) for 0 kGy, 1.77 kGy, and 5.89 kGy, respectively. The z-average crystallite thickness, l_z, increases with increasing radiation (Table 3 and Figure 20): 25.24 ± 2.72 nm, 28.41 ± 1.38 nm (3.17 nm increase from control), and 30.81 ± 2.67 nm (2.4 nm increase from 1.77 kGy) for 0 kGy, 1.77 kGy, and 5.89 kGy, respectively. The crystallizable fraction increases with increasing radiation (Table 4): 0.964 (0 kGy), 0.970 (1.77 kGy), and 0.971 (5.89 kGy). The crystallizable sequence length increases with increasing radiation (Table 4): 82 repeat units (0 kGy), 98 repeat units (1.77 kGy), and 100 repeat units (5.89 kGy).

Melting Behavior of Thermally Treated Proton Irradiated UHMWPE (Run 2)

The effect of integral dose on the melting behavior of thermally treated (run 2) proton irradiated samples is displayed in the percent crystallinity (Table 5), crystallite thickness distribution (Figure 21), the first moment of the distribution (Figure 22), and the second moment of the distribution (Figure 23). The percent crystallinity shows no significant changes (outside of standard deviation), as seen in Table 5. With increasing radiation there is a decrease in the number average crystallite thickness, l_n, (Table 6 and Figure 24): 17.41 ± 1.82 nm, 16.62 ± 0.76 nm (0.79 nm decrease from control), and 12.04 ± 0.18 nm (4.58 nm decrease from 1.77 kGy) for 0 kGy, 1.77 kGy, and 5.89 kGy, respectively.

Table 4: Crystallizable Fraction and Sequence Length for Proton Irradiated Samples in the First DSC Run

Dose (kGy)	Crystallizable Fraction	Sequence Length
0	0.964	82
1.77	0.970	98
5.89	0.971	100

Table 5: Effect of Radiation for Run 2 of Proton Irradiated Samples

Dose (kGy)	Average	Standard Deviation
0	58%	3%
1.77	62%	4%
5.89	55%	4%

Table 6: Median Crystallite Thicknesses for Proton Irradiation Samples in the Second DSC Run

Dose (kGy)	Crystallite Thickness Distribution, l_n		First Moment, l_w		Second Moment, l_z		l_w/l_n	l_z/l_n
	Average	StdDev	Average	StdDev	Average	StdDev		
0.00	17.41	1.82	18.98	2.96	20.09	2.60	1.09	1.15
1.77	16.62	0.76	18.43	0.62	19.57	0.71	1.11	1.18
5.89	12.04	0.18	12.76	0.18	13.27	0.19	1.06	1.10

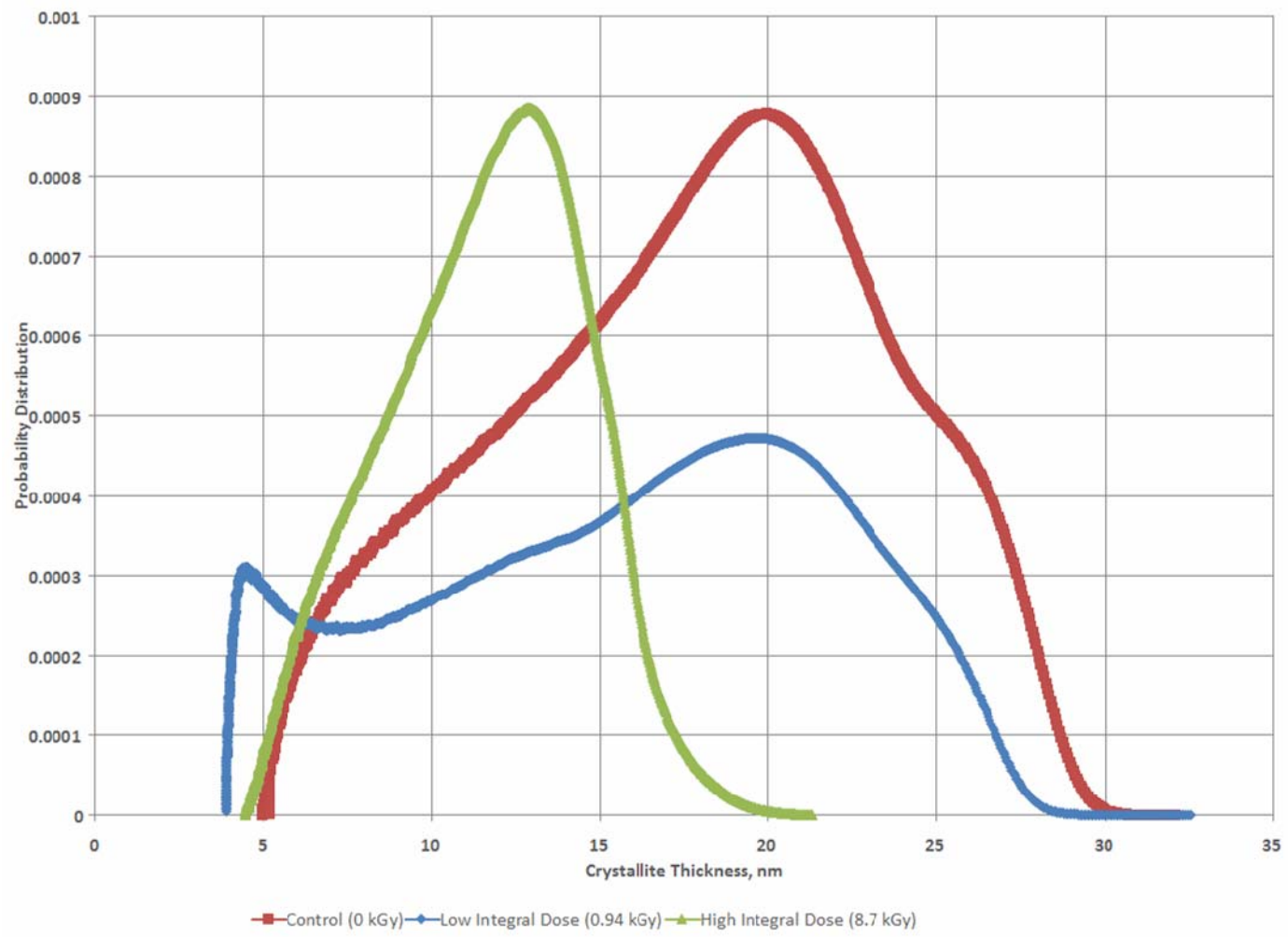

Figure 21: Crystallite Thickness Distribution for Run 2

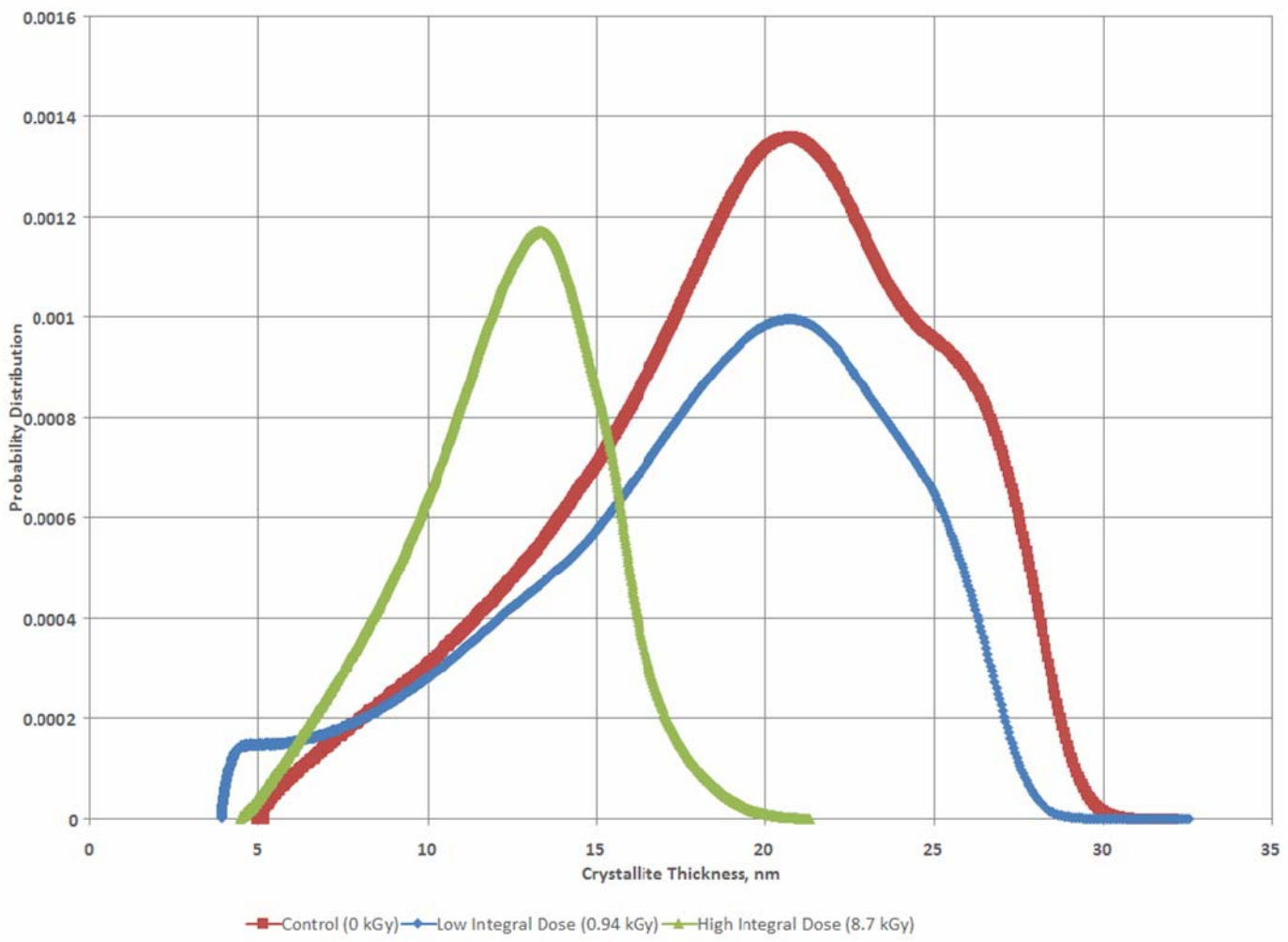

Figure 22: First Moment in Crystallite Thickness Distribution for Run 2

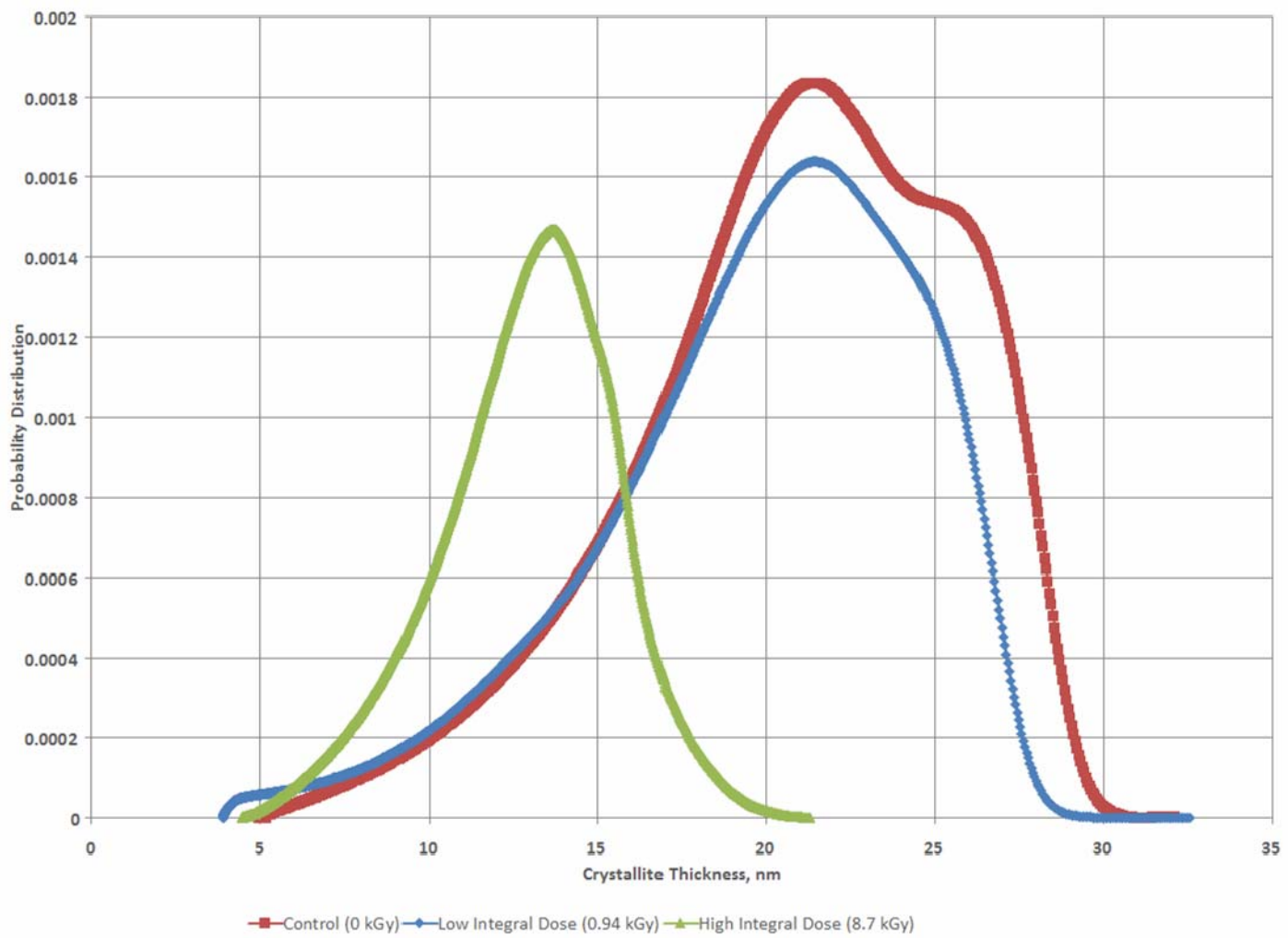

Figure 23: Second Moment in Crystallite Thickness Distribution for Run 2

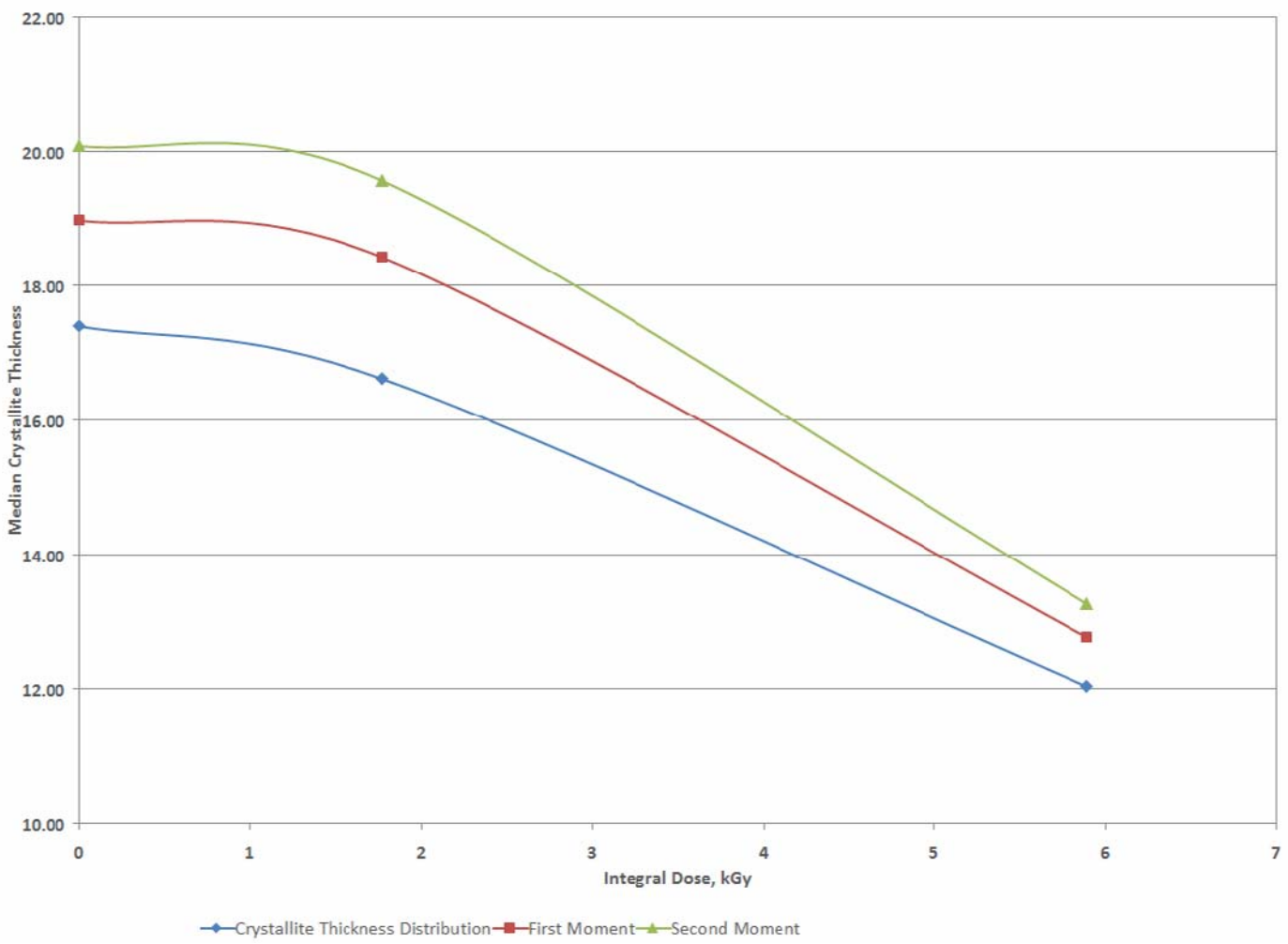

Figure 24: Crystallite Thicknesses for Proton Irradiated Samples in the Second DSC Run

The weight average crystallite thickness, l_w, decreases with increasing radiation (Table 6 and Figure 24): 18.98 ± 2.96 nm, 18.43 ± 0.62 nm (0.55 nm decrease from control), and 12.76 ± 0.18 nm (5.67 nm decrease from 1.77 kGy) for 0 kGy, 1.77 kGy, and 5.89 kGy, respectively. The z-average crystallite thickness, l_z, decreases with increasing radiation (Table 6 and Figure 24): 20.09 ± 2.60 nm, 19.57 ± 0.71 nm (0.52 nm decrease from control), and 13.27 ± 0.19 nm (6.3 nm decrease from 1.77 kGy) for 0 kGy, 1.77 kGy, and 5.89 kGy, respectively. The crystallizable fraction decreases with increasing radiation (Table 7): 0.956 (0 kGy), 0.954 (1.77 kGy), and 0.937 (5.89 kGy) . The crystallizable sequence length decreases with increasing radiation (Table 7): 68 units (0 kGy), 65 units (1.77 kGy), and 47 units (5.89 kGy).

Table 7: Crystallizable Fraction and Sequence Length for Proton Irradiation Samples in the Second DSC Run

Dose (kGy)	Crystallizable Fraction	Sequence Length
0	0.956	68
1.77	0.954	65
5.89	0.937	47

5. Results of Gamma Irradiation

Differential Scanning Calorimeter (DSC)

The DSC endotherms for the gamma irradiated samples are displayed in Appendix 3 (Figure 186 to Figure 189). The crystallite thickness probability distributions are displayed in Appendix 3 (Figure 190 to Figure 199). The area calculations for the gamma irradiated samples are displayed in Appendix 4 (Figure 200 to Figure 229).

Effect of Dose Rate

Dose rate is one of the main parameters that must be addressed during a polymer irradiation study. The effect of dose rate on the surface of the UHMWPE sample irradiated at 75 kGy (Figure 25) is not significant, as seen by the increase in median crystallite thickness, l_n, from 26.98 nm to 27.21 nm (0.23 nm increase in crystallite thickness) for high dose rate (Table 8) and low dose rate (Table 9), respectively. The effect of dose rate on the surface of UHMWPE irradiated at 150 kGy (Figure 26) is significant, as seen by the increase in median crystallite thickness, l_n, from 26.30 nm to 29.67 nm (3.37 nm increase in crystallite thickness) for high dose rate (Table 8) and low dose rate (Table 9), respectively. On the surface, the percent crystallinity increases more for a given integral dose at low dose rates (75 kGy: 64% and 150 kGy: 68%) than high dose rates (75 kGy: 62% and 150 kGy: 65%), as shown in Table 10.

Table 8: Median Crystallite Thickness for the Surface of the Gamma High Dose Rate Irradiation

Dose (kGy)	Crystallite Thickness Distribution, l_n	First Moment, l_w	Second Moment, l_z	l_w/l_n	l_z/l_n
0	19.16	21.55	23.00	1.12	1.20
75	26.98	30.46	32.66	1.13	1.21
150	26.30	30.86	33.24	1.17	1.26

Table 9: Median Crystallite Thickness for the Surface of the Gamma Low Dose Rate Irradiation

Dose (kGy)	Crystallite Thickness Distribution, l_n	First Moment, l_w	Second Moment, l_z	l_w/l_n	l_z/l_n
0	19.16	21.55	23.00	1.12	1.20
75	27.21	30.47	32.66	1.12	1.20
150	29.67	33.87	36.69	1.14	1.24

Table 10: Effect of Radiation on the Surface of the Gamma Irradiated Samples

Dose	Low Dose Rate	High Dose Rate
0	51.22%	51.22%
75	64.15%	62.21%
150	67.65%	65.53%

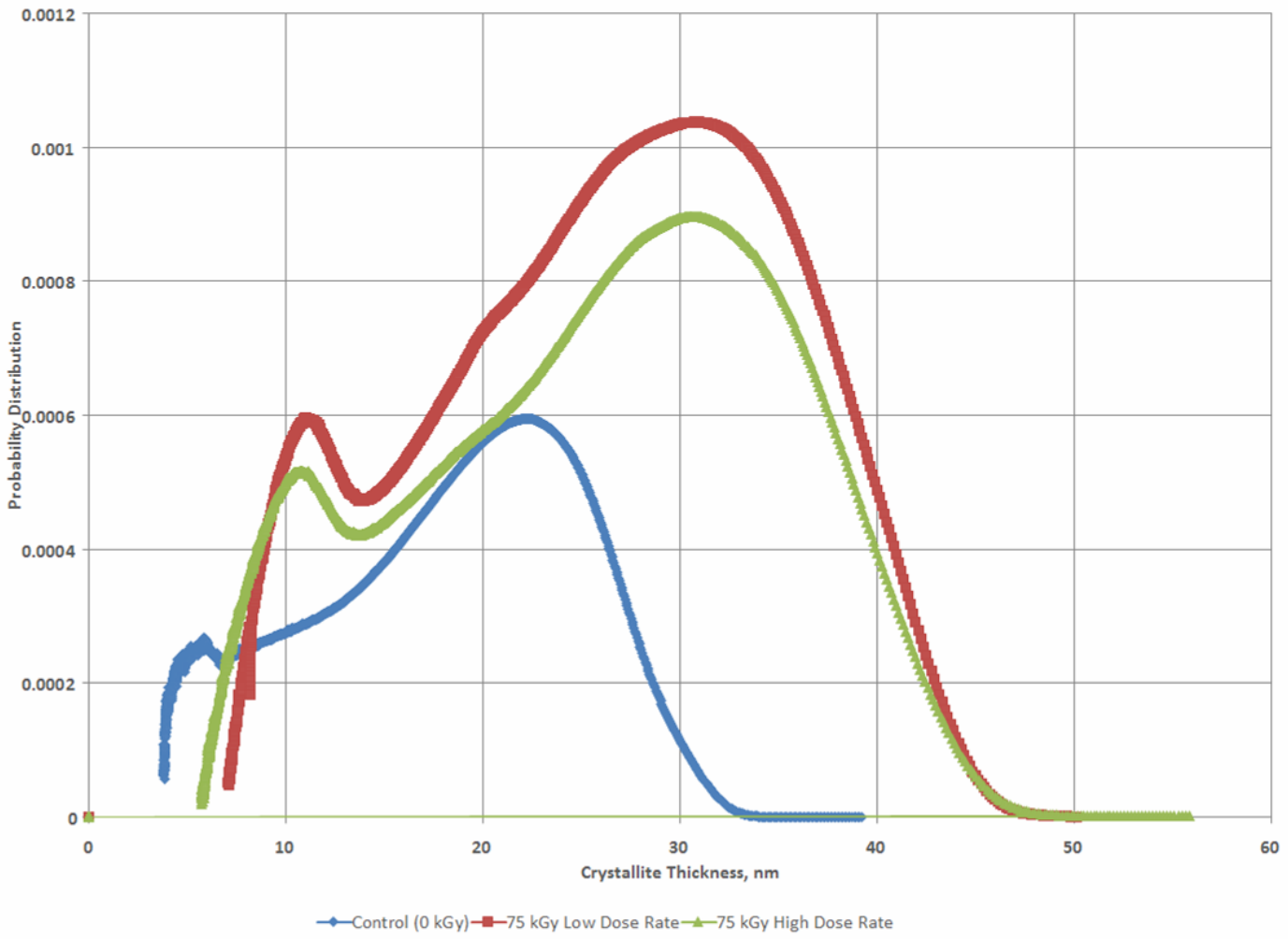

Figure 25: Effect of Dose Rate on the Surface of the 75 kGy Gamma Irradiated Crystallite Thickness Distribution

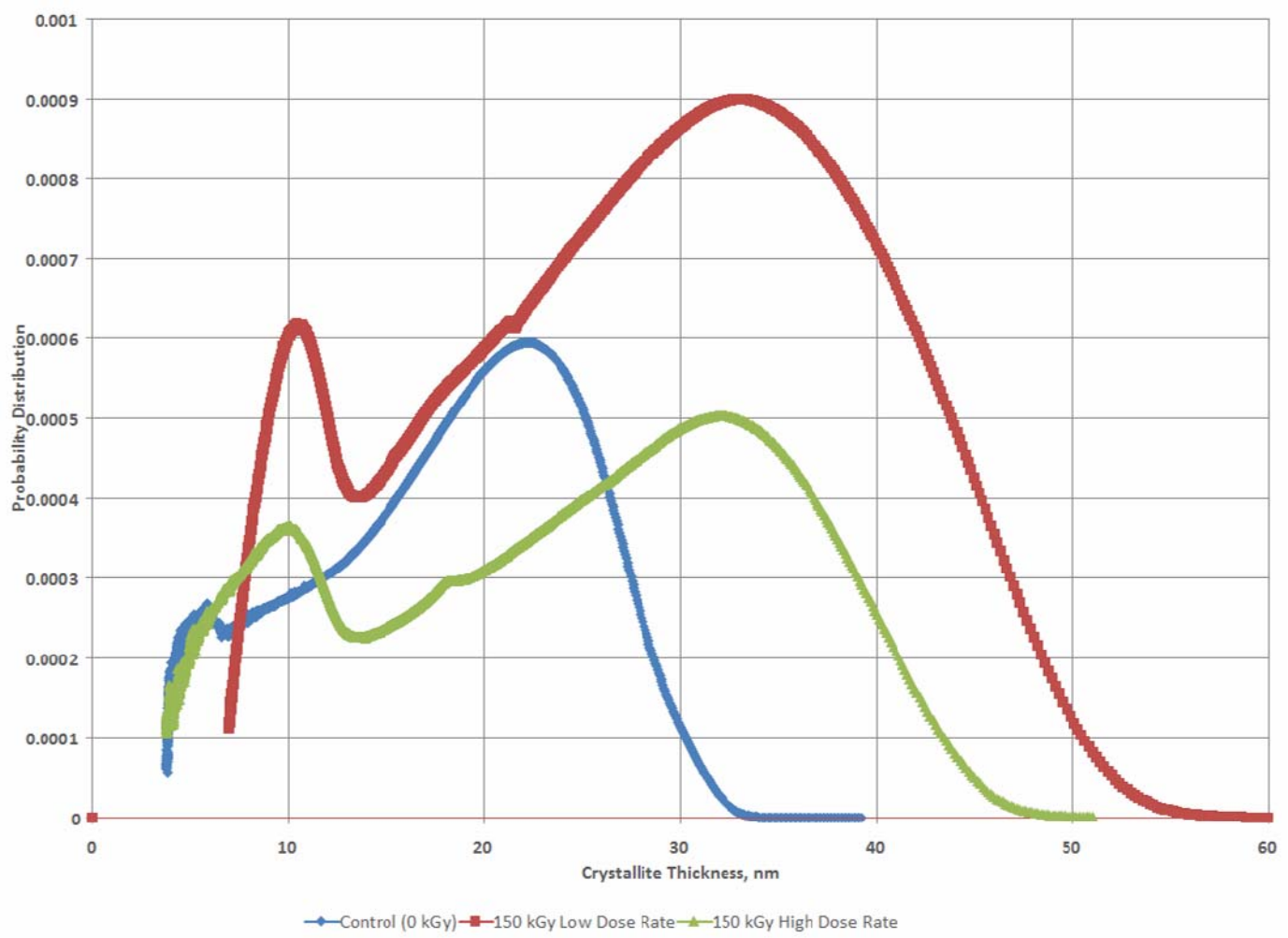

Figure 26: Effect of Dose Rate on the Surface of the 150 kGy Gamma Irradiated Crystallite Thickness Distribution

The molecular modification induced by gamma irradiation at different dose rates was determined by comparing crystallite size on sections obtained from the center of the sample. The effect of dose rate on the center at 75 kGy (Figure 27, Figure 33, Figure 34, and Figure 35) induced significant changes, as seen by the increase in median crystallite thickness, l_n, from 30.04 nm to 32.81 nm (2.77 nm increase in crystallite thickness) for samples subjected to high dose rate (Table 11) and low dose rate (Table 12), respectively. At integral dose of 150 kGy (Figure 28, Figure 33, Figure 34, and Figure 35) the effect of dose rate becomes very apparent, as seen by the decrease in median crystallite thickness, l_n, from 40.01 nm to 34.62 nm (5.39 nm decrease in crystallite thickness) for high dose rate (Table 11) and low dose rate (Table 12) samples, respectively.

High Dose Rate

The effect of high gamma irradiation dose rate on the surface of the UHMWPE sample produces the same trend in median crystallite thickness distribution, crystallizable fraction, and sequence length; this trend is an increase in the values of the aforementioned parameters from the control (0 kGy to 75 kGy), but no significant increase from 75 kGy to 150 kGy, as seen in Figure 29. The effect of integral dose for a high dose rate (2.9 kGy hr^{-1}) on the surface of the sample is displayed in the crystallite thickness distribution, l_n, (Figure 30) the first moment of the distribution, l_w, (Figure 31) and the second moment of the distribution, l_z, (Figure 32).

Table 11: Median Crystallite Thickness for the Center of the Gamma High Dose Rate Irradiation

Dose (kGy)	Crystallite Thickness Distribution, l_n	First Moment, l_w	Second Moment, l_z	l_w/l_n	l_z/l_n
0	20.52	22.19	23.42	1.08	1.14
75	30.04	40.61	45.60	1.35	1.52
150	40.01	51.32	61.06	1.28	1.53

Table 12: Median Crystallite Thickness for the Center of the Gamma Low Dose Rate Irradiation

Dose (kGy)	Crystallite Thickness Distribution, l_n	First Moment, l_w	Second Moment, l_z	l_w/l_n	l_z/l_n
0	20.52	22.19	23.42	1.08	1.14
75	32.81	37.78	41.74	1.15	1.27
150	34.62	43.05	53.33	1.24	1.54

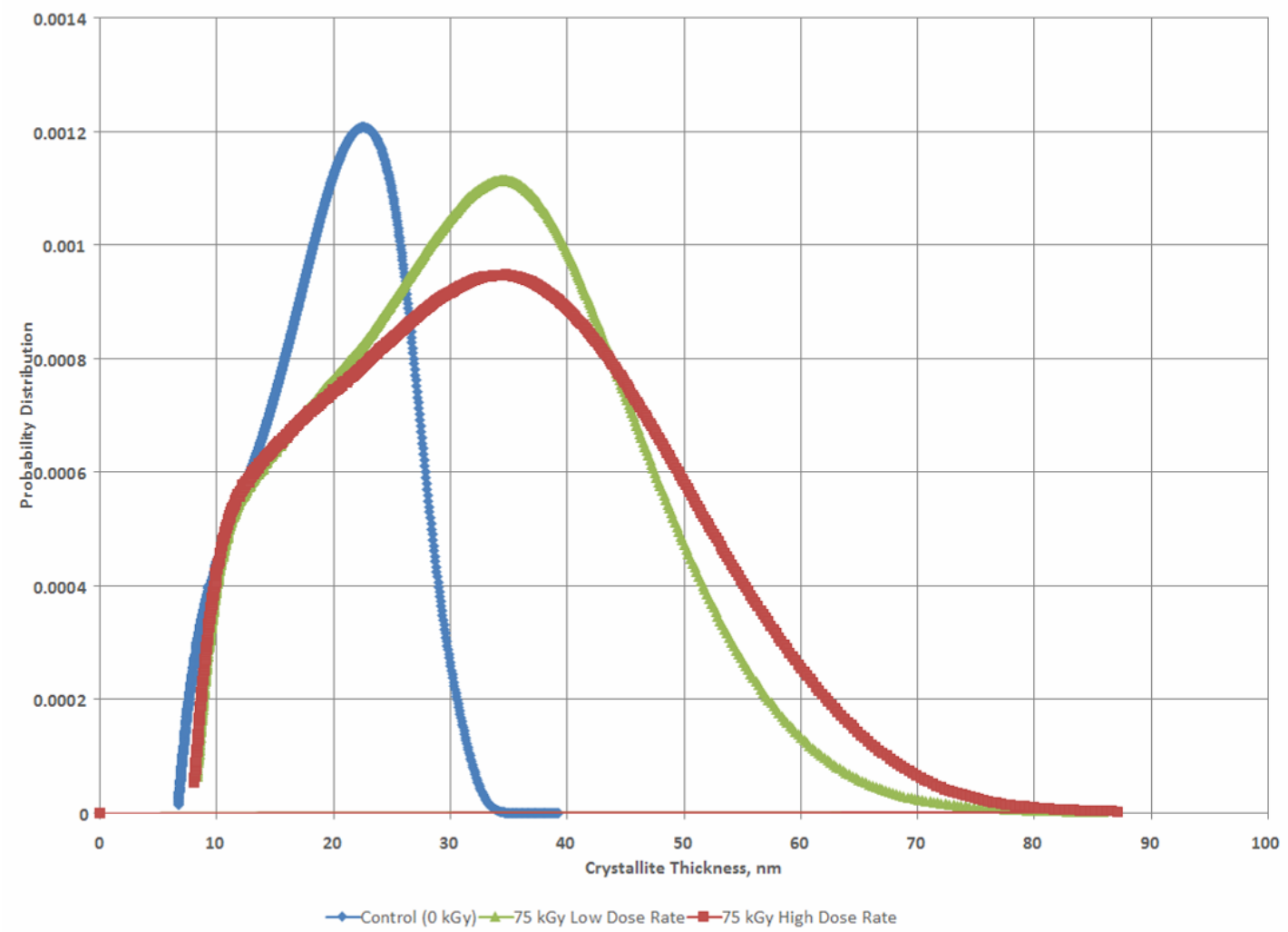

Figure 27: Effect of Dose Rate on the Center of the 75 kGy Gamma Irradiated Crystallite Thickness Distribution

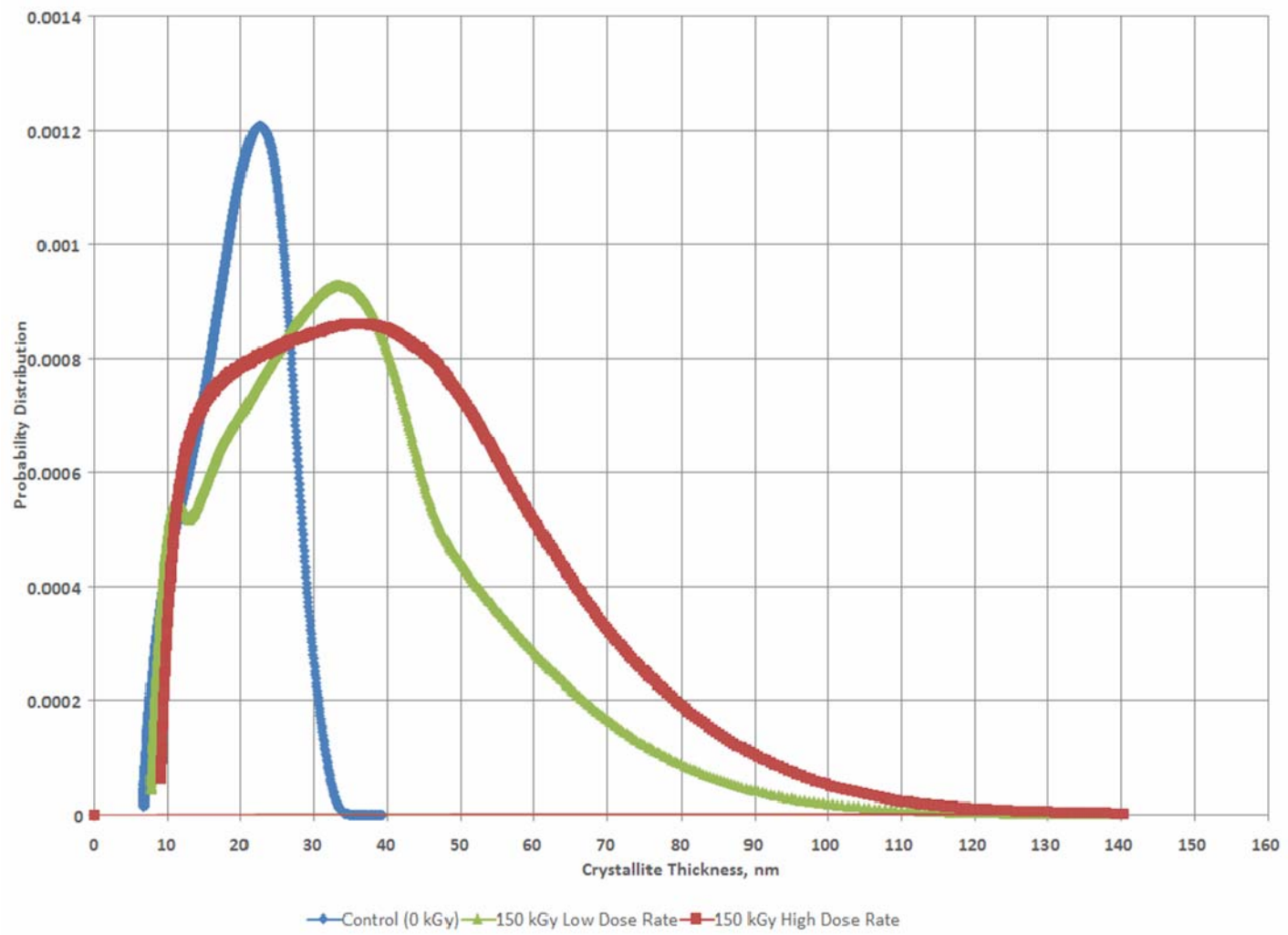

Figure 28: Effect of Dose Rate on the Center of the 150 kGy Gamma Irradiated Crystallite Thickness Distribution

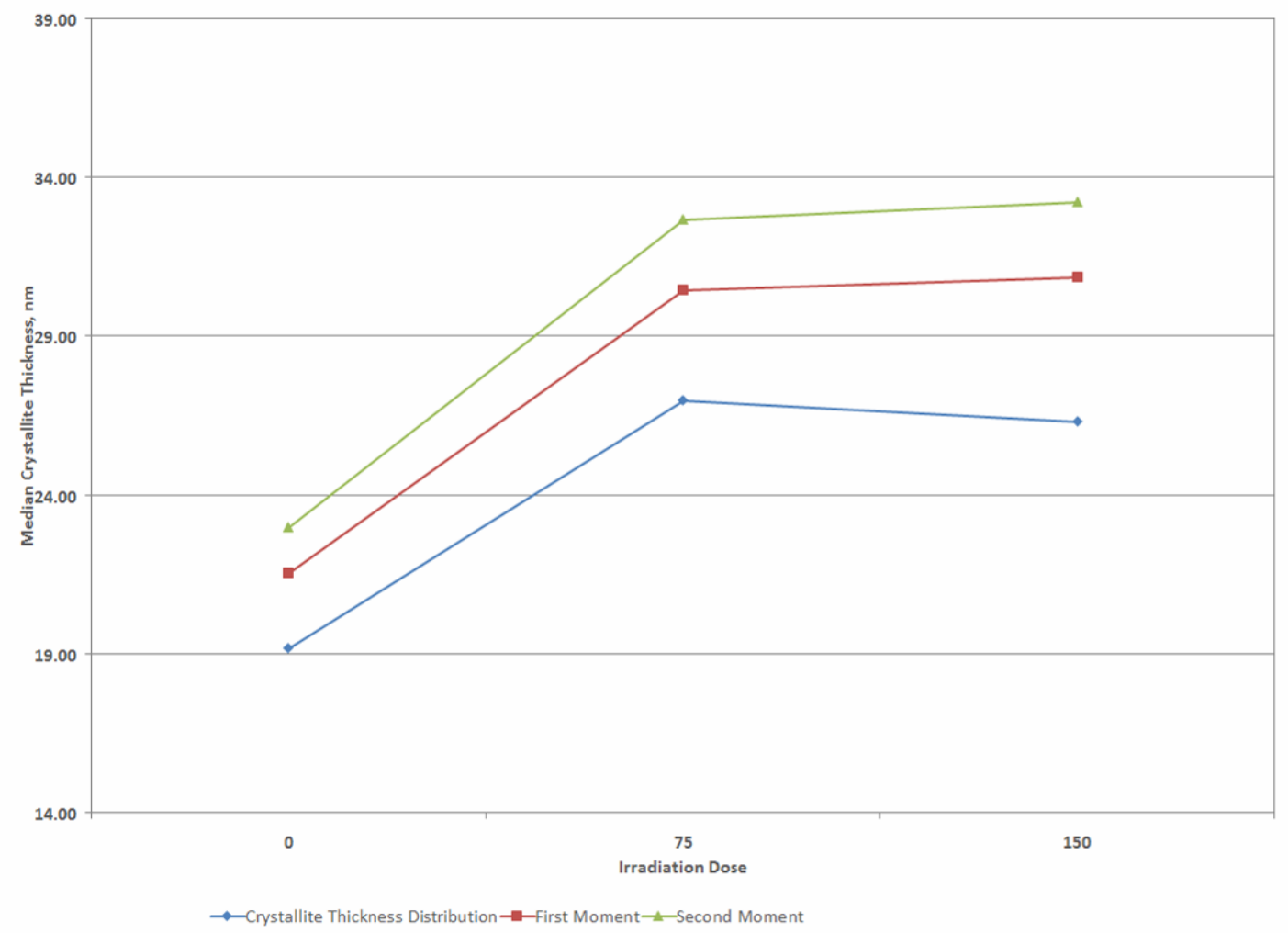

Figure 29: Median Crystallite Thickness for the Surface of the Gamma High Dose Rate Irradiation

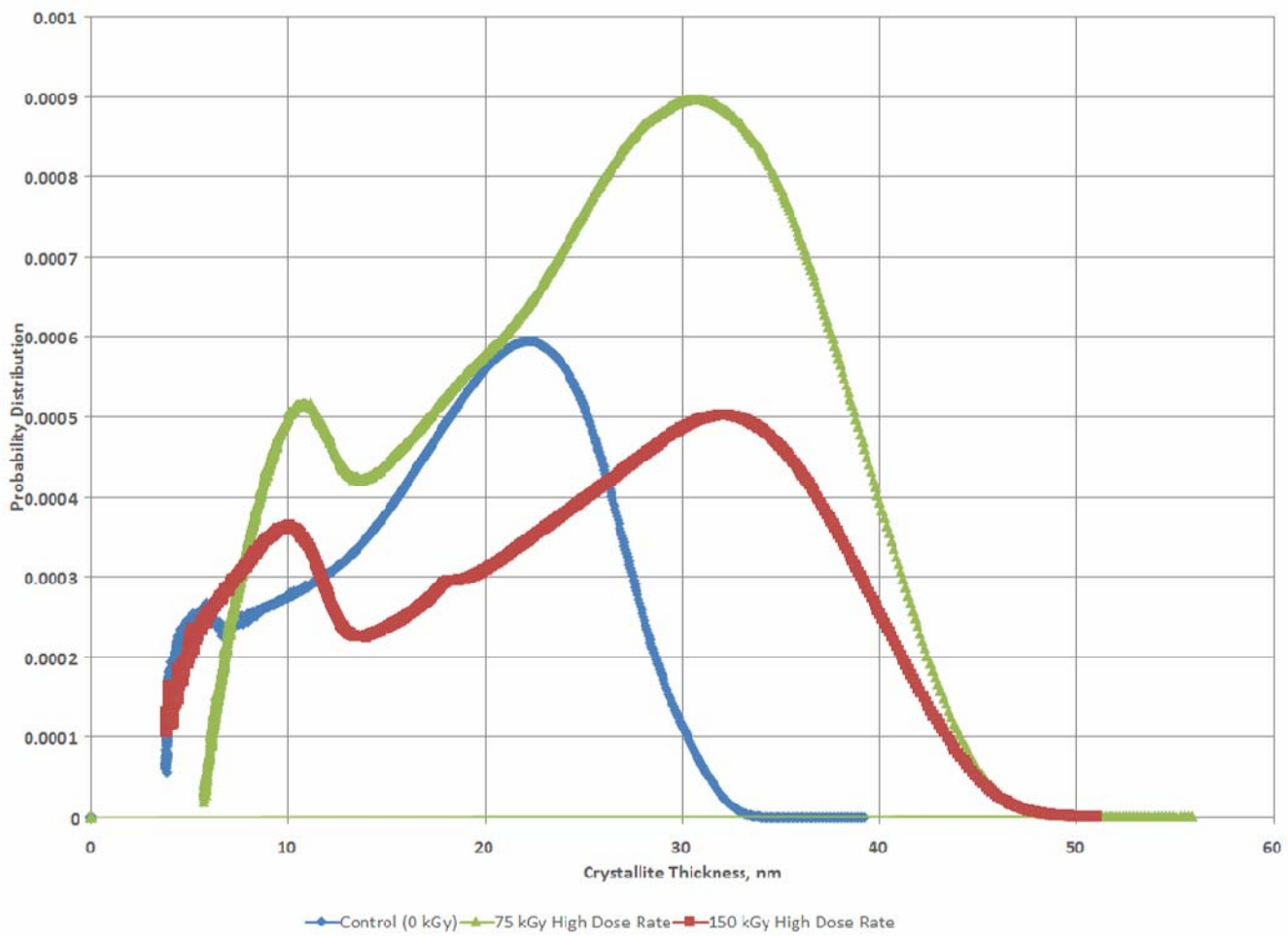

Figure 30: Effect of Integral Dose on the Surface of the Crystallite Thickness Distribution (High Dose Rate)

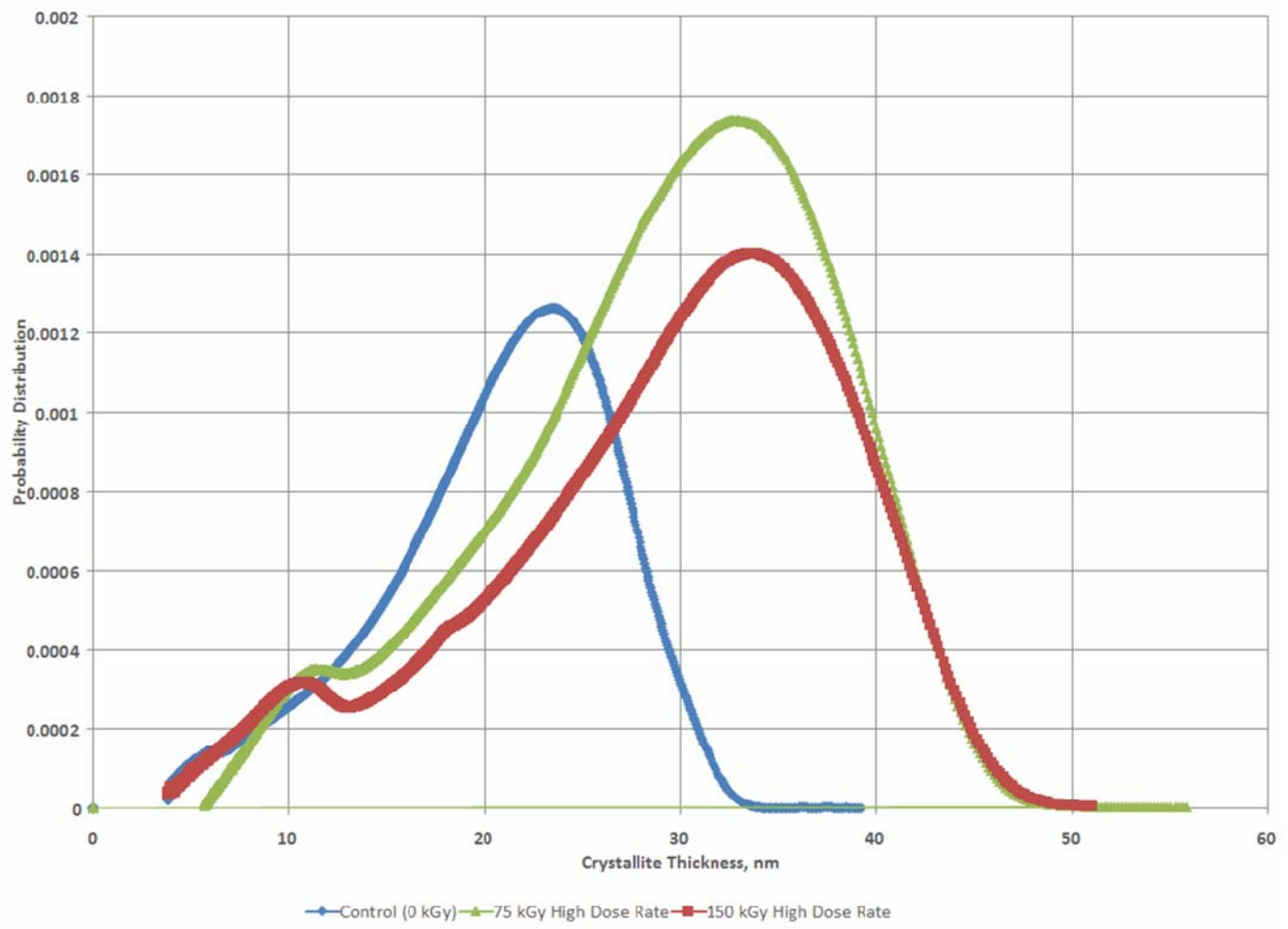

Figure 31: Effect of Integral Dose on the Surface of the First Moment of Crystallite Thickness Distribution (High Dose Rate)

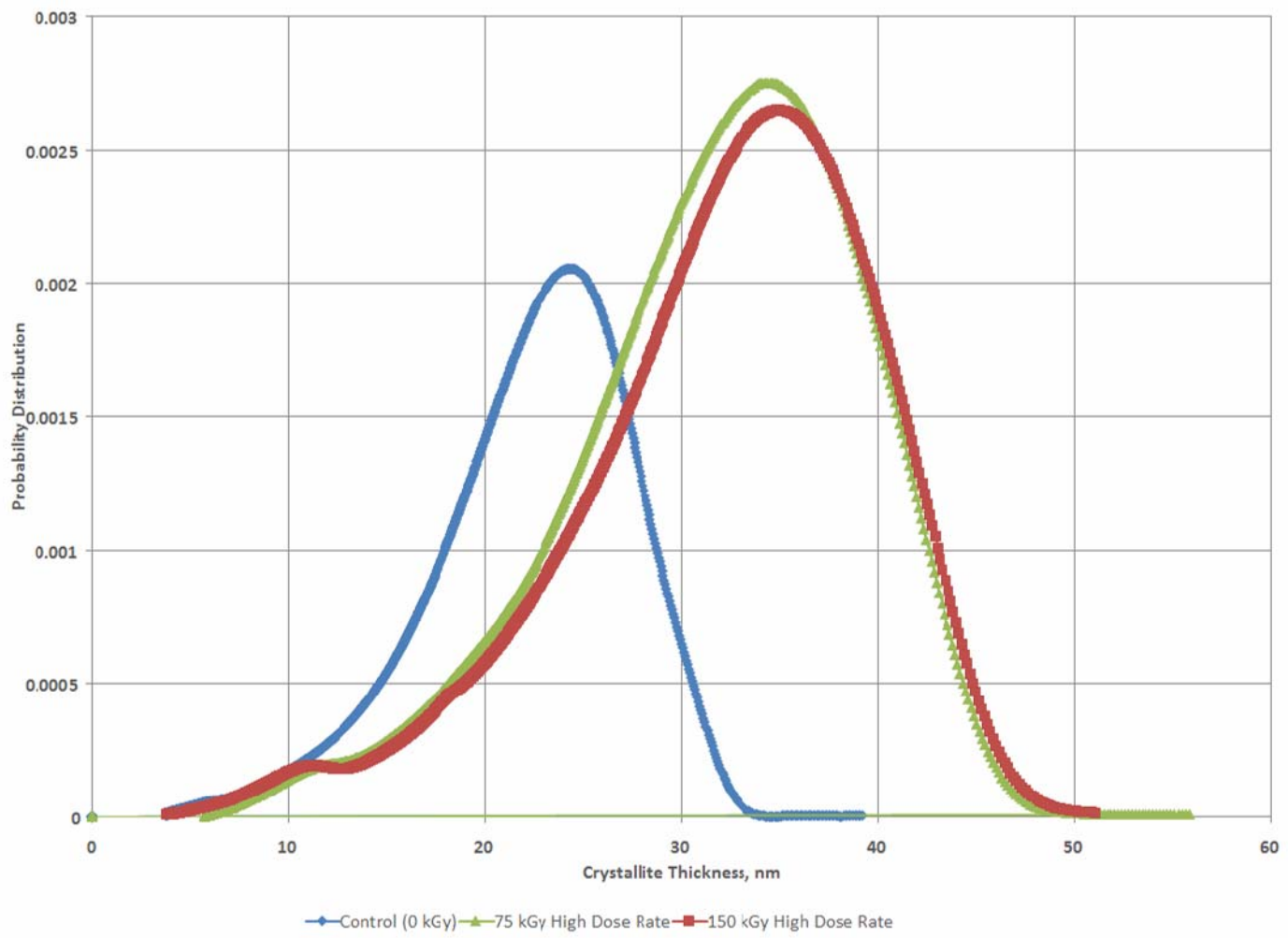

Figure 32: Effect of Integral Dose on the Surface of the Second Moment of Crystallite Thickness Distribution (High Dose Rate)

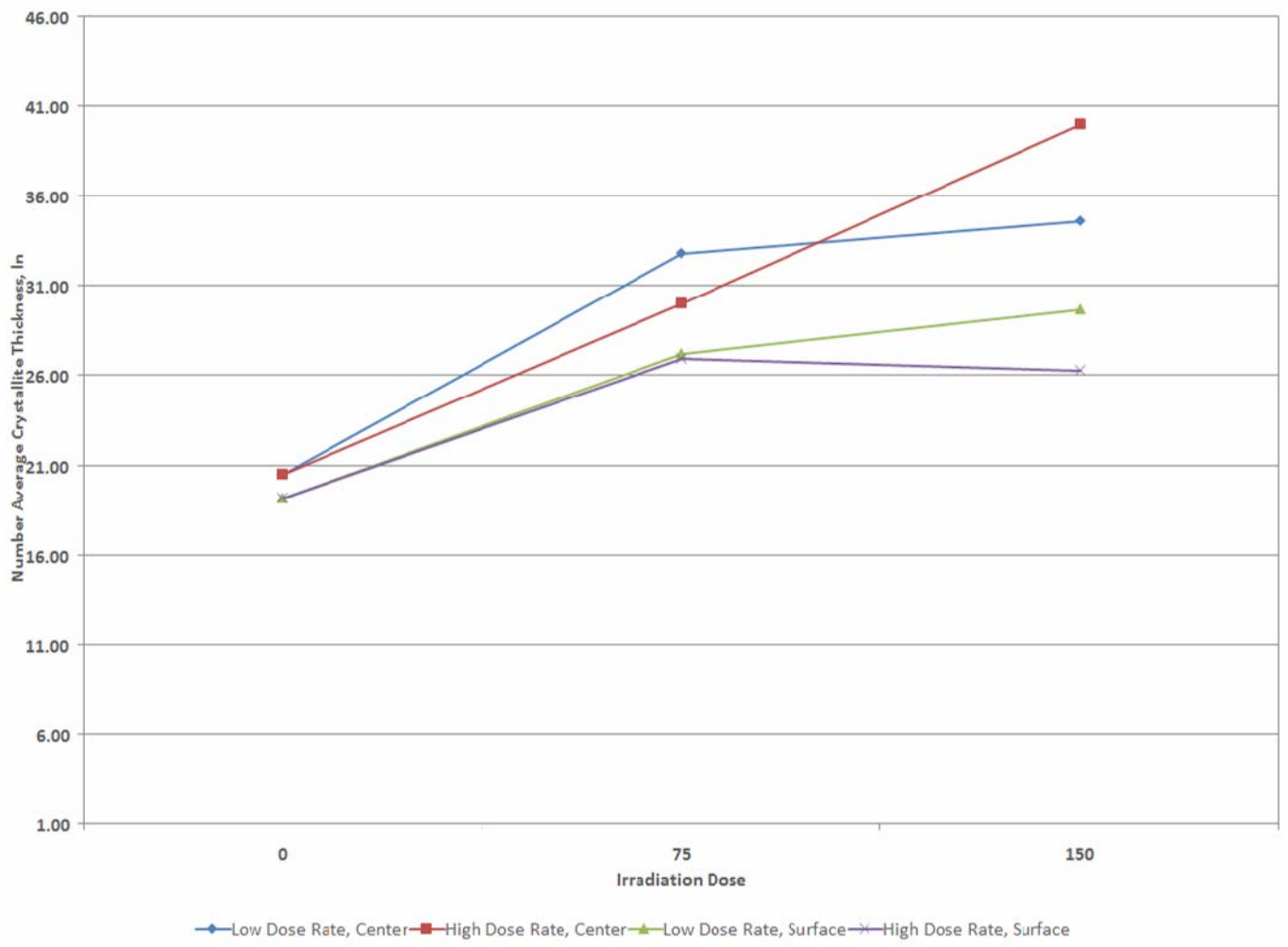

Figure 33: Number Average of Crystallite Thickness, l_n, for Gamma Irradiated UHMWPE

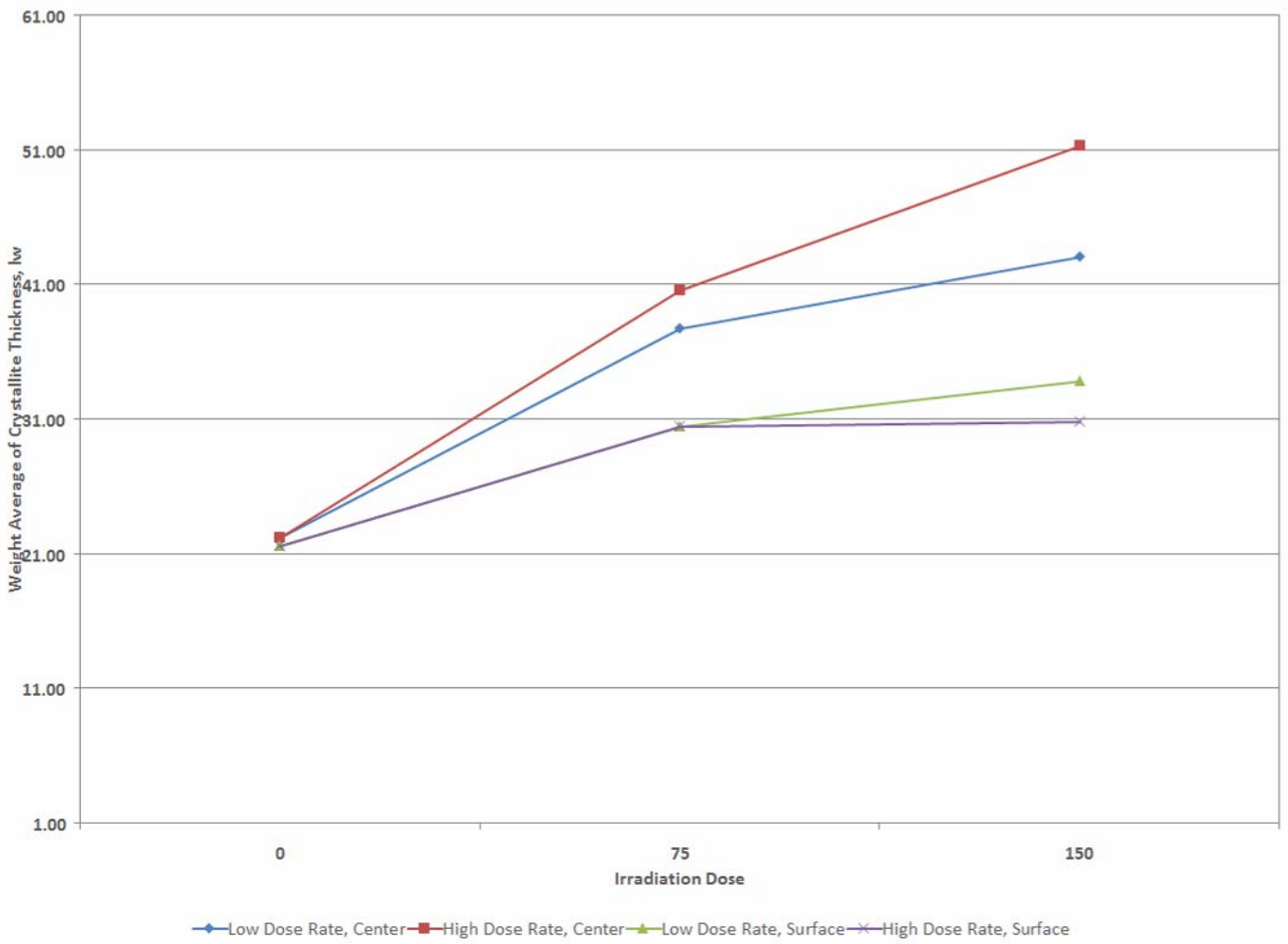

Figure 34: Weight Average of Crystallite Thickness, l_w, for Gamma Irradiated UHMWPE

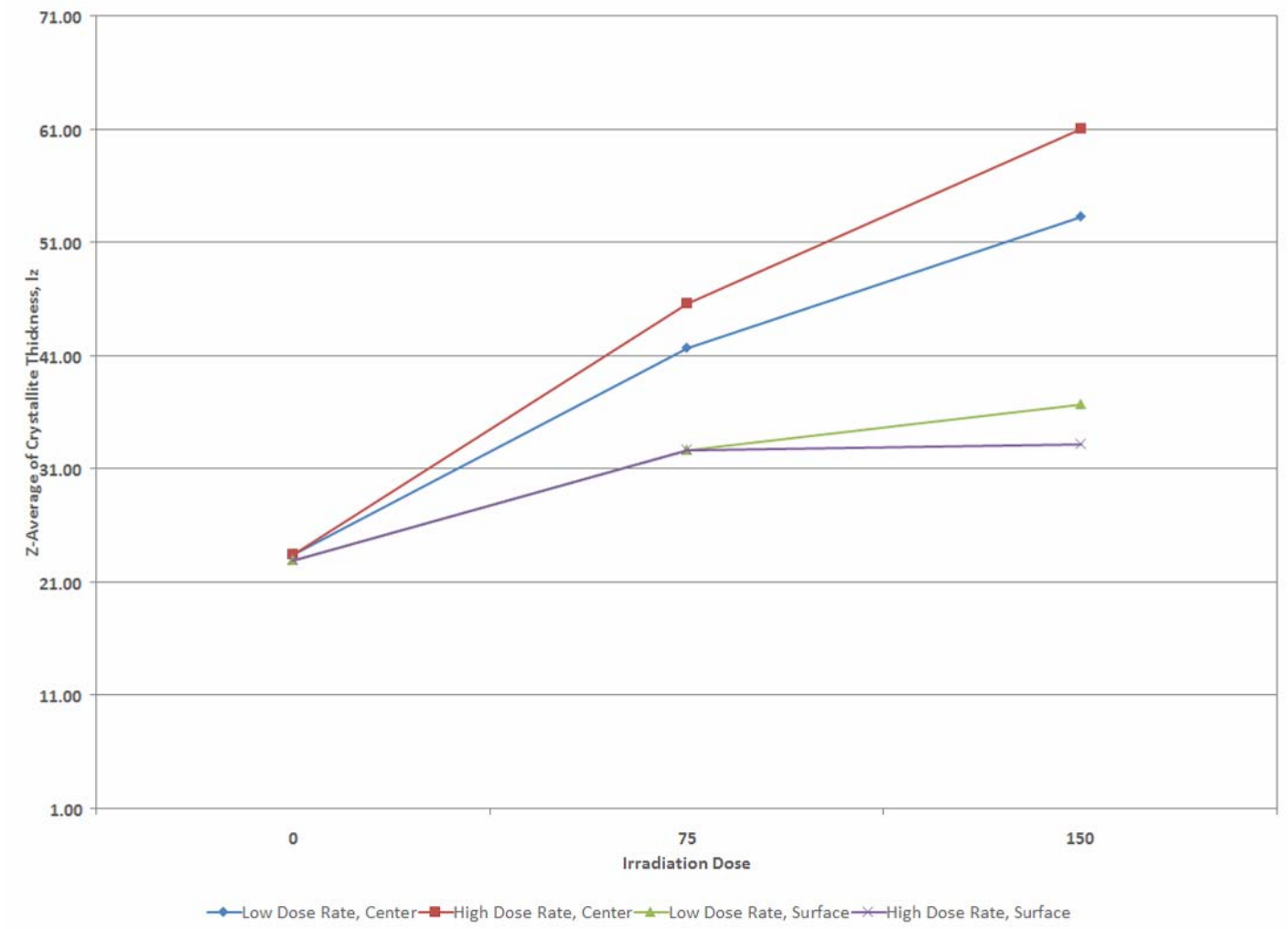

Figure 35: Z-Average of Crystallite Thickness, l_z, for Gamma Irradiated UHMWPE

The median crystallite thickness, l_n, on the surface (Table 8 and Figure 29) increases from 19.16 nm to 26.98 nm (7.82 nm increase from control) and 26.30 nm (7.14 nm increase from control) for 0 kGy, 75 kGy, and 150 kGy, respectively. The first moment, l_w, on the surface (Table 8 and Figure 29) also increases from 21.55 nm to 30.46 nm (8.91 nm increase from control) and 30.86 nm (9.31 nm increase from control) for 0 kGy, 75 kGy, and 150 kGy, respectively. The second moment, l_z, on the surface (Table 8 and Figure 29) also increases from 23.00 nm to 32.66 nm (9.66 nm increase from control) and 33.24 nm (10.24 nm increase from control) for 0 kGy, 75 kGy, and 150 kGy, respectively. The ratio of l_n to l_w and l_z both increase from 75 kGy to 150 kGy, as seen in Figure 40 and Table 8. The crystallizable sequence length (Table 13) increases from 75 to 106 and 103 for 0 kGy, 75 kGy, and 150 kGy, respectively. The crystallizable fraction (Table 13) increases from 0.961 to 0.972 and 0.971 for 0 kGy, 75 kGy, and 150 kGy, respectively. On the surface, there is an increase in percent crystallinity (Table 10): 51% to 62% to 65% for 0 kGy, 75 kGy, and 150 kGy, respectively.

The effect of integral dose for a high dose rate on the center of the sample is displayed in the crystallite thickness distribution (Figure 36) the first moment of the distribution (Figure 37) and second moment of the distribution (Figure 38). The median crystallite thickness, l_n, (Table 11 and Figure 39) increases with integral radiation dose: 20.52 nm to 30.04 nm (9.97 nm increase from control) to 40.01 nm (9.52 nm increase from 75 kGy) for 0 kGy, 75 kGy, and 150 kGy, respectively.

Table 13: Crystallizable Fraction and Sequence Length for the Surface of the Gamma High Dose Rate Irradiation

Dose (kGy)	Crystallizable Fraction	Sequence Length
0	0.961	75
75	0.972	106
150	0.971	103

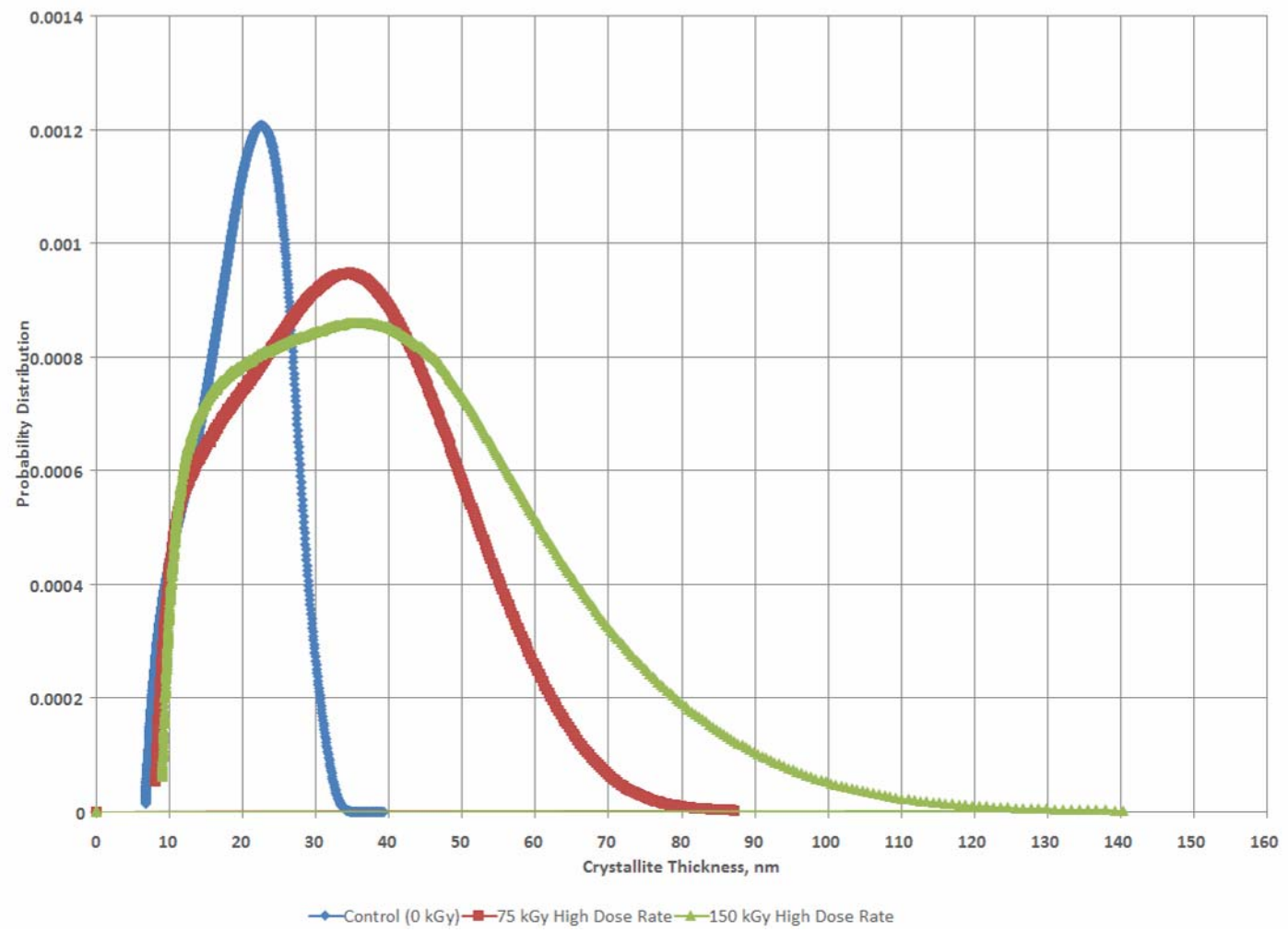

Figure 36: Effect of Integral Dose on the Center of the Crystallite Thickness Distribution (High Dose Rate)

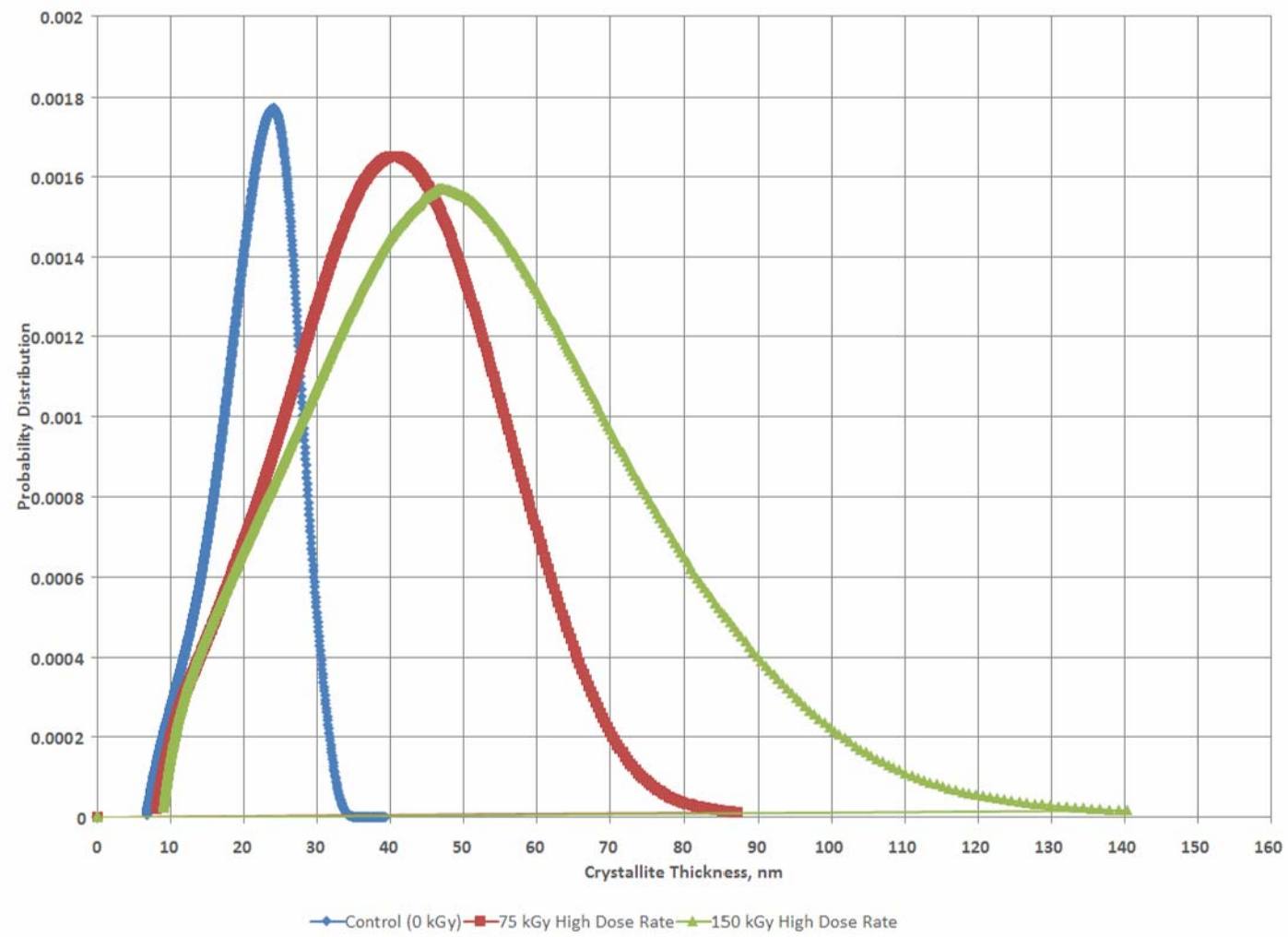

Figure 37: Effect of Integral Dose on the Center of the First Moment of Crystallite Thickness Distribution (High Dose Rate)

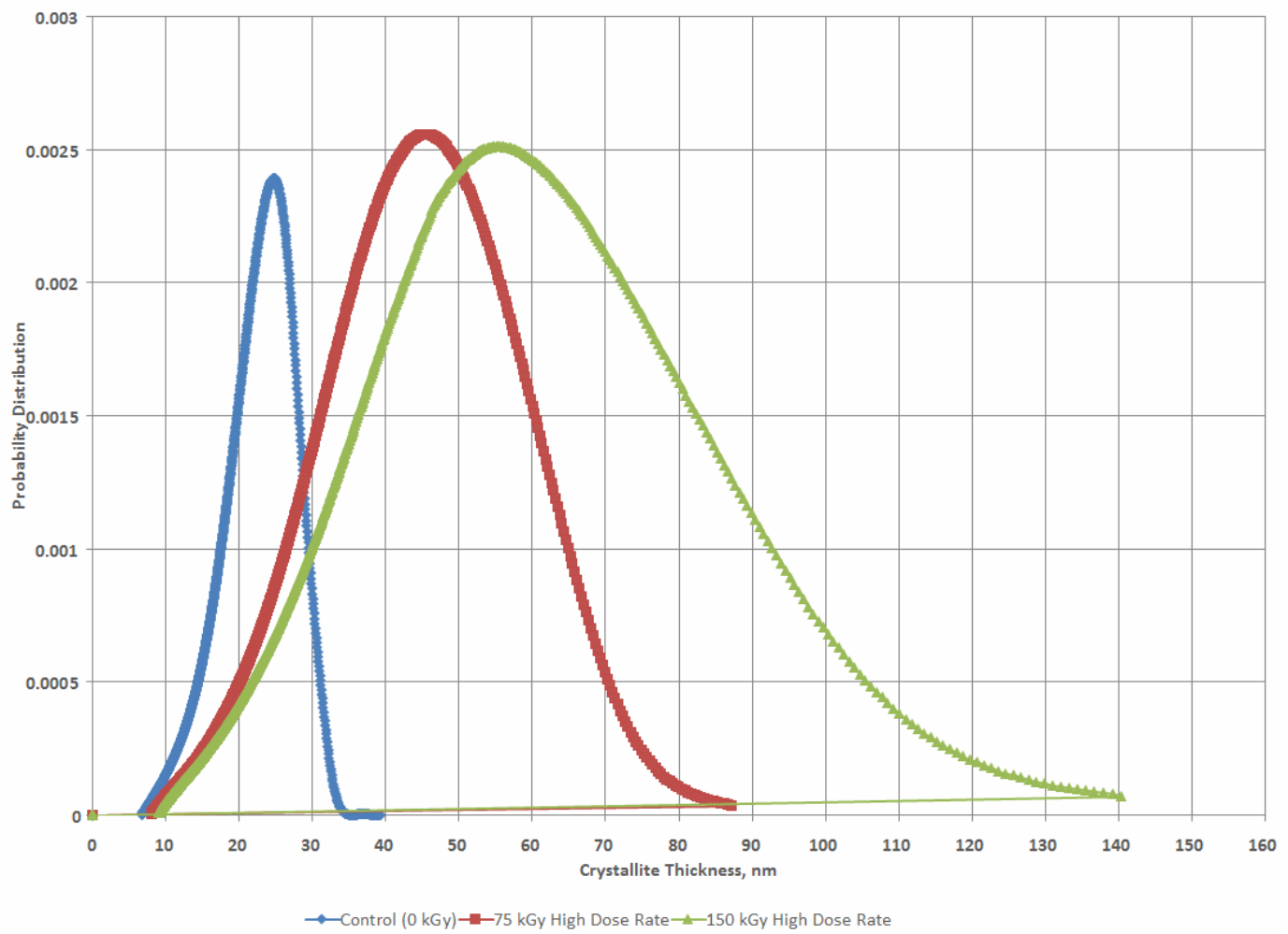

Figure 38: Effect of Integral Dose on the Center of the Second Moment of Crystallite Thickness Distribution (High Dose Rate)

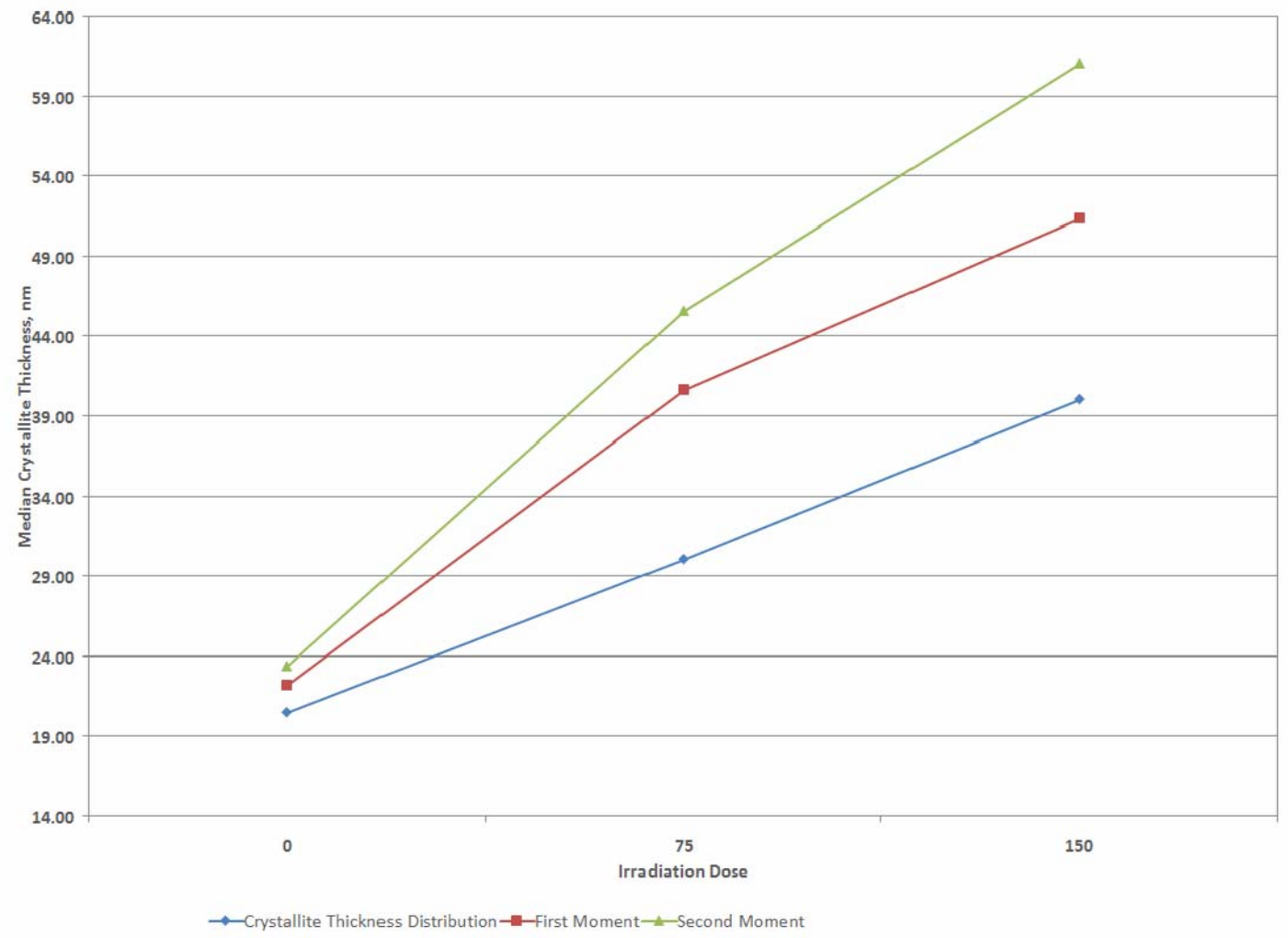

Figure 39: Median Crystallite Thickness for the Center of the Gamma High Dose Rate Irradiation

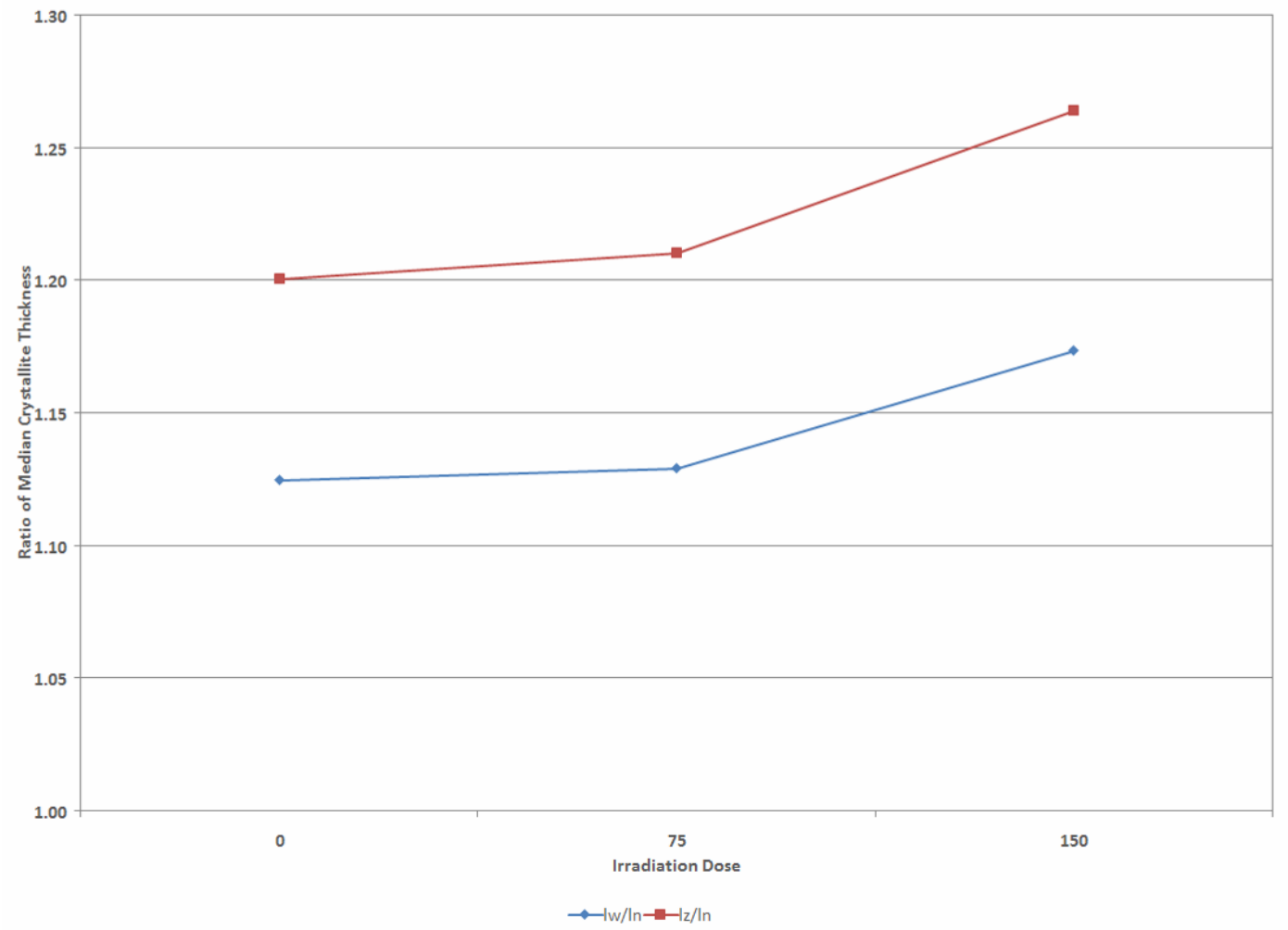

Figure 40: Ratio of Median Crystallite Thicknesses for the Surface of the High Dose Rate Gamma Irradiation

The weight-average median crystallite thickness, l_w, (Table 11 and Figure 39) increases with integral radiation dose: 20.19 nm to 40.61 nm (20.42 nm increase from control) to 51.32 nm (10.71 nm increase from 75 kGy) for 0 kGy, 75 kGy, and 150 kGy, respectively. As the moment of the crystallite thickness increases, the separation of the values increases as seen in the increased separation in the z-average crystallite thickness (l_z) (Table 11 and Figure 39): 23.42 nm to 45.60 nm (15.46 nm increase from control) to 61.06 nm (22.18 nm increase from 75 kGy) for 0 kGy, 75 kGy, and 150 kGy, respectively. The ratio of l_n to l_w and l_z (breadth of the probability distribution) both increase from 0 kGy to 75 kGy, but levels off from 75 kGy to 150 kGy, as seen in Table 11 and Figure 41. The crystallizable sequence length (Table 14) increases from 80 to 129 and 136 for 0 kGy, 75 kGy, and 150 kGy, respectively. The crystallizable fraction (Table 14) increases from 0.963 to 0.977 and 0.978 for 0 kGy, 75 kGy, and 150 kGy, respectively. In the center, there is very little change in percent crystallinity (Table 15): 55% to 56% to 58% for 0 kGy, 75 kGy, and 150 kGy, respectively.

Low Dose Rate

The effect of low dose rate gamma irradiation on the surface of the sample produces the similar trend in median crystallite thickness distribution, crystallizable fraction, and sequence length for the number, weight, and z averages. In the sections removed from the center of the sample all variables show an increase in value with increasing integral radiation dose.

Table 14: Crystallizable Fraction and Sequence Length for Gamma High Dose Rate Irradiation (DSC Run 2)

Dose (kGy)	Crystallizable Fraction	Sequence Length
0	0.963	80
75	0.977	129
150	0.978	136

Table 15: Effect of Radiation on the Middle of the Gamma Irradiated Samples

Dose	Low Dose Rate	High Dose Rate
0	55.61%	55.61%
75	56.925	56.25%
150	59.72%	57.70%

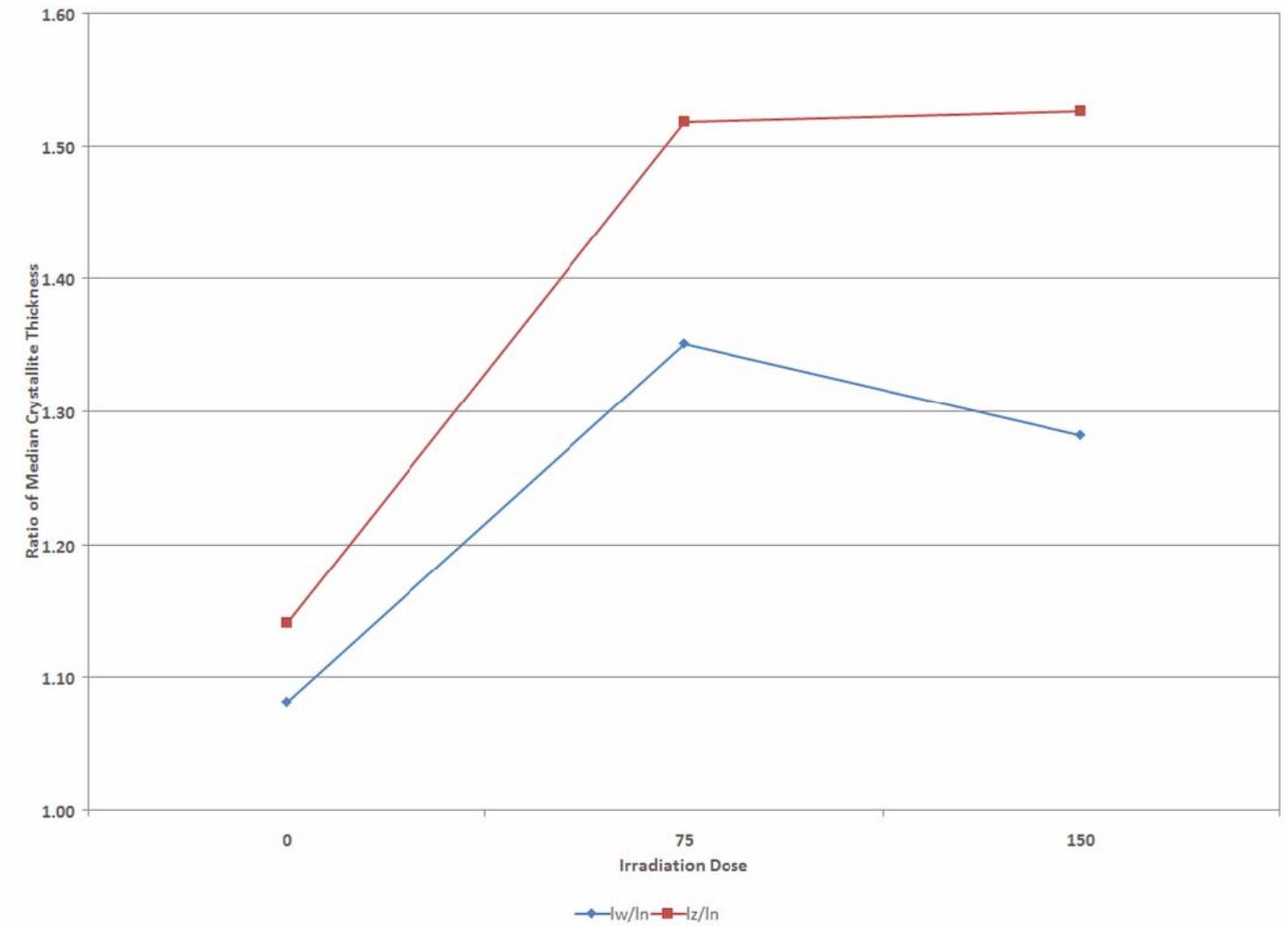

Figure 41: Ratio of Median Crystallite Thicknesses for the Center of the High Dose Rate Gamma Irradiation

The effect of integral dose for a low dose rate (0.25 kGy hr^{-1}) on the surface of the sample is displayed in the crystallite thickness distribution, l_n, (Figure 42), the first moment of the distribution, l_w, (Figure 43), and the second moment of the distribution, l_z, (Figure 44). The median crystallite thickness, l_n, (Table 9 and Figure 45) increases as the integral radiation dose is increased: 19.16 nm to 27.21 nm (8.05 nm increase from control) to 29.67 nm (2.46 nm increase from 75 kGy) for 0 kGy, 75 kGy, and 150 kGy, respectively. The weight-average median crystallite thickness, l_w, (Table 9 and Figure 45) increases as the integral radiation dose is increased: 21.55 nm to 30.47 nm (8.92 nm increase from control) to 33.87 nm (3.4 nm increase from 75 kGy) for 0 kGy, 75 kGy, and 150 kGy respectively. The separation between the values of the median crystallite thickness increases with increasing moment. The z-average crystallite thickness (Table 9) increases from 23.00 nm to 32.66 nm (9.66 nm increase from control) to 36.69 nm (4.03 nm increase from 75 kGy) for 0 kGy, 75 kGy, and 150 kGy respectively. The ratio of l_n to l_w and l_z both increase from 75 kGy to 150 kGy, as seen in Figure 46 and Table 9. The sequence length (Table 16) increases from 75 to 107 and 116 for 0 kGy, 75 kGy, and 150 kGy, respectively. The crystallizable fraction (Table 16) increases from 0.961 to 0.972 and 0.975 for 0 kGy, 75 kGy, and 150 kGy, respectively. On the surface, there is an increase in percent crystallinity (Table 10): 51% to 64% to 68% for 0 kGy, 75 kGy, and 150 kGy, respectively.

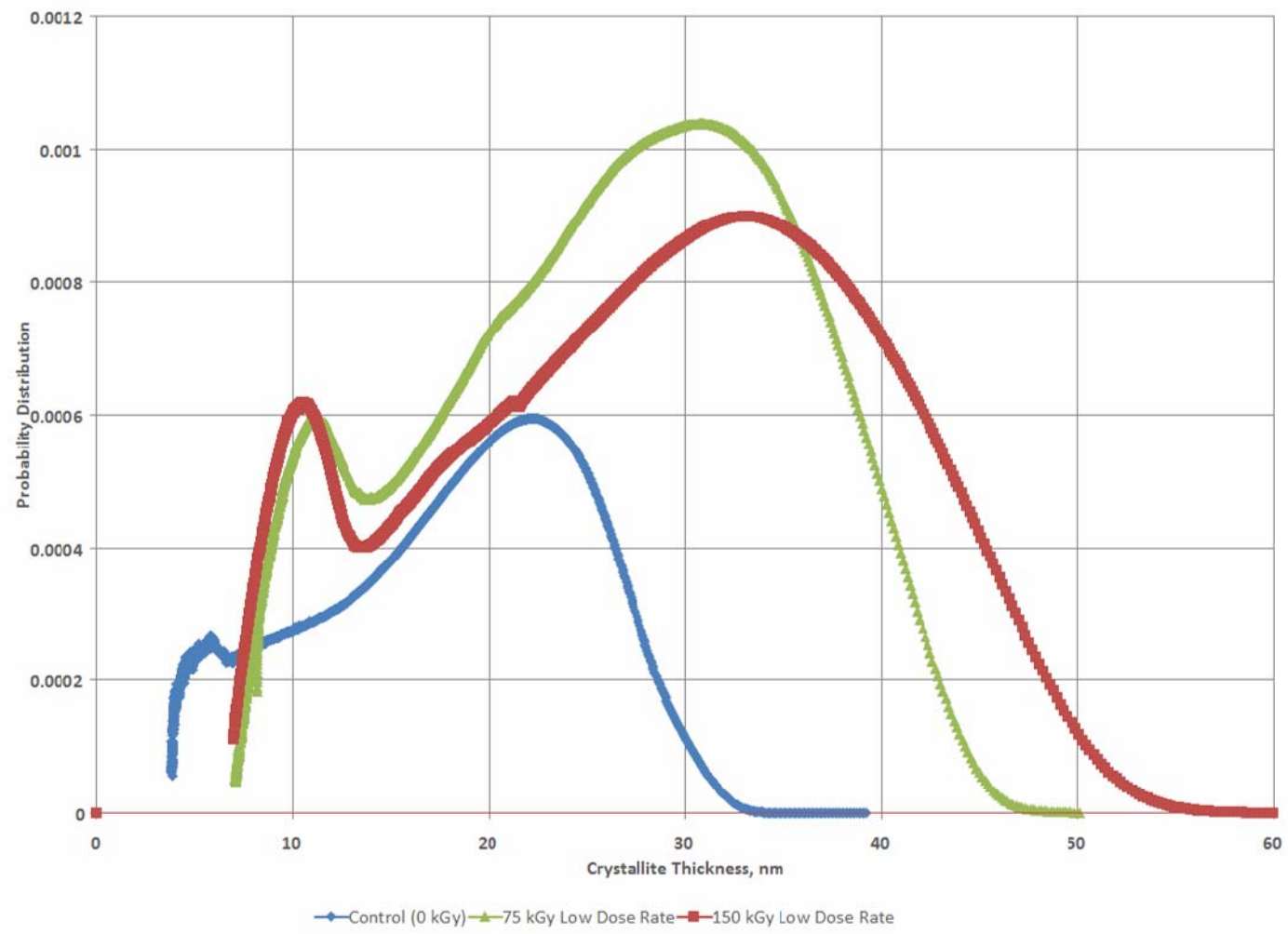

Figure 42: Effect of Integral Dose on the Surface of the Crystallite Thickness Distribution (Low Dose Rate)

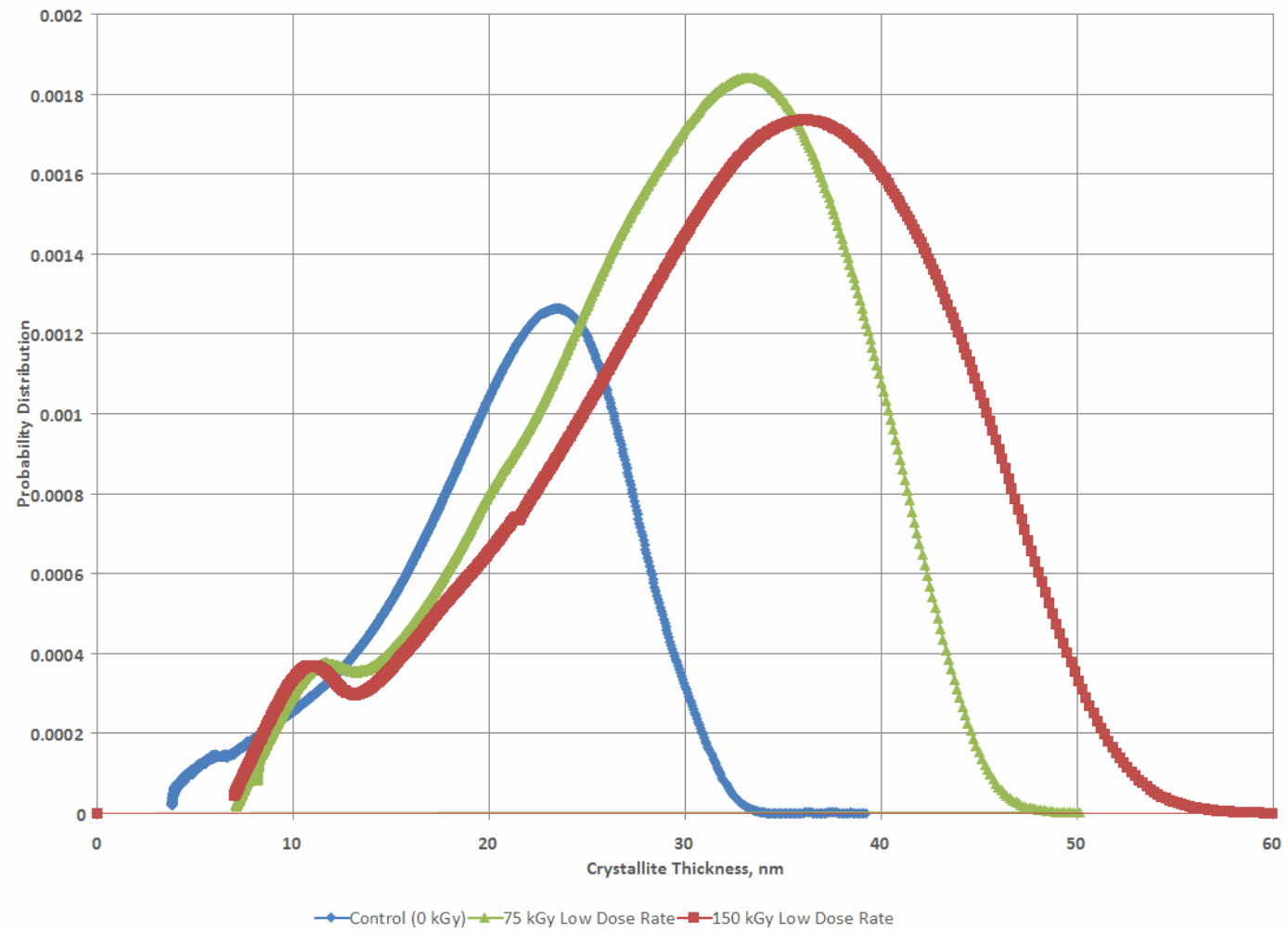

Figure 43: Effect of Integral Dose on the Surface of the First Moment of Crystallite Thickness Distribution (Low Dose Rate)

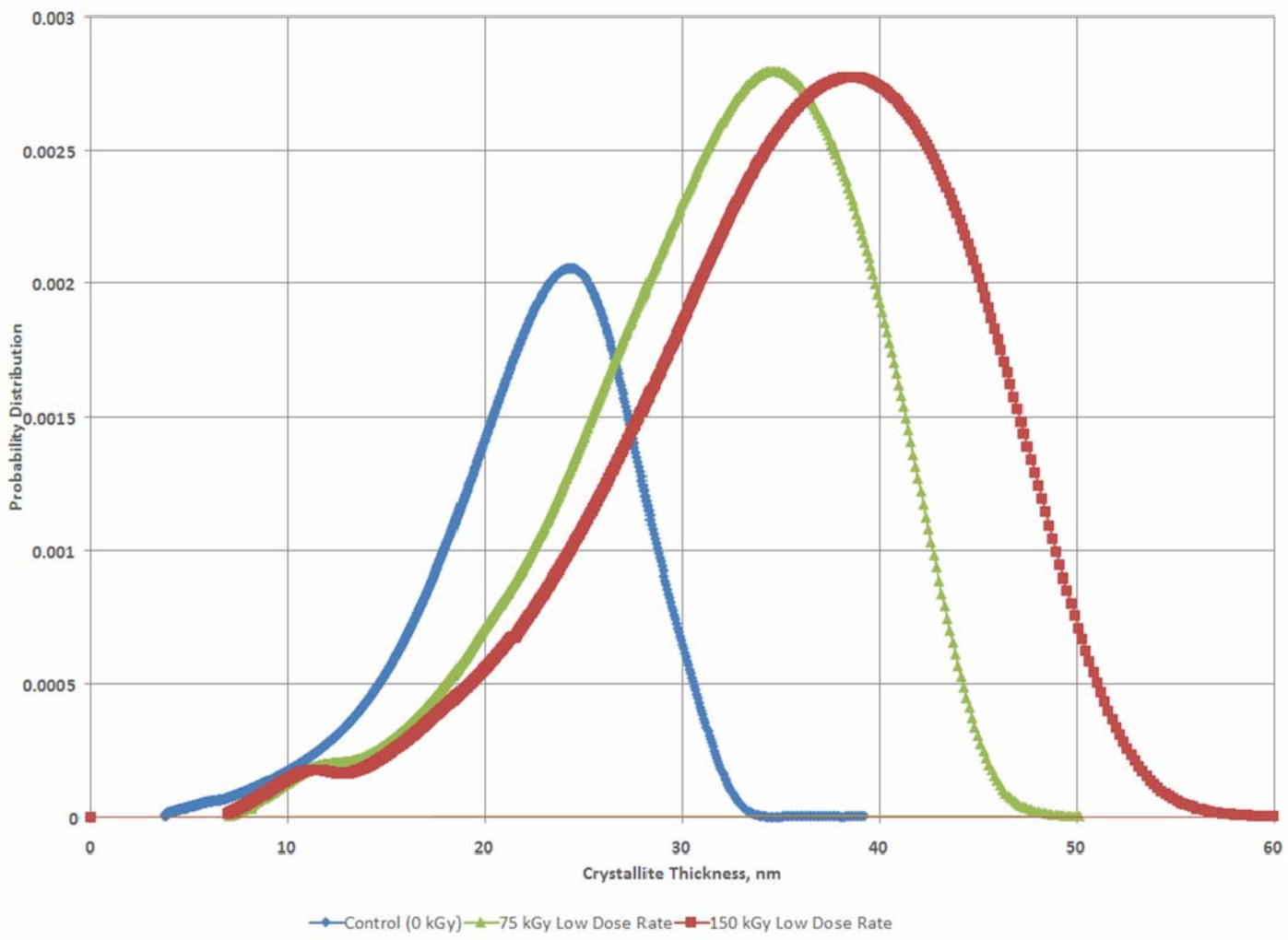

Figure 44: Effect of Integral Dose on the Surface of the Second Moment of Crystallite Thickness Distribution (Low Dose Rate)

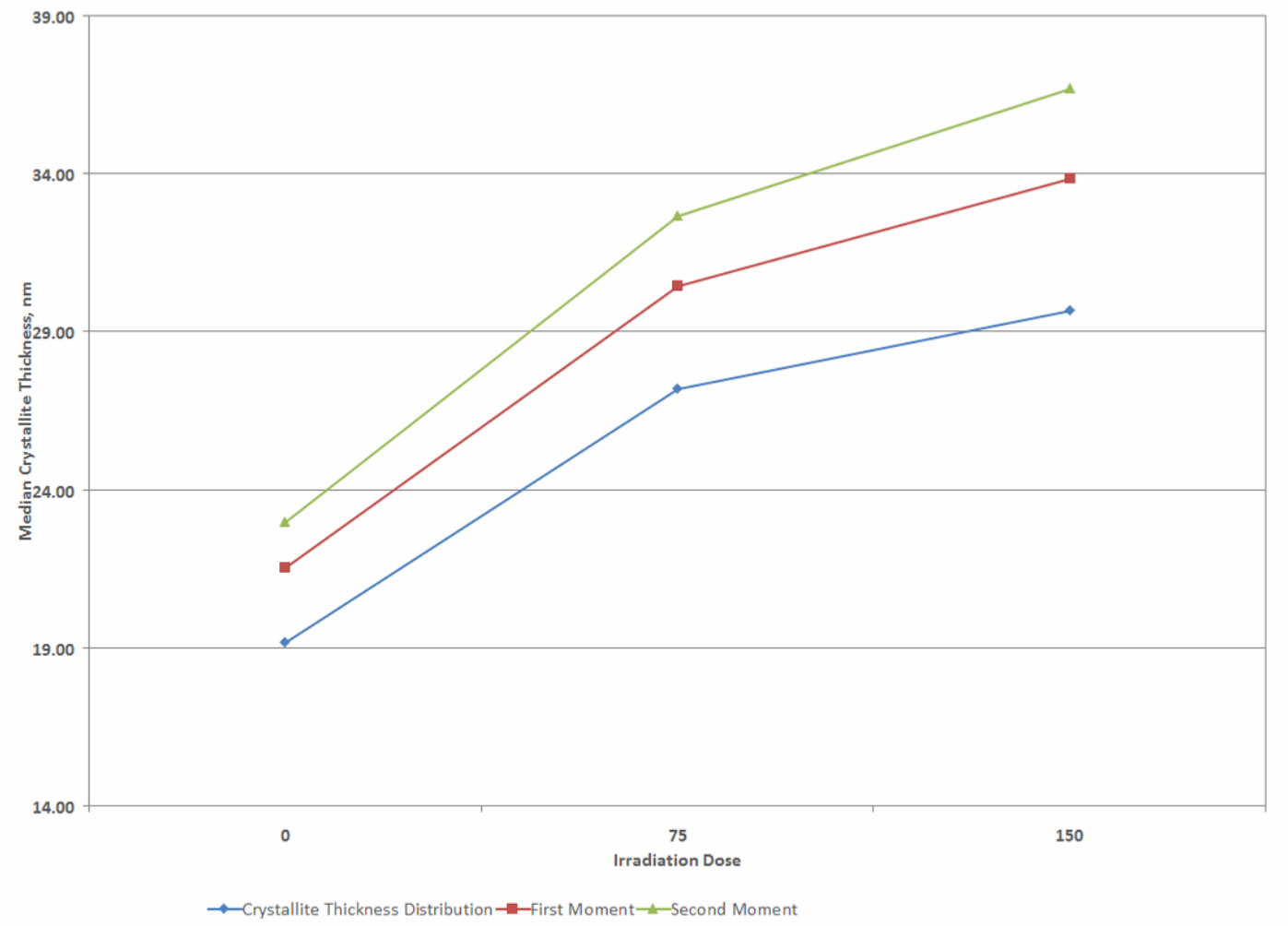

Figure 45: Median Crystallite Thickness for the Surface of the Gamma Low Dose Rate Irradiation

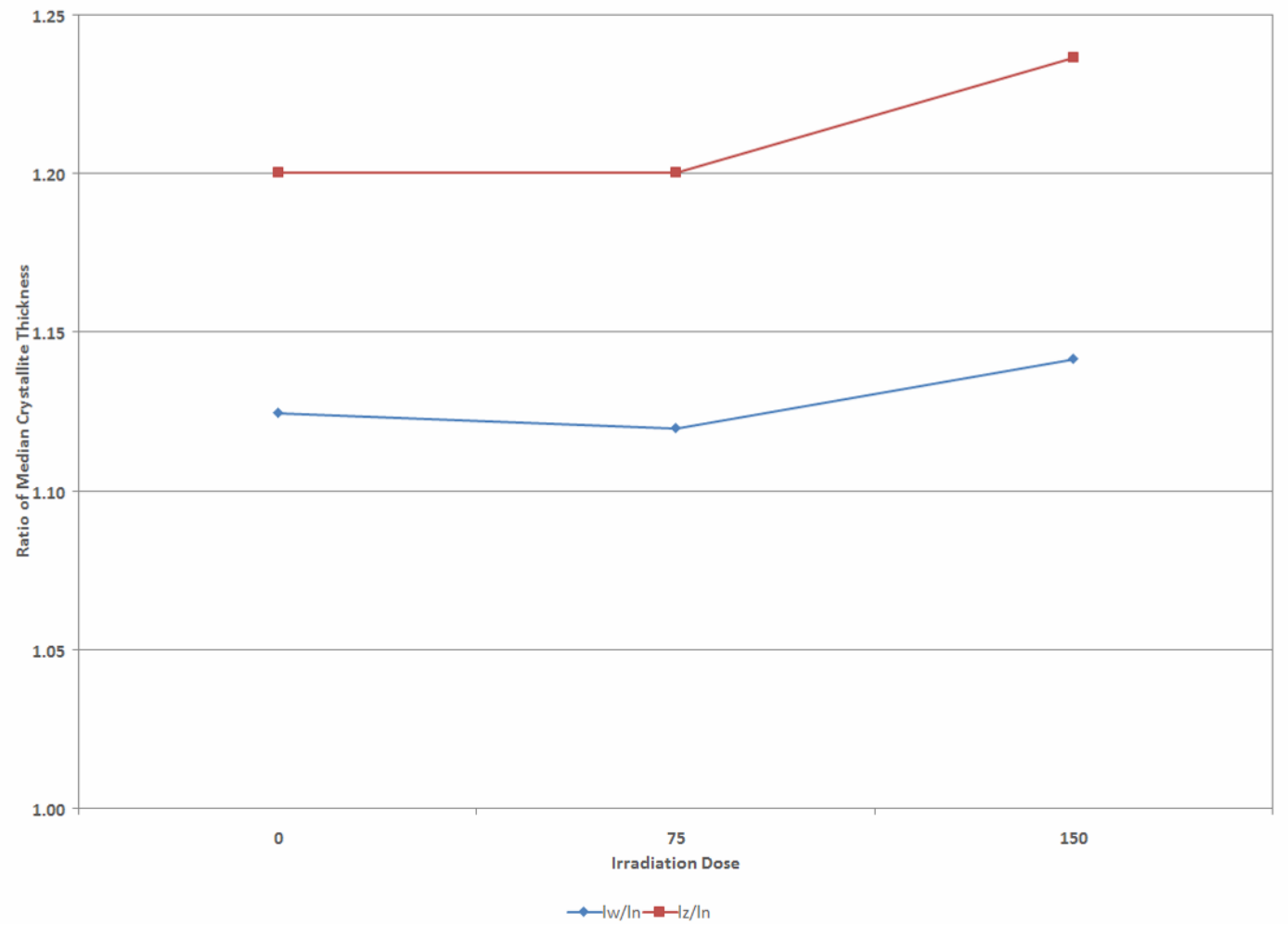

Figure 46: Ratio of Median Crystallite Thicknesses for the Surface of the Low Dose Rate Gamma Irradiation

Table 16: Crystallizable Fraction and Sequence Length for the Surface of the Gamma Low Dose Rate Irradiation

Dose (kGy)	Crystallizable Fraction	Sequence Length
0	0.961	75
75	0.972	107
150	0.975	116

The effect of integral dose for a low dose rate on sections taken from the center of the sample is displayed in the crystallite thickness distribution (Figure 47), the first moment of the distribution (Figure 48), and the second moment of the distribution (Figure 49). The median crystallite thickness (Table 12 and Figure 50) increases as the integral radiation is increased: 20.52 nm to 32.81 nm (12.29 nm increase from control) to 34.62 nm (1.81 nm increase from 75 kGy) for 0 kGy, 75 kGy, and 150 kGy, respectively. The weight-average median crystallite thickness (Table 12 and Figure 50) increases as the integral radiation is increased: 22.19 nm to 37.78 nm (15.59 nm increase from control) to 43.05 nm (5.27 nm increase from 75 kGy) for 0 kGy, 75 kGy, and 150 kGy, respectively. The z-average crystallite thickness shows a much larger dependency on integral dose than the number average because the distribution is being shifted toward larger crystals (Table 12): 23.42 nm to 41.74 nm (18.32 nm increase from control) to 53.33 nm (11.59 nm increase from 75 kGy) for 0 kGy, 75 kGy, and 150 kGy, respectively. The ratio of l_n to l_w and l_z both increase from 0 kGy to 75 kGy and from 75 kGy to 150 kGy (Figure 51 and Table 12). The crystallizable sequence length (Table 17) increases from 80 to 118 and 157 for 0 kGy, 75 kGy, and 150 kGy, respectively. The crystallizable fraction (Table 17) increases from 0.963 to 0.975 and 0.981 for 0 kGy, 75 kGy, and 150 kGy, respectively. In the center, there is very little change in percent crystallinity (Table 15): 55% to 57% to 60% for 0 kGy, 75 kGy, and 150 kGy, respectively.

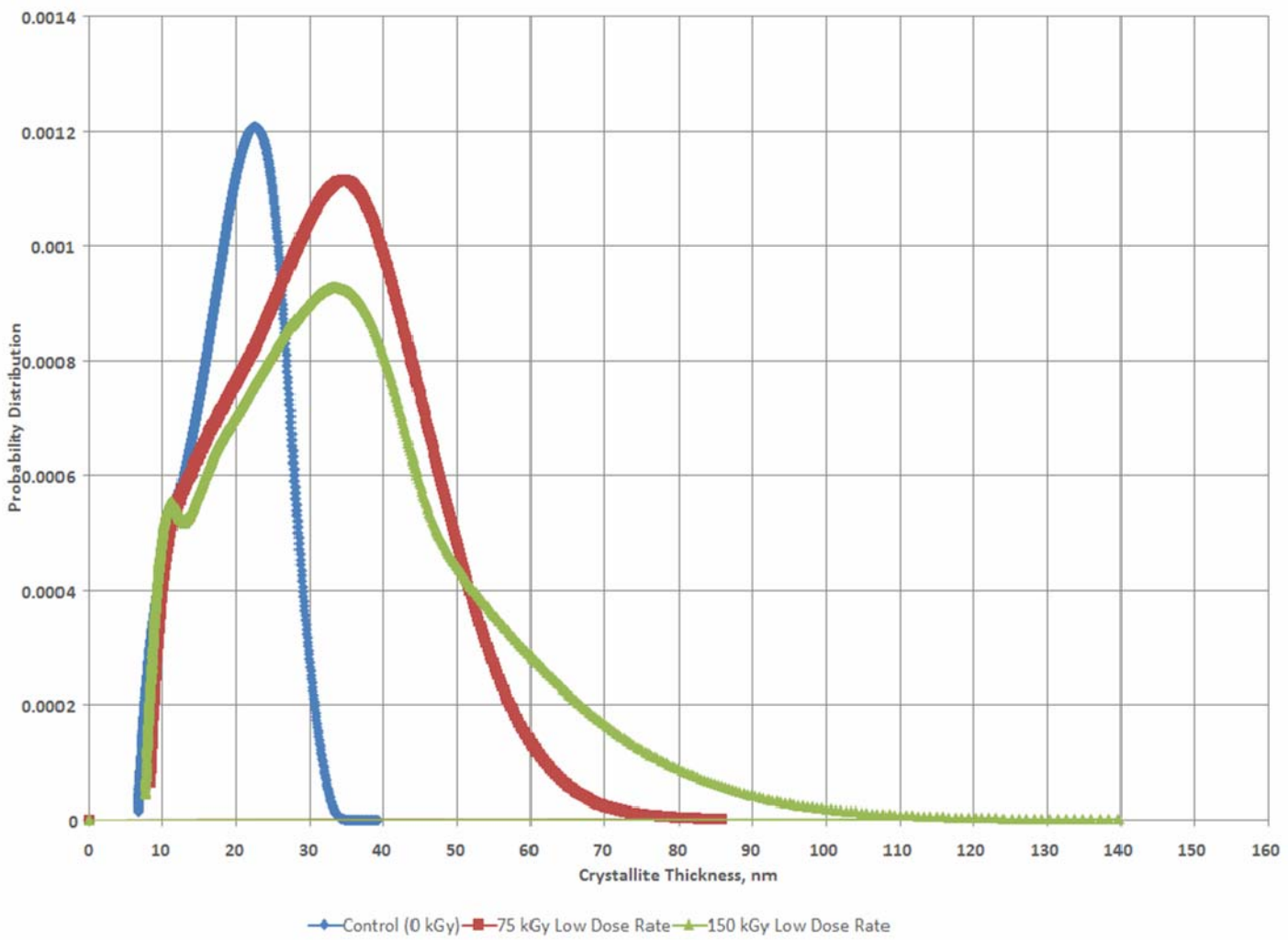

Figure 47: Effect of Integral Dose on the Center of the Crystallite Thickness Distribution (Low Dose Rate)

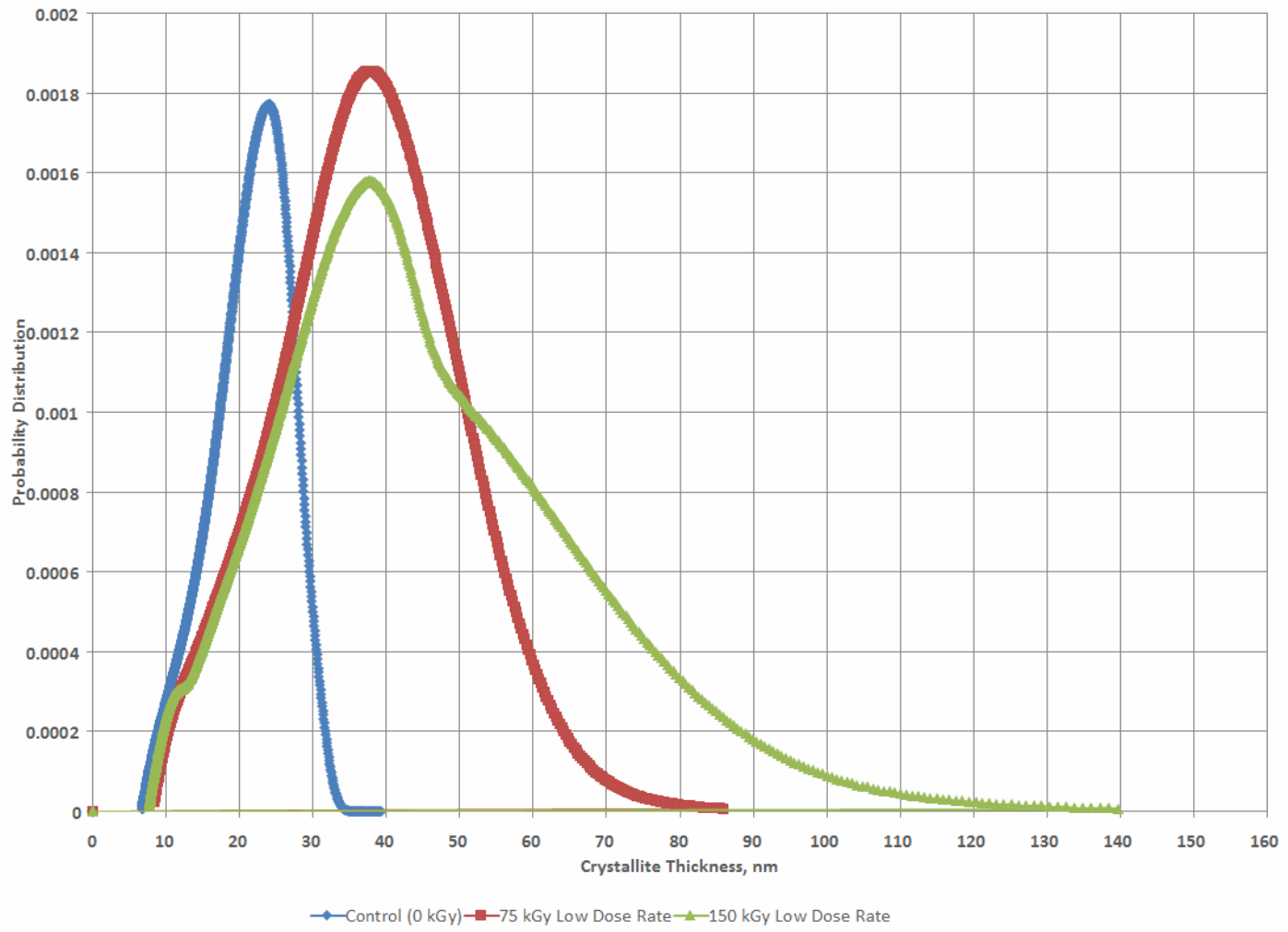

Figure 48: Effect of Integral Dose on the Center of the First Moment of Crystallite Thickness Distribution (Low Dose Rate)

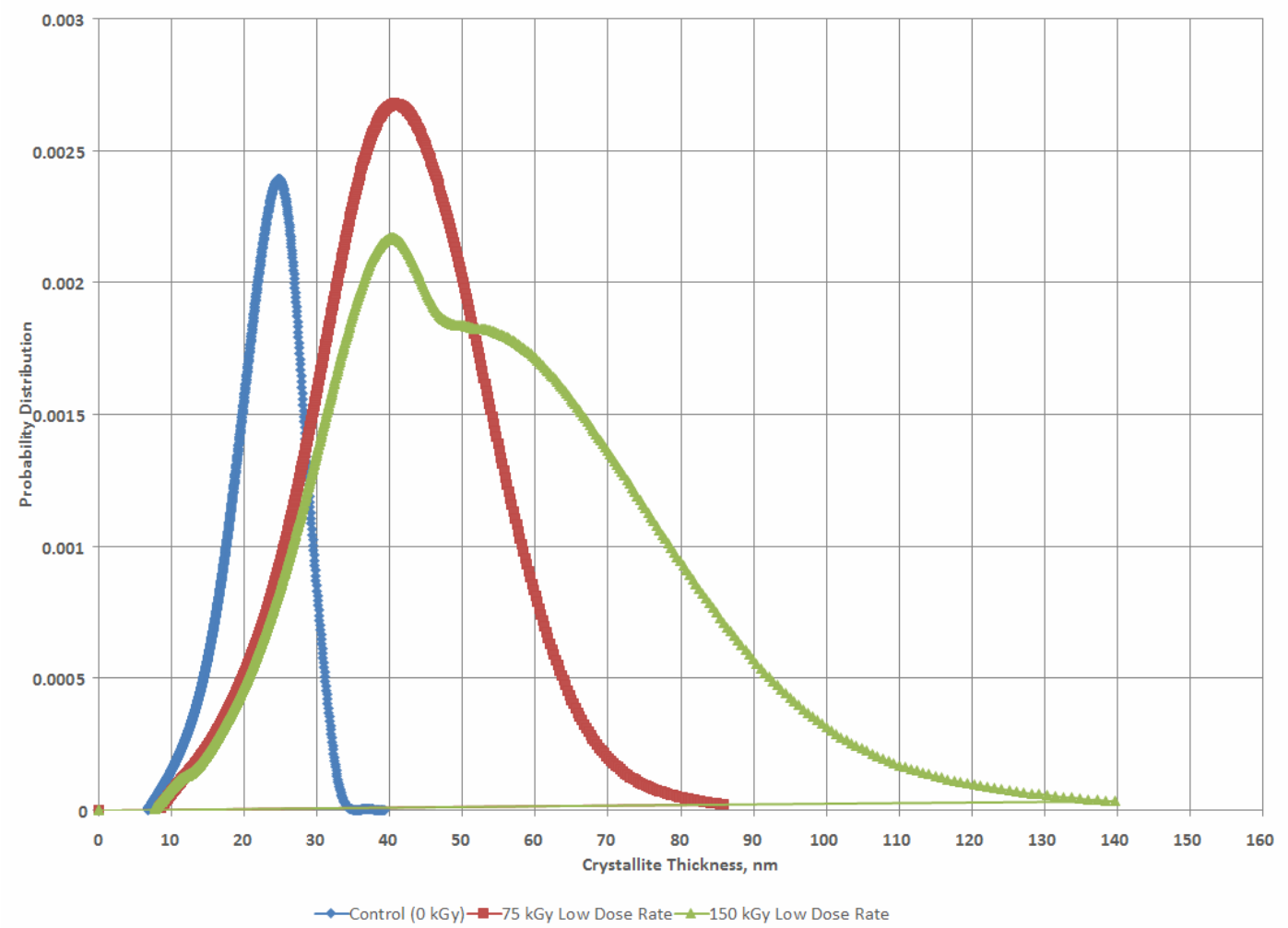

Figure 49: Effect of Integral Dose on the center of the Second Moment of Crystallite Thickness Distribution (Low Dose Rate)

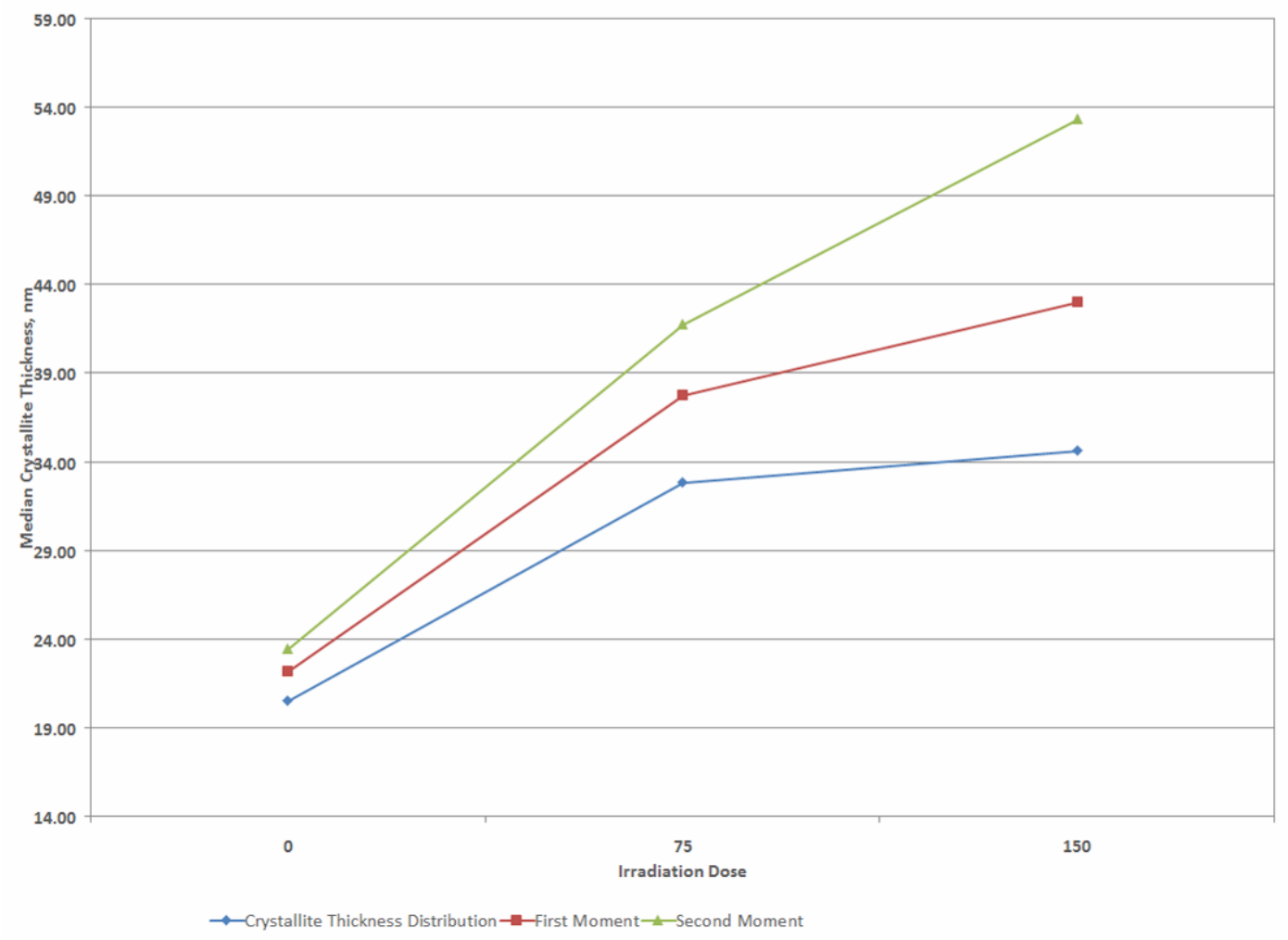

Figure 50: Median Crystallite Thickness for the Center of the Gamma Low Dose Rate Irradiation

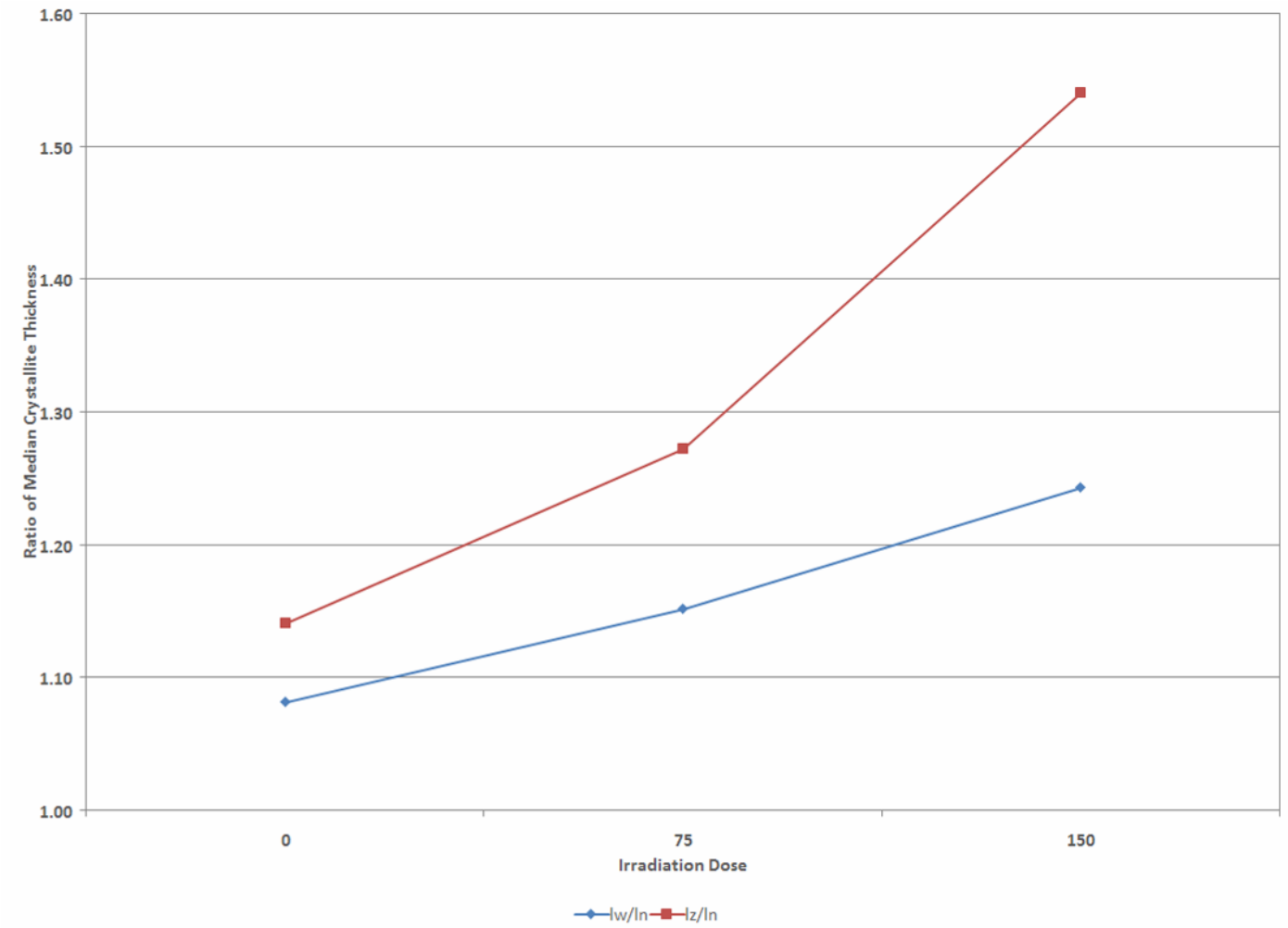

Figure 51: Ratio of Median Crystallite Thicknesses for the Center of the Low Dose Rate Gamma Irradiation

Table 17: Crystallizable Fraction and Sequence Length for the Center of the Gamma Low Dose Rate Irradiation

Dose (kGy)	Crystallizable Fraction	Sequence Length
0	0.963	80
75	0.975	118
150	0.981	157

Number Average Crystallite Thickness

By looking at the control sample prior to irradiation it can be seen that the median crystallite thickness was reduced on the surface (Figure 33, Table 8, and Table 11) from 20.52 nm in the unmodified center of the sample to 19.16 nm (1.36 nm decrease from the center of the sample) on the machined surface (surface of the sample). There is a minimum separation (Figure 33) of 2.83 nm between the center (Table 11 and Table 12) and the surface (Table 8 and Table 9) of the sample at 75 kGy with values of 30.04 nm (high dose rate) and 27.21 (low dose rate), respectively. There is a minimum separation (Figure 33) of 3.14 nm between the center (Table 11 and Table 12) and the surface (Table 8 and Table 9) of the sample at 150 kGy with values of 32.81 nm (high dose rate) and 29.67 nm (low dose rate), respectively. There is no significant effect of dose rate on the median crystallite thickness for an integral dose of 75 kGy.

Weight Average Crystallite Thickness

The weight average median crystallite thickness (Figure 34, Table 8, and Table 11) does not show a significant difference between the center and surface of the sample for the control (0 kGy). In the center of the sample (Figure 34, Table 11, and Table 12) the high dose rate sample has thicker crystals than the low dose rate sample, where the values are 40.61 nm and 37.78 nm (2.83 nm decrease) for 75 kGy and 51.32 nm and 43.05 nm (8.27 nm decrease) for 150 kGy, respectively. On the surface of the sample (Figure 34, Table 8, and Table 9) the low dose rate sample has a thicker crystal than the high dose rate

sample at 150 kGy, as seen by the values 33.87 nm and 30.86 nm (3.01 nm decrease), respectively.

Z-Average Crystallite Thickness

The z-average median crystallite thickness (Figure 35, Table 8, and Table 11) does not show a significant difference between the center and surface of the sample for the control (0 kGy). In the center of the sample (Figure 35, Table 11, and Table 12) the high dose rate sample has thicker crystals than the low dose rate sample, where the values are 45.60 nm and 41.74 nm (3.86 nm decrease) for 75 kGy and 61.06 nm and 53.33 nm (7.73 nm decrease) for 150 kGy, respectively. On the surface of the sample (Figure 35, Table 8, and Table 9) the low dose rate sample has a thicker crystal than the high dose rate sample at 150 kGy, as seen by the values 36.69 nm and 33.24 nm (3.45 nm decrease), respectively.

Small Angle X-Ray Scattering (SAXS)

UHMWPE exposed to gamma irradiation leads to a decrease in the average long period. This trend is seen in low dose rate 65.88 nm to 62.43 nm (decrease of 3.45 nm from 0 kGy) and 61.29 nm (decrease of 4.59 nm from 0 kGy) for 0 kGy, 75 kGy, and 150 kGy respectively. At a high dose rate the variation in the average long period is 65.88 nm to 62.96 nm (decrease of 2.92 nm from 0 kGy) and 63.11 nm (decrease of 2.77 nm from 0 kGy) for 0 kGy, 1.77 kGy, and 5.89 kGy, respectively. The variation in the average long period is summarized in Table 18 and Table 19.

Table 18: Effect of Integral Dose on the Average Long Period for UHMWPE Irradiated at a Low Dose Rate

Dose (kGy)	Average Long Period (nm)
0	65.88 ± 0.5
75	62.43 ± 0.1
150	61.29 ± 0.5

Table 19: Effect of Integral Dose on the Average Long Period for UHMWPE Irradiated at a High Dose Rate

Dose (kGy)	Average Long Period (nm)
0	65.88 ± 0.5
75	62.96 ± 0.3
150	63.11 ± 1.5

Wide-Angle X-Ray Diffraction (WAXD)

There is very little change in the WAXD crystallinity, as seen in Table 20.

Three-Phase Crystallite Model

The three-phase crystallite model can be assembled by using DSC crystallinity, WAXD crystallinity, and SAXS long period. This representation shows increases in both crystalline and amorphous regions with a shrinkage in the interfacial region at low (Figure 52 and Table 21) and high (Figure 53 and Table 22) dose rates.

Nano-Indentation

Irradiation of UHMWPE leads to an increase in hardness (Table 23 and Figure 54) from 38 MPa to 47 MPa to 53 MPa for 0 kGy, 75 kGy, and 150 kGy respectively. With increased irradiation there is an increase in modulus (Table 23 and Figure 55) from 1200 MPa to 1490 MPa to 1620 MPa for 0 kGy, 1.77 kGy, and 5.89 kGy, respectively.

Table 20: Wide-Angle X-Ray Diffraction Determined Crystallinity

Dose (kGy)	Low Dose Rate	High Dose Rate
0	75.14%	75.14%
75	79.94%	70.76%
150	70.34%	73.54%

Table 21: Three Phase Model for Low Dose Rate Gamma Irradiation on the Surface

Dose (kGy)	Crystalline, nm	Interfacial, nm	Amorphous, nm
0	33.7	15.8	16.4
75	40.0	9.8	12.5
150	41.3	1.6	18.1

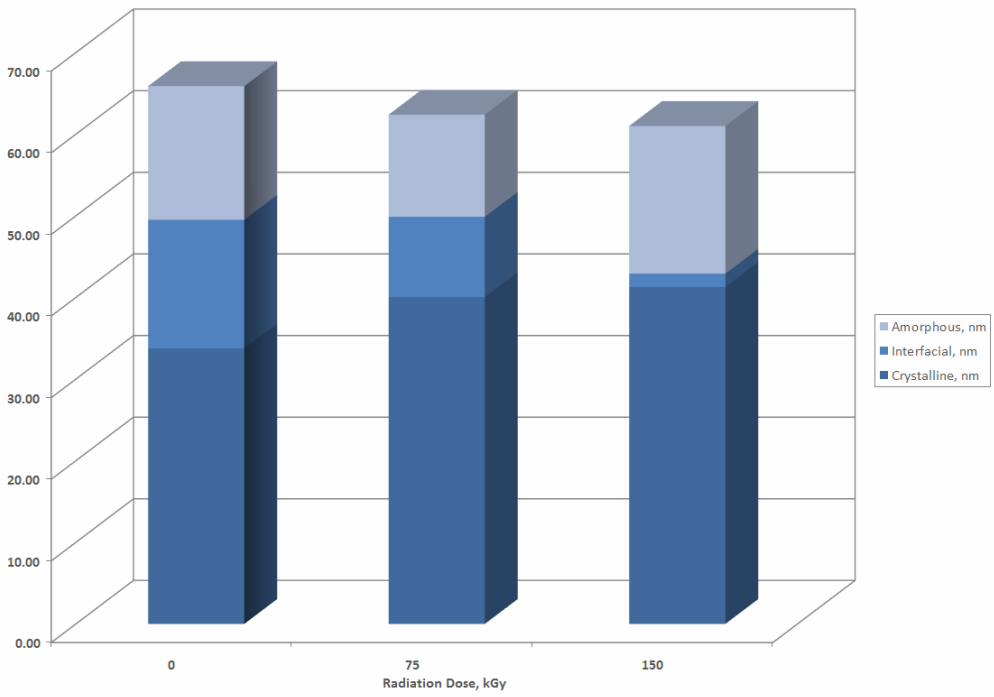

Figure 52: Three Phase Crystal Model for Low Dose Rate Gamma Irradiation

Table 22: Three Phase Model for High Dose Rate Gamma Irradiation on the Surface

Dose (kGy)	Crystalline, nm	Interfacial, nm	Amorphous, nm
0	33.7	15.8	16.4
75	39.1	5.4	18.4
150	41.6	5.1	16.8

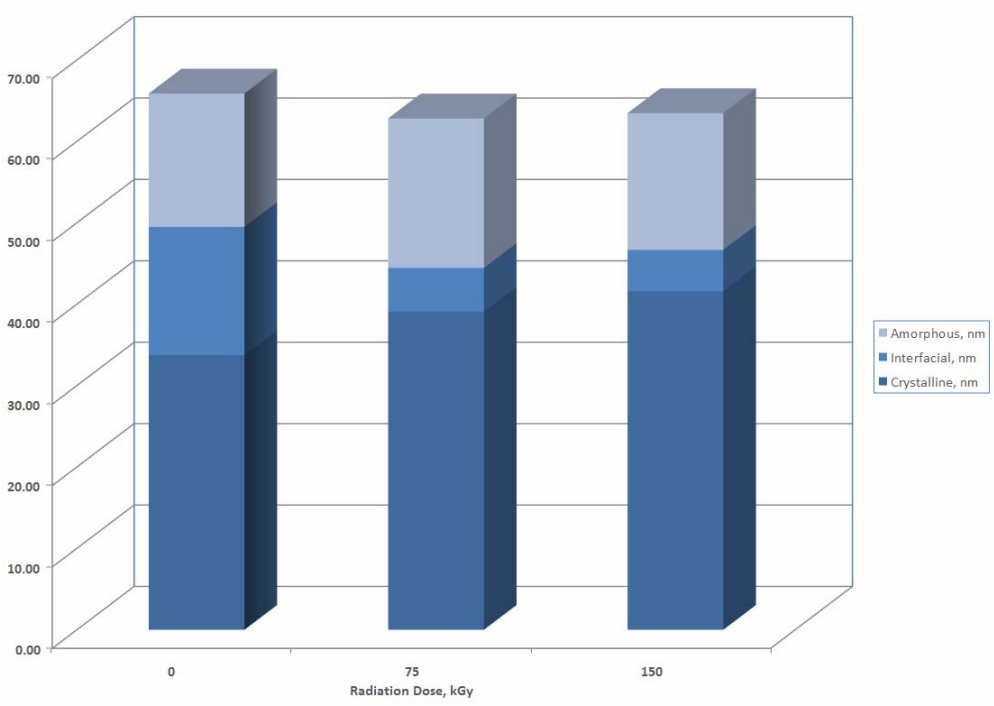

Figure 53: Three Phase Crystal Model for High Dose Rate Gamma Irradiation

Table 23: Effect of Crystal Size on Plateau Hardness and Modulus

Dose (kGy)	Plateau Hardness (MPa)	Plateau Modulus (MPa)
0	38	1200
75	47	1490
150	53	1620

Table 24: Comparison of Crystal Hardness (H_C)

Dose (kGy)	Plateau Hardness (MPa)	H_C (MPa)	Y (MPa)
0	38	69.78	23.26
75	47	71.56	23.85
150	53	77.41	25.80

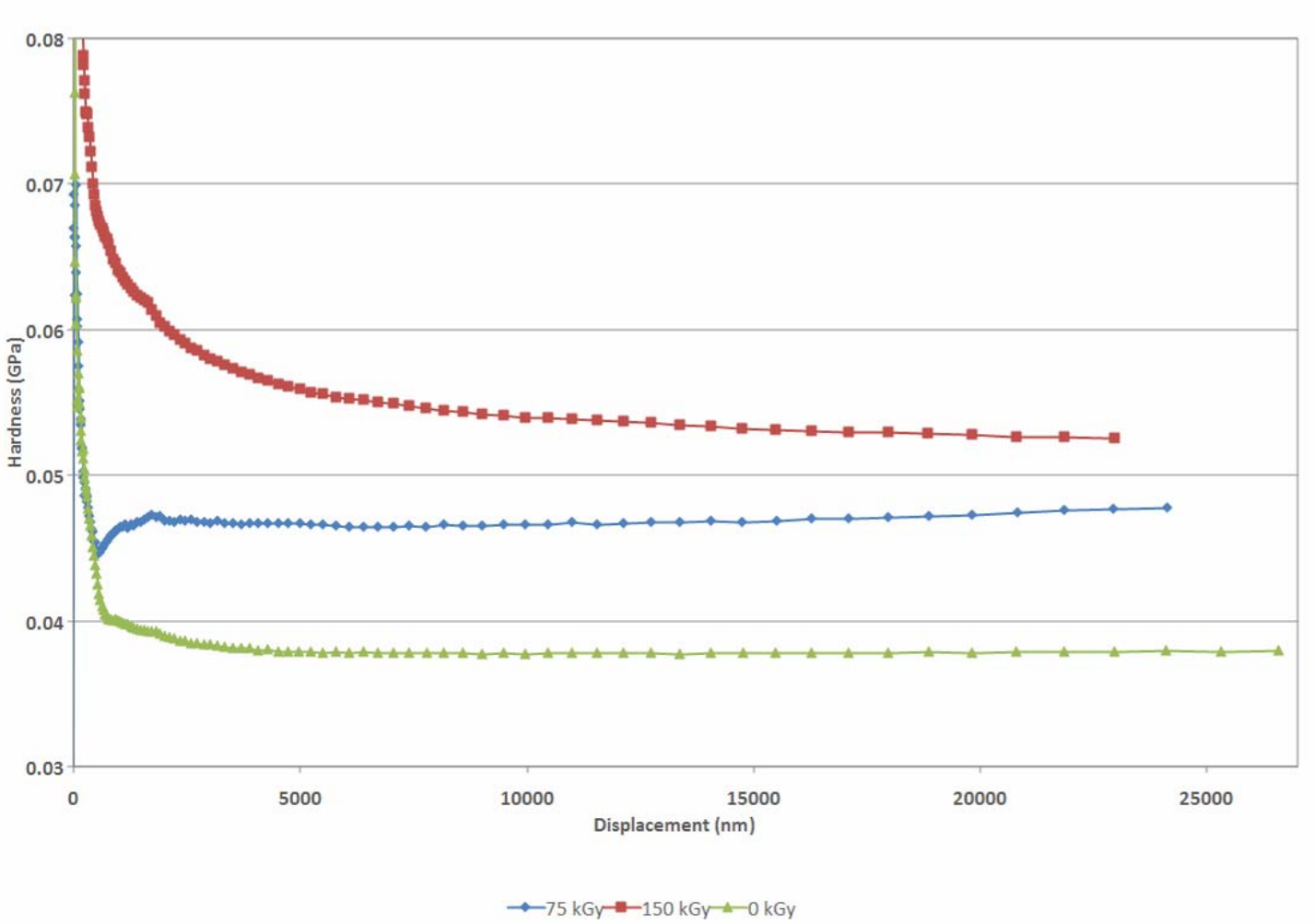

Figure 54: Effect of Integral Dose on Hardness as a Function of Depth

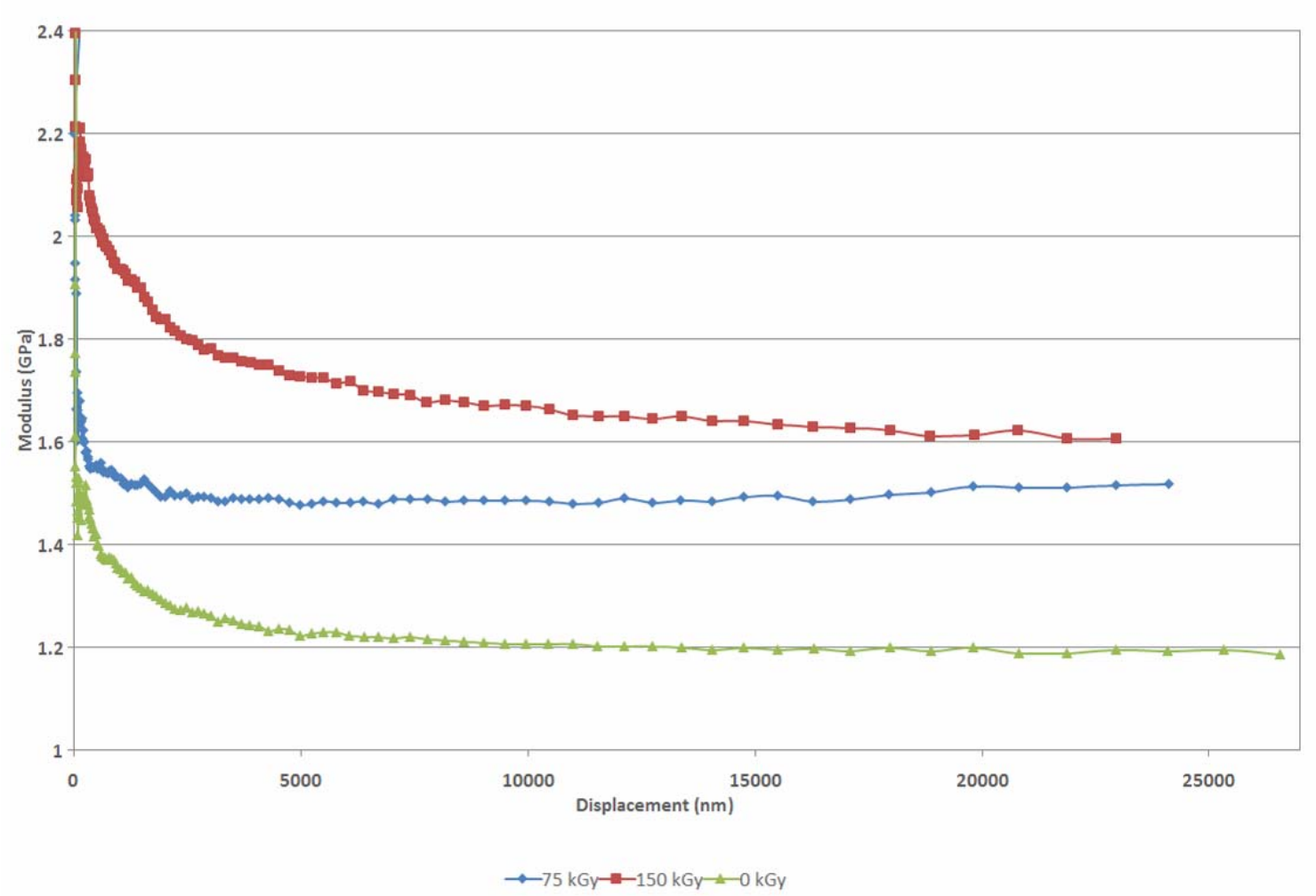

Figure 55: Effect of Integral Dose on Modulus as a Function of Depth

6. Discussion

Proton Irradiation

Post-irradiation analysis indicates that there is an increase in all moments of crystallite thickness (l_n increases 4 nm, l_w increases 2 nm, and l_z increases 3 nm) from 0 kGy to 1.77 kGy and an increase in l_w (increases 2 nm) and l_z (increases 2 nm) from 1.77 kGy to 5.89 kGy (Figure 56). In addition, increases are also observed in crystallizable sequence length (increases 10 repeat units) from 0 kGy to 1.77 kGy.

Post-heat treatment, there is also a large decrease in sequence length from 1.77 kGy to 5.89 kGy (decreases 18 repeat units). The trends in post- heat treatment analysis show that proton irradiation formed free radicals that allowed for both relaxations of entanglements strained molecular chains to further crystallize. Heat treatment of the irradiated samples shows there is very little decrease in crystallite thickness within the range of 0 kGy to 1.77 kGy, however there are large decreases in crystallite thickness in all moments (l_n decreases 4.6 nm, l_w decreases 5.7 nm, and l_z decreases 6.3 nm) in the higher energy range from 1.77 kGy to 5.89 kGy (Figure 57). The trends in heat treatment analysis show high levels of radiation (1.77 kGy to 5.89 kGy) produce enough crosslinking to significantly interfere with recrystallization.

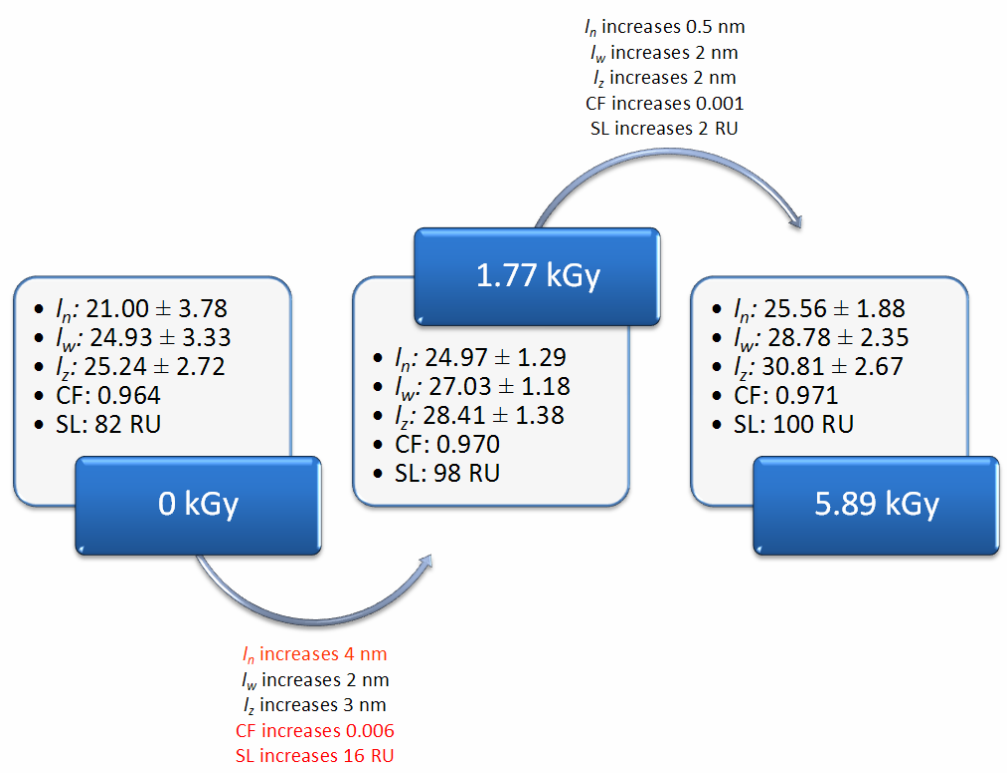

Figure 56: Significant Changes for Proton Irradiated Samples in the Post-Irradiation Analysis

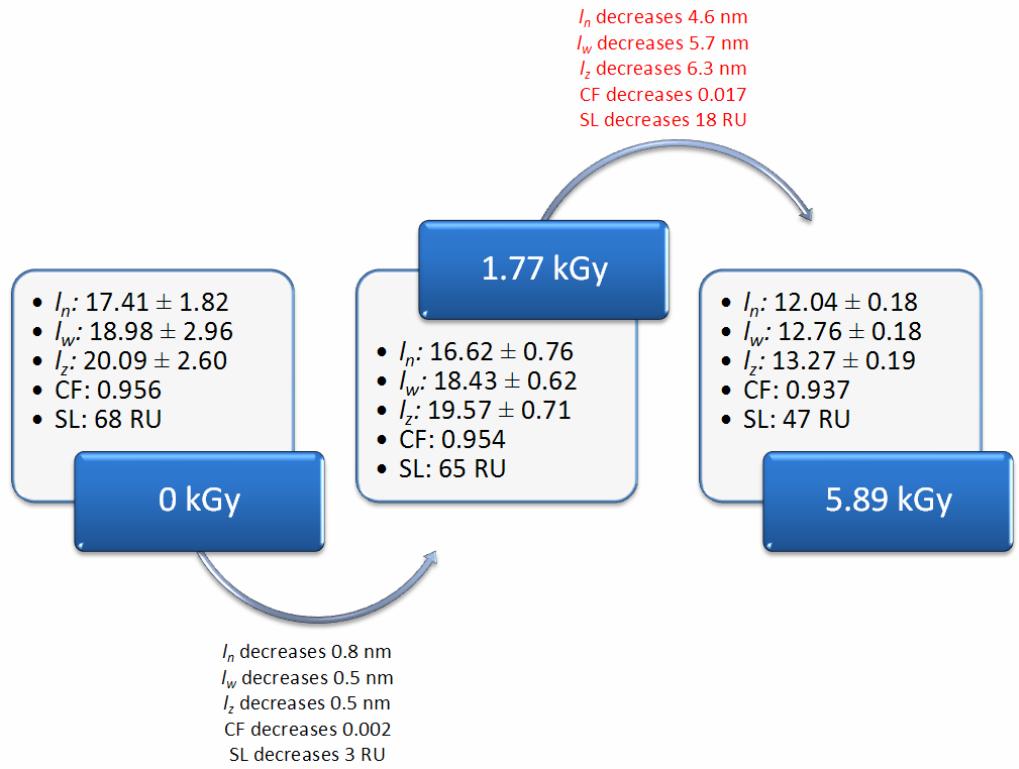

Figure 57: Significant Changes for Proton Irradiated Samples in the Post-Heat Treatment Analysis

These trends imply that there was most likely two steps that occurred during irradiation of the polymer: 1) free radical formation, allowing for relaxation of strained molecular chains (entanglements, tie chains, and taught loops), 2) Reaction of the free radicals into oxididized chain ends and crosslinks. Since the samples tested came from the top 1 mm of the sample it is expected the some of the free radicals oxidized. However, the combination of very low levels of increased crystallinity in post-irradiation analysis and high enough crosslinking in the heat treatment to significantly reduce the crystallizable sequence length from 100 to 47 repeat units at 5.89 kGy imply that the predominate reaction is crosslinking.

Gamma Irradiation

Effect of Dose Rate

On the surface, there is an increase in l_n of 3 nm at 150 kGy with dose rate (from high dose rate to low dose rate). In the center of the sample, there is an increase in l_n of 3 nm at 75 kGy and 5 nm at 150 kGy (from high dose rate to low dose rate). These results show that dose rate plays a very minor to no role at all in the crystalline morphology of irradiated UHMWPE. Since the kinetics of crosslinking and oxygen diffusion are much slower than the irradiation time, the only reason crystalline morphology would be dependent on dose rate is if there is a difference in the number of free radicals formed. However, the literature states that there is no correlation between dose rate and the number of free radicals generated, so there should be no effect of dose rate on crystalline morphology [40].

Effect of Integral Dose

With applied radiation of any dose there is a decrease in long period. This is believed to be because of new smaller crystals being produced in the amorphous regions with much smaller long periods. This is supported by SAXS results produced by Premnath et al., where two peaks were discovered in the scattering pattern (signifying two long periods: 490 Å, seen in control, and 130 Å, appears with irradiation) [7]. Both high dose rate and low dose rate exposures show the same trends. On the surface, there is a minor increase in crystallite thickness and crystallizable sequence length that occurs from 0 kGy to 75 kGy. This results agree with the literature because the surface of the sample (first ~ 1 mm) is not exposed to the full applied dose, meaning that the maximum kinetic energy transfer does not occur until about 1 mm into the sample, as seen in Figure 2 [17]. In the center of the sample, the crystallizable sequence length and median crystallite thickness is highly dependent, in a positive manner, on integral dose. The strong dependency of crystallite thickness on integral radiation dose in the center also agrees with the literature because the with an increase in radiation dose there is an increase in free radicals generated allowing for relaxation of chains for crystallization [17, 40]. The increase in sequence length is due to the breaking of tie chains, entanglements, and loop. When these strained molecular chains are broken and given the freedom to reptate they can then crystallize on an already established crystal or initiate a new smaller crystal. This newly formed molecular chain end could then react to form an oxidation product (chain scission) or an inter-molecular crosslink depending on its access to oxygen (depth within the sample).

High Dose Rate

At high dose rates, there is a decrease in long period of approximately 3 nm with irradiation. On the surface, there is an increase in all moment of crystallite thickness (l_n increases 7-8 nm, l_w increases 8-9 nm, and l_z increases 9-10 nm) from 0 kGy to irradiated state (Figure 58). On the surface, there is also an increase in the crystallizable sequence length of 28 repeat units from 0 kGy to irradiated state. The three-phase crystallite model also supports this increase in crystallite size.

In the center of the sample, there is a large increase in all moments of crystallite thickness (l_n increases 10 nm, l_w increases 20 nm, and l_z increases 15 nm) from 0 kGy to 75 kGy and an equally as large increase in all moments (l_n increases 9 nm, l_w increases 11 nm, and l_z increases 22 nm) from 75 kGy to 150 kGy (Figure 59). In the center of the sample, there is also an increase in crystallizable sequence length from 0 kGy to 75 kGy (49 repeat units) and a much smaller increase from 75 kGy to 150 kGy (7 repeat units). In the center of the sample there is also a large increase in the breadth of the crystallite thickness distribution, as seen by the increase in l_w/l_n (increases 0.27) and l_z/l_n (increases 0.38) from 0 kGy to 75 kGy.

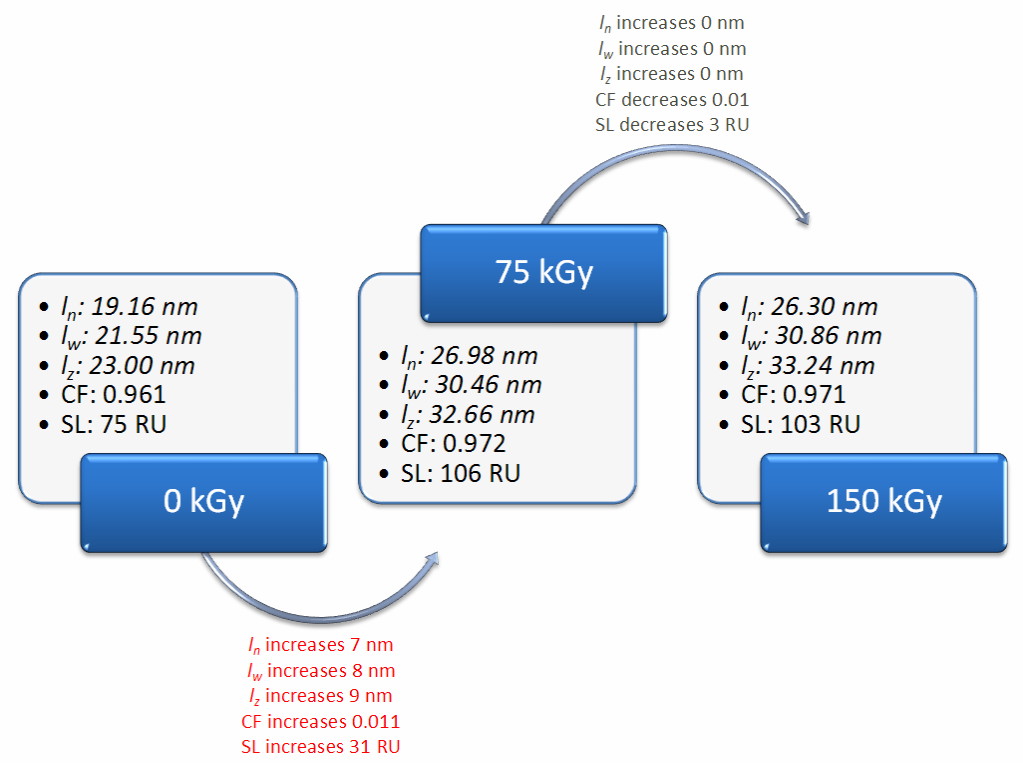

Figure 58: Significant Changes on the Surface of the High Dose Rate Gamma Irradiated Sample

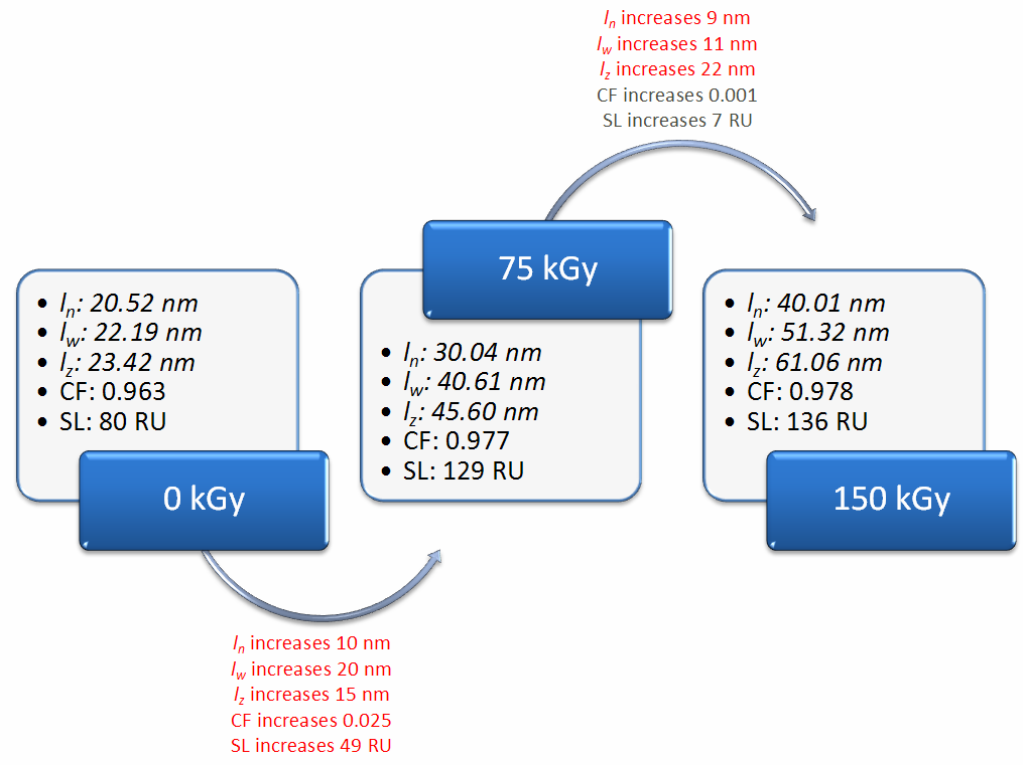

Figure 59: Significant Changes in the Center of the High Dose Rate Gamma Irradiated Samples

Low Dose Rate

At low dose rates, there is a decrease in long period of 3-4 nm with irradiation. On the surface, there is a large increase in all moments of crystallite thickness (l_n increases 8 nm, l_w increases 9 nm, and l_z increases 10 nm) from 0 kGy to 75 kGy and a much smaller increase in all moment (l_n increases 2 nm, l_w increases 3 nm, and l_z increases 4 nm) from 75 kGy to 150 kGy (Figure 60). On the surface, the sequence length increases from 0 kGy to 75 kGy (32 repeat units) and from 75 kGy to 150 kGy (9 repeat units). The three-phase crystallite model also supports this increase in crystallite size.

In the center of the sample, there is a large increase in all moments of crystallite thickness (l_n increases 12 nm, l_w increases 16 nm, and l_z increases 18 nm) from 0 kGy to 75 kGy and an increase in l_w (increase of 5 nm) and l_z (increase of 12 nm) from 75 kGy to 150 kGy (Figure 61). In the center of the sample, the crystallizable sequence length increases from 0 kGy to 75 kGy (38 repeat units) and from 75 kGy to 150 kGy (39 repeat units). In the center of the sample, there is an increase in the crystallite thickness distribution (l_z/l_n increases 0.27) from 75 kGy to 150 kGy.

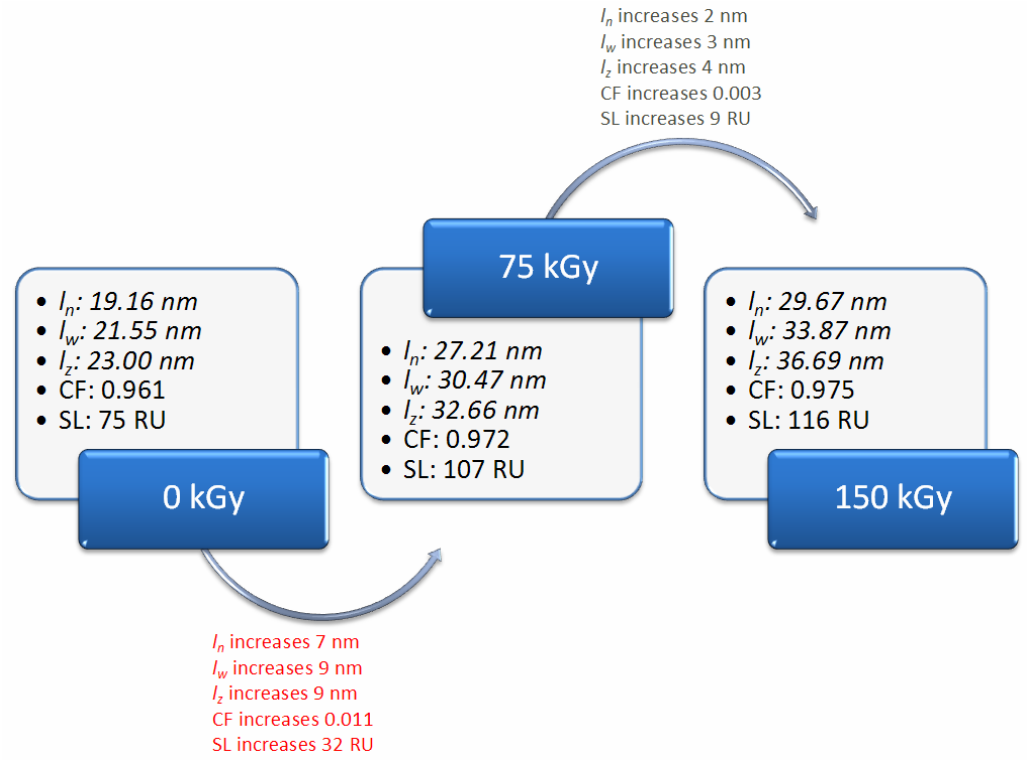

Figure 60: Significant Changes on the Surface of the Low Dose Rate Gamma Irradiated Samples

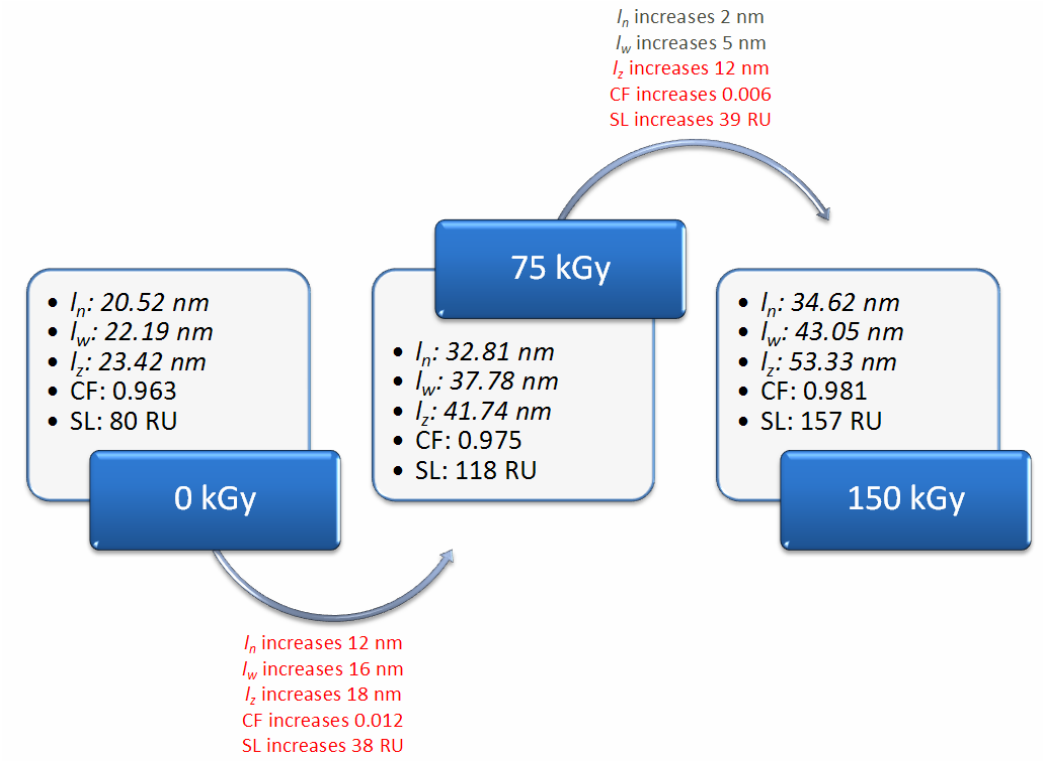

Figure 61: Significant Changes in the Center of the Low Dose Rate Gamma Irradiated Samples

Relationship to Hardness

The samples used to measure hardness are different from the samples used to measure lamella thickness, l_c, by DSC, because of this fact, the lamella thickness and nanohardness cannot be directly compared. However, the trends of each material can be compared relative to each other. On the surface of UHMWPE, at a low does rate, there is an increase in l_n from 19.16 nm to 27.21 nm to 29.67 nm, which give l_c^{-1} values of 0.052 nm^{-1}, 0.037 nm^{-1}, and 0.034 nm^{-1} for 0 kGy, 75 kGy, and 150 kGy, respectively. Based on the Experimental data from Santa Cruz et al. data, depicted in Figure 62, the expected H_c values for our samples are approximately 148 MPa, 170 MPa, and 180 MPa for 0 kGy, 75 kGy, and 150 kGy, respectively. The values of Hc measured by nanoindentation, at a depth of 20 μm, are 70 MPa, 71 MPa, and 77 MPa for 0 kGy, 75 kGy, and 150 kGy, respectively. The trend in the H_c values is the similar, however the absolute values are different. This deviation in absolute hardness values is most likely due to differences in the method of calculating the hardness value between microindentation and nanoindentation, however the trend is still the same. Now that it has been established that there is an increase in H_c with radiation, the effect of hardness on microabrassive wear can be addressed. It can be seen from Figure 63 that as the hardness of the material increases, there is an increase in the wear rate. This is counterintuitive because normally as the hardness of a material increases the wear rate reduces, but this is based on the assumption that the material plastically deforms. However, the results produced by Buchanan et al. (Figure 63) show that crosslinked

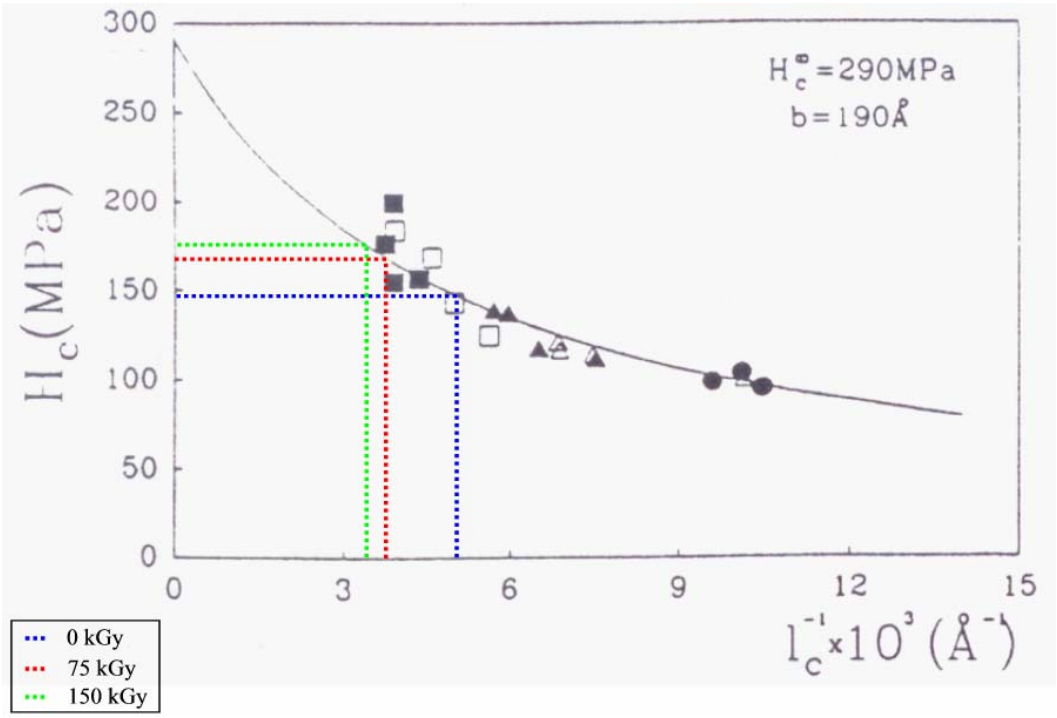

Figure 62: Experimental Data on the Effect of Lamella Thickness, l_c, on Crystal Hardness, H_c [34]

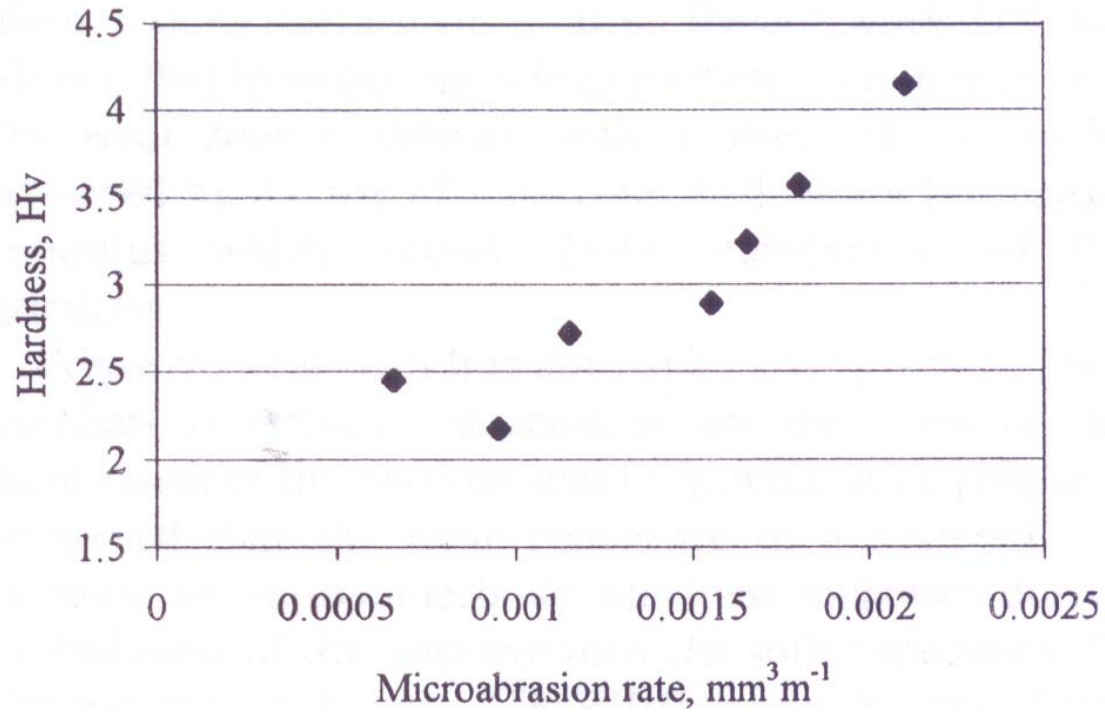

Figure 63: Relationship Between Microabrassion and Hardness for Irradiated UHMWPE [41]

UHMWPE deforms by a brittle method during wear tests [41]. This reinforces the fact that the increase in lamella thickness and hardness on the surface is due to chain scissioning followed by further crystallization, which would reduce the interconnection between crystalline lamella.

7. Conclusions

Proton Irradiation

Post-irradiation, there is a very gradual increase in crystallite thickness with irradiation in the tested dose range (0-5.89 kGy). After heat treatment, high doses of proton irradiation induced enough crosslinking to severely hinder recrystallization after melting. These two trends tend to imply that the polymer, even though it is sampled from the surface (high oxygen concentration), the UHMWPE tends to crosslink over oxidation.

Gamma Irradiation

With irradiation there is an increase in the breadth of the crystallite thickness distribution and a decrease in long period, which signifies that there is a development of new smaller crystals in the amorphous region and a growth of some of the existing crystals. The primary difference is seen between the surface and the center of the sample. The surface has an increase in all moments of crystallite thickness from 0 kGy to 75 kGy, but little to no change from 75 kGy to 150 kGy. In the center of the sample there is large increase in all moments from 0 kGy to 75 kGy, but only an increase in the higher moments from 75 kGy to 150 kGy. The most probable explanation of this effect has to do with diffusion of oxygen from the surface to the free radical. As seen in Figure 5, chain scissioning occurs on the subsurface due to the depth dependence of the absorbed dose. This depth dependence of the absorbed dose means that the surface, ~ 1 mm deep, is exposed to a

much lower integral dose than the bulk of the UHMWPE, as seen in Figure 2. Since the center of the sample is exposed to the complete applied irradiation dose and oxygen must diffuse in to produce chain scissions, crosslinking is the predominate reaction at this depth. Since chain scissioning is in high concentration ~ 1 mm below the surface most of the material tested in the surface experiment had very little modification from the control sample. However, in the center of the sample the absorbed dose was the full applied dose, so the maximum concentration of free radicals was formed leading to relaxation of entanglements to further crystallize followed by crosslinking. Another reason that there is a larger increase in the lamella thickness in the center of the sample is due to the fact that the kinetics for crosslinking is much slower than oxidation, which gives more time for the newly relaxed chain to further crystallized before a non-crystallizable (oxidation product or crosslink) unit is integrated into the chain. There is also an increase in hardness on the surface of the irradiated UHMWPE which is a function of integral dose. It has been shown that an increase in hardness leads to an increase in wear rate, since crosslinked UHMWPE wears in a brittle manner over a plastic manner. The molecular reason for this increased wear rate is because of a decrease in the inter-lamella connectivity (i.e. tie chains and entangled loops).

Future Work

Future analysis of radiation effects on UHMWPE should also include Electron Spin Resonance (ESR) experiments, so that the concentration of free radicals can be tracked. Depth dependent swelling properties should also be measured as a function of time to determine the progression of both crosslinking and chain scissioning kinetics.

References

1. Landy, M.M.a.W., P.S., J. Arthroplasty (suppl.), 1988. **S73**.
2. Wright, T.M., C.M. Rinmac, S.D. Stulberg, Clinical Orthop. Rel. Res. 276, 1992. **126**.
3. Schmidt, M., Trans. Soc. Biomaterials, Hawaii, 2000.
4. Lewis, G., *Properties of crosslinked ultra-high-molecular-weight polyethylene.* Biomaterials, 2001. **22**: p. 371-401.
5. Mansur, L., et al., *Assessment of shielding material performance for deep space missions*, in *Materials for space applications*, M. Chipara, et al., Editors. 2005, Materials Reserach Society: Warrendale, PA.
6. Banks, B., K.d. Groh, and S. Miller, *Low earth orbital atomic oxygen interactions with spacecraft materials*, in *Materials for space applications*, M. Chipara, et al., Editors. 2005, Materials Reserach Society: Warrendale, PA.
7. Premnath, V., A. Bellare, E.W. Merrill, M. Jasty, W.H. Harris, *Molecular rearrangements in ultra high molecular weight polyethylene after irradiation and long-term storage in air.* Polymer, 1999. **40**: p. 2215-2229.
8. Benson, R.S., C.P. Stephens, Ma. E. Martinez-Pardo, *Study of the relationship between crystal size and nano-hardness in ultra-high molecular weight polyethylene.* Journal of Applied Medical Polymers, 2002. **6**(2).
9. Tretinnikov, O., S. Ogata, Y. Ikada, *Surface crosslinking of polyethylene by electron beam irradiation in air.* Polymer, 1998. **39**(24): p. 6115-6120.
10. Morrison, M., *Effect of crosslinking on the tribological properties of ultra-high molecular weight polyethylene,* in *Materials Science and Engineering*. 2002, University of Tennessee: Knoxville, TN.
11. Hollis, B., *Analysis of the wear behavior of VUV radiated ultra high molecular weight polyethylene.* 1999, The University of Tennessee: Knoxville, TN.
12. Guadagno, L., et al., *Chemical and morphological modifications of irradiated linear low density polyethylene (LLDPE.* Polymer Degradation and Stability, 2001. **72**(1): p. 175-186.
13. Wilson, J.F., et al., *Study of hydrogen annealing of ultrahigh molecular weight polyethylene irradiated with high-energy protons.* Journal of Materials Research, 1999. **14**(11): p. 4431-4436.
14. Wilson, J.F., et al., *Proton modification of ultra high molecular weight polyethylene to promote crosslinking for enhanced chemical and physical properties.* Mater. Res. Soc. Symp. Proc., 1996. **396**(Ion-Solid Interactions for Materials Modification and Processing): p. 311-316.
15. Sasuga, T., H. Kudoh, and T. Seguchi, *High energy ion irradiation effects on polymer materials-changes in mechanical properties of PE, PSF and PES.* Polymer, 1999. **40**(18): p. 5095-5102.
16. Martinez-Pardo, M.E., et al., *Characterization of MeV proton irradiated PS and LDPE thin films.* Nucl. Instrum. Methods Phys. Res., Sect. B, 1998. **140**(3,4): p. 325-340.

17. Premnath, V., et al., *Gamma Sterilization of UHMWPE Articular Implants: An Analysis of the Oxidation Problem.* Biomaterials, 1996. **17**: p. 1741-1753.
18. Blanchet, T. and B. Burroughs, *Numerical Oxidation Model for Gamma Radiation-Sterilized UHMWPE: Consideration of Dose-Depth Profile.* Journal of Biomedical Materials Research, 2001. **58**: p. 684-693.
19. Dawes, K. and L.C. Glover, *Effects of electron beam and gamma-irradiation on polymer*, in *Physical properties of polymers handbook*, J. Mark, Editor. 1996, American Institute of Physics: Woodbury, NY.
20. Zhu, L., et al., *Physical constants of poly(ethylene)*, in *Polymer Handbook*, A. Abe and D.R. Bloch, Editors. 1999, John Wiley and Sons, Inc.: New York.
21. Wert, J.A., *Materials science and engineering laboratories, Chapter 2: X-ray diffraction laboratory*: Techische Univertitat Darmstadt.
22. Kavesh, S. and J. Schultz, *Meaning and Measurement of Crystallinity in Polymers: A Review.* Polymer Engineering and Science, 1969. **9**(6): p. 452-460.
23. Hama, H. and K. Tashiro, *Structural changes in isothermal crystallization process of polyoxymethylene investigated by time-resolved FTIR, SAXS and WAXS measurements.* Polymer, 2003. **44**: p. 6973–6988.
24. Patel, G. and A. Keller, *Crystallinity and the Effect of Ionizing Radiation in Polyethylene. I. Crosslinking and the Crystal Core.* Journal of Polymer Science, Polymer Physics Edition, 1975. **13**(2): p. 303-21.
25. Crist, B. and F.M. Mirabella, *Crystal thickness distribution from melting homopolymers or random copolymers.* Journal of Polymer Science: Part B: Polymer Physics, 1999. **37**: p. 3131-3140.
26. Cook, J.T.E., et al., *The morphology of nascent and molded ultra-high molecular weight polyethylene. Insights from solid-state NMR, nitric acid etching, GPC and DSC.* Polymer, 2000. **41**: p. 8615-8623.
27. Valles-Llunch, A., L. Contat-Rodrigo, and A. Ribes-Greus, *Differential scanning Calorimetry studies on high- and low-density annealed and irradiated polyethylenes: Influence of aging.* Journal of Applied Polymer Science, 2003. **89**: p. 3260-3271.
28. Flory, P., J. Trans. Faraday Soc., 1955. **51**: p. 848.
29. Wignall, G.D., *Neutron and X-Ray Scattering*, in *Physical Properties of Polymer Handbook*, J.E. Mark, Editor. 1996, American Institute of Physics: Woodbury, New York. p. 299-310.
30. Kim, M.-H., *The melting behavior and structure of ethylene copolymers from metallocene catalysts*, in *Materials Science and Engineering*. 1996, The University of Tennessee: Knoxville.
31. Schmidt, M.A., *Surface texture and micromechanics of ultra high molecular weight polyethylene (UHMWPE) orthopedic implant bearings*, in *Materials Science and Engineering*. 2001, The University of Tennessee: Knoxville.
32. Thomas, S.G., *Influence of silicon concentration on the nanoindentation and nanoscatch behavior of pyrolytic carbon*, in *Materials Science and Engineering*. 2000, University of Tennessee: Knoxville.

33. Balta Calleja, F.J., L. Giri, I.M. Ward, D.L.M. Cansfield, *Microstructure of Bulk Crystallized Linear Polyethylene: Correlation of Microhardness and Yield Stress.* Journal of Materials Science, 1995. **30**: p. 1139-1143.
34. Santa Cruz, C., F.J. Balta Calleja, T. Asano, I.M. Ward, *Plastic deformation in polyethylene crystals studied by microindentation hardness.* Philosophical Magazine A, 1993. **68**(1): p. 209-224.
35. Rodriguez, F., *Principles of Polymer Systems*. 4 ed. 1996: Taylor and Francis. 671-675.
36. Zachariades, A.E. and J.A. Logan, Journal of Polymer Science B: Polymer Physics, 1983. **37**: p. 3131.
37. Stephens, C.P. *The Effect of Dose Rate on the Morphology of Gamma Irradiated Ultra High Molecular Weight Polyethylene (UHMWPE).* in *Society of Plastics Engineers Annual Technical Conference*. 2003. Nashville, TN.
38. Oliver, W.C., G. M. Pharr, J. Mater. Res., 1992. **7**(1564).
39. Wright, T.M.e.a., Trans ORS, 1991. **16**(248).
40. Auerbach, I., *Irradiated Polyethylene II- Free Radical Formation.* Polymer, 1996. **8**: p. 63-77.
41. Buchanan, F. and P. Shipway, *Microabrasion- A Simple Method to Assess Surface Degradation of UHMWPE Following Sterilization and Ageing.* Biomaterials, 2002. **23**: p. 93-100.

Appendix

Appendix 1: Proton Irradiated DSC

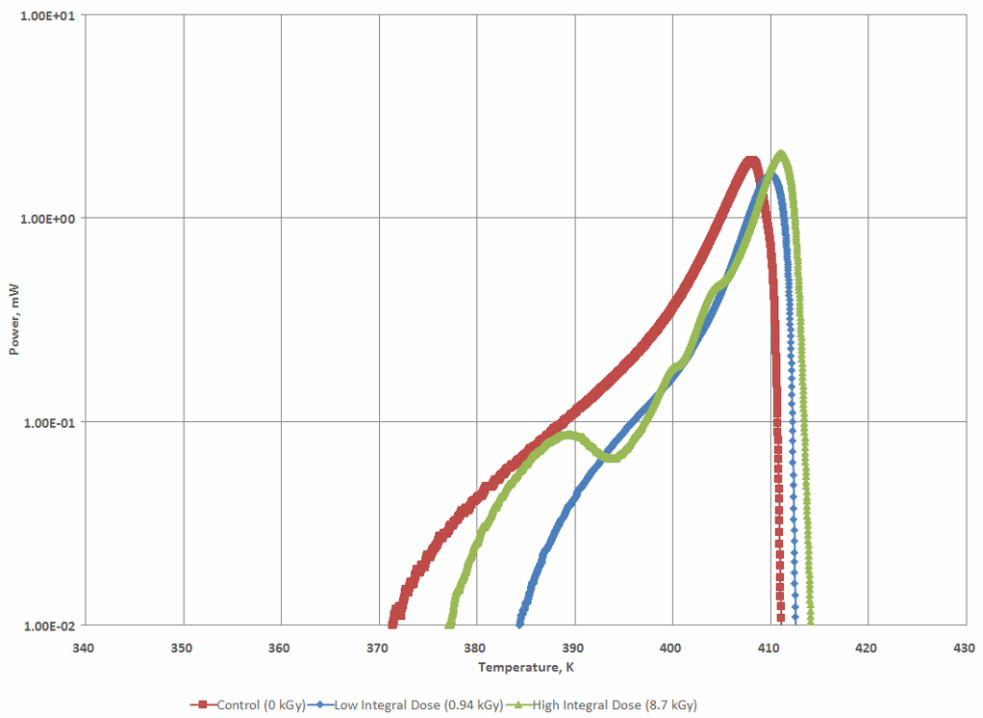

Figure 64: Endotherm for Run 1 of Proton Irradiated Samples

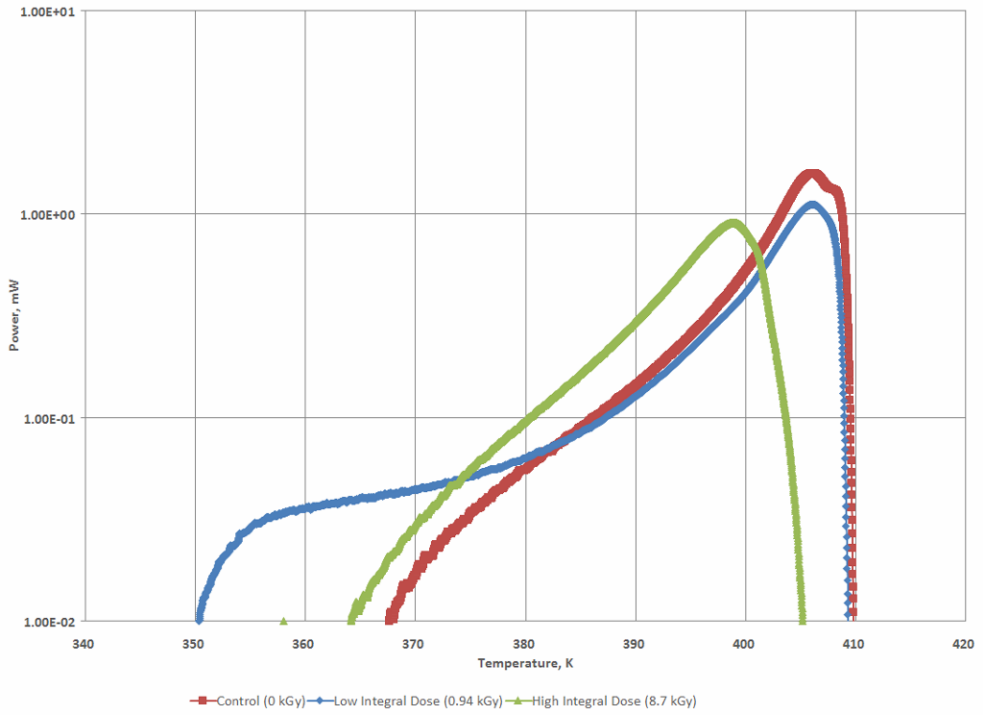

Figure 65: Endotherm for Run 2 of Proton Irradiated Samples

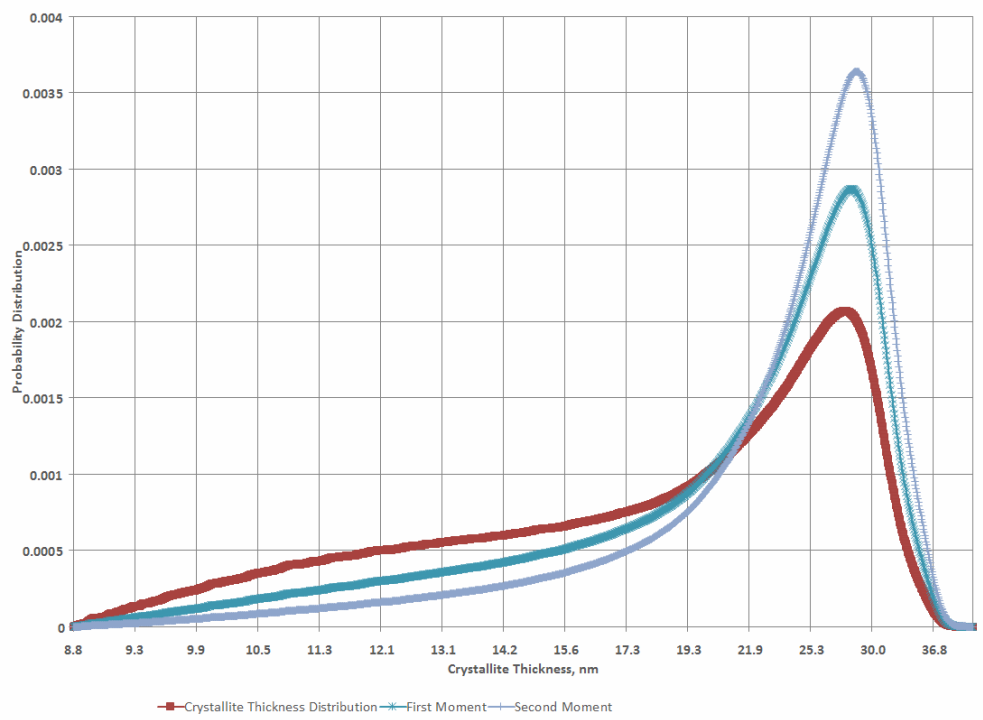

Figure 66: Run 1 of 0.96 kGy Proton Irradiated Sample (CPS04015A_1F)

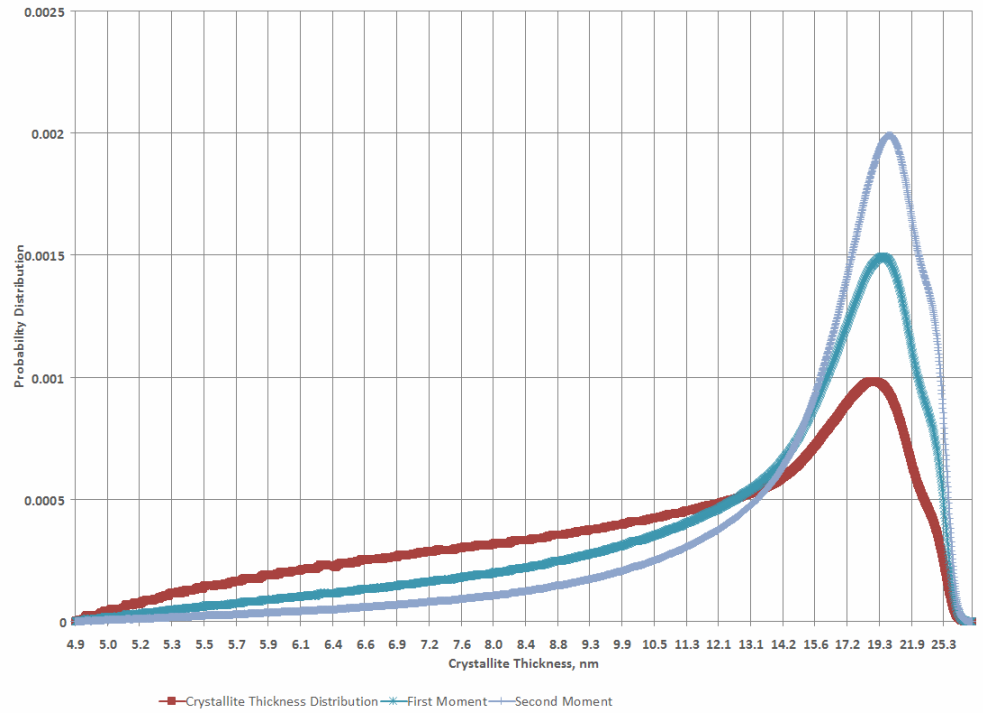

Figure 67: Run 2 of 0.96 kGy Proton Irradiated Sample (CPS04015A_3F)

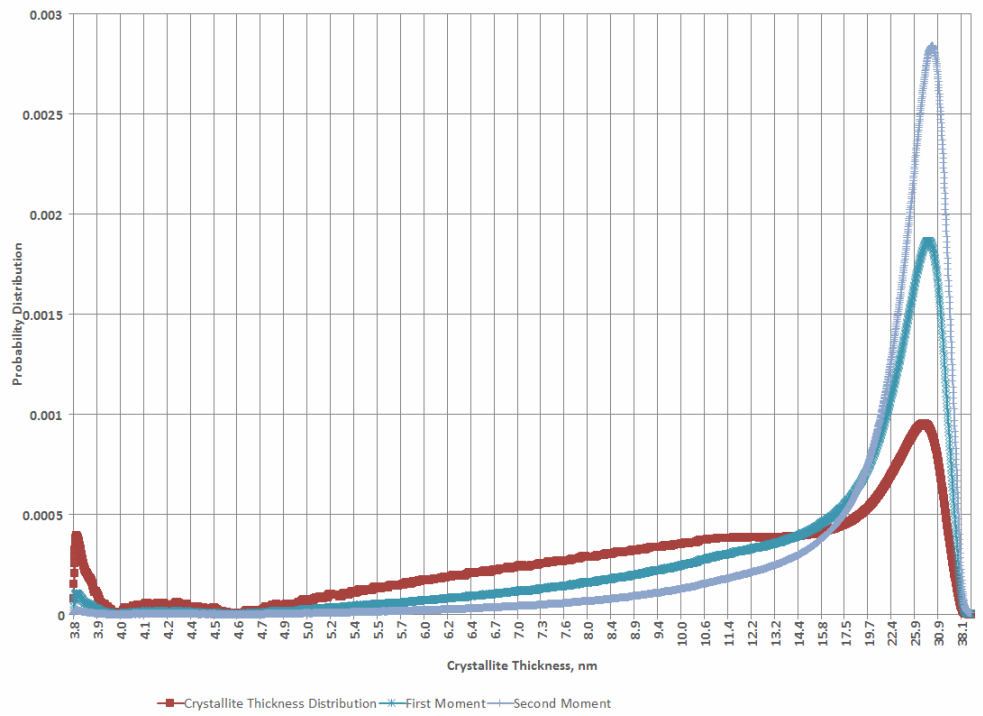

Figure 68: Run 1 of 1.08 kGy Proton Irradiated Sample (CPS04015B_1F)

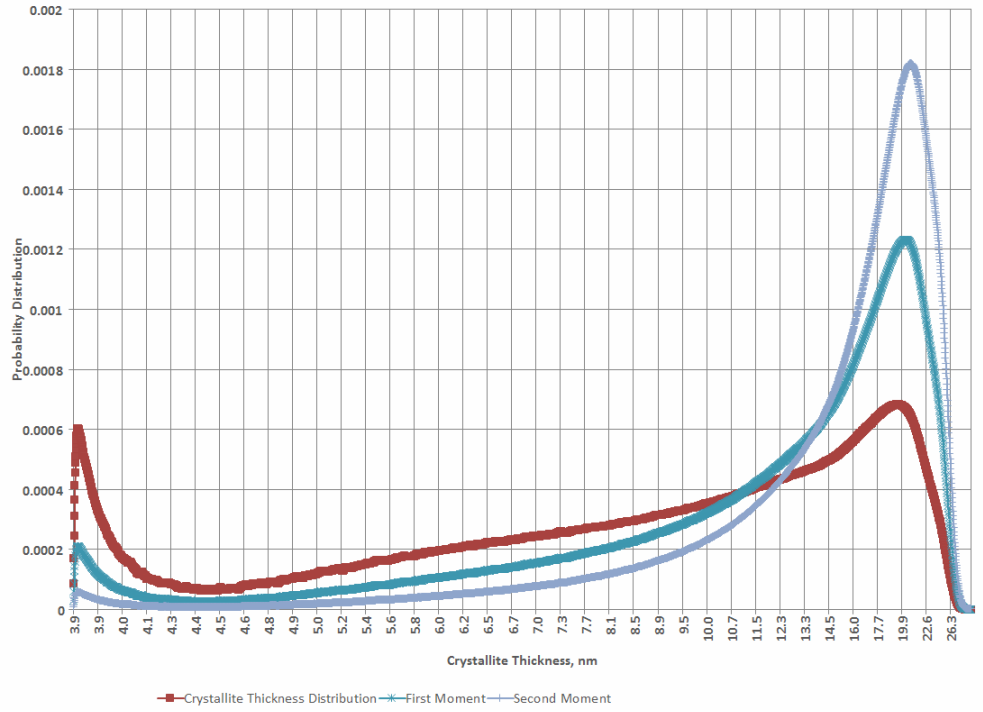

Figure 69: Run 2 of 1.08 kGy Proton Irradiated Sample (CPS04015B_3F)

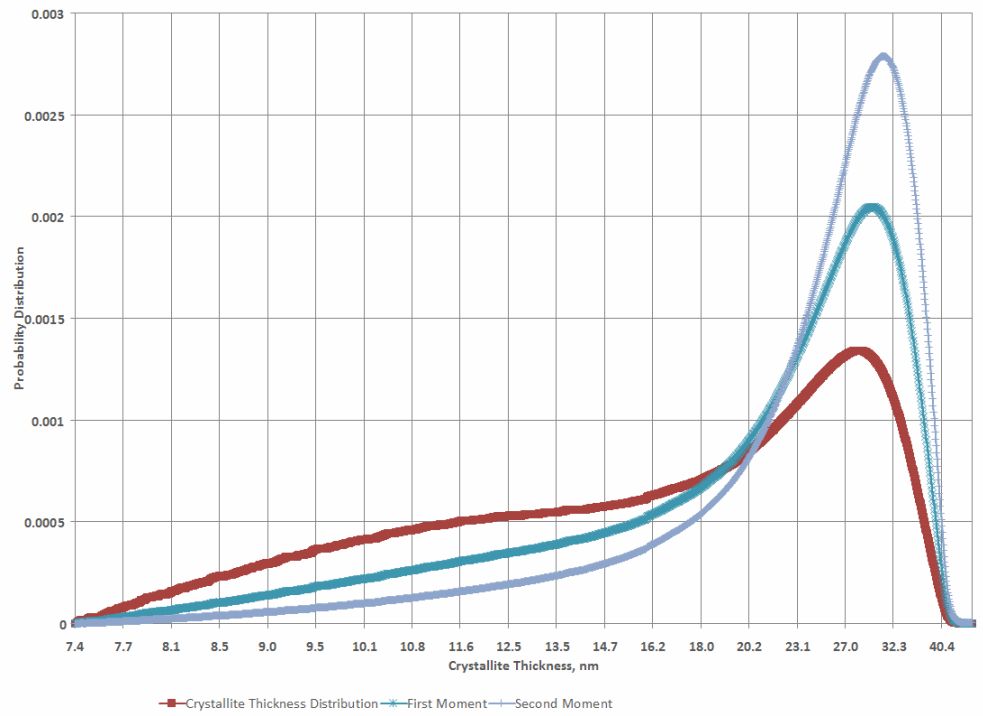

Figure 70: Run 1 of 0.94 kGy Proton Irradiated Sample (CPS04015C_1F)

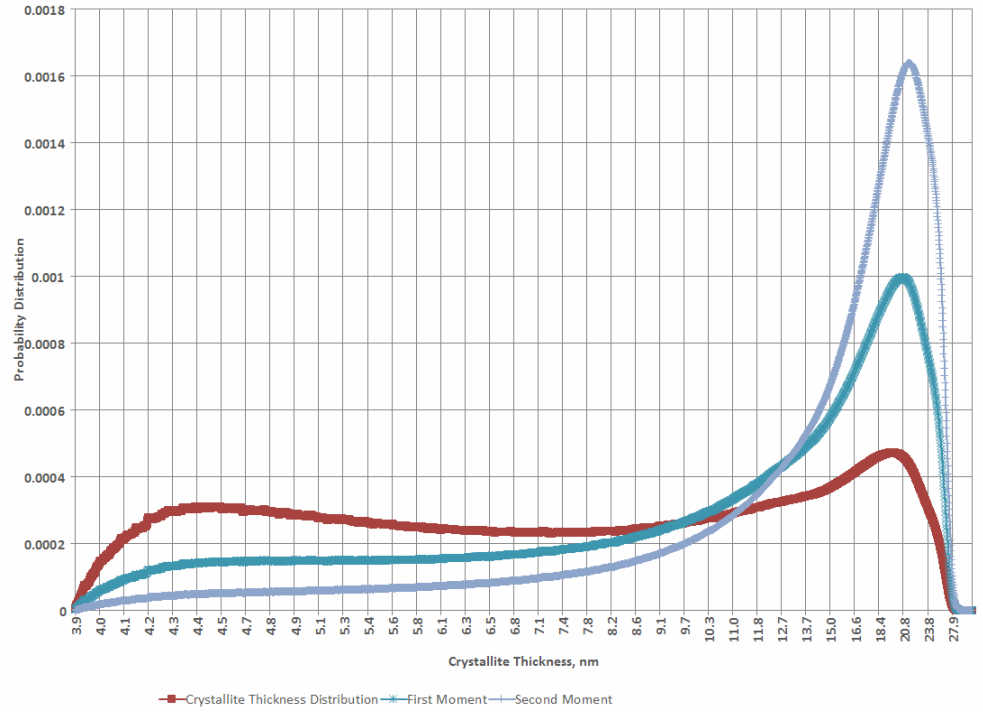

Figure 71: Run 2 of 0.94 kGy Proton Irradiated Sample (CPS04015C_3F)

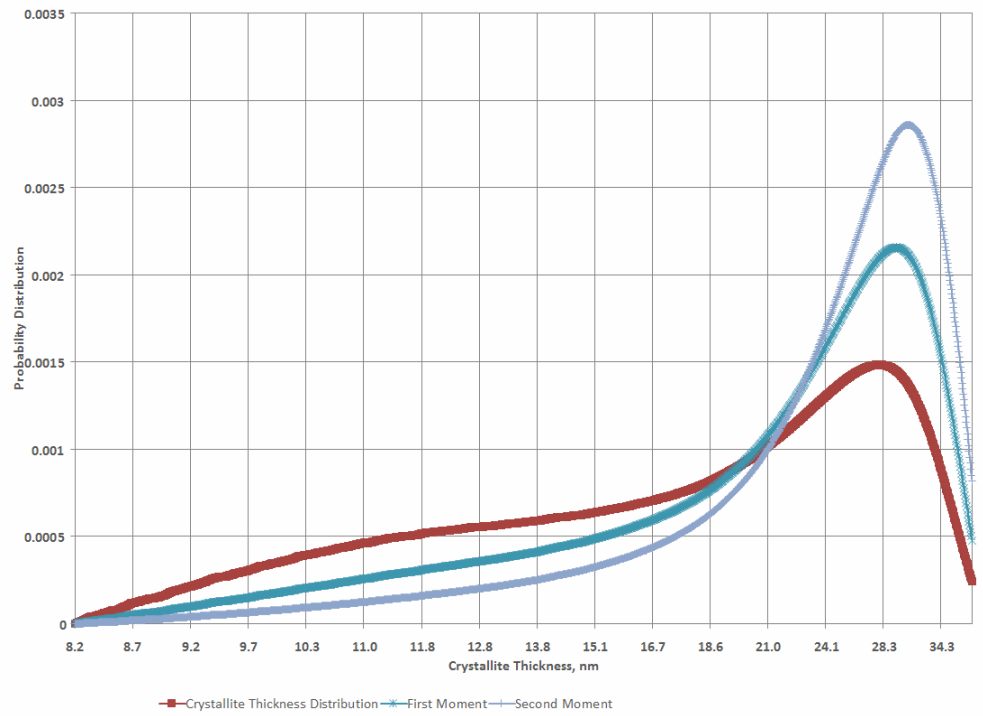

Figure 72: Run 1 of 1.15 kGy Proton Irradiated Sample (CPS04015D_1F)

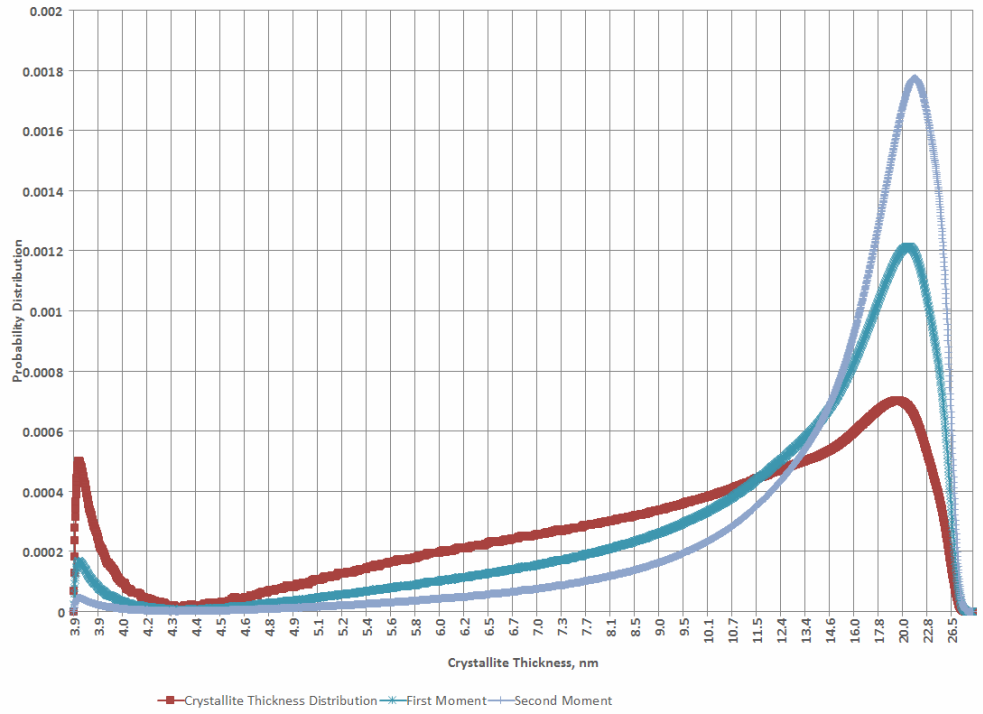

Figure 73: Run 2 of 1.15 kGy Proton Irradiated Sample (CPS04015D_3F)

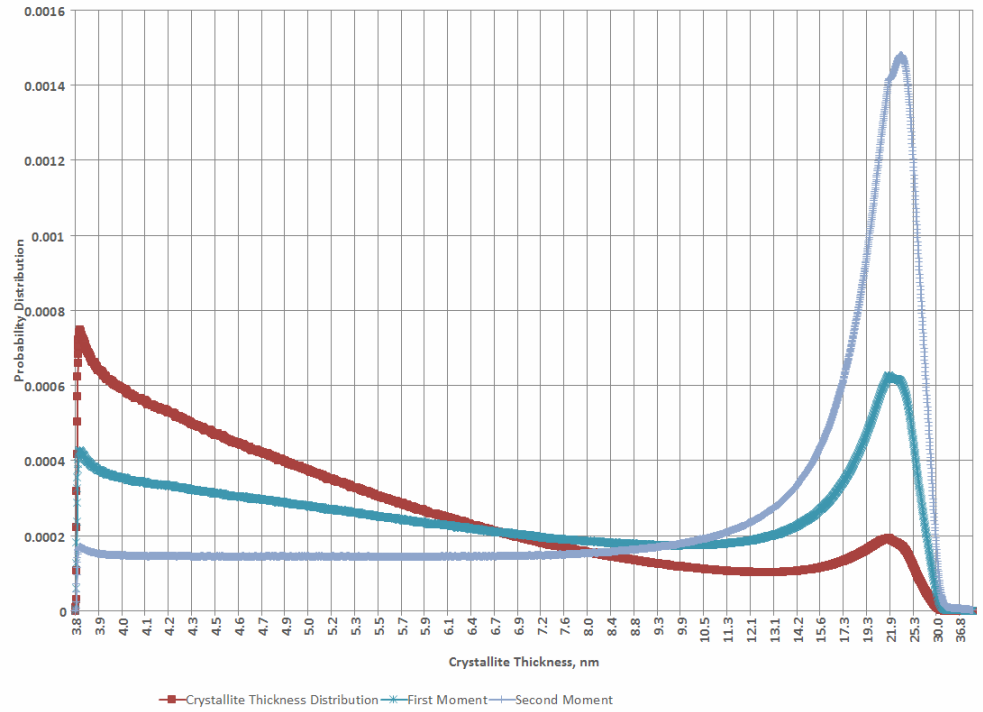

Figure 74: Run 1 of 0 kGy (Control) Proton Irradiated Sample (CPS04018B_1F)

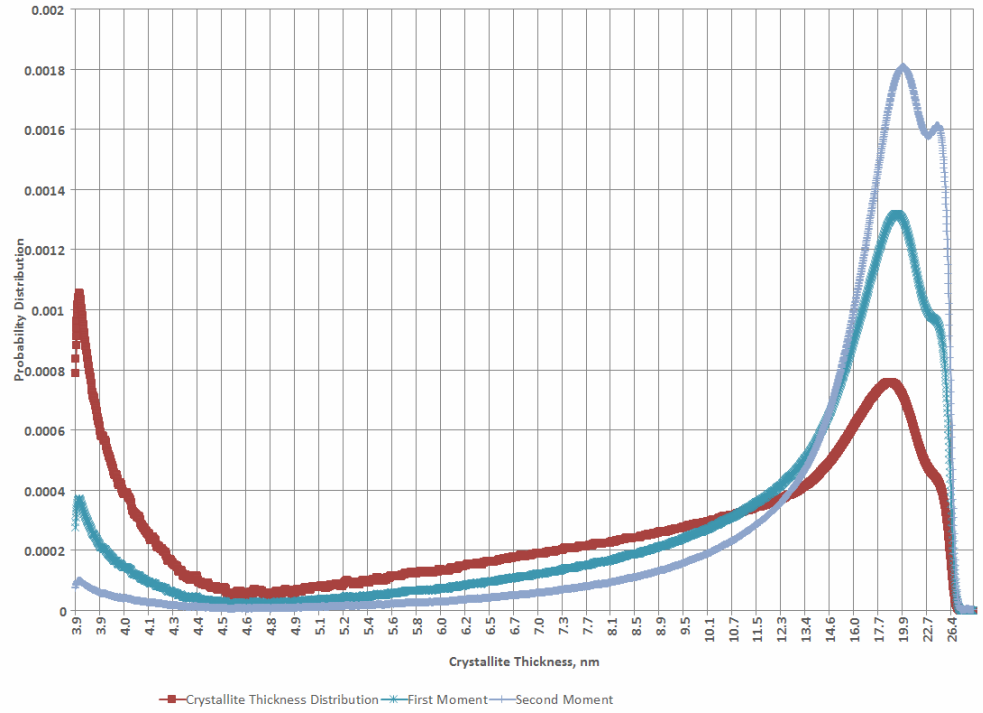

Figure 75: Run 2 of 0 kGy (Control) Proton Irradiated Sample (CPS04018B_3F)

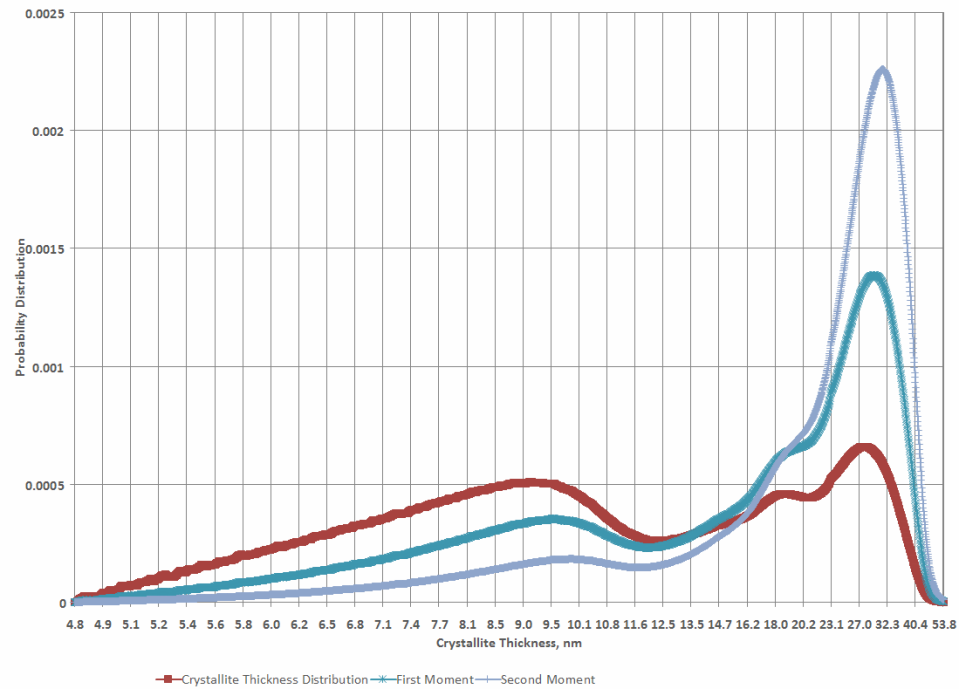

Figure 76: Run 1 of 6.8 kGy Proton Irradiated Sample (CPS04018C_1F)

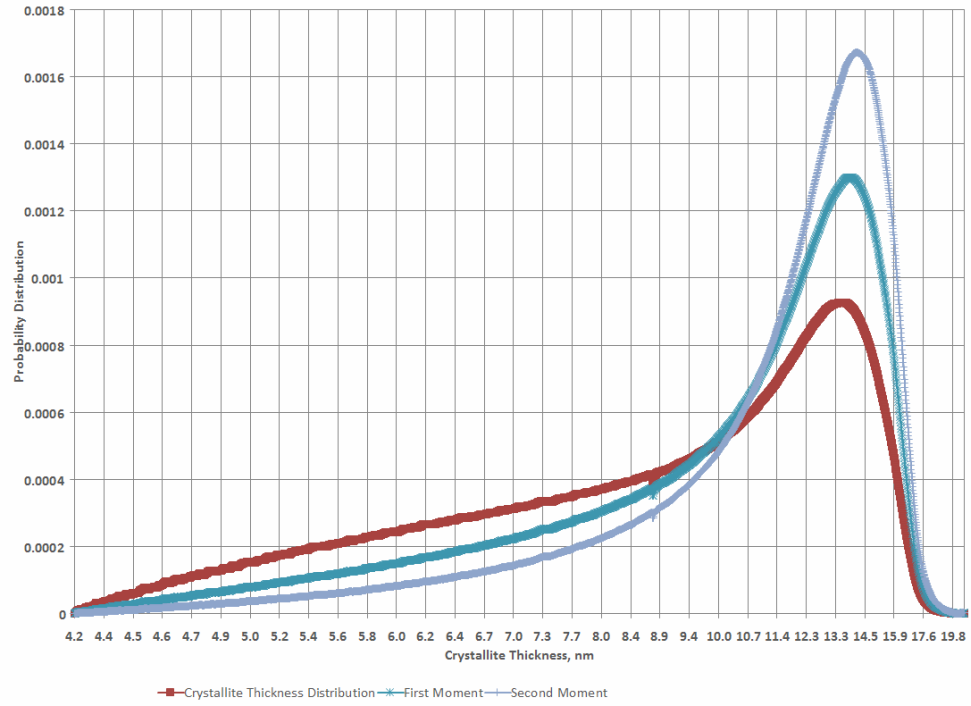

Figure 77: Run 2 of 6.8 kGy Proton Irradiated Sample (CPS04018C_3F)

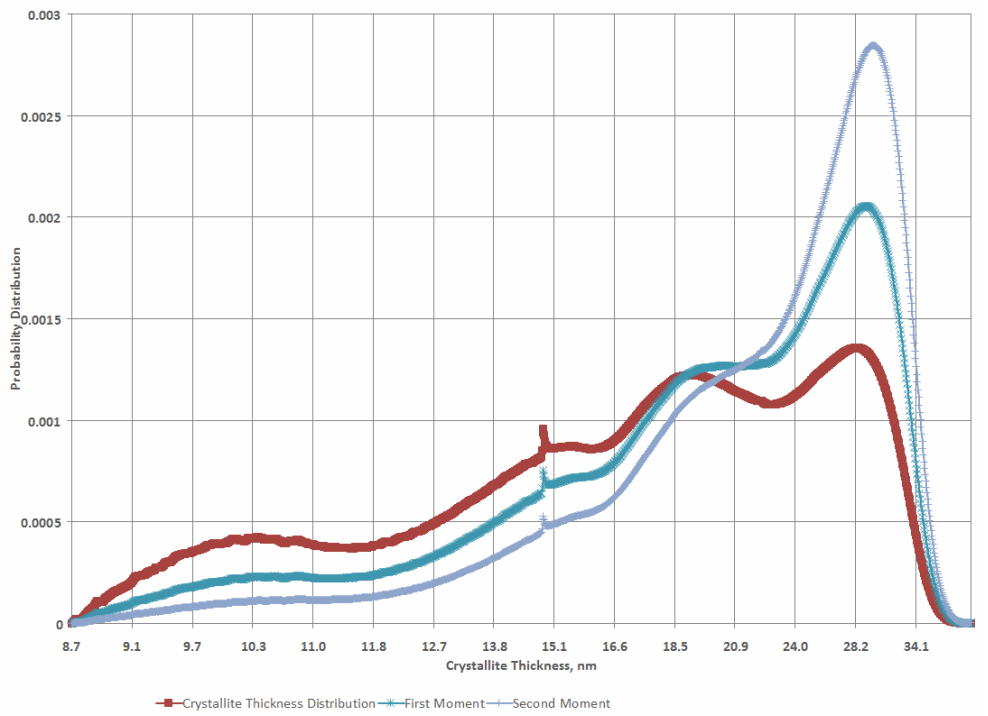

Figure 78: Run 1 of 8.3 kGy Proton Irradiated Sample (CPS04018D_1F)

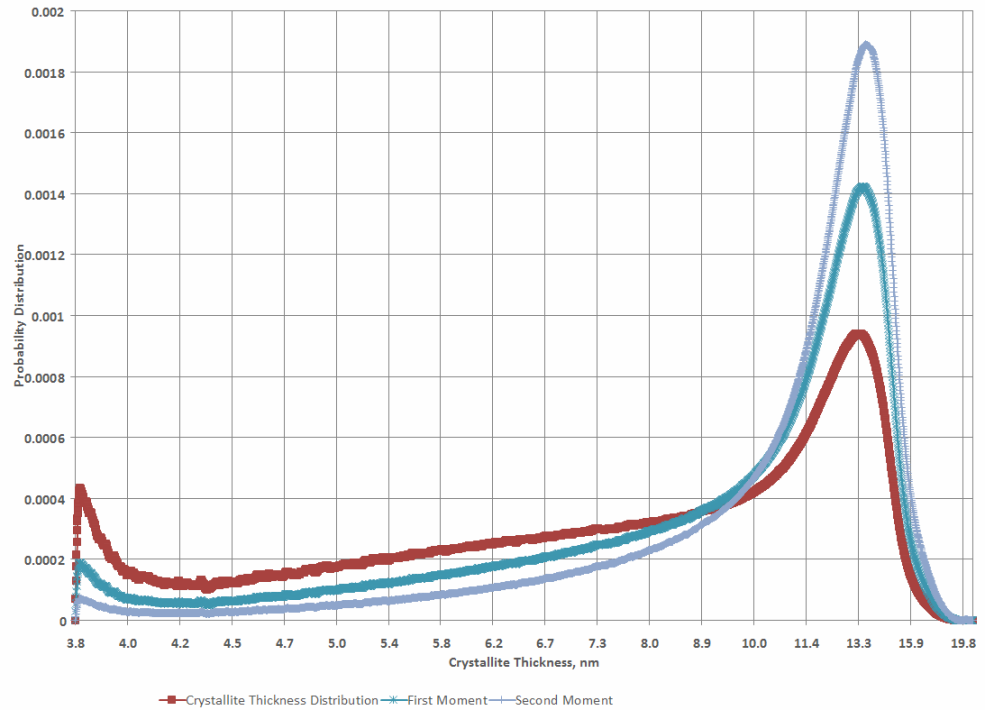

Figure 79: Run 2 of 8.3 kGy Proton Irradiated Sample (CPS04018D_3F)

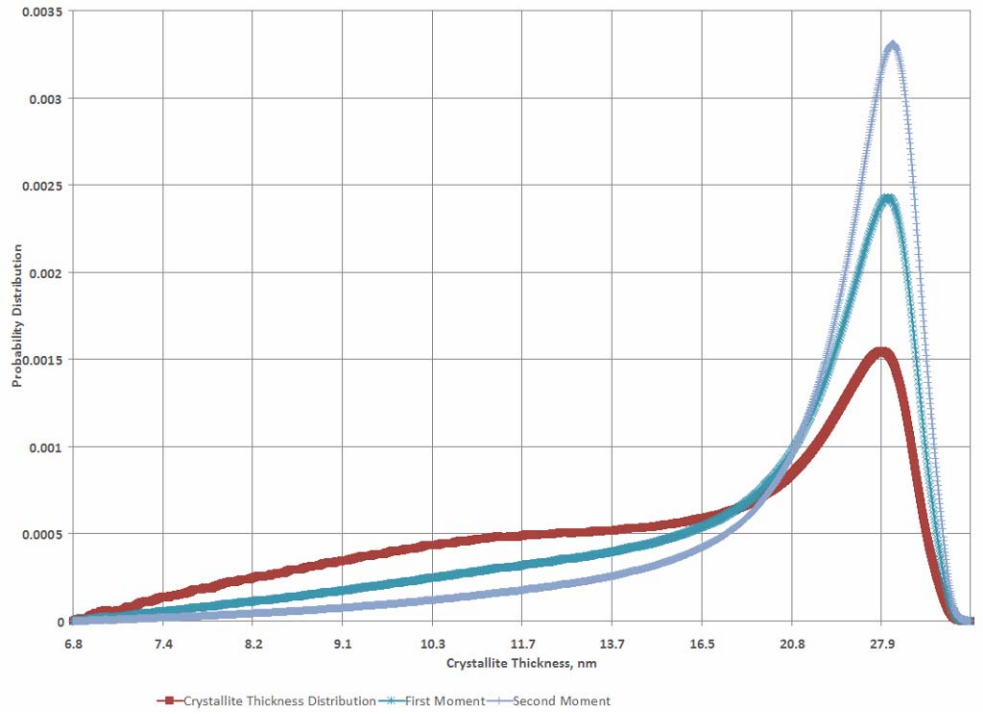

Figure 80: Run 1 of 3.7 kGy Proton Irradiated Sample (CPS04019A_1F)

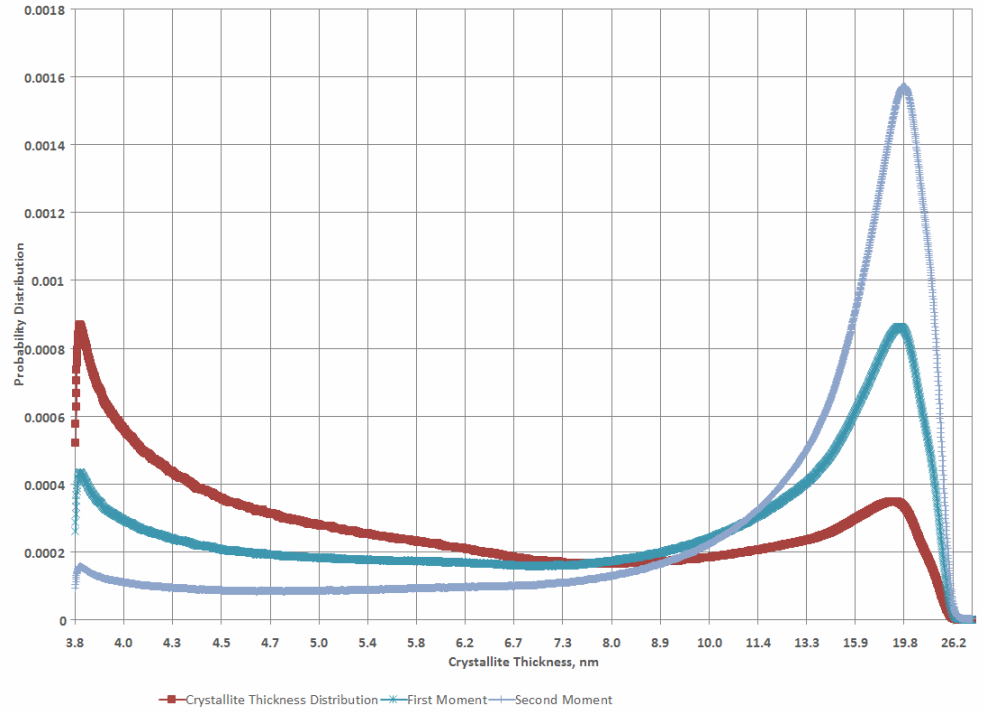

Figure 81: Run 2 of 3.7 kGy Proton Irradiated Sample (CPS04019A_3F)

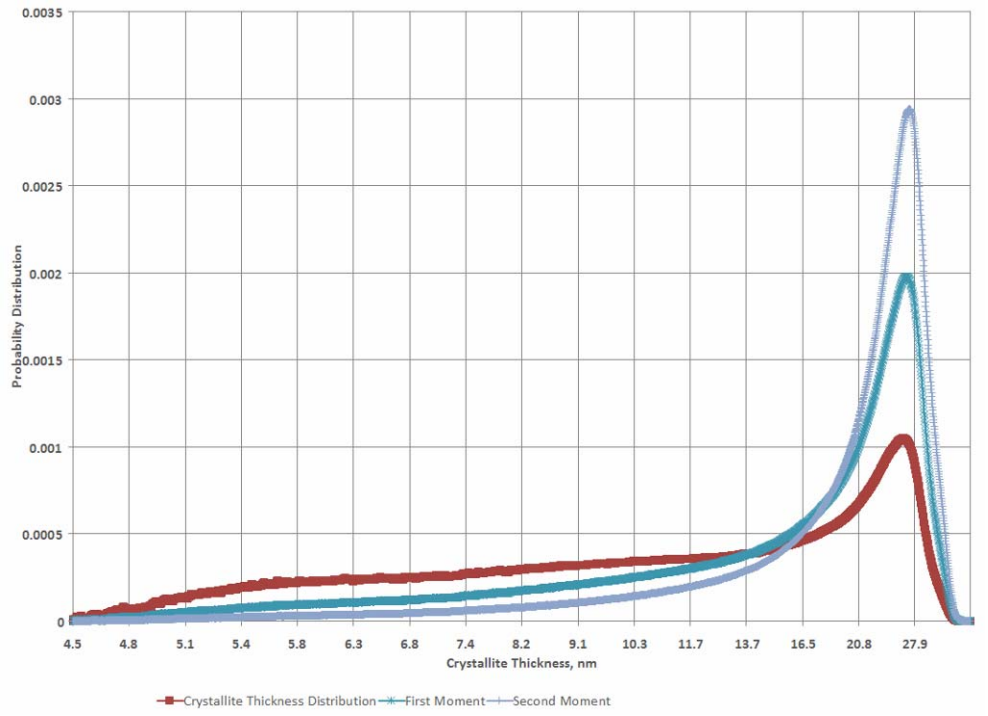

Figure 82: Run 1 of 1.33 kGy Proton Irradiated Sample (CPS04019B_1F)

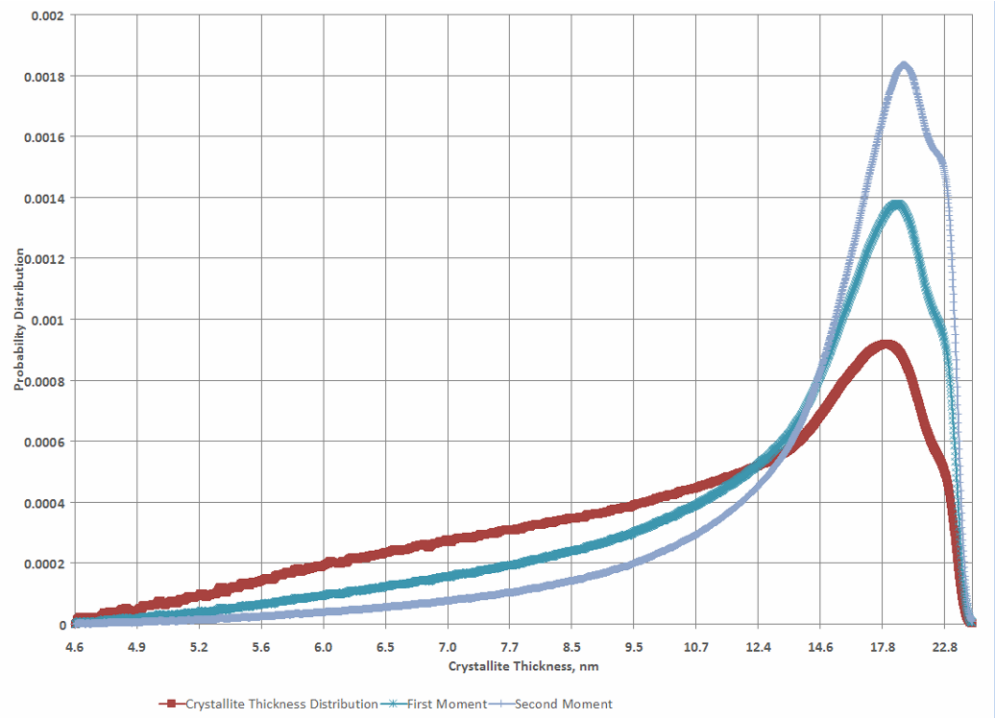

Figure 83: Run 2 of 1.33 kGy Proton Irradiated Sample (CPS04019B_3F)

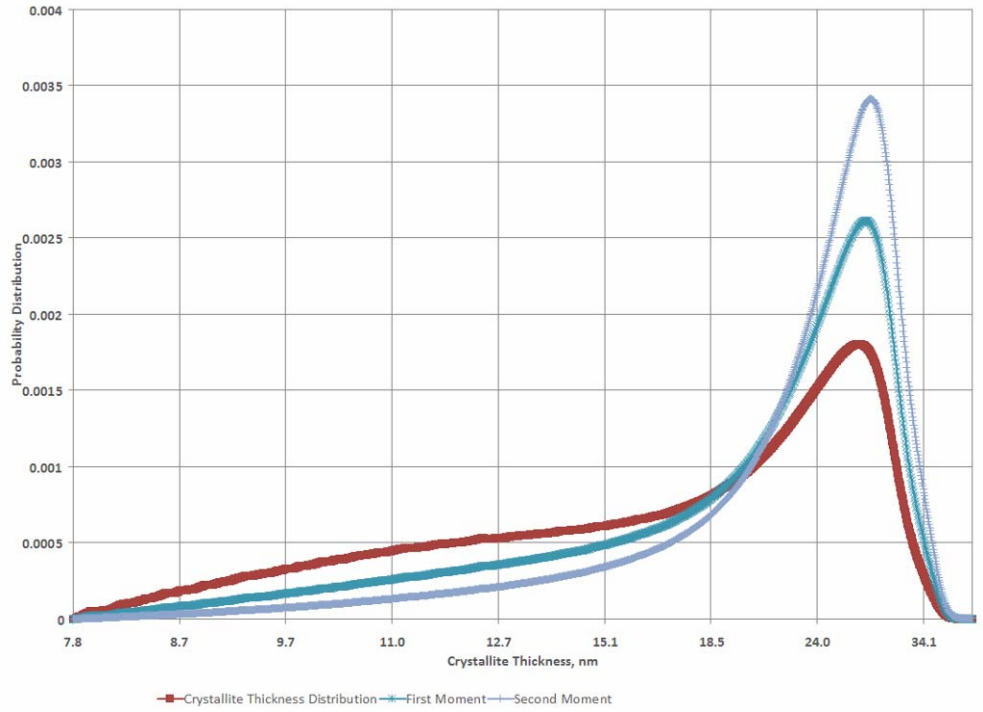

Figure 84: Run 1 of 0 kGy (Control) Proton Irradiated Sample (CPS04019C_1F)

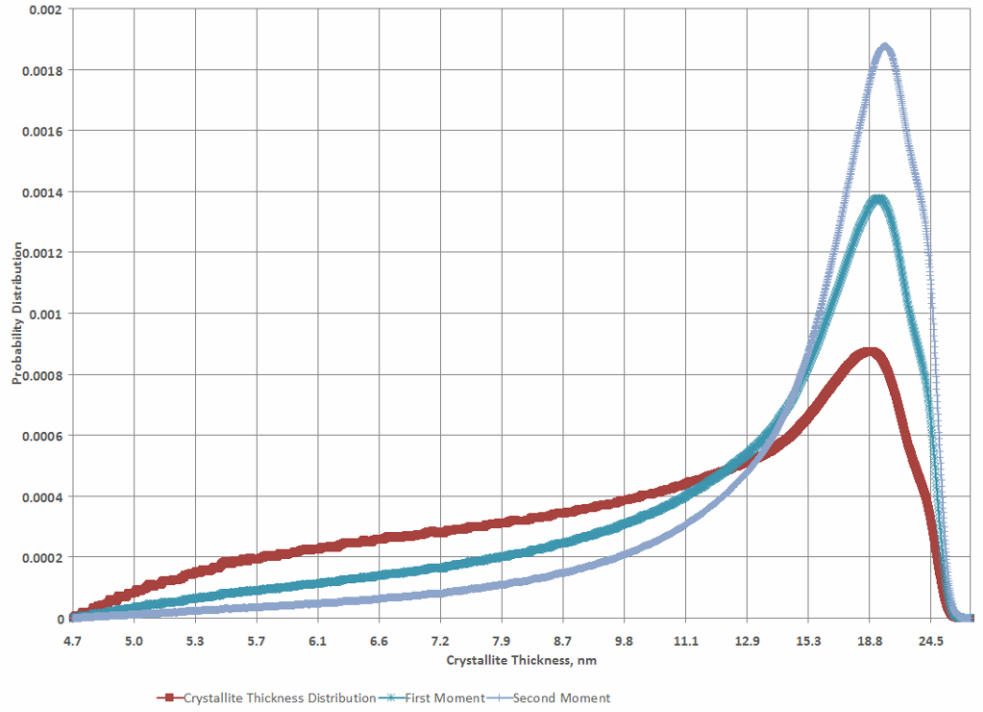

Figure 85: Run 2 of 0 kGy (Control) Proton Irradiated Sample (CPS04019C_3F)

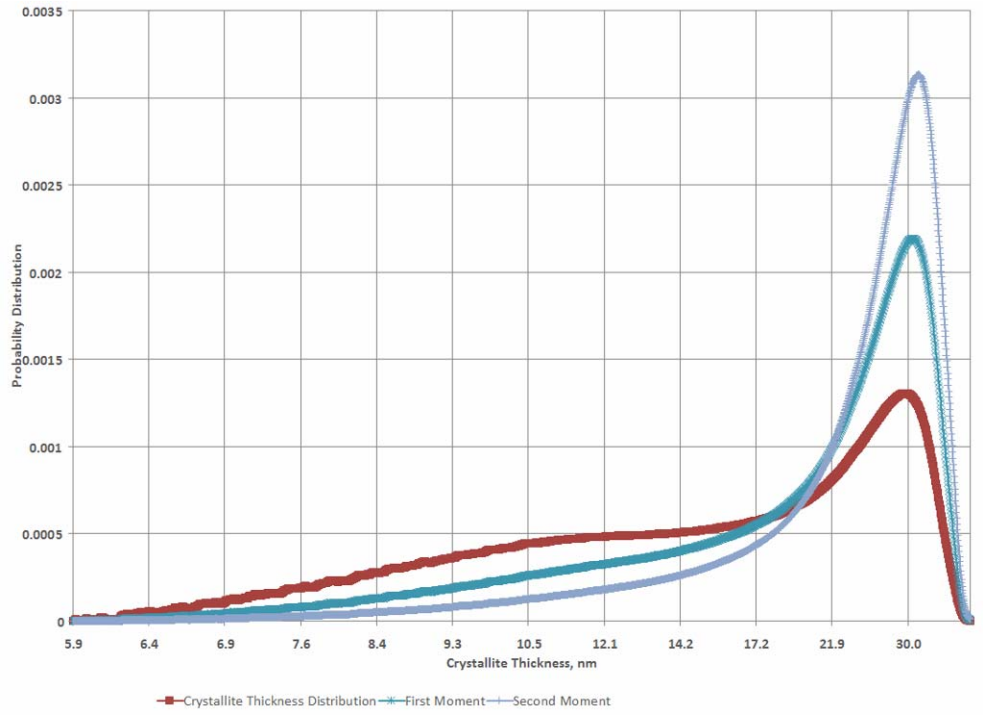

Figure 86: Run 1 of 3.7 kGy Proton Irradiated Sample (CPS04020A_1F)

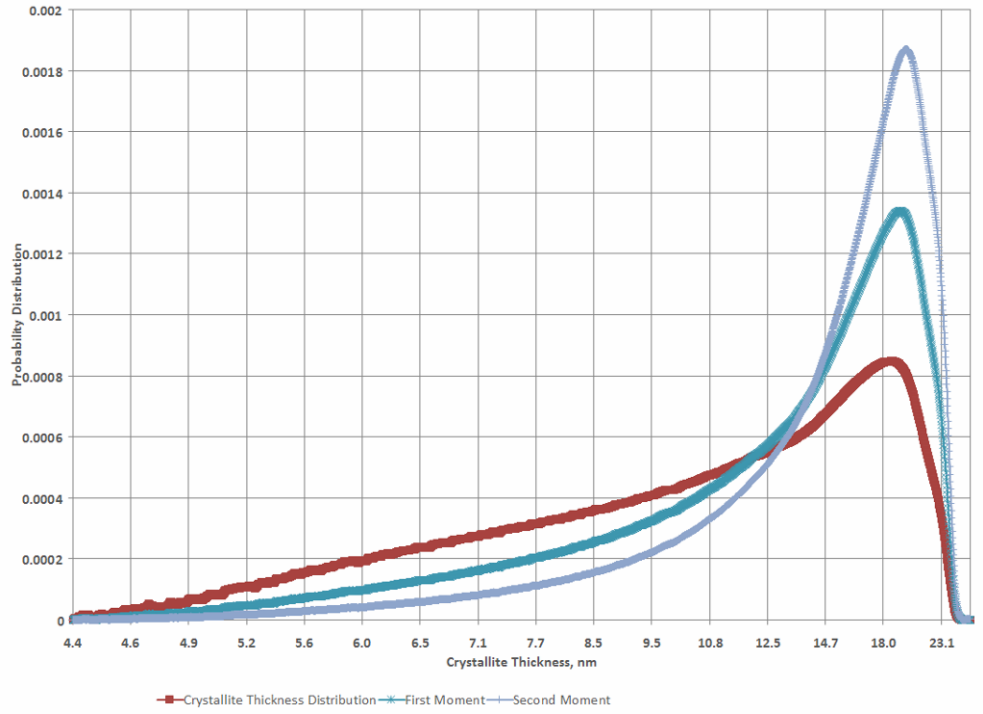

Figure 87: Run 2 of 3.7 kGy Proton Irradiated Sample (CPS04020A_3F)

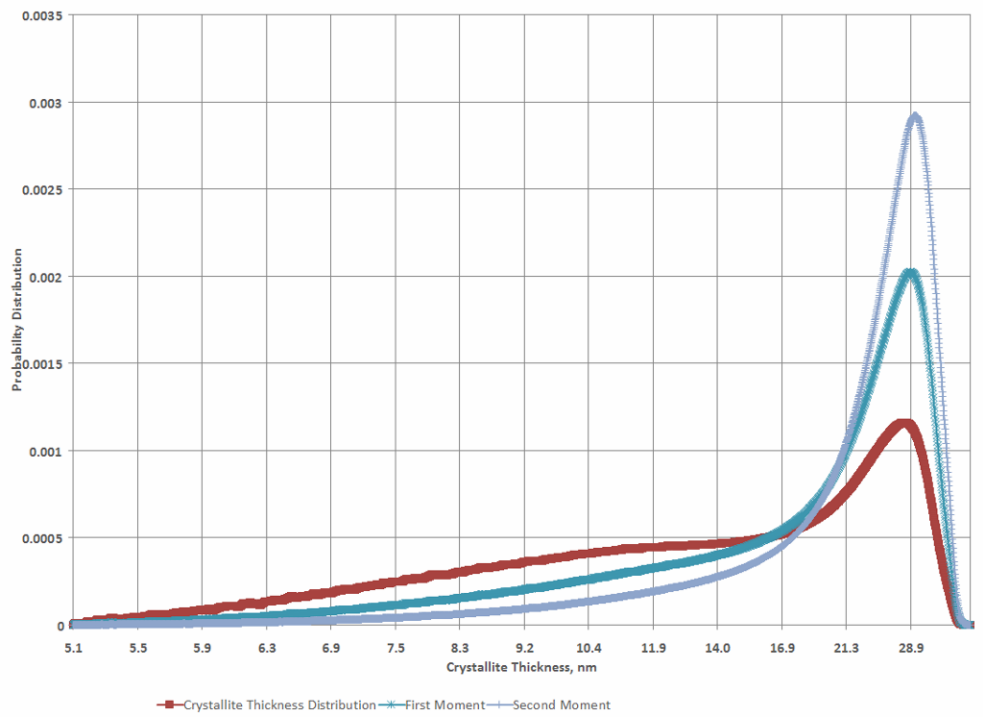

Figure 88: Run 1 of 1.33 kGy Proton Irradiated Sample (CPS04020B_1F)

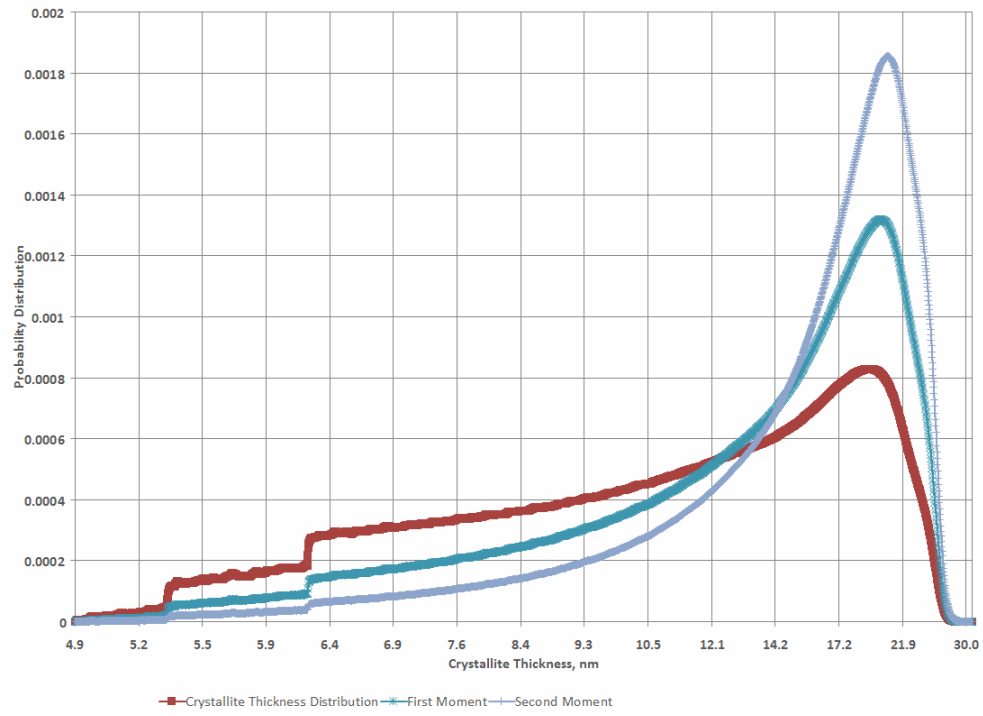

Figure 89: Run 2 of 1.33 kGy Proton Irradiated Sample (CPS04020B_3F)

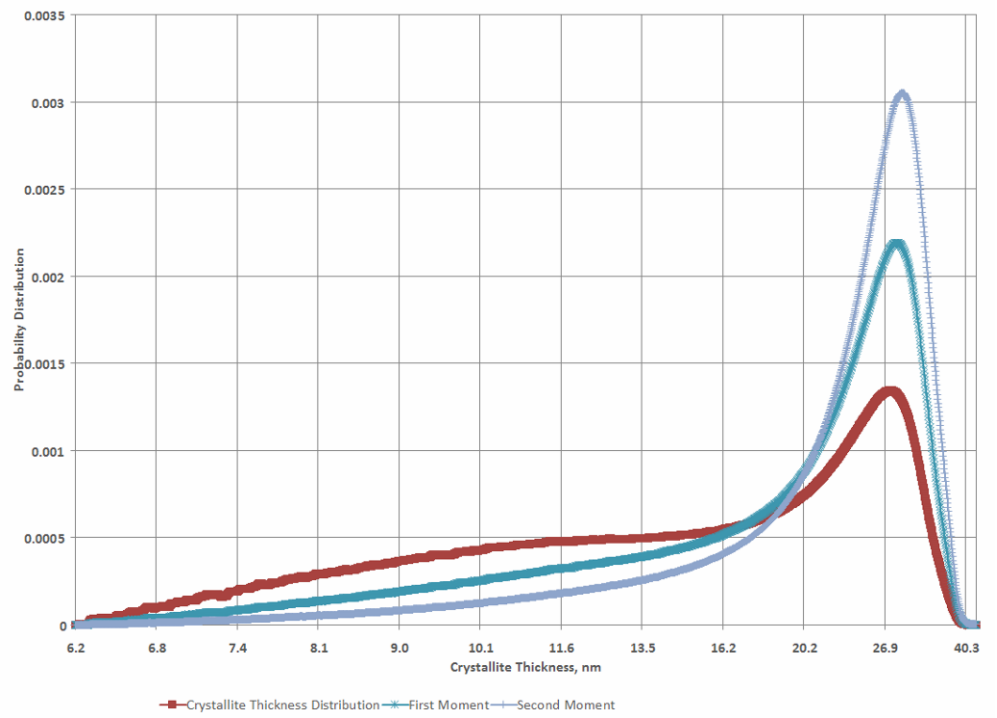

Figure 90: Run 1 of 0 kGy (Control) Proton Irradiated Sample (CPS04020C_1F)

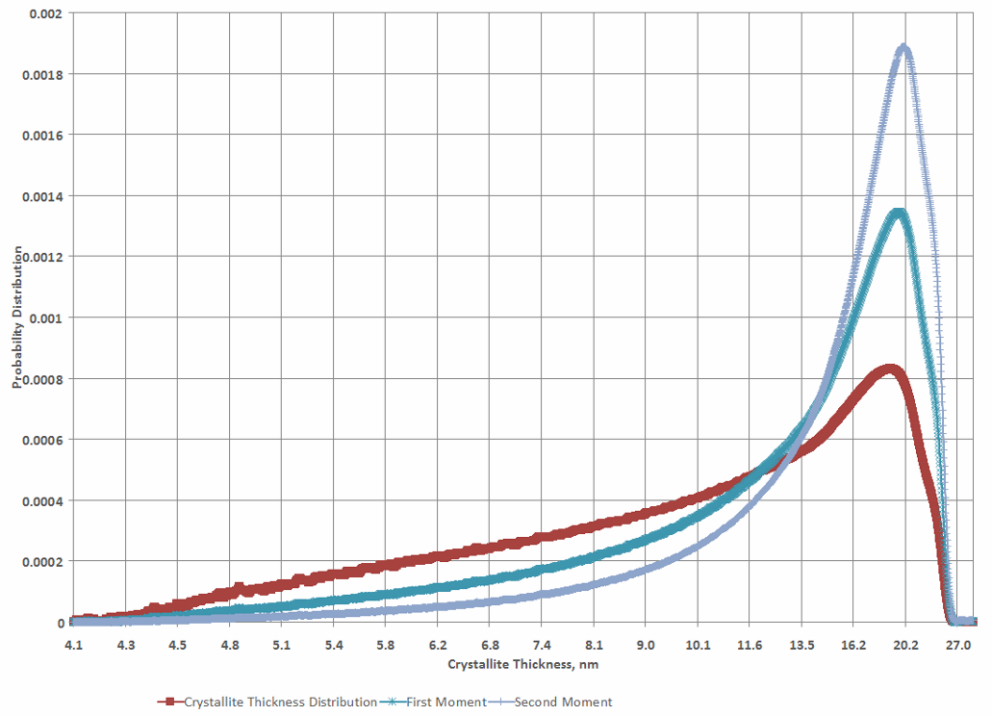

Figure 91: Run 2 of 0 kGy (Control) Proton Irradiated Sample (CPS04020C_3F)

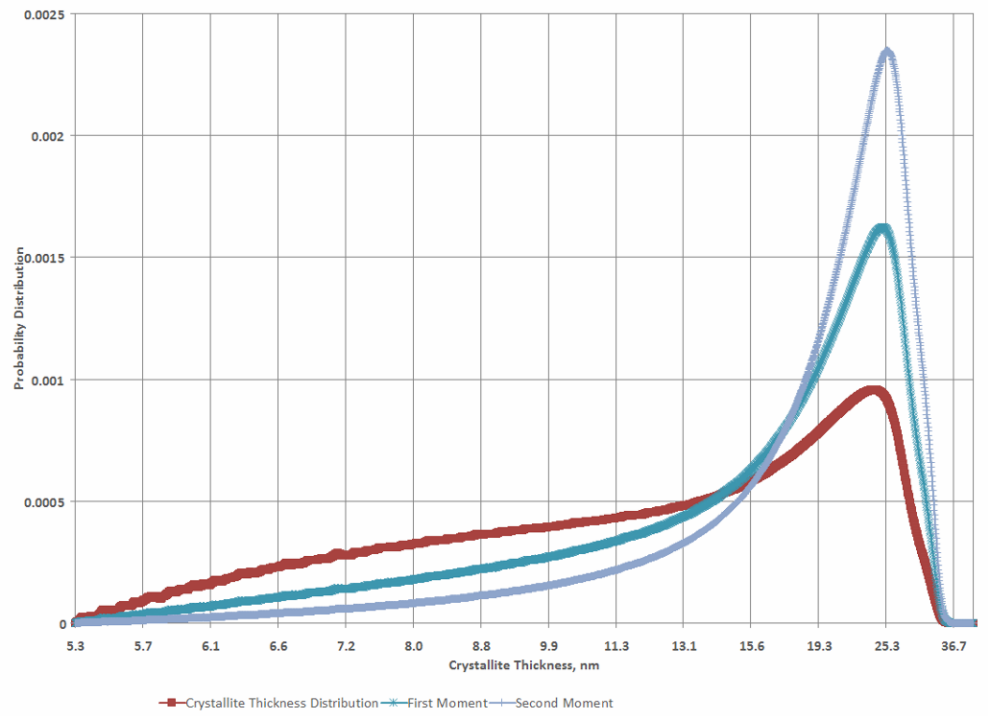

Figure 92: Run 1 of 0 kGy (Control) Proton Irradiated Sample (CPS04021A_1)

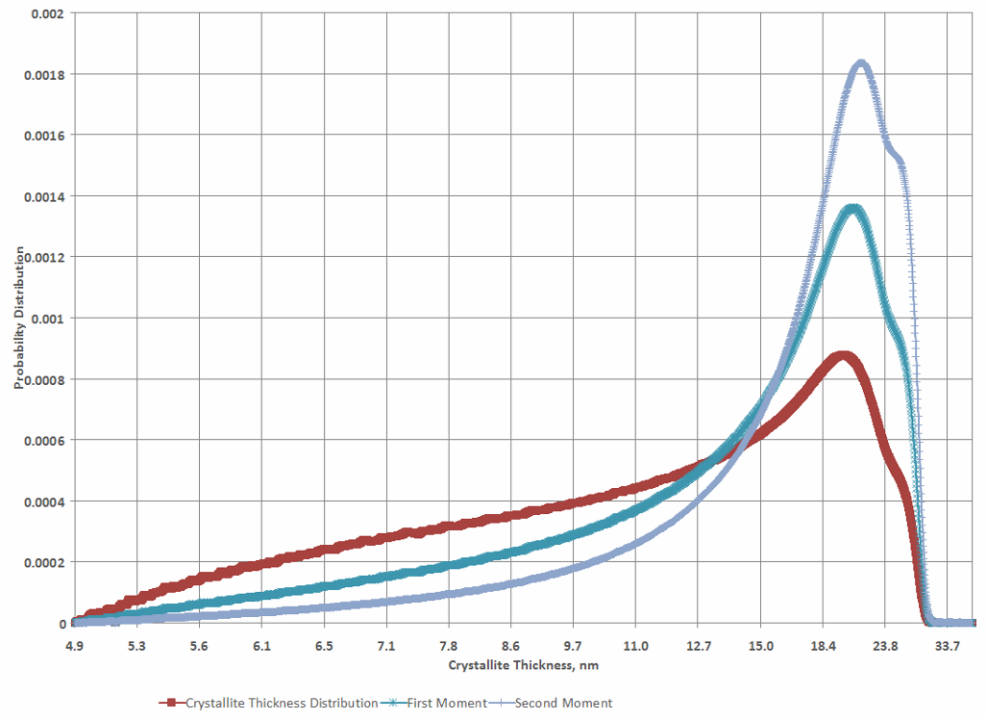

Figure 93: Run 2 of 0 kGy (Control) Proton Irradiated Sample (CPS04021A_3)

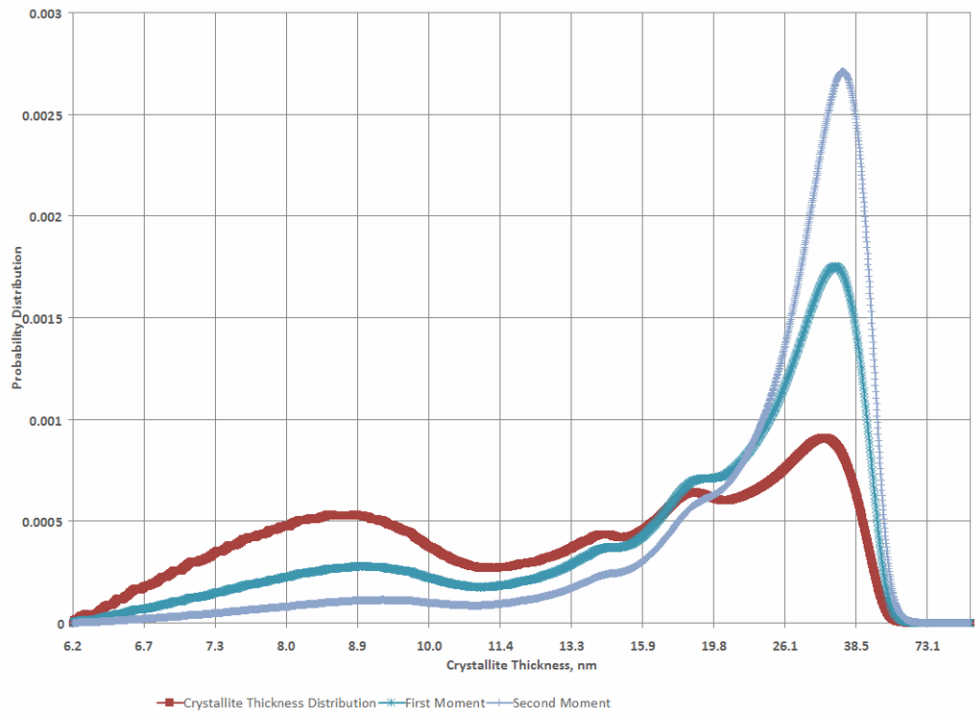

Figure 94: Run 1 of 8.7 kGy (Control) Proton Irradiated Sample (CPS04021B_1)

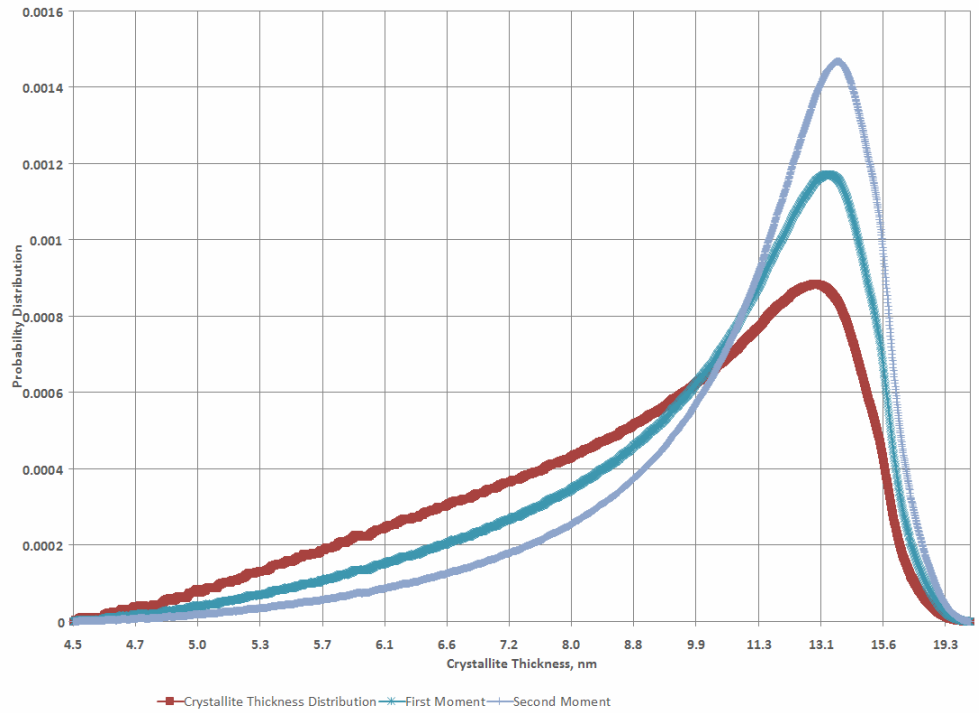

Figure 95: Run 2 of 8.7 kGy (Control) Proton Irradiated Sample (CPS04021B_3)

Appendix 2: Proton Irradiated Median Crystallite Thickness

Table 25: Median and Maximum Crystallite Thicknesses for Proton Irradiation Control Samples

	Integral Dose	0.00		0.00		0.00		0.00					
	Sample Number	19C		18B		20C		21A		Average		StdDev	
	Run Number	1	2	1	2	1	2	1	2	1	2	1	2
Crystallite Thickness Distribution	Middle	24.53	17.06	14.01	17.63	24.71	16.65	20.76	18.30	21.00	17.41	3.78	1.82
	Maximum	41.74	27.61	31.28	30.87	40.39	29.79	35.45	29.63	37.22	29.48	5.02	3.90
First Moment	Middle	25.98	18.53	20.00	19.17	26.66	18.14	27.06	20.07	24.93	18.98	3.33	2.96
	Maximum	39.70	27.61	36.82	27.76	41.42	27.47	35.07	34.55	38.25	29.35	2.70	4.99
Second Moment	Middle	27.02	19.56	21.88	20.27	27.90	19.17	24.16	21.34	25.24	20.09	2.72	2.60
	Maximum	41.11	28.09	40.29	30.93	41.53	28.44	35.14	34.55	39.52	30.50	3.20	4.88

Table 26: Median and Maximum Crystallite Thicknesses for Low Integral Dose Proton Irradiation Samples

	Integral Dose	0.96		1.08		0.94		1.15		3.70		1.33		3.70		1.33	
	Sample Number	15A		15B		15C		15D		19A		19B		20A		20B	
	Run Number	1	2	1	2	1	2	1	2	1	2	1	2	1	2	1	2
Crystallite Thickness Distribution	Middle	25.25	17.36	24.31	17.02	26.02	16.65	25.90	17.24	25.06	14.96	22.24	16.60	26.27	16.24	24.71	16.90
	Maximum	40.49	27.20	40.09	27.99	40.00	28.44	41.85	28.44	39.03	26.27	39.60	25.41	41.63	24.94	41.85	27.43
First Moment	Middle	26.62	18.71	26.66	18.86	28.29	19.06	27.95	19.10	26.79	17.55	24.71	17.94	28.29	17.69	26.93	18.53
	Maximum	41.42	27.52	41.53	29.15	44.61	29.41	42.39	28.98	39.99	26.40	39.41	25.69	42.62	26.32	40.09	27.61
Second Moment	Middle	27.57	19.68	28.09	20.02	29.96	20.47	29.47	20.37	27.94	18.81	25.90	18.88	30.01	18.66	28.34	19.63
	Maximum	42.17	27.66	41.85	29.31	47.76	28.94	42.28	29.31	41.63	29.52	39.89	25.69	42.73	25.25	40.90	28.39

	Sample Number	Average		StdDev	
	Run Number	1	2	1	2
Crystallite Thickness Distribution	Middle	24.97	16.62	1.29	0.76
	Maximum	40.57	27.02	1.09	1.34
First Moment	Middle	27.03	18.43	1.18	0.62
	Maximum	41.51	27.64	1.71	1.43
Second Moment	Middle	28.41	19.57	1.38	0.71
	Maximum	42.40	28.01	2.34	1.68

Table 27: Median and Maximum Crystallite Thicknesses for High Integral Dose Proton Irradiation Samples

	Integral Dose	0.68		8.30		8.70					
	Sample Number	18C		18D		21B		Average		StdDev	
	Run Number	1	2	1	2	1	2	1	2	1	2
Crystallite Thickness Distribution	Middle	24.83	12.29	23.70	11.99	28.14	11.85	25.56	12.04	1.88	0.18
	Maximum	49.81	19.44	39.03	18.53	59.69	19.26	49.51	19.08	8.44	0.39
First Moment	Middle	28.54	13.02	26.02	12.66	31.77	12.61	28.78	12.76	2.35	0.18
	Maximum	53.41	19.28	39.89	18.28	60.81	20.92	51.37	19.49	8.66	1.09
Second Moment	Middle	30.75	13.53	27.57	13.09	34.11	13.18	30.81	13.27	2.67	0.19
	Maximum	53.41	18.92	40.39	19.56	61.74	20.30	51.85	19.59	8.79	0.56

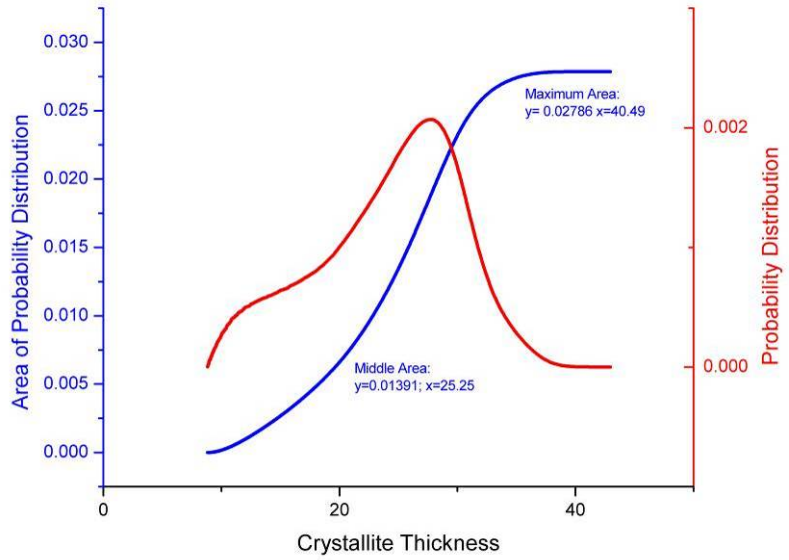

Figure 96: 0.963 kGy Proton Irradiated (Sample 66) Crystallite Thickness Distribution for Run 1 (Area Calculations)

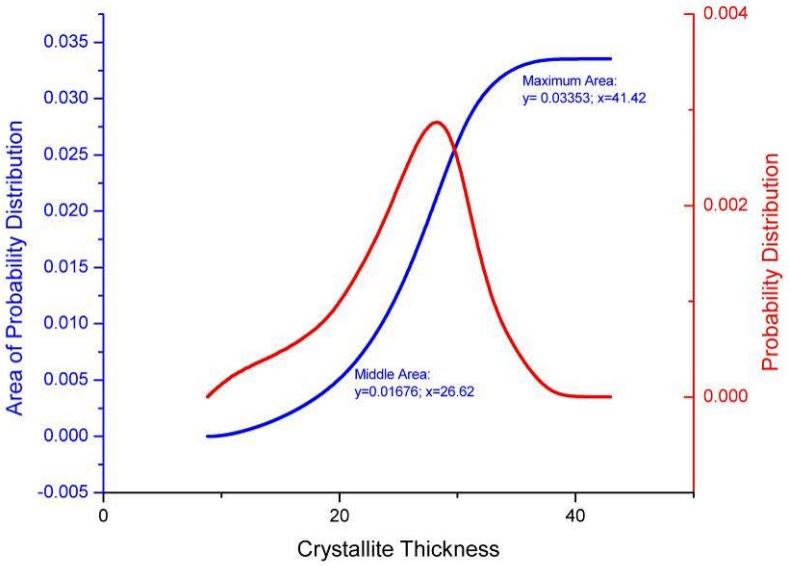

Figure 97: First Moment of 0.963 kGy Proton Irradiated (Sample 66) Crystallite Thickness Distribution for Run 1 (Area Calculations)

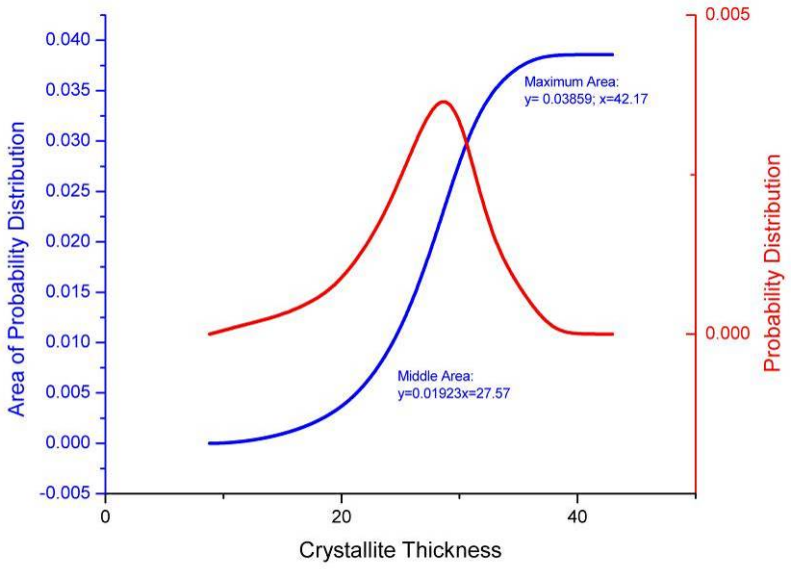

Figure 98 Second Moment of 0.963 kGy Proton Irradiated (Sample 66) Crystallite Thickness Distribution for Run 1 (Area Calculations)

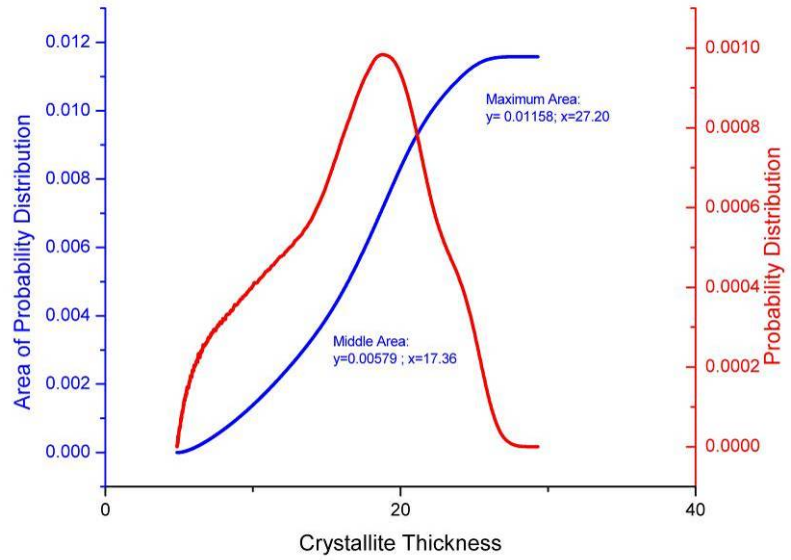

Figure 99: 0.963 kGy Proton Irradiated (Sample 66) Crystallite Thickness Distribution for Run 2 (Area Calculations)

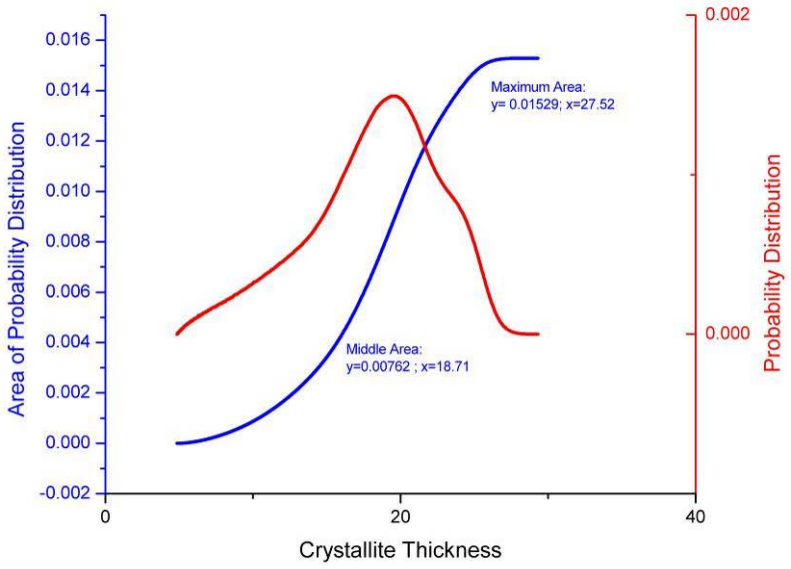

Figure 100: First Moment of 0.963 kGy Proton Irradiated (Sample 66) Crystallite Thickness Distribution for Run 2 (Area Calculations)

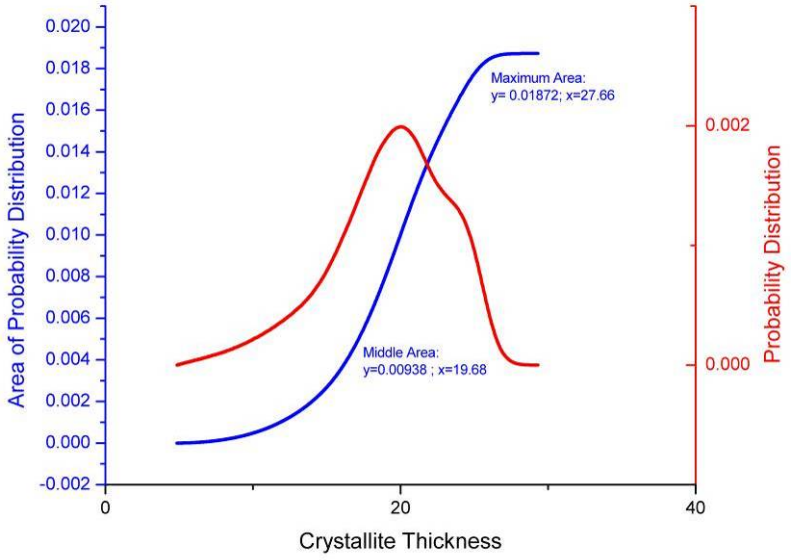

Figure 101: Second Moment of 0.963 kGy Proton Irradiated (Sample 66) Crystallite Thickness Distribution for Run 2 (Area Calculations)

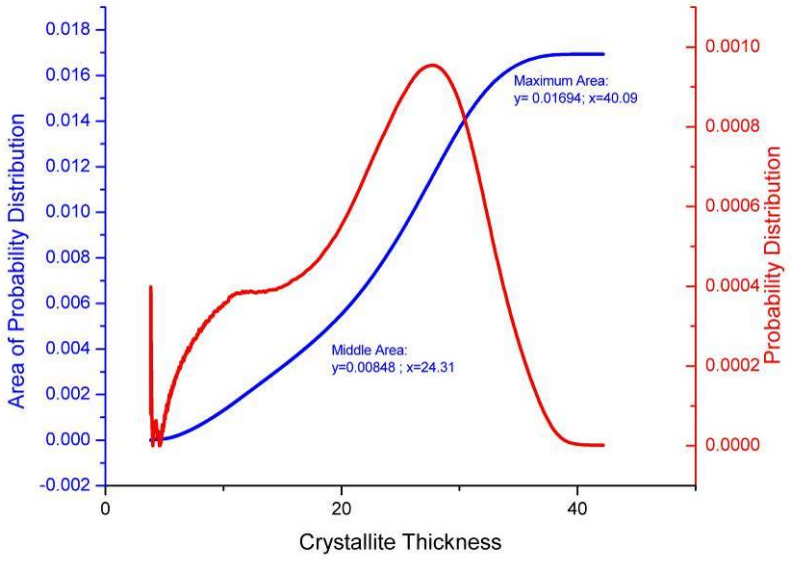

Figure 102: 1.0773 kGy Proton Irradiated (Sample 63) Crystallite Thickness Distribution for Run 1 (Area Calculations)

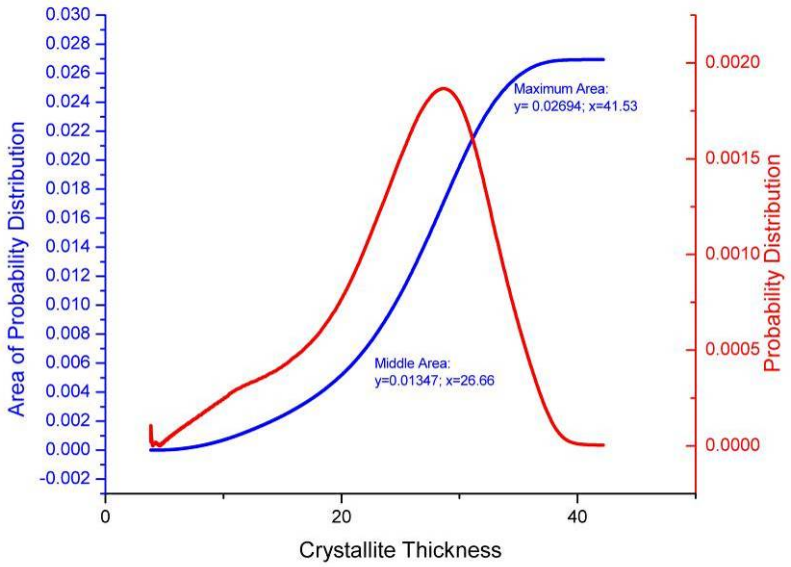

Figure 103: First Moment of 1.0773 kGy Proton Irradiated (Sample 63) Crystallite Thickness Distribution for Run 1 (Area Calculations)

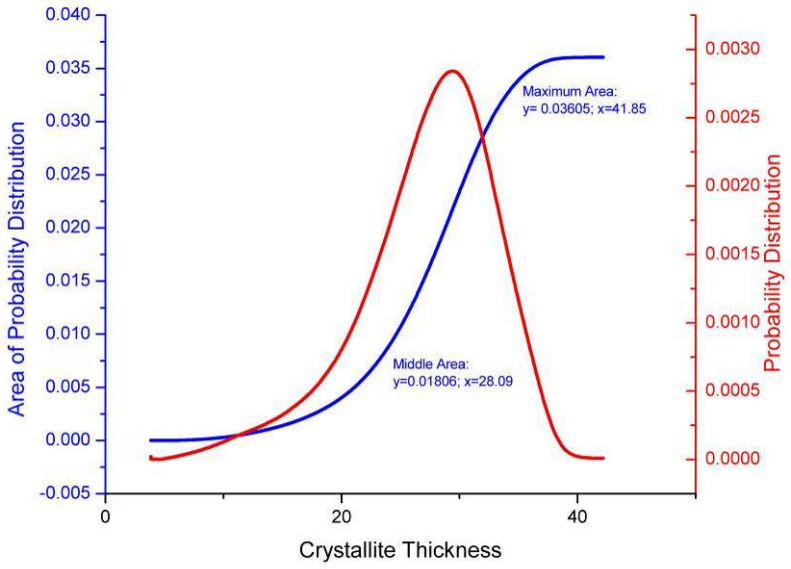

Figure 104: Second Moment of 1.0773 kGy Proton Irradiated (Sample 63) Crystallite Thickness Distribution for Run 1 (Area Calculations)

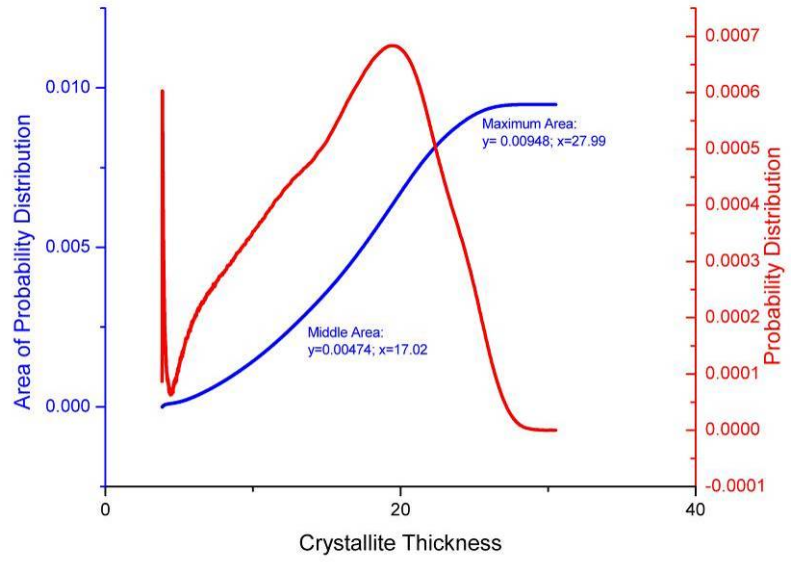

Figure 105: 1.0773 kGy Proton Irradiated (Sample 63) Crystallite Thickness Distribution for Run 2 (Area Calculations)

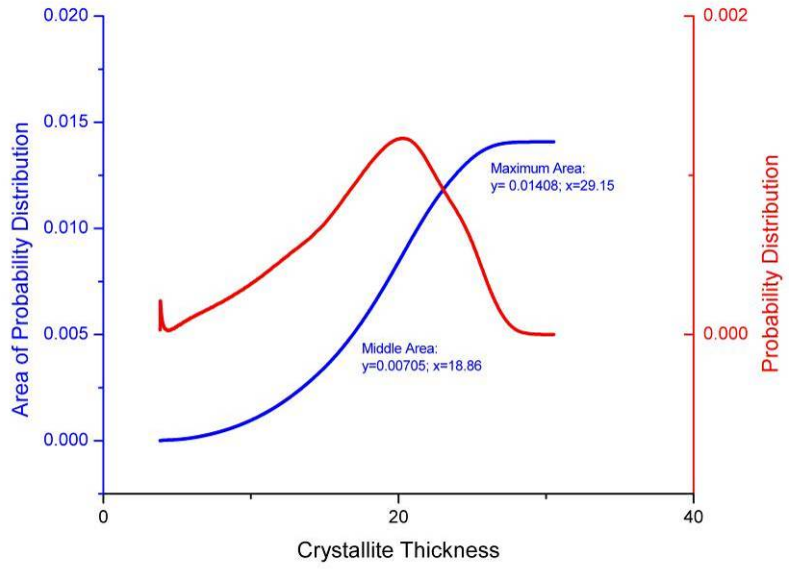

Figure 106: First Moment of 1.0773 kGy Proton Irradiated (Sample 63) Crystallite Thickness Distribution for Run 2 (Area Calculations)

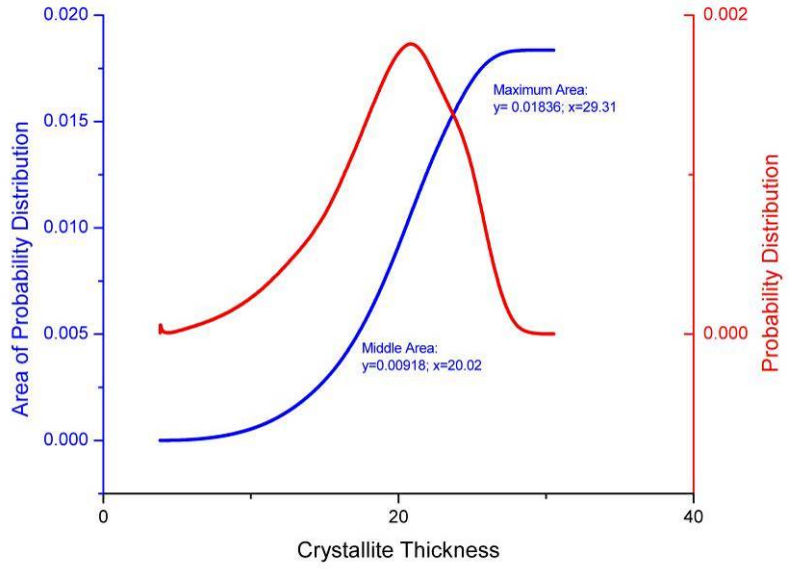

Figure 107: Second Moment of 1.0773 kGy Proton Irradiated (Sample 63) Crystallite Thickness Distribution for Run 2 (Area Calculations)

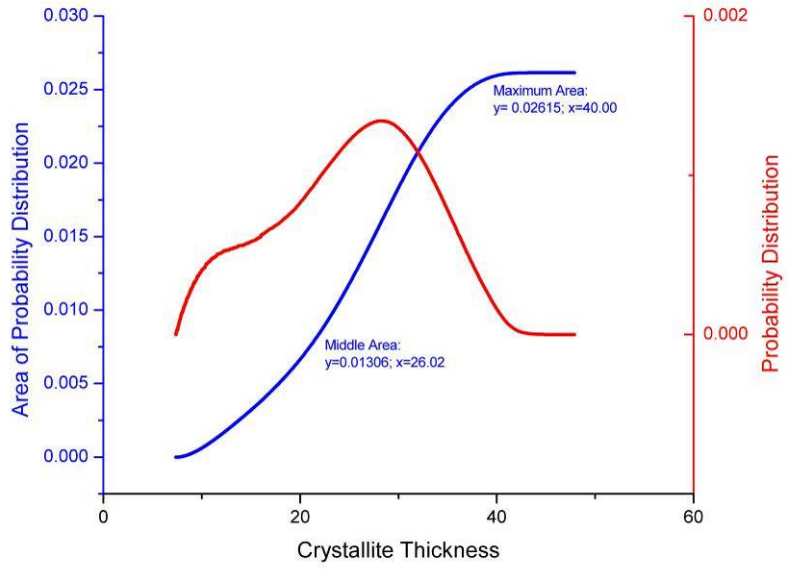

Figure 108: 0.9402 kGy Proton Irradiated (Sample 74) Crystallite Thickness Distribution for Run 1 (Area Calculations)

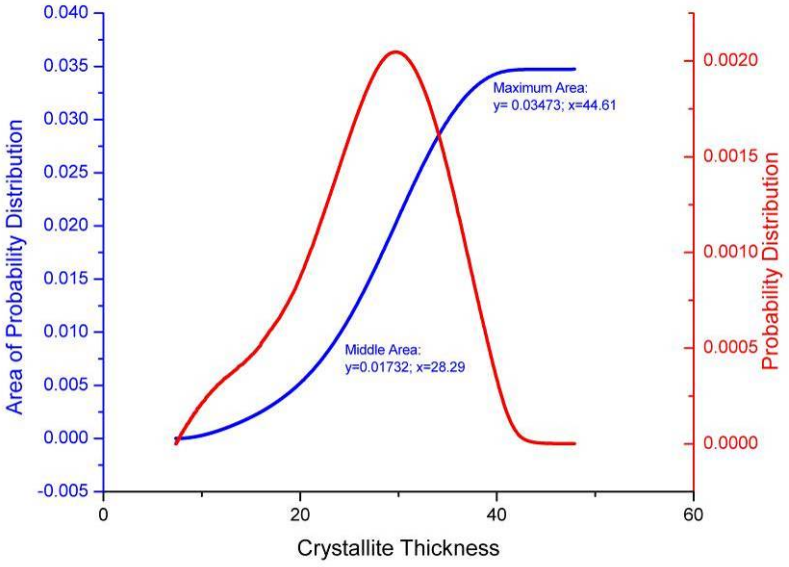

Figure 109: First Moment of 0.9402 kGy Proton Irradiated (Sample 74) Crystallite Thickness Distribution for Run 1 (Area Calculations)

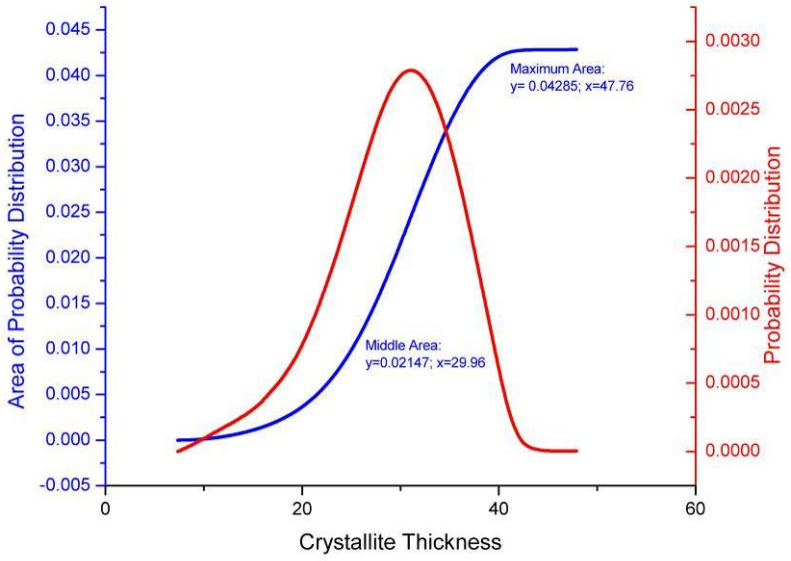

Figure 110: Second Moment of 0.9402 kGy Proton Irradiated (Sample 74) Crystallite Thickness Distribution for Run 1 (Area Calculations)

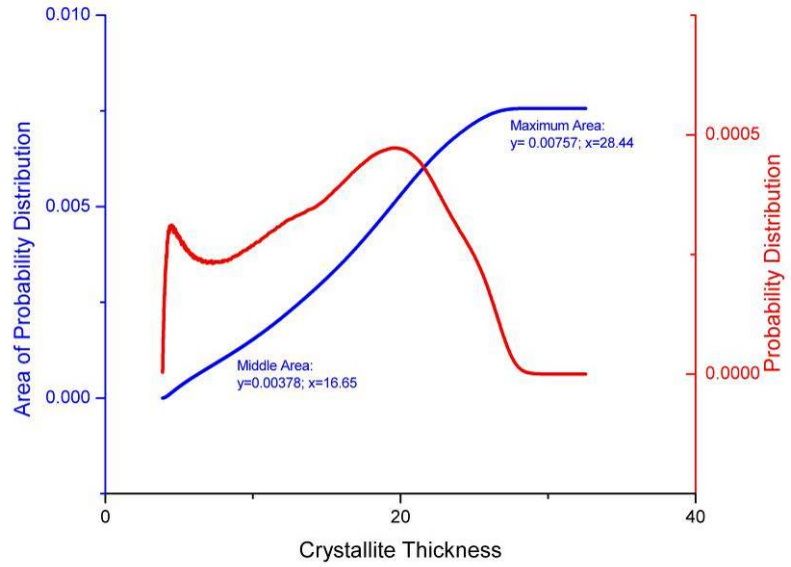

Figure 111: 0.9402 kGy Proton Irradiated (Sample 74) Crystallite Thickness Distribution for Run 2 (Area Calculations)

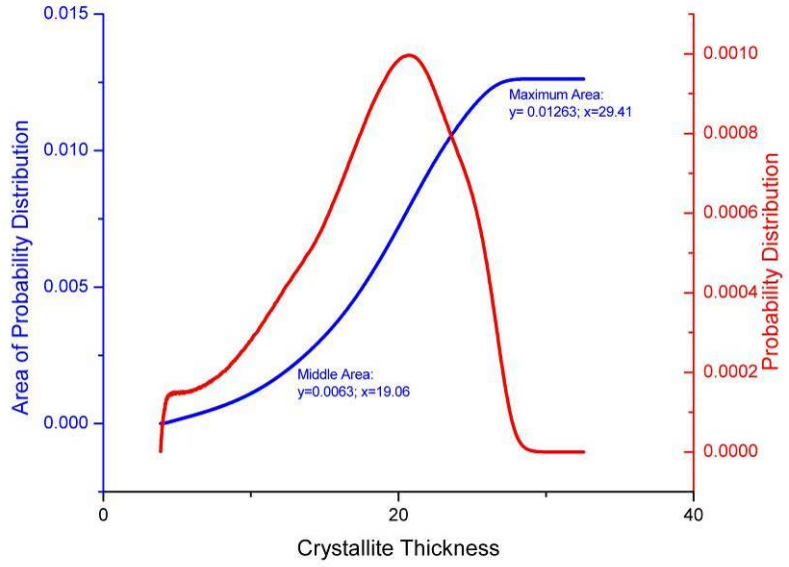

Figure 112: First Moment of 0.9402 kGy Proton Irradiated (Sample 74) Crystallite Thickness Distribution for Run 2 (Area Calculations)

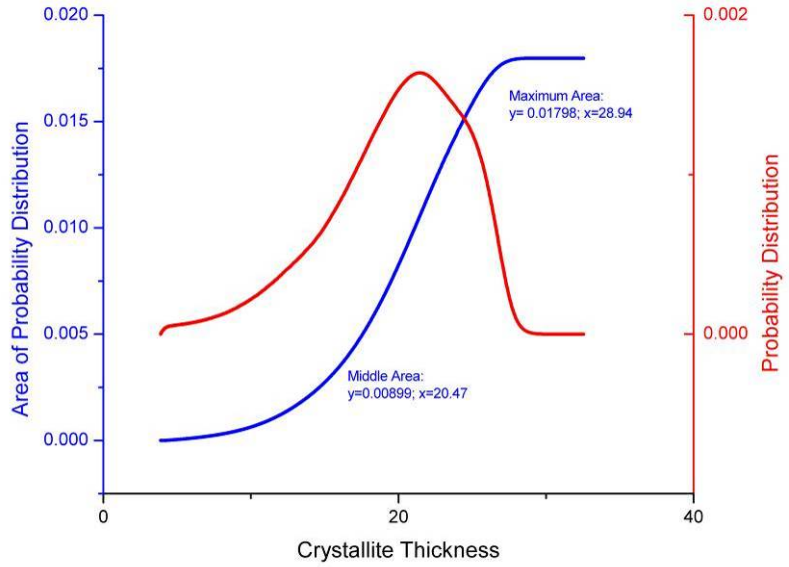

Figure 113: Second Moment of 0.9402 kGy Proton Irradiated (Sample 74) Crystallite Thickness Distribution for Run 2 (Area Calculations)

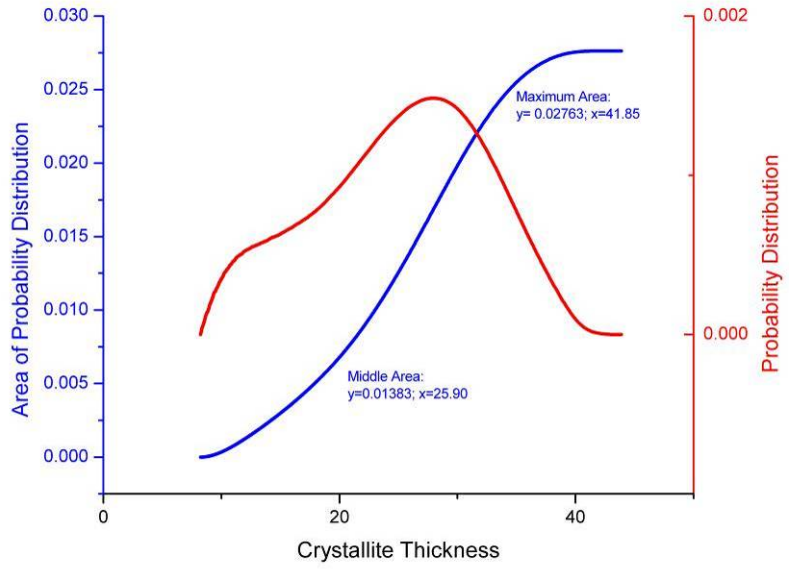

Figure 114: 1.1506 kGy Proton Irradiated (Sample 70) Crystallite Thickness Distribution for Run 1 (Area Calculations)

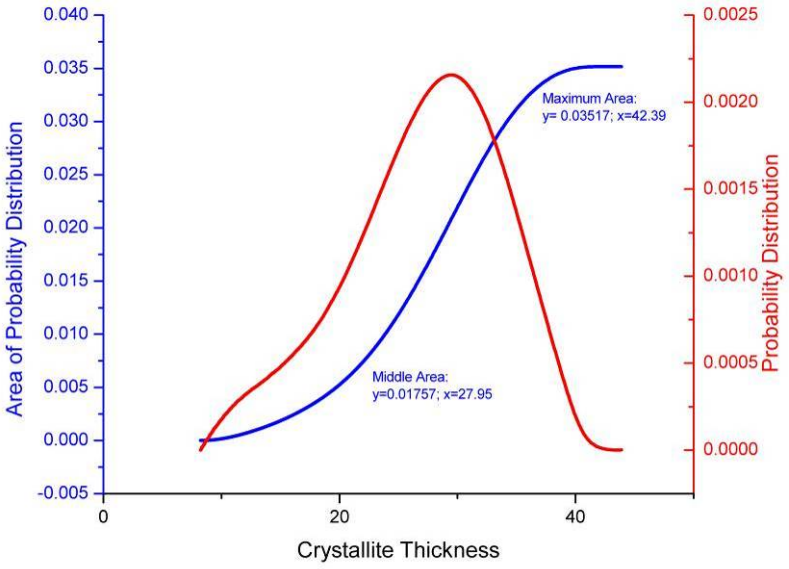

Figure 115: First Moment of 1.1506 kGy Proton Irradiated (Sample 70) Crystallite Thickness Distribution for Run 1 (Area Calculations)

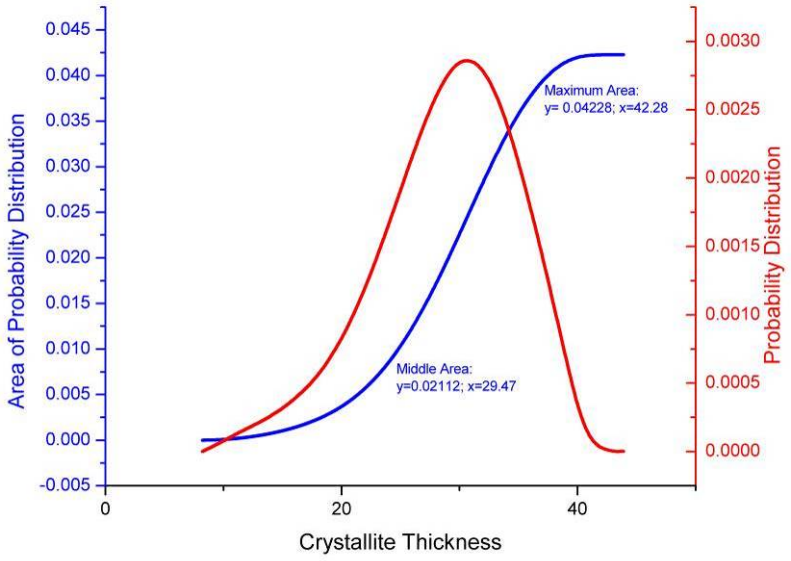

Figure 116: Second Moment of 1.1506 kGy Proton Irradiated (Sample 70) Crystallite Thickness Distribution for Run 1 (Area Calculations)

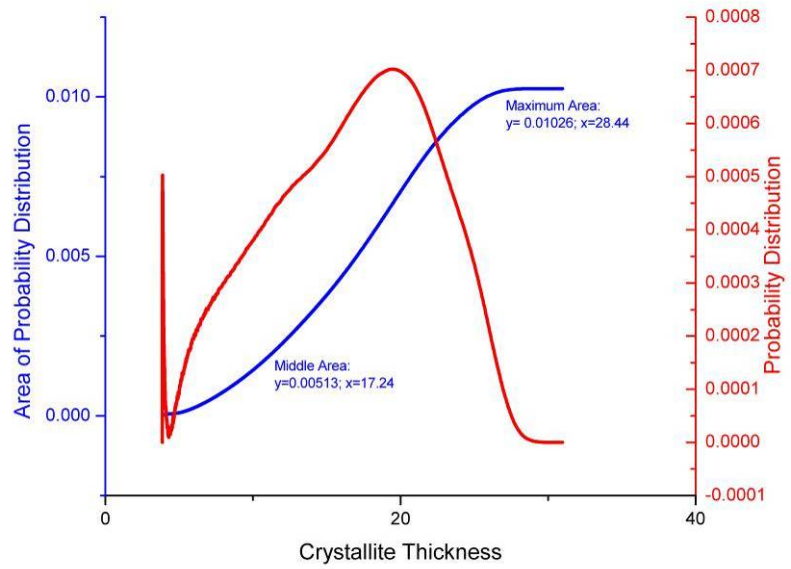

Figure 117: 1.1506 kGy Proton Irradiated (Sample 70) Crystallite Thickness Distribution for Run 2 (Area Calculations)

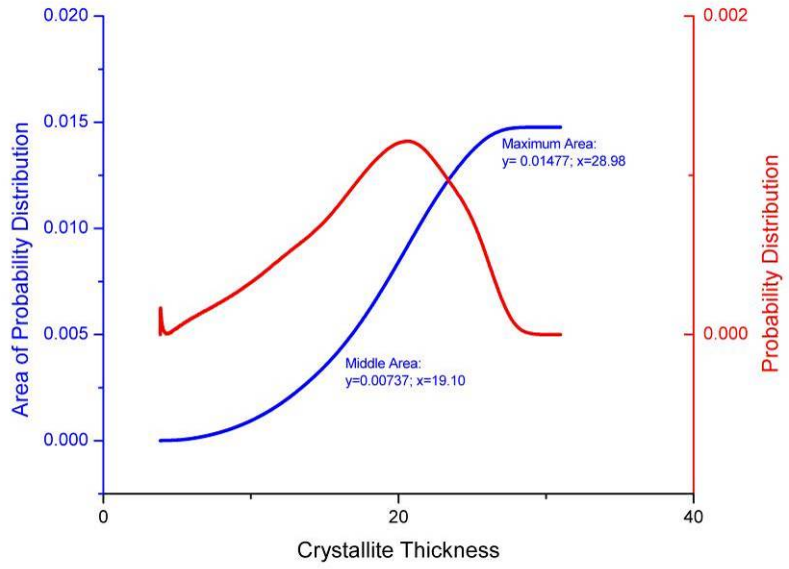

Figure 118: First Moment of 1.1506 kGy Proton Irradiated (Sample 70) Crystallite Thickness Distribution for Run 2 (Area Calculations)

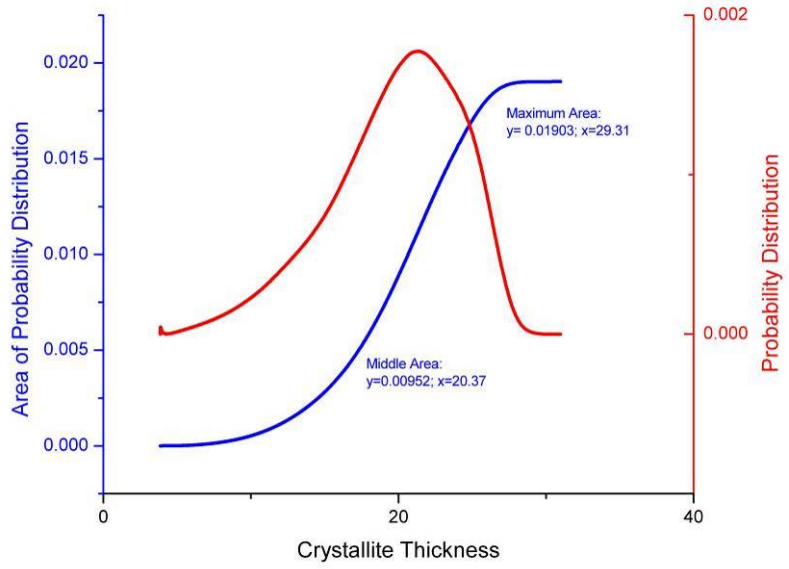

Figure 119: Second Moment of 1.1506 kGy Proton Irradiated (Sample 70) Crystallite Thickness Distribution for Run 2 (Area Calculations)

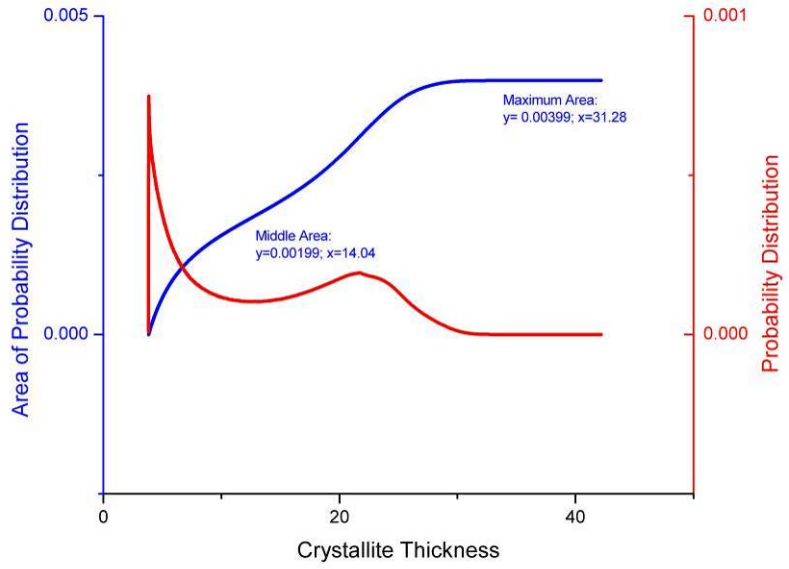

Figure 120: Control (0 kGy) Proton Irradiated (Sample 30) Crystallite Thickness Distribution for Run 1 (Area Calculations)

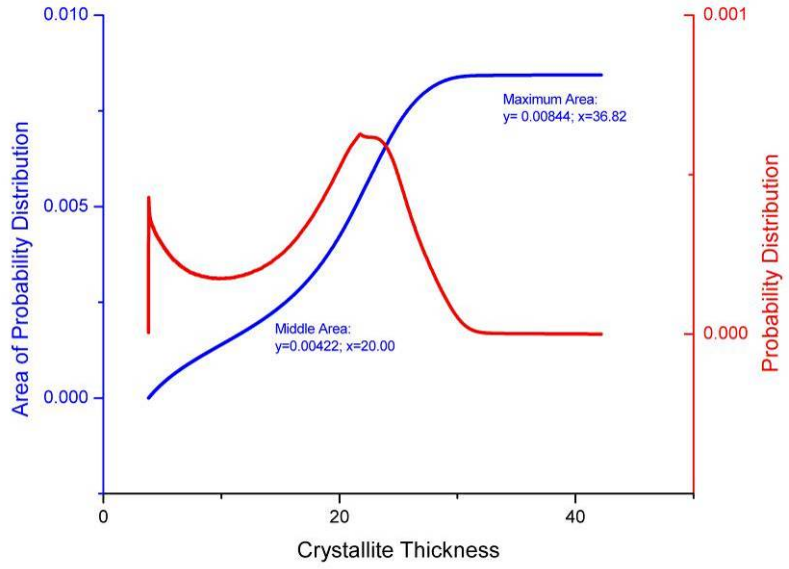

Figure 121: First Moment of Control (0 kGy) Proton Irradiated (Sample 30) Crystallite Thickness Distribution for Run 1 (Area Calculations)

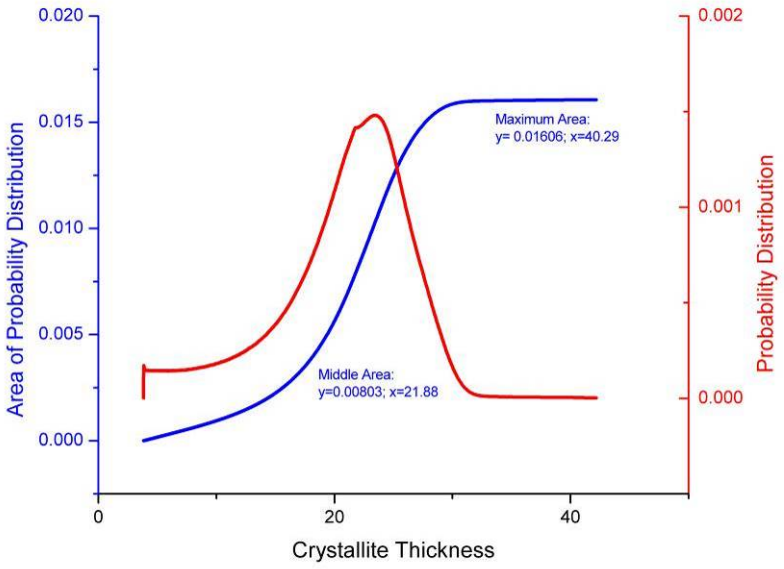

Figure 122: Second Moment of Control (0 kGy) Proton Irradiated (Sample 30) Crystallite Thickness Distribution for Run 1 (Area Calculations)

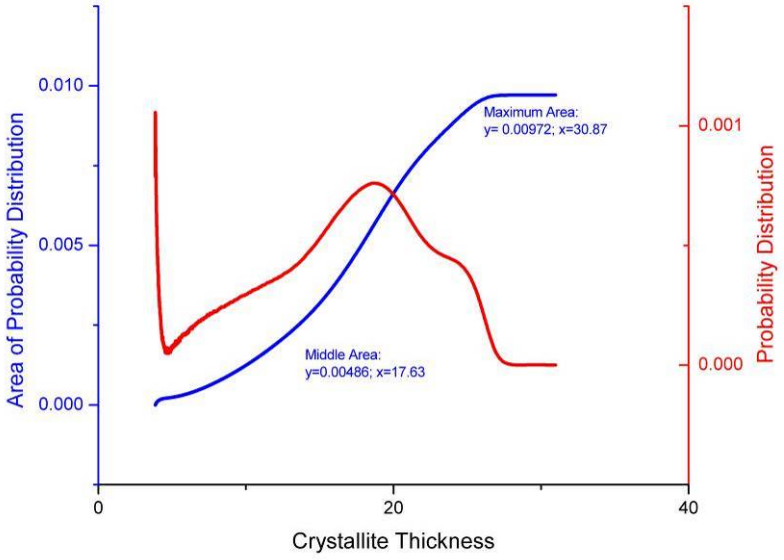

Figure 123: Control (0 kGy) Proton Irradiated (Sample 30) Crystallite Thickness Distribution for Run 2 (Area Calculations)

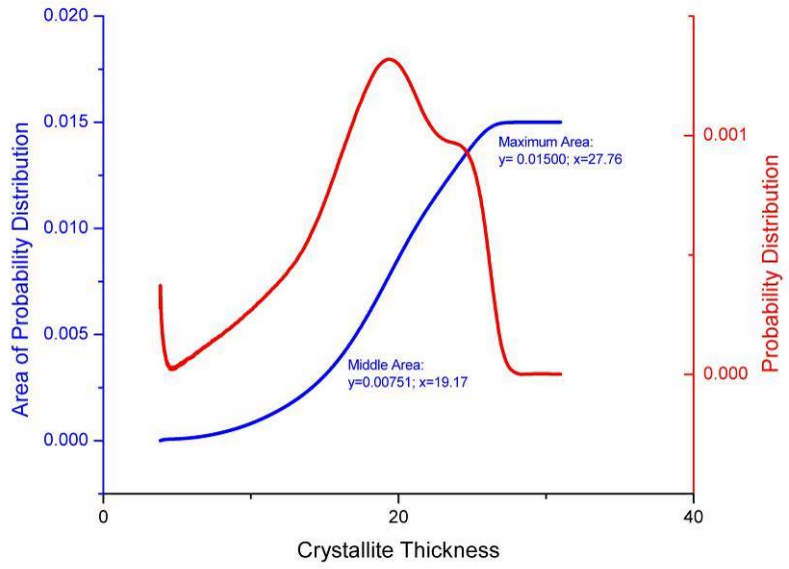

Figure 124: First Moment of Control (0 kGy) Proton Irradiated (Sample 30) Crystallite Thickness Distribution for Run 2 (Area Calculations)

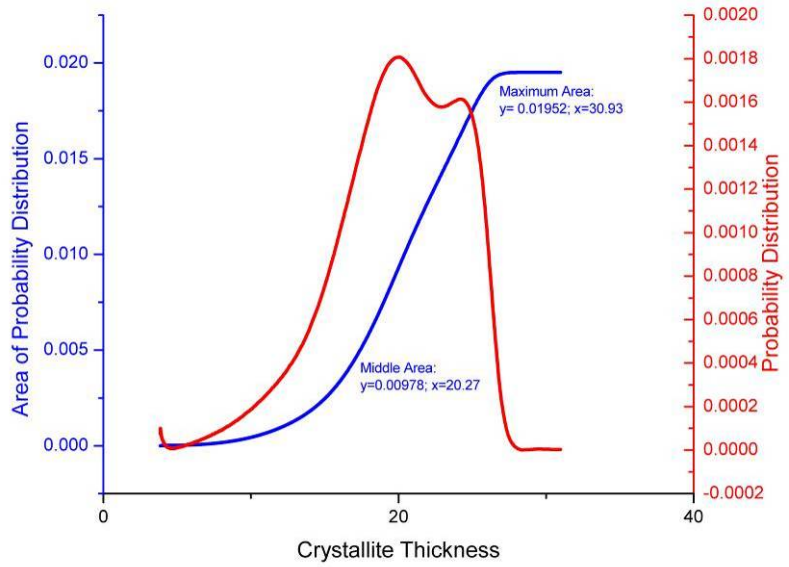

Figure 125: Second Moment of Control (0 kGy) Proton Irradiated (Sample 30) Crystallite Thickness Distribution for Run 2 (Area Calculations)

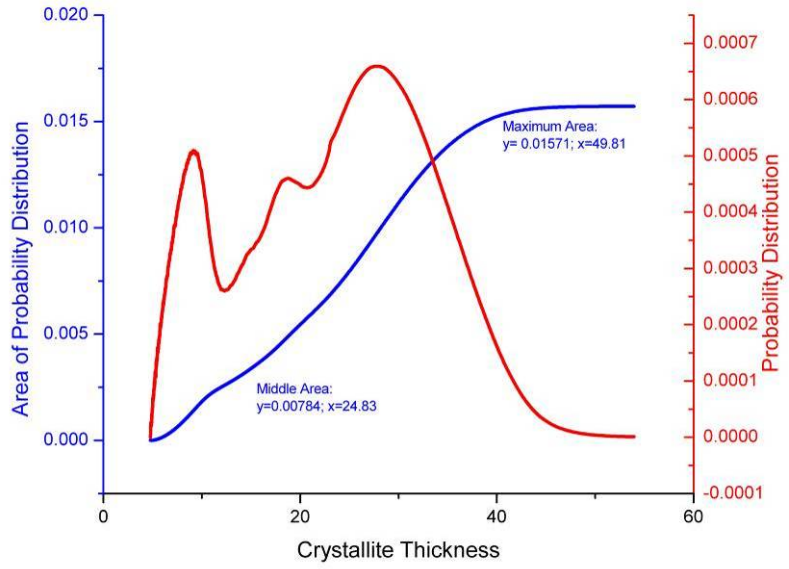

Figure 126: 6.8 kGy Proton Irradiated (Sample 87) Crystallite Thickness Distribution for Run 1 (Area Calculations)

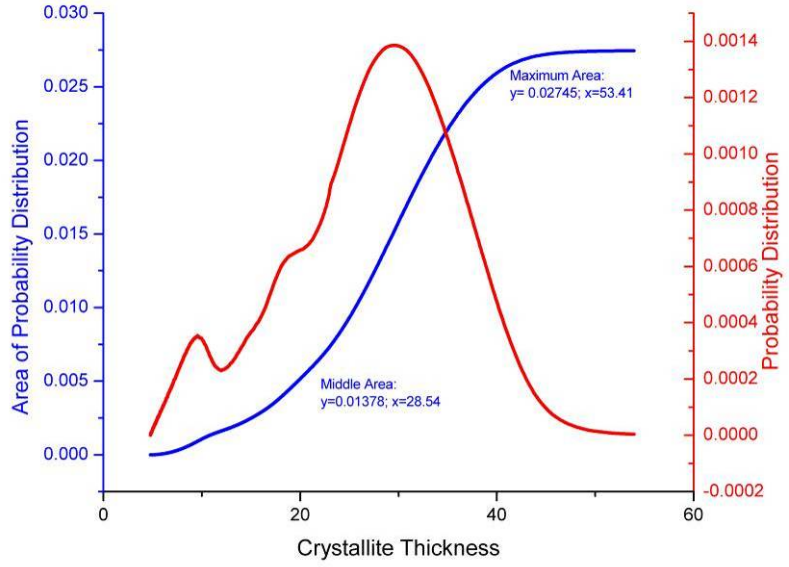

Figure 127: First Moment of 6.8 kGy Proton Irradiated (Sample 87) Crystallite Thickness Distribution for Run 1 (Area Calculations)

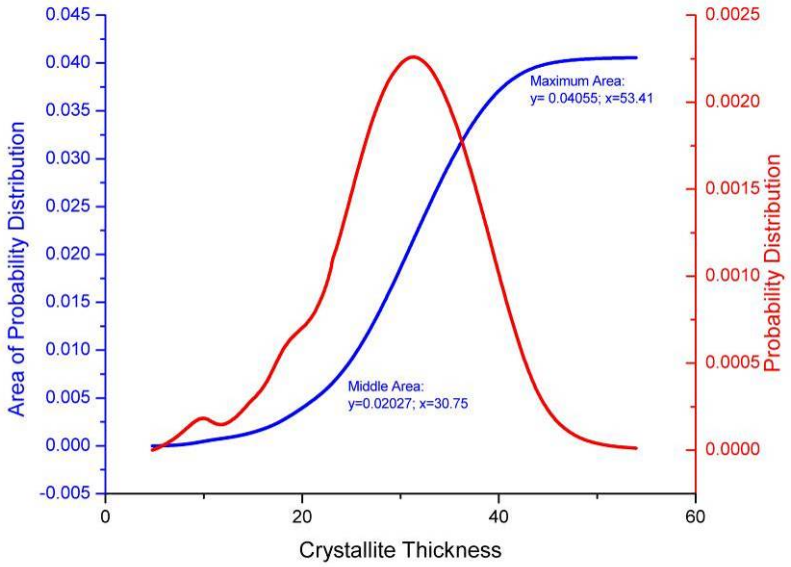

Figure 128: Second Moment of 6.8 kGy Proton Irradiated (Sample 87) Crystallite Thickness Distribution for Run 1 (Area Calculations)

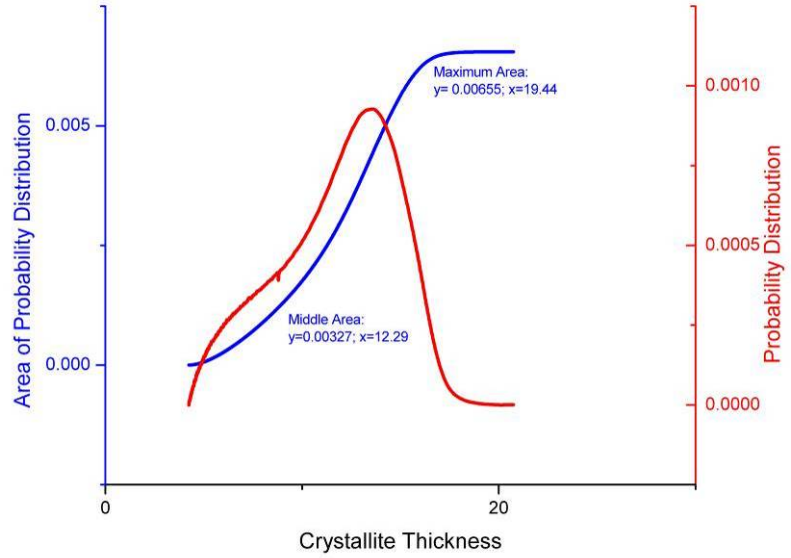

Figure 129: 6.8 kGy Proton Irradiated (Sample 87) Crystallite Thickness Distribution for Run 2 (Area Calculations)

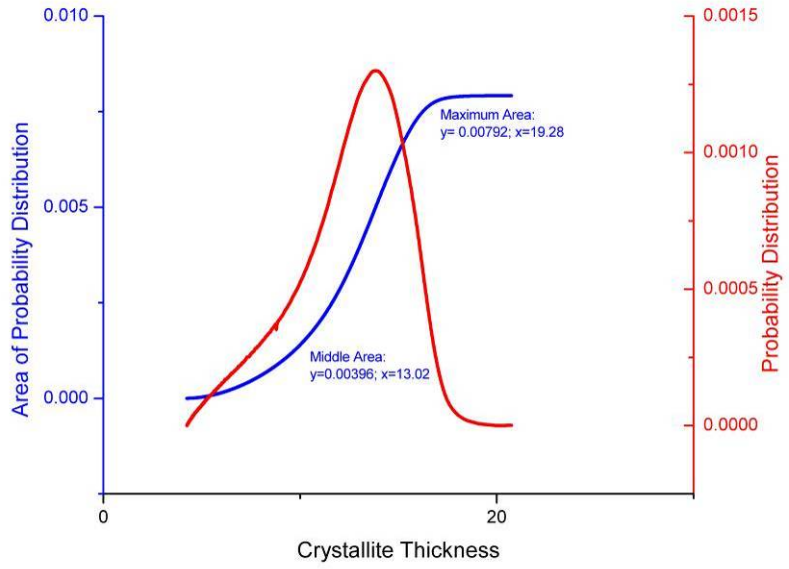

Figure 130: First Moment of 6.8 kGy Proton Irradiated (Sample 87) Crystallite Thickness Distribution for Run 2 (Area Calculations)

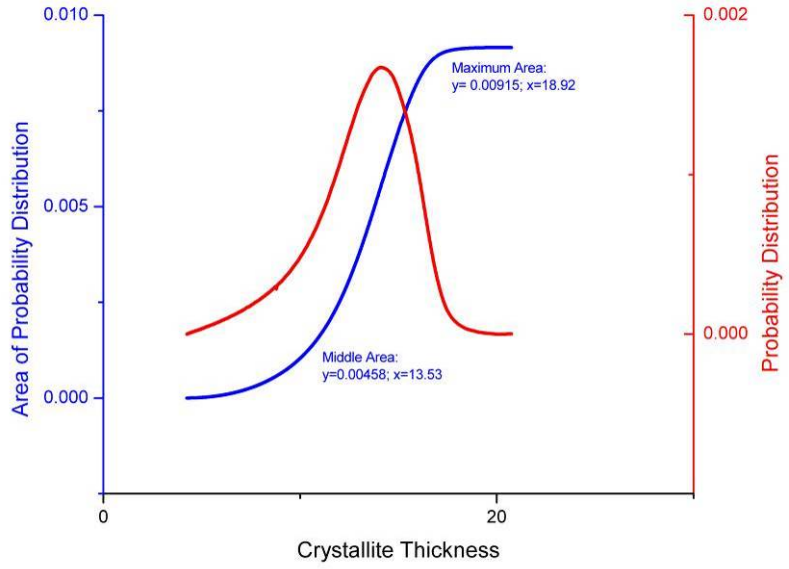

Figure 131: Second Moment of 6.8 kGy Proton Irradiated (Sample 87) Crystallite Thickness Distribution for Run 2 (Area Calculations)

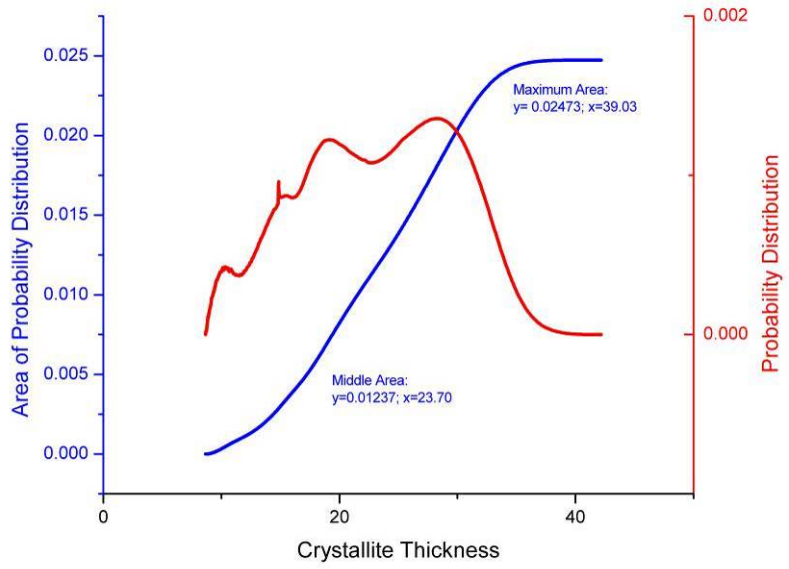

Figure 132: 8.3 kGy Proton Irradiated (Sample 80) Crystallite Thickness Distribution for Run 1 (Area Calculations)

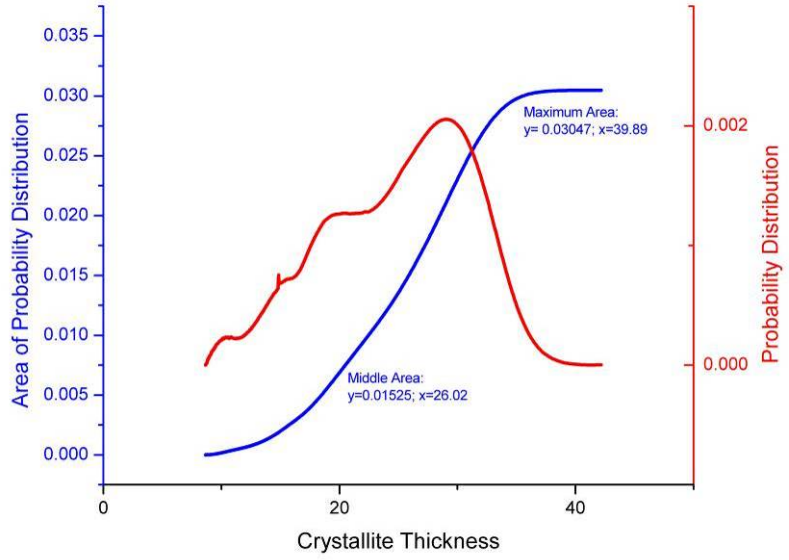

Figure 133: First Moment of 8.3 kGy Proton Irradiated (Sample 80) Crystallite Thickness Distribution for Run 1 (Area Calculations)

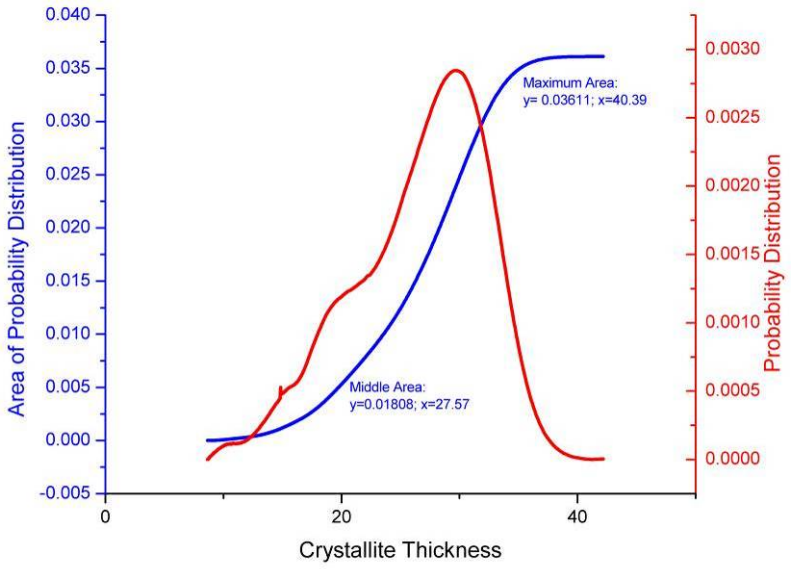

Figure 134: Second Moment of 8.3 kGy Proton Irradiated (Sample 80) Crystallite Thickness Distribution for Run 1 (Area Calculations)

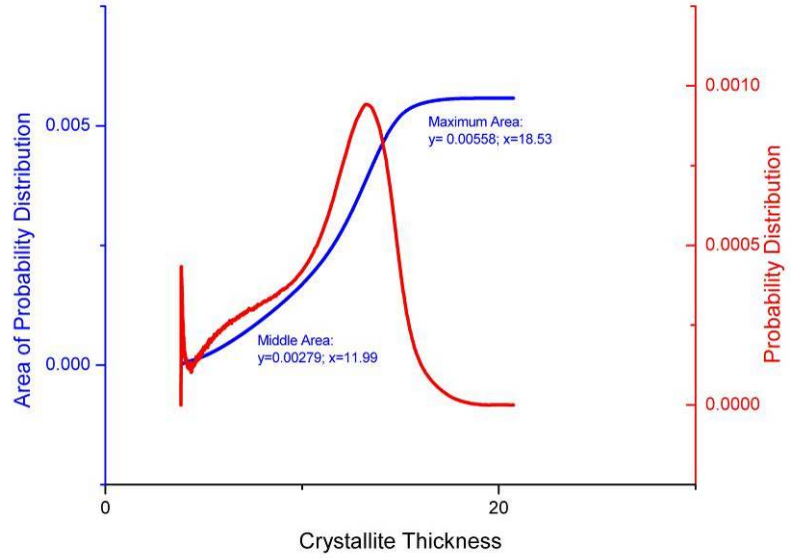

Figure 135: 8.3 kGy Proton Irradiated (Sample 80) Crystallite Thickness Distribution for Run 2 (Area Calculations)

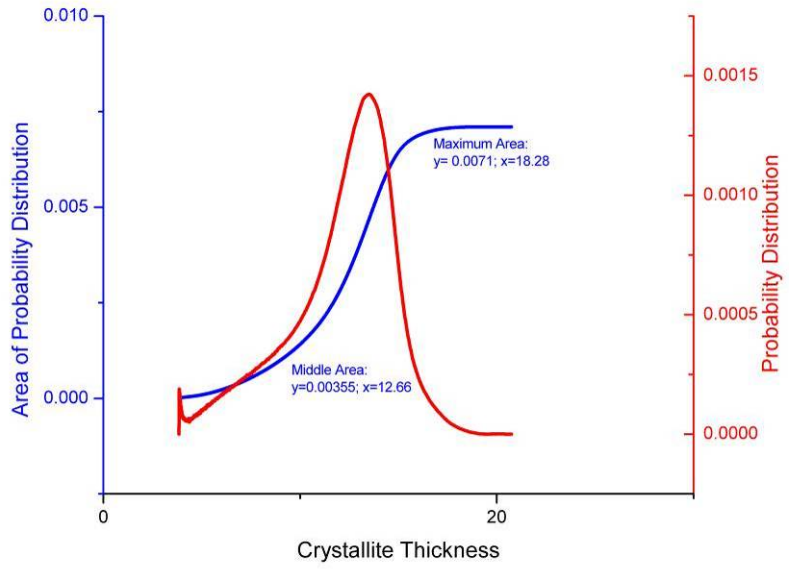

Figure 136: First Moment of 8.3 kGy Proton Irradiated (Sample 80) Crystallite Thickness Distribution for Run 2 (Area Calculations)

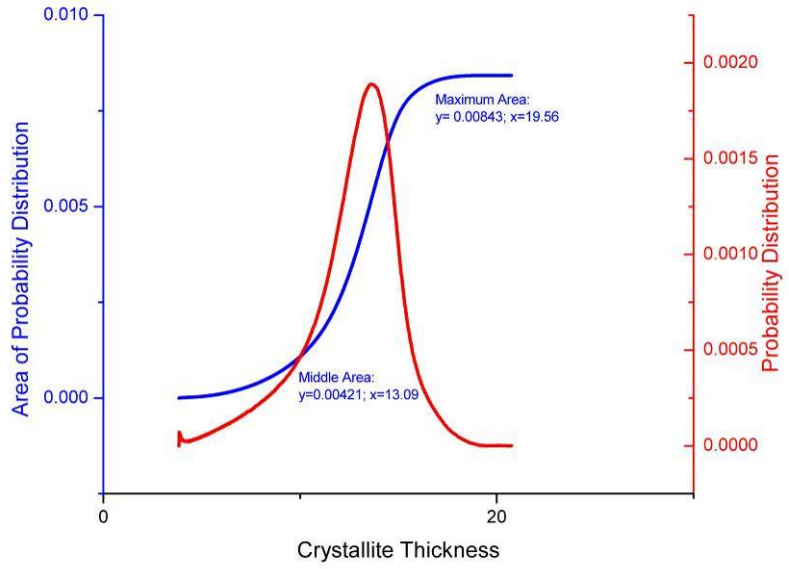

Figure 137: Second Moment of 8.3 kGy Proton Irradiated (Sample 80) Crystallite Thickness Distribution for Run 2 (Area Calculations)

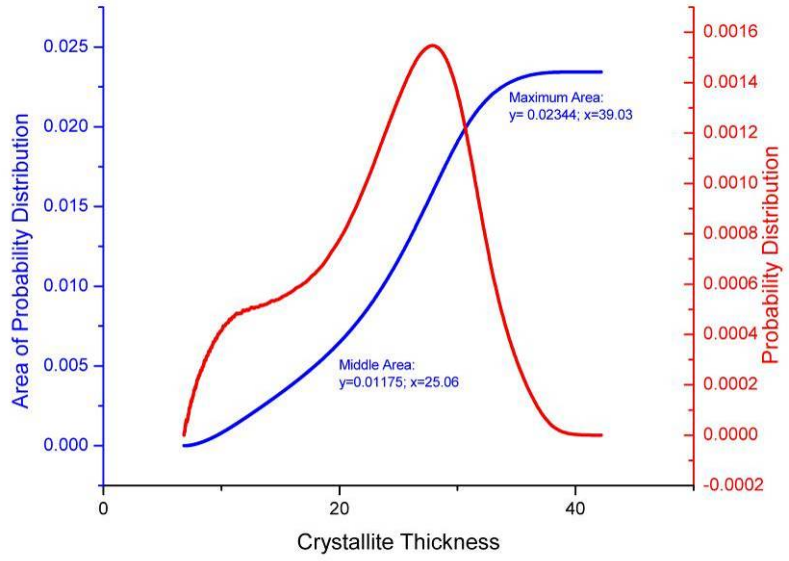

Figure 138: 3.7 kGy Proton Irradiated (Sample 58) Crystallite Thickness Distribution for Run 1 (Area Calculations)

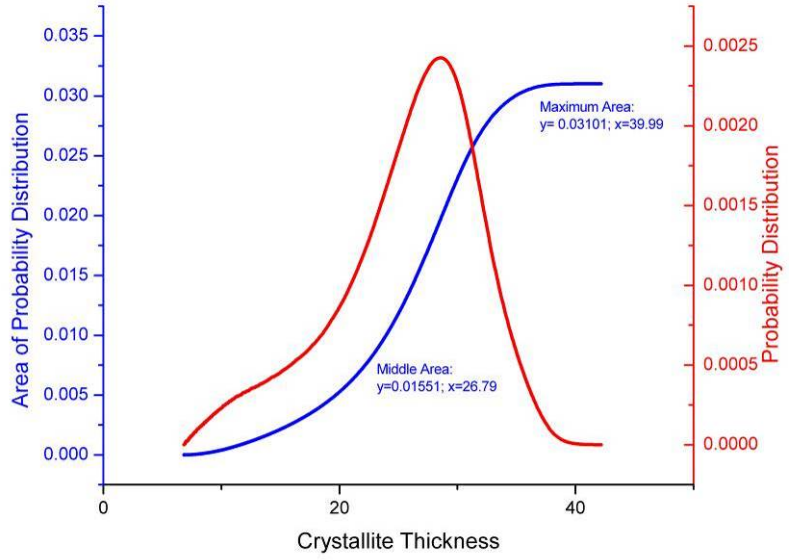

Figure 139: First Moment of 3.7 kGy Proton Irradiated (Sample 58) Crystallite Thickness Distribution for Run 1 (Area Calculations)

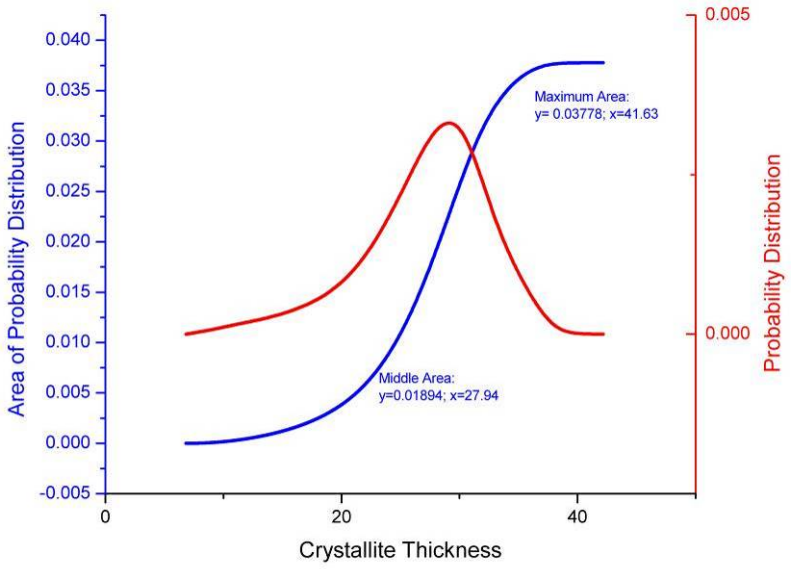

Figure 140: Second Moment of 3.7 kGy Proton Irradiated (Sample 58) Crystallite Thickness Distribution for Run 1 (Area Calculations)

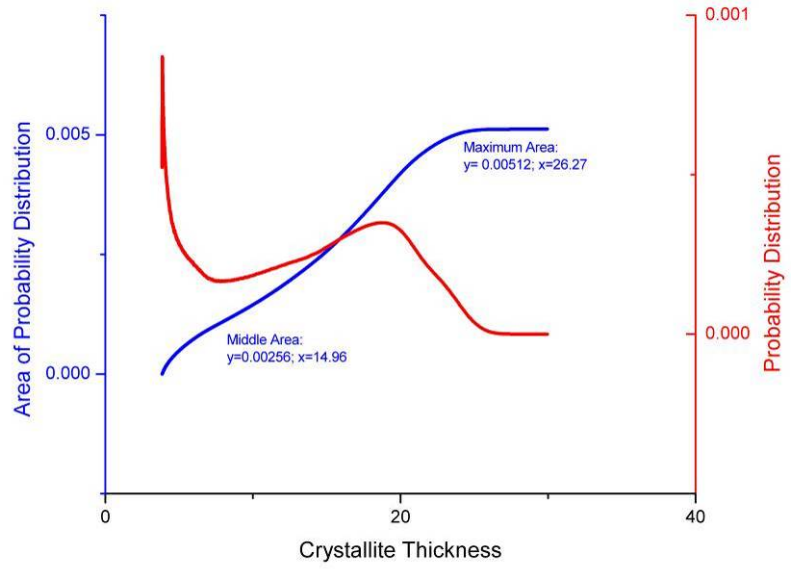

Figure 141: 3.7 kGy Proton Irradiated (Sample 58) Crystallite Thickness Distribution for Run 2 (Area Calculations)

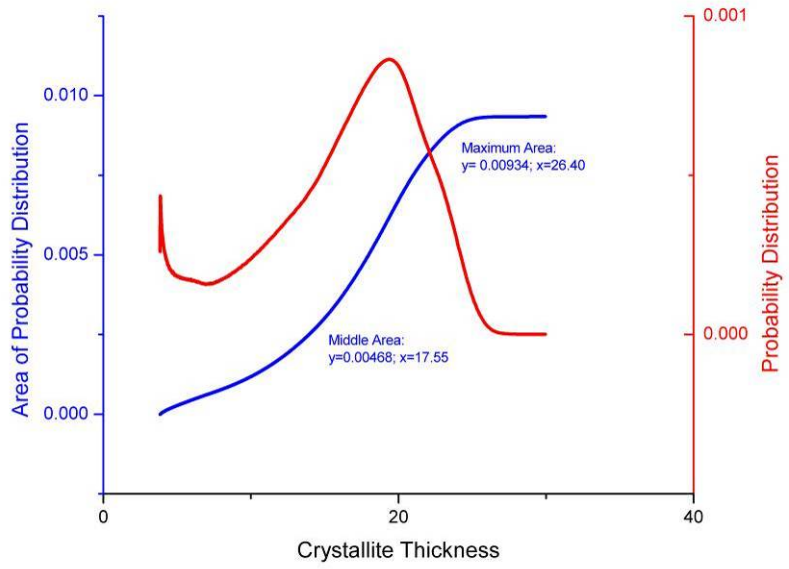

Figure 142: First Moment of 3.7 kGy Proton Irradiated (Sample 58) Crystallite Thickness Distribution for Run 2 (Area Calculations)

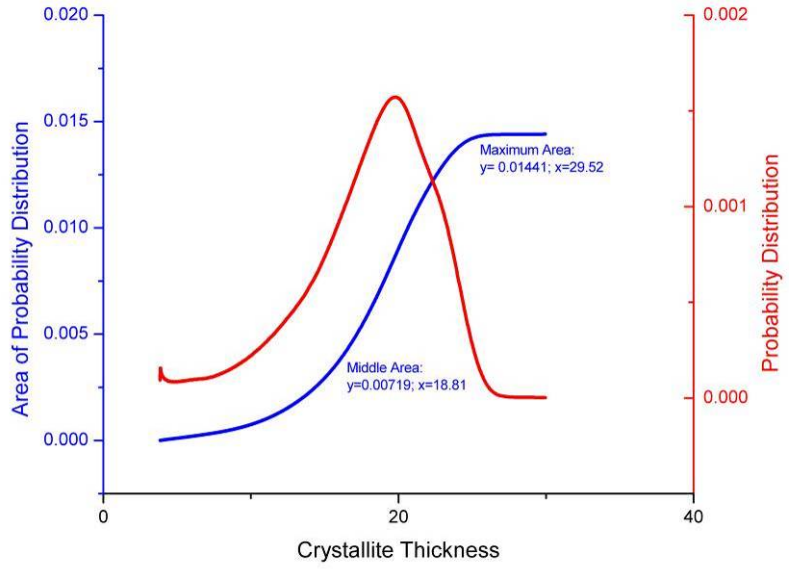

Figure 143: Second Moment of 3.7 kGy Proton Irradiated (Sample 58) Crystallite Thickness Distribution for Run 2 (Area Calculations)

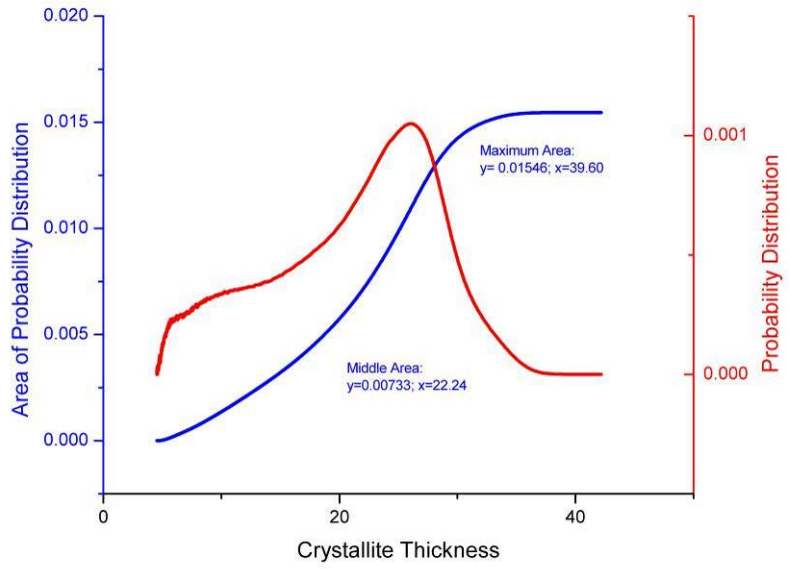

Figure 144: 1.3289 kGy Proton Irradiated (Sample 57) Crystallite Thickness Distribution for Run 1 (Area Calculations)

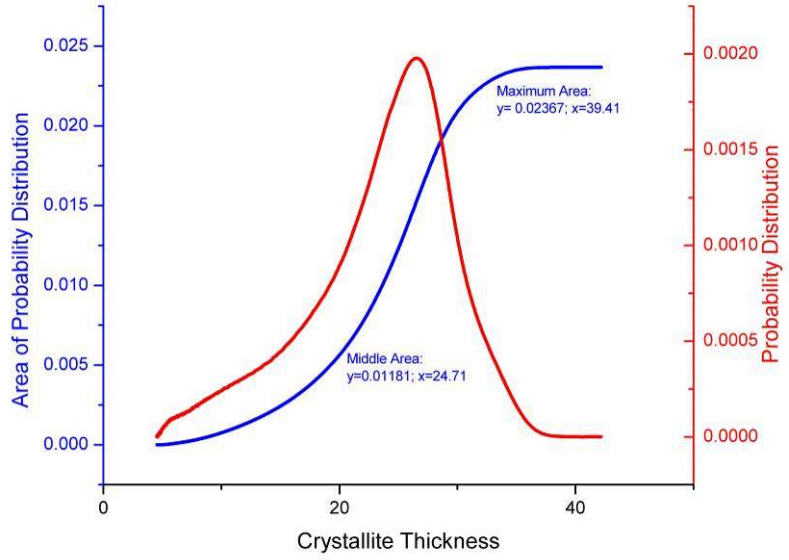

Figure 145: First Moment of 1.3289 kGy Proton Irradiated (Sample 57) Crystallite Thickness Distribution for Run 1 (Area Calculations)

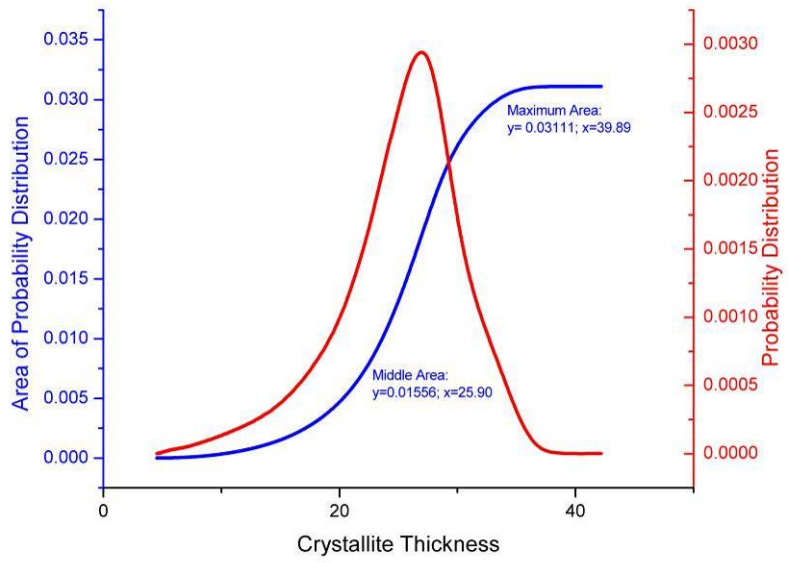

Figure 146: Second Moment of 1.3289 kGy Proton Irradiated (Sample 57) Crystallite Thickness Distribution for Run 1 (Area Calculations)

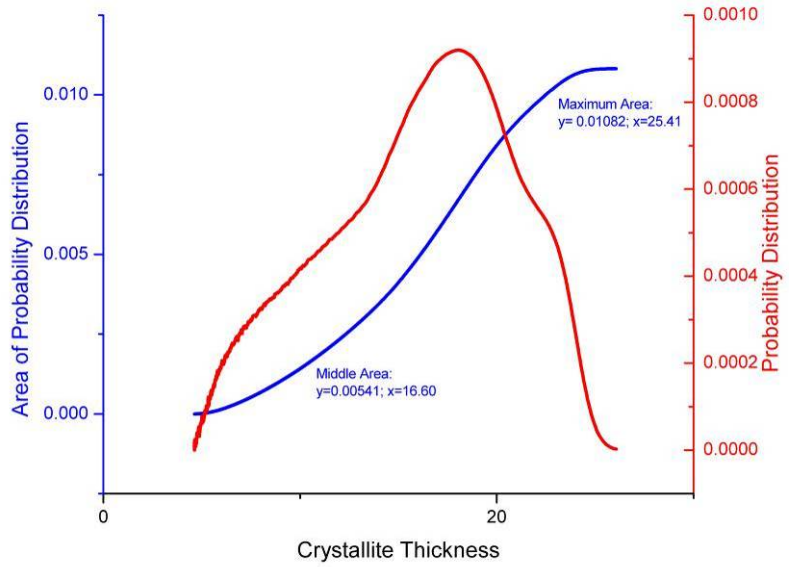

Figure 147: 1.3289 kGy Proton Irradiated (Sample 57) Crystallite Thickness Distribution for Run 2 (Area Calculations)

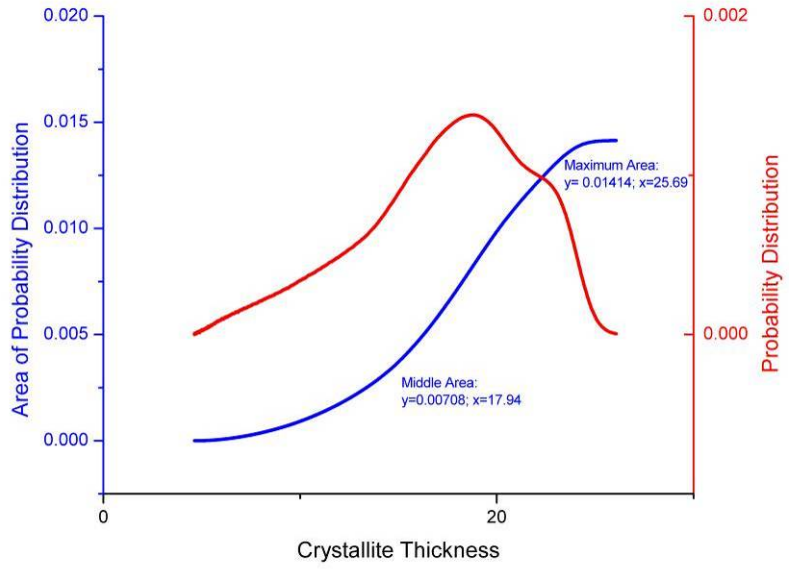

Figure 148: First Moment of 1.3289 kGy Proton Irradiated (Sample 57) Crystallite Thickness Distribution for Run 2 (Area Calculations)

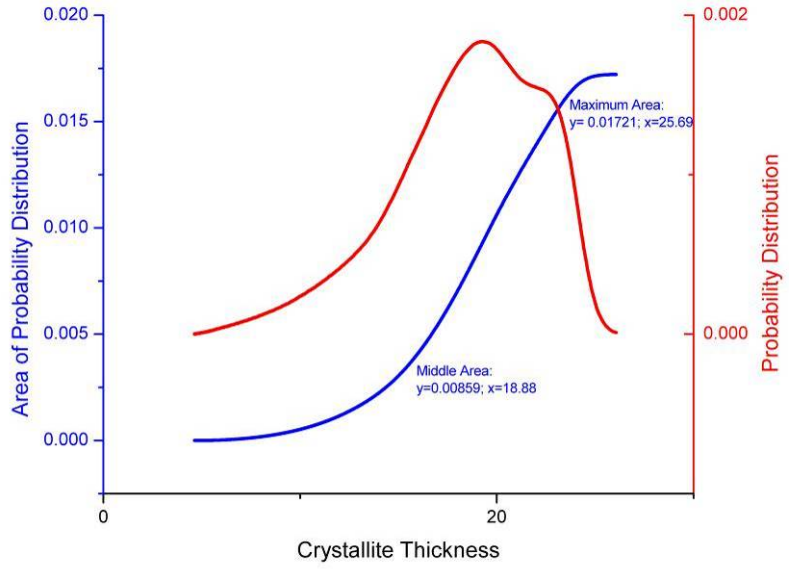

Figure 149: Second Moment of 1.3289 kGy Proton Irradiated (Sample 57) Crystallite Thickness Distribution for Run 2 (Area Calculations)

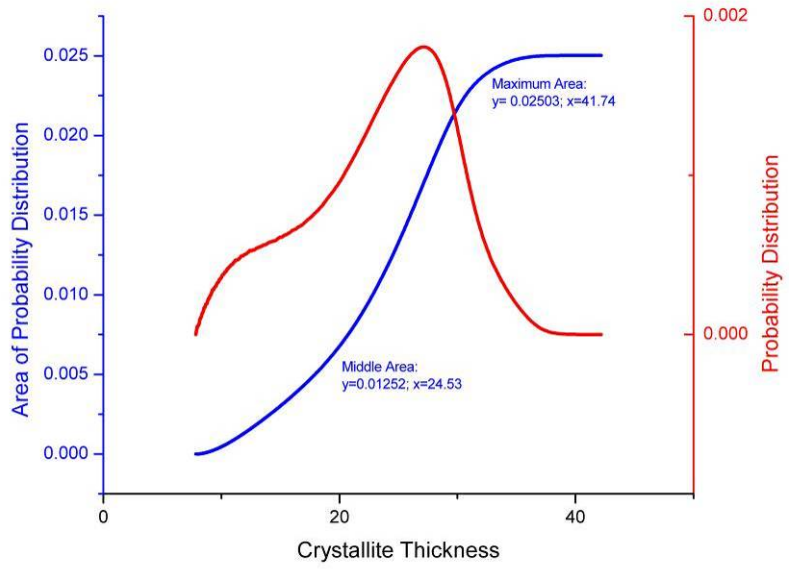

Figure 150: Control (0 kGy) Proton Irradiated (Sample 68) Crystallite Thickness Distribution for Run 1 (Area Calculations)

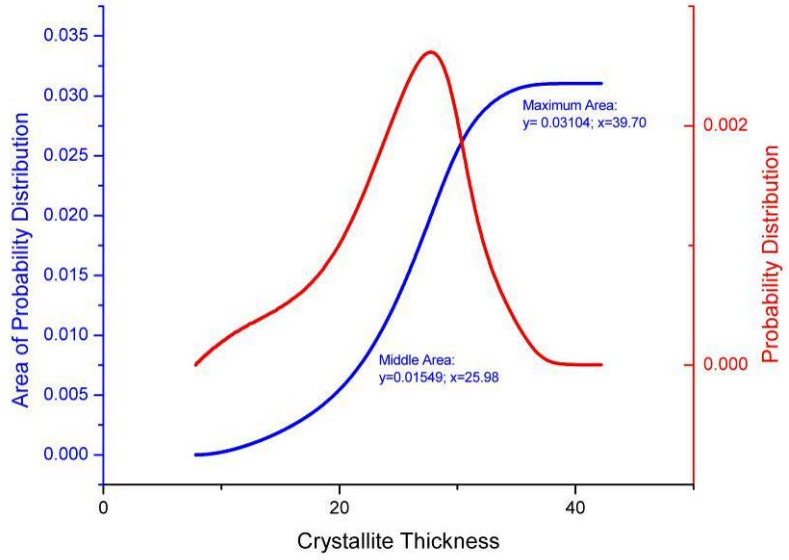

Figure 151: First Moment of Control (0 kGy) Proton Irradiated (Sample 68) Crystallite Thickness Distribution for Run 1 (Area Calculations)

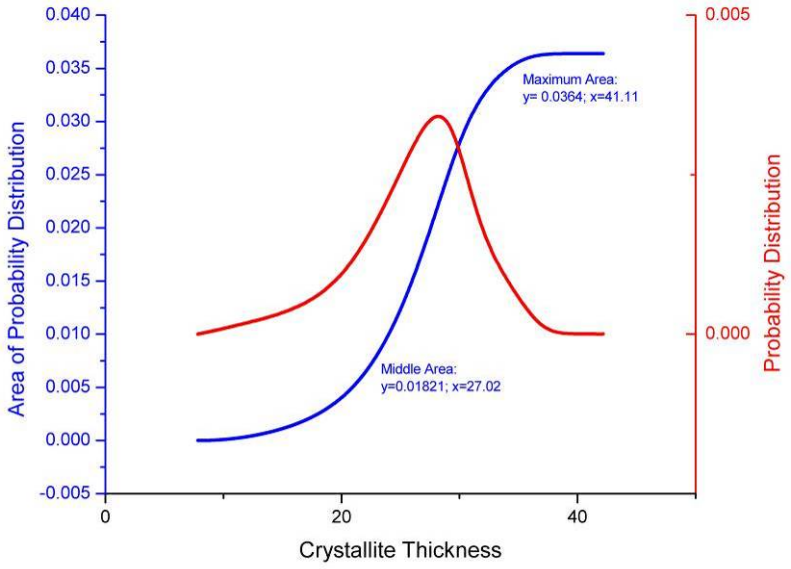

Figure 152: Second Moment of Control (0 kGy) Proton Irradiated (Sample 68) Crystallite Thickness Distribution for Run 1 (Area Calculations)

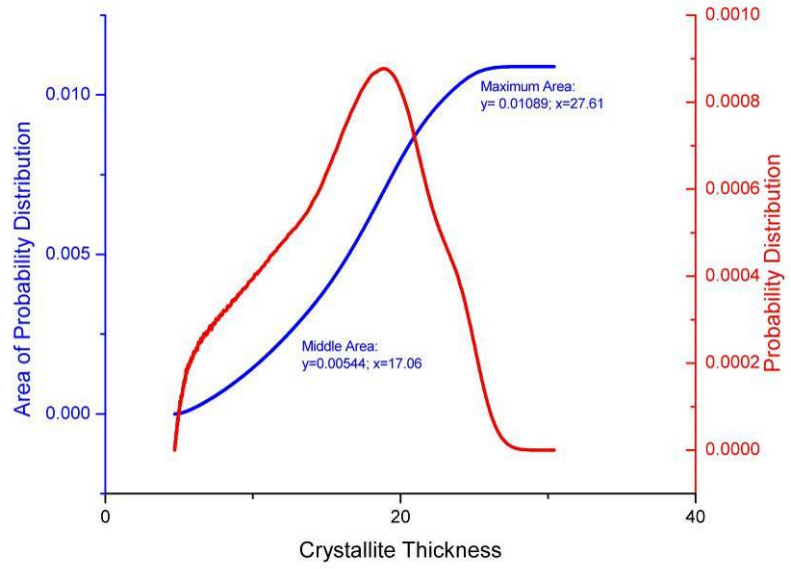

Figure 153: Control (0 kGy) Proton Irradiated (Sample 68) Crystallite Thickness Distribution for Run 2 (Area Calculations)

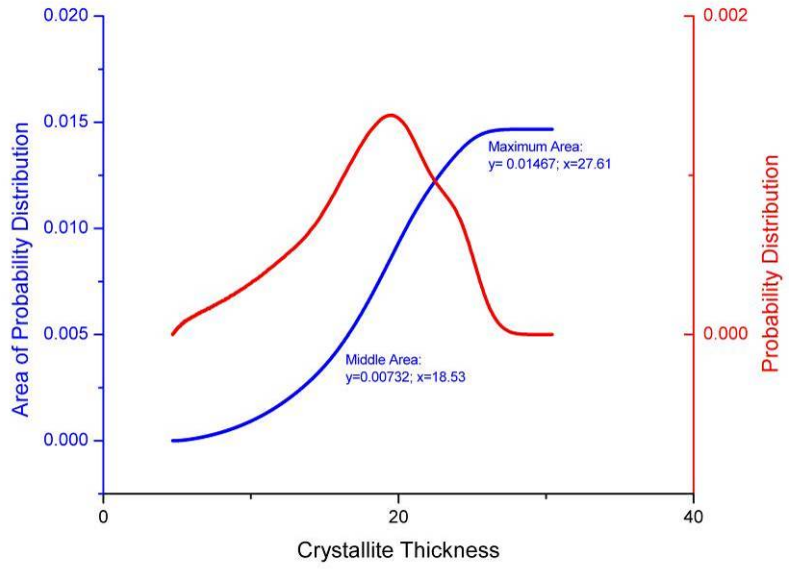

Figure 154: First Moment of Control (0 kGy) Proton Irradiated (Sample 68) Crystallite Thickness Distribution for Run 2 (Area Calculations)

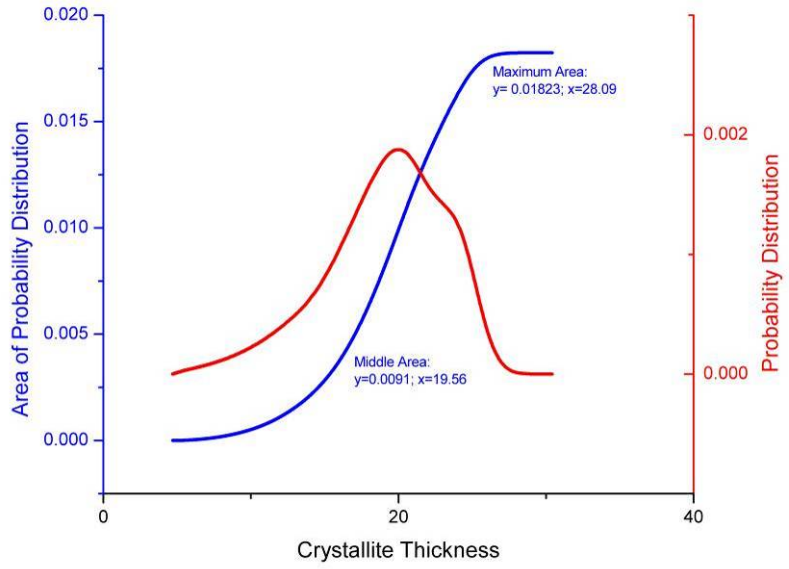

Figure 155: Second Moment of Control (0 kGy) Proton Irradiated (Sample 68) Crystallite Thickness Distribution for Run 2 (Area Calculations)

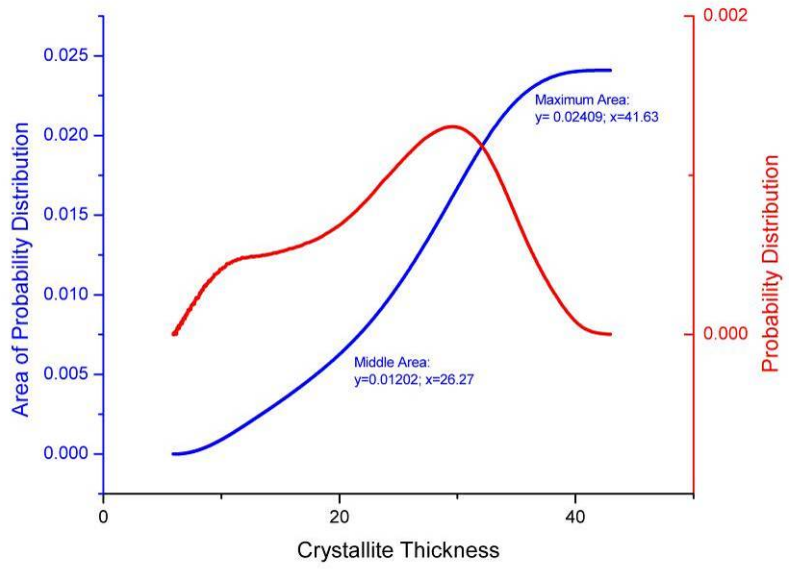

Figure 156: 3.7 kGy Proton Irradiated (Sample 58) Crystallite Thickness Distribution for Run 1 (Area Calculations)

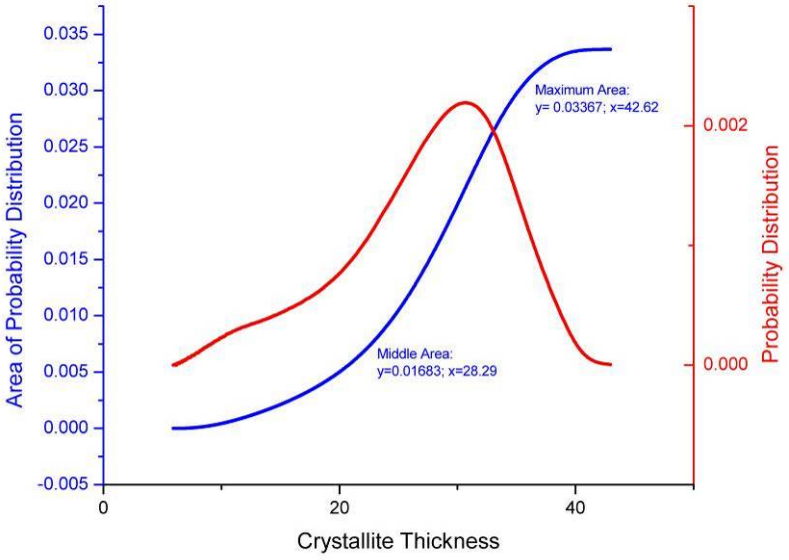

Figure 157: First Moment of 3.7 kGy Proton Irradiated (Sample 58) Crystallite Thickness Distribution for Run 1 (Area Calculations)

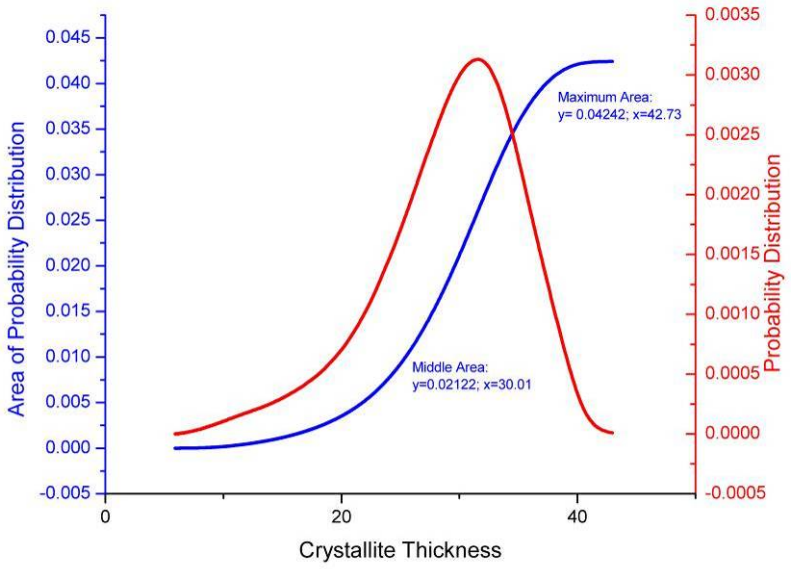

Figure 158: Second Moment of 3.7 kGy Proton Irradiated (Sample 58) Crystallite Thickness Distribution for Run 1 (Area Calculations)

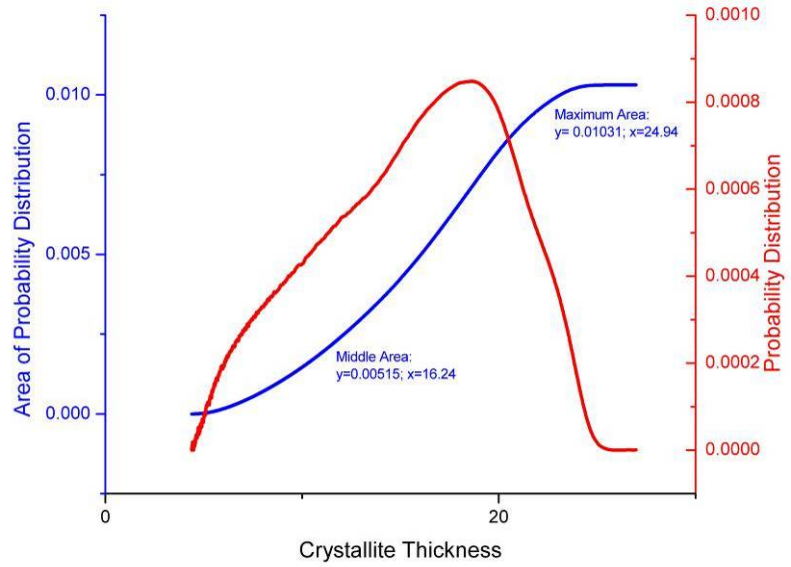

Figure 159: 3.7 kGy Proton Irradiated (Sample 58) Crystallite Thickness Distribution for Run 2 (Area Calculations)

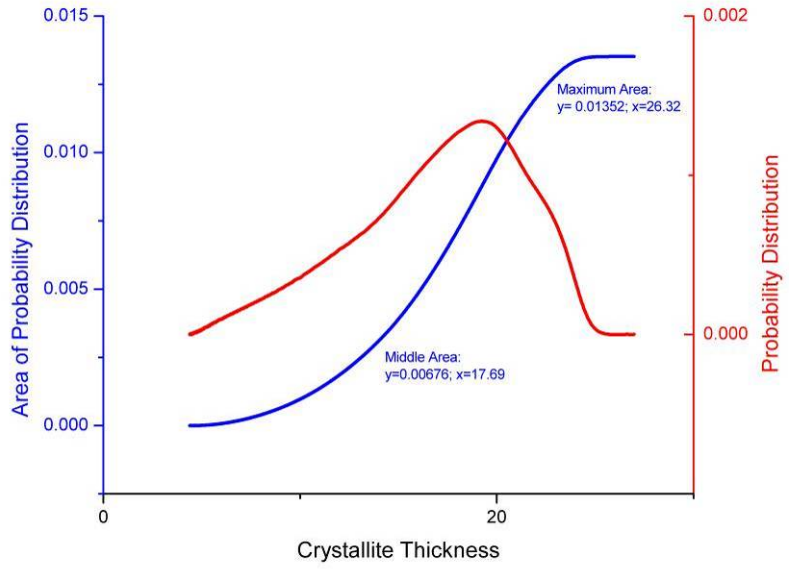

Figure 160: First Moment of 3.7 kGy Proton Irradiated (Sample 58) Crystallite Thickness Distribution for Run 2 (Area Calculations)

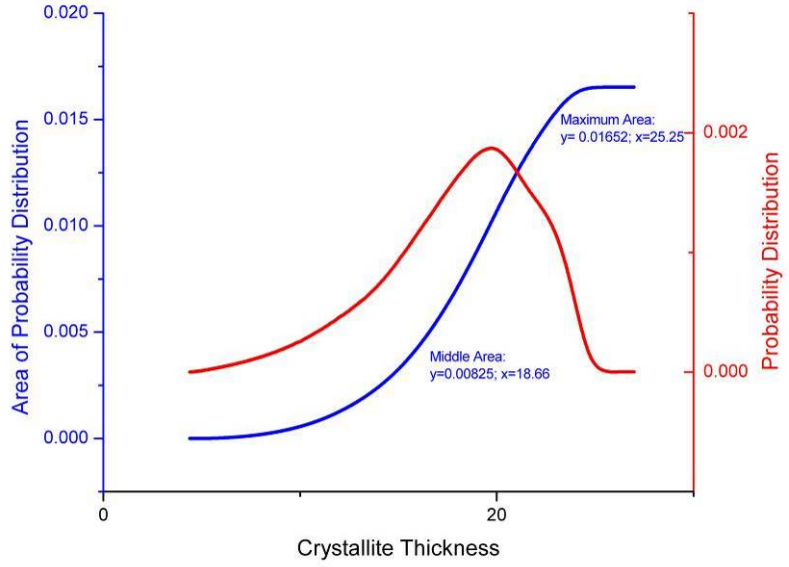

Figure 161: Second Moment of 3.7 kGy Proton Irradiated (Sample 58) Crystallite Thickness Distribution for Run 2 (Area Calculations)

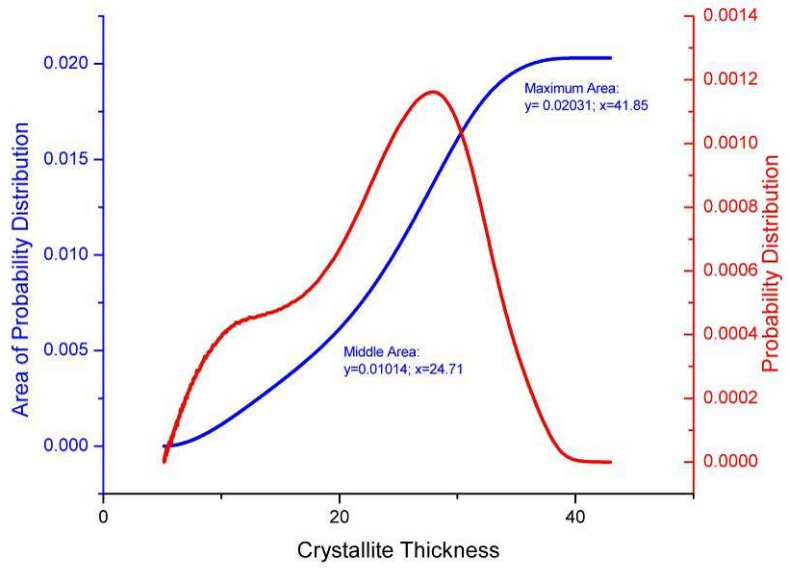

Figure 162: 1.3289 kGy Proton Irradiated (Sample 57) Crystallite Thickness Distribution for Run 1 (Area Calculations)

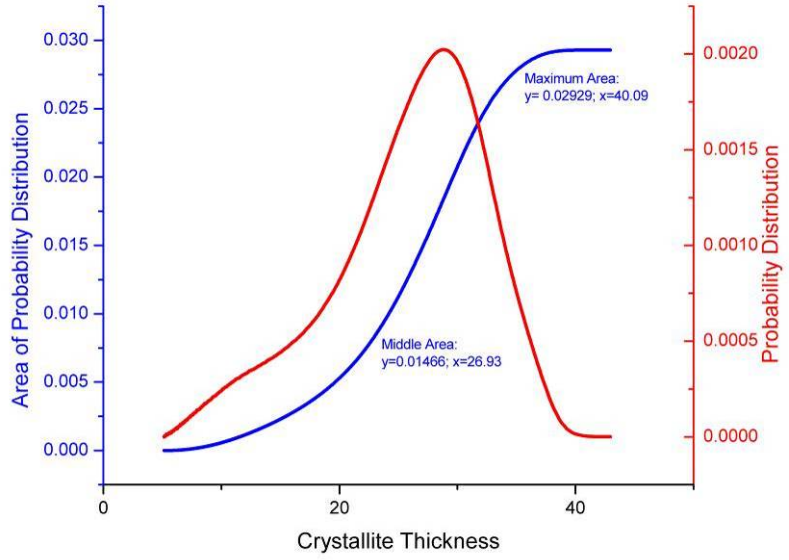

Figure 163: First Moment of 1.3289 kGy Proton Irradiated (Sample 57) Crystallite Thickness Distribution for Run 1 (Area Calculations)

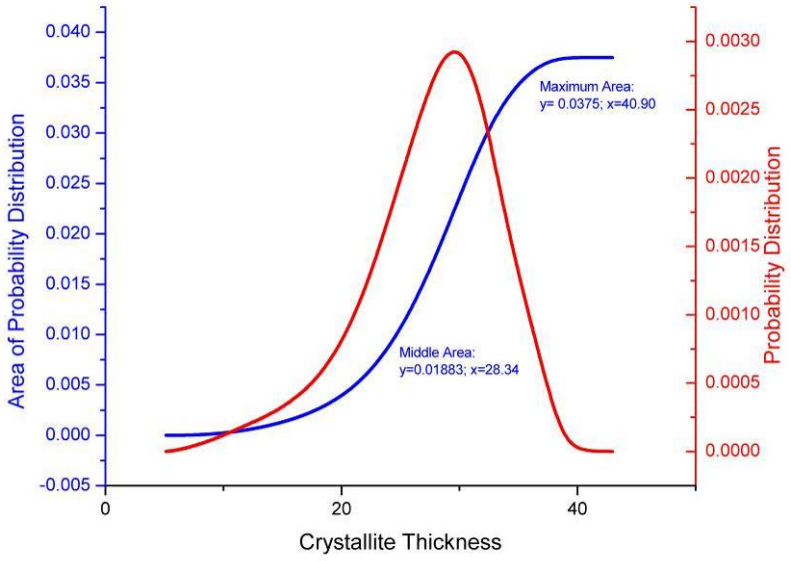

Figure 164: Second Moment of 1.3289 kGy Proton Irradiated (Sample 57) Crystallite Thickness Distribution for Run 1 (Area Calculations)

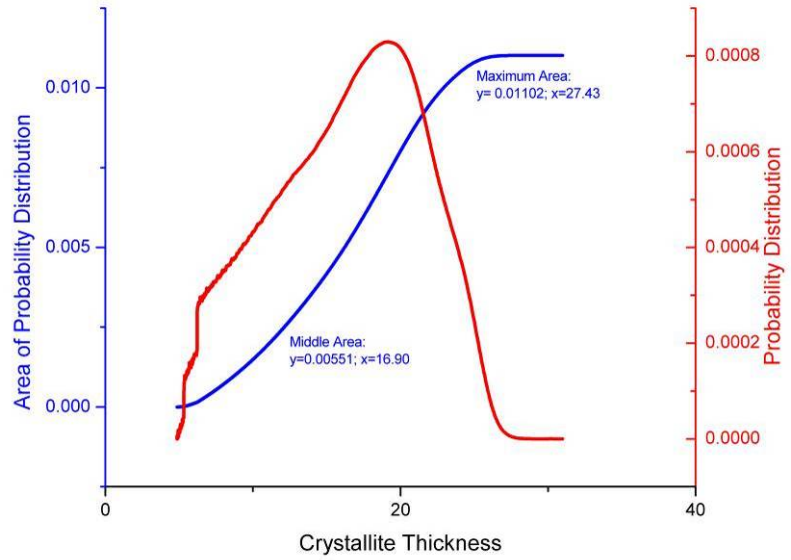

Figure 165: 1.3289 kGy Proton Irradiated (Sample 57) Crystallite Thickness Distribution for Run 2 (Area Calculations)

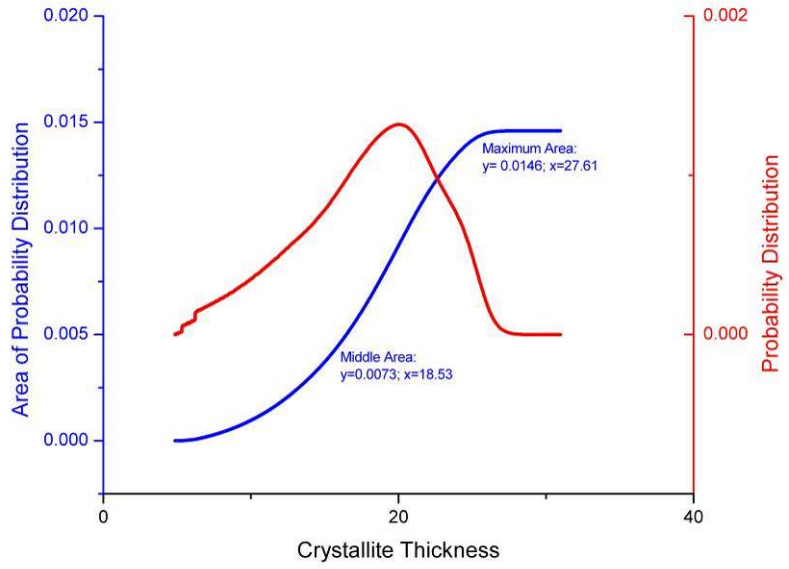

Figure 166: First Moment of 1.3289 kGy Proton Irradiated (Sample 57) Crystallite Thickness Distribution for Run 2 (Area Calculations)

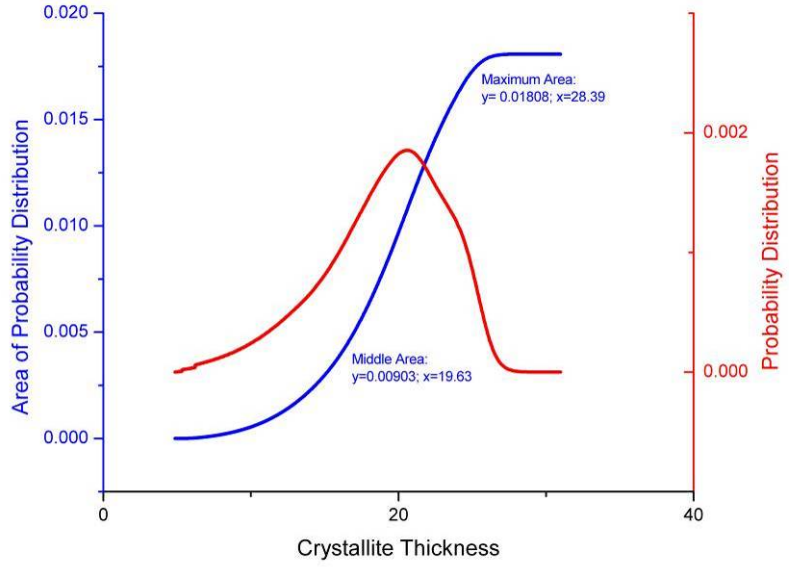

Figure 167: Second Moment of 1.3289 kGy Proton Irradiated (Sample 57) Crystallite Thickness Distribution for Run 2 (Area Calculations)

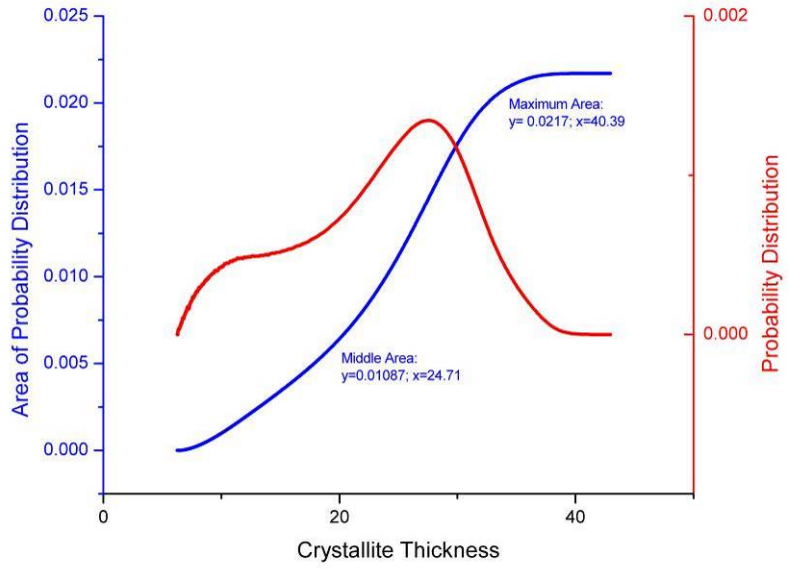

Figure 168: Control (0 kGy) Proton Irradiated (Sample 68) Crystallite Thickness Distribution for Run 1 (Area Calculations)

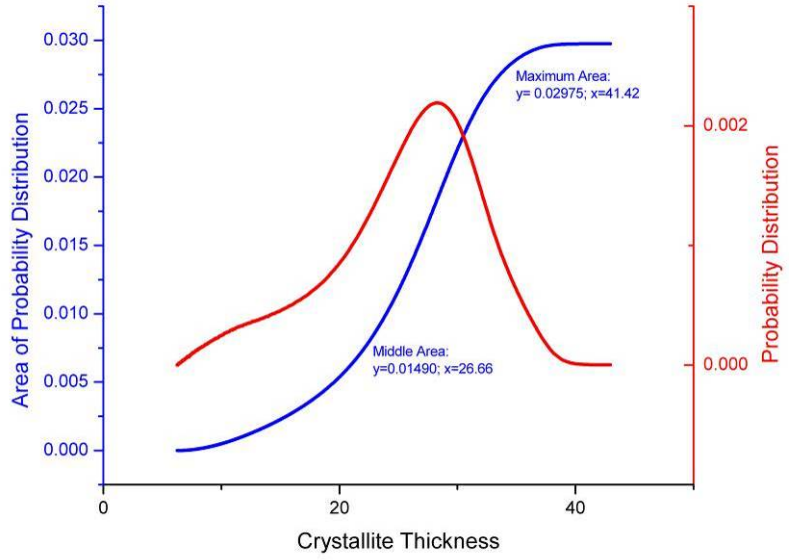

Figure 169: First Moment of Control (0 kGy) Proton Irradiated (Sample 68) Crystallite Thickness Distribution for Run 1 (Area Calculations)

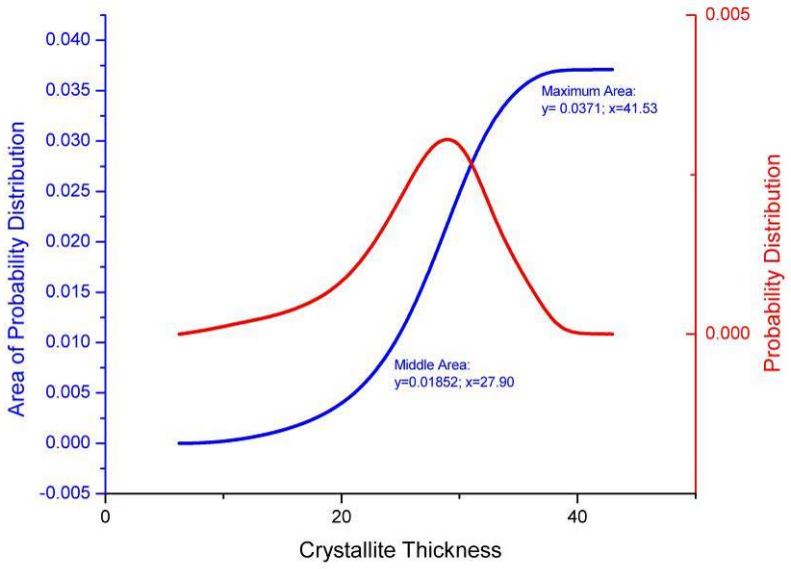

Figure 170: Second Moment of Control (0 kGy) Proton Irradiated (Sample 68) Crystallite Thickness Distribution for Run 1 (Area Calculations)

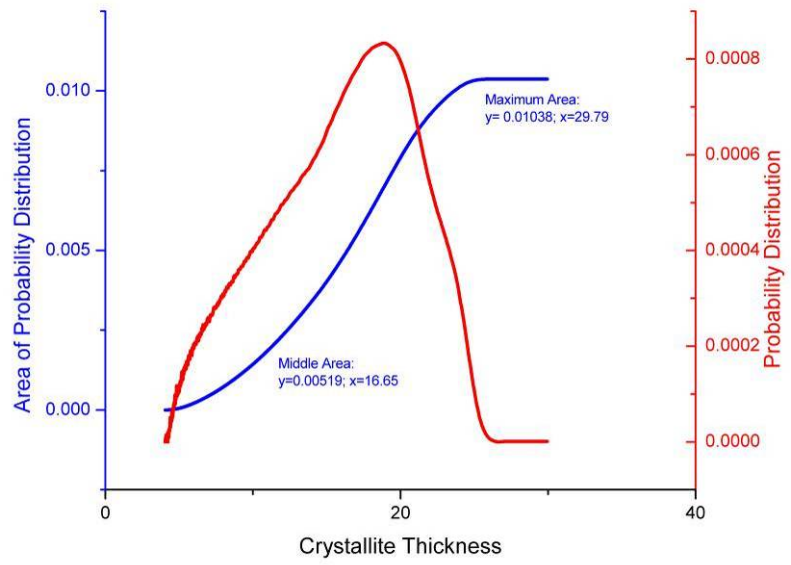

Figure 171: Control (0 kGy) Proton Irradiated (Sample 68) Crystallite Thickness Distribution for Run 2 (Area Calculations)

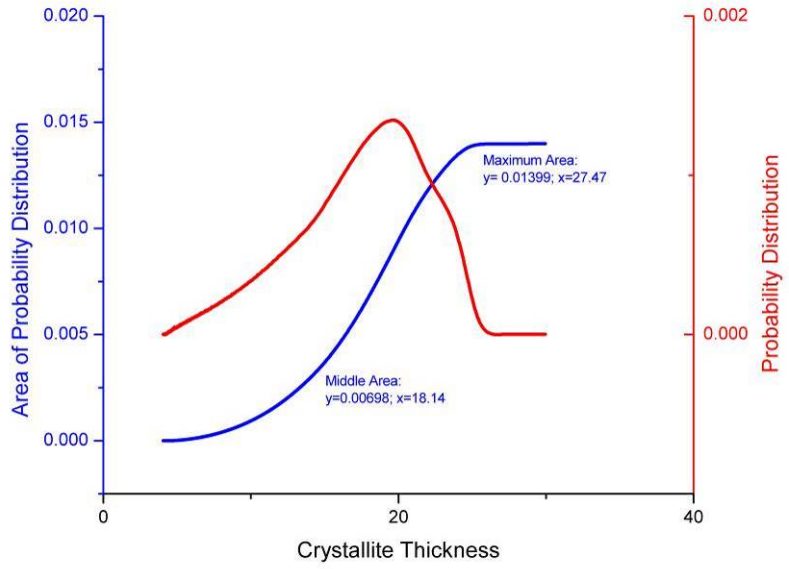

Figure 172: First Moment of Control (0 kGy) Proton Irradiated (Sample 68) Crystallite Thickness Distribution for Run 2 (Area Calculations)

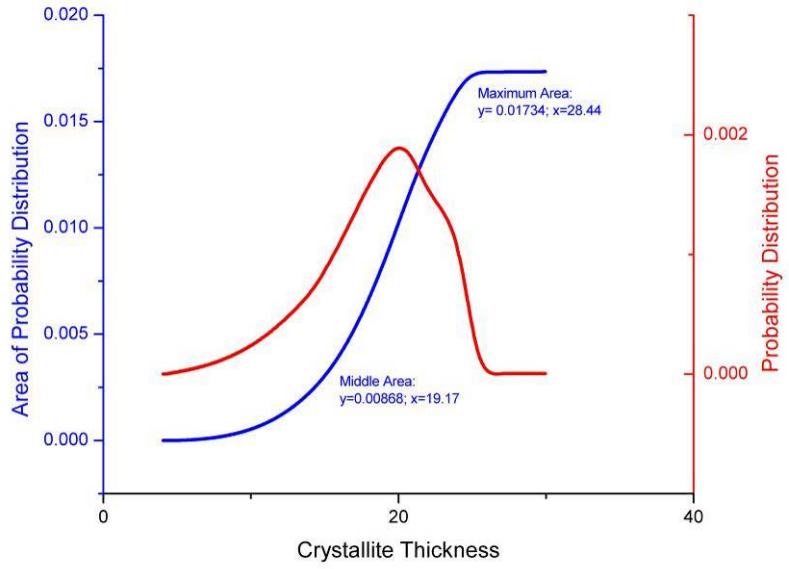

Figure 173: Second Moment of Control (0 kGy) Proton Irradiated (Sample 68) Crystallite Thickness Distribution for Run 2 (Area Calculations)

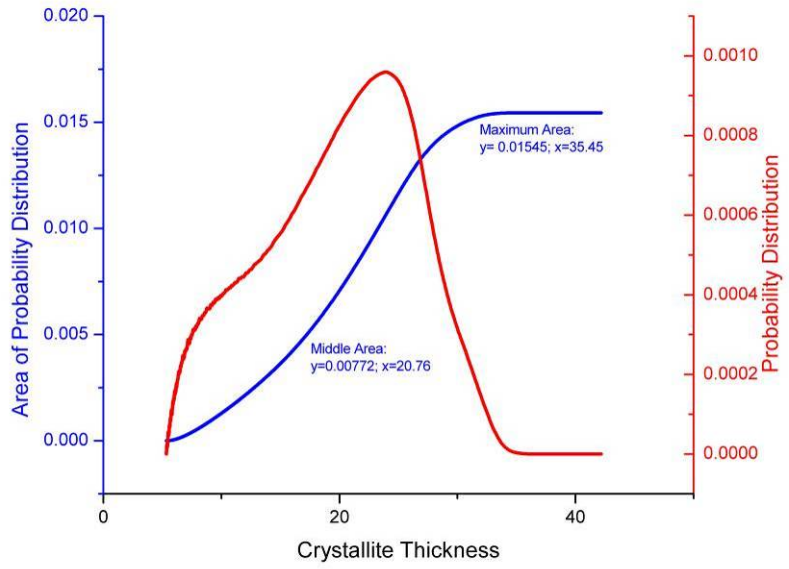

Figure 174: Control (0 kGy) Proton Irradiated (Sample 26) Crystallite Thickness Distribution for Run 1 (Area Calculations)

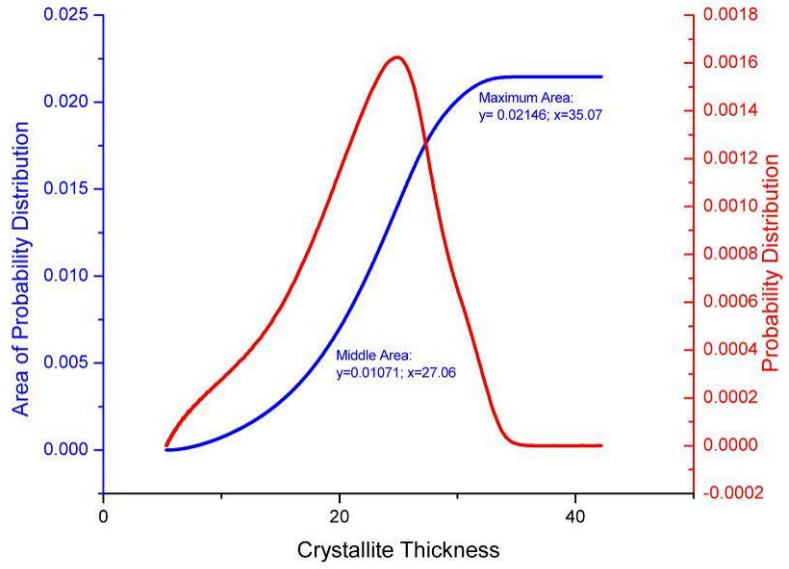

Figure 175: First Moment of Control (0 kGy) Proton Irradiated (Sample 26) Crystallite Thickness Distribution for Run 1 (Area Calculations)

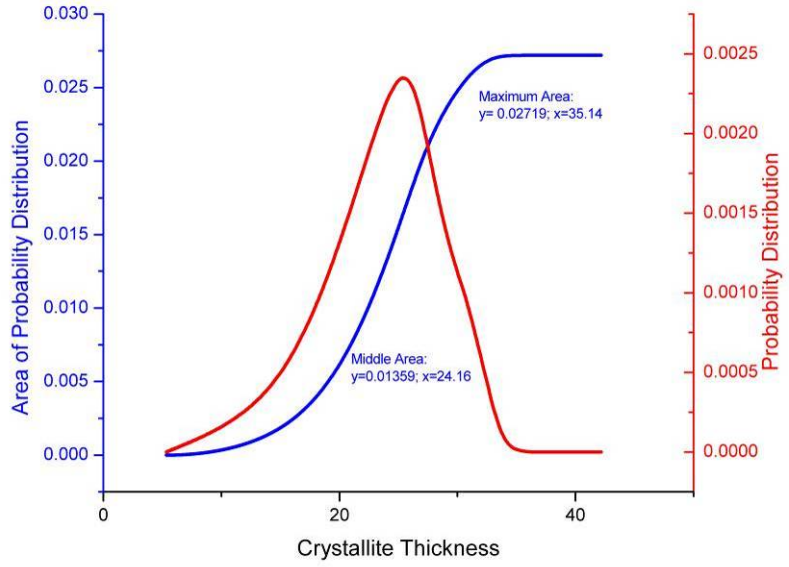

Figure 176: Second Moment of Control (0 kGy) Proton Irradiated (Sample 26) Crystallite Thickness Distribution for Run 1 (Area Calculations)

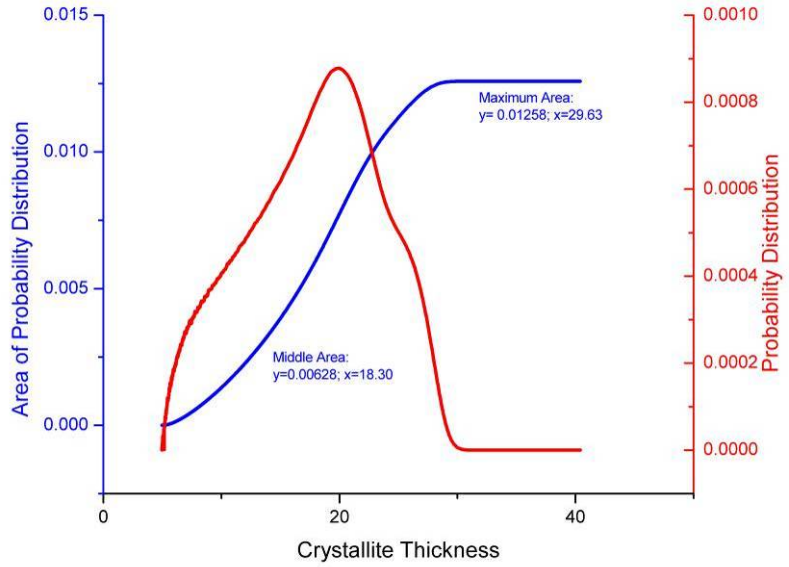

Figure 177: Control (0 kGy) Proton Irradiated (Sample 26) Crystallite Thickness Distribution for Run 2 (Area Calculations)

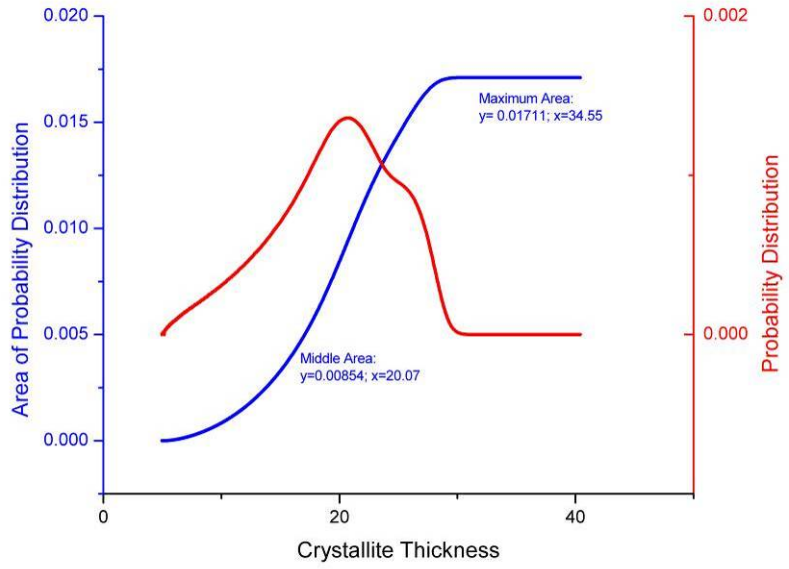

Figure 178: First Moment of Control (0 kGy) Proton Irradiated (Sample 26) Crystallite Thickness Distribution for Run 2 (Area Calculations)

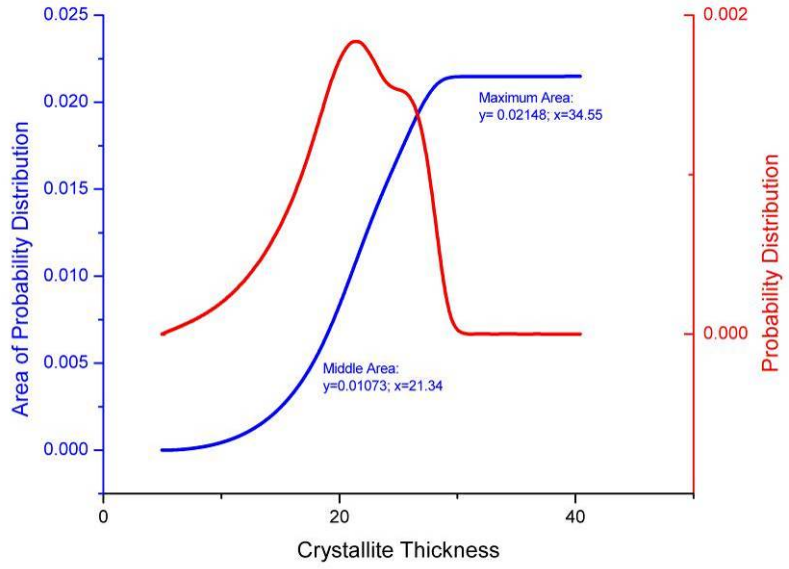

Figure 179: Second Moment of Control (0 kGy) Proton Irradiated (Sample 26) Crystallite Thickness Distribution for Run 1 (Area Calculations)

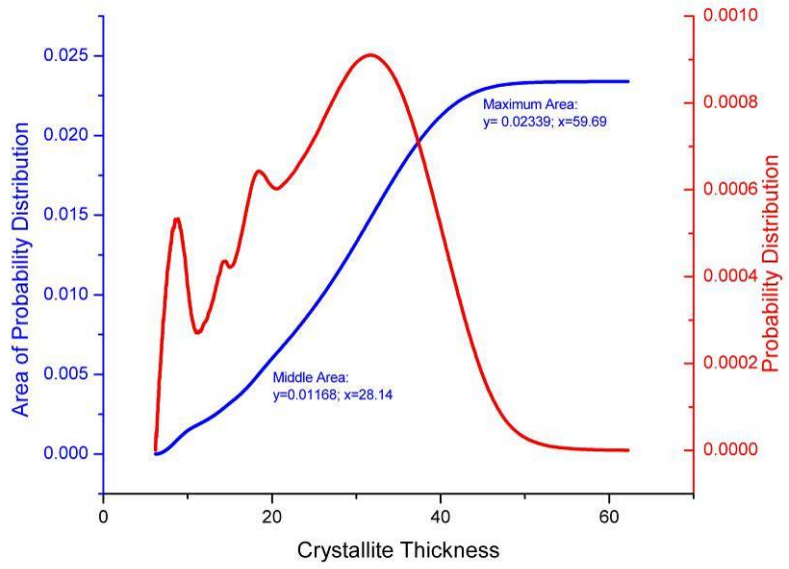

Figure 180: 8.7 kGy Proton Irradiated (Sample 83) Crystallite Thickness Distribution for Run 1 (Area Calculations)

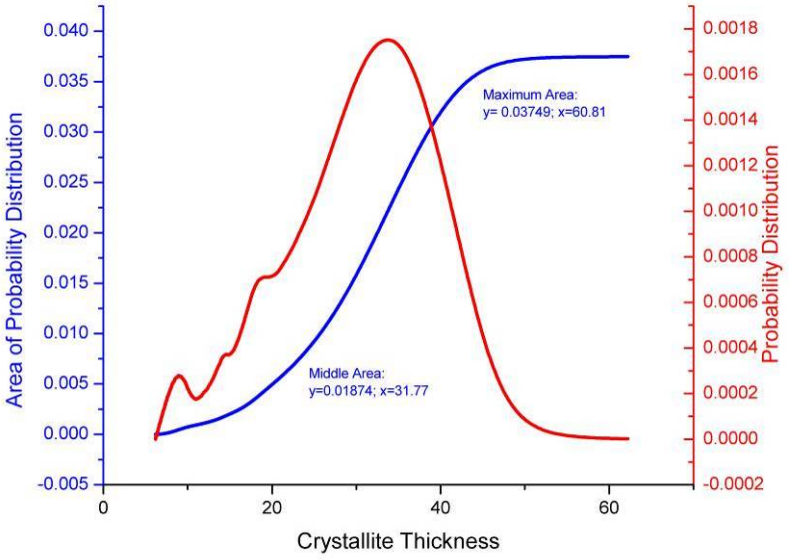

Figure 181: First Moment of 8.7 kGy Proton Irradiated (Sample 83) Crystallite Thickness Distribution for Run 1 (Area Calculations)

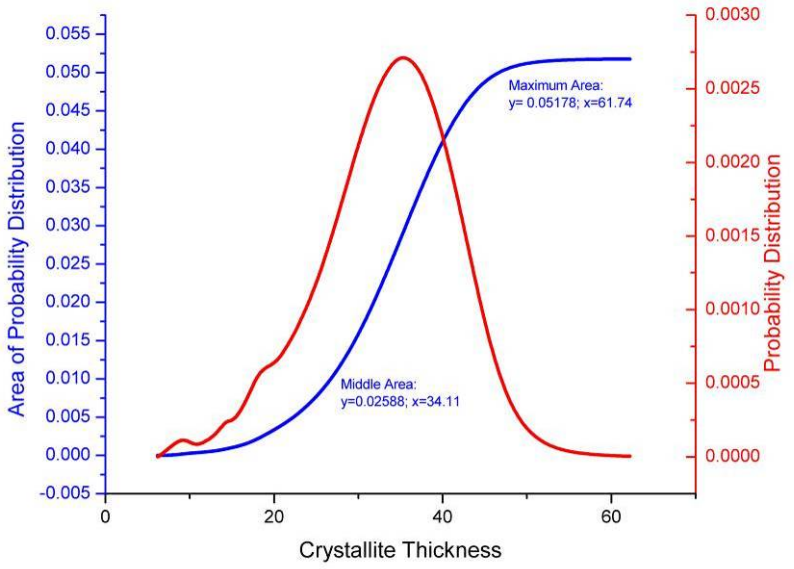

Figure 182: Second Moment of 8.7 kGy Proton Irradiated (Sample 83) Crystallite Thickness Distribution for Run 1 (Area Calculations)

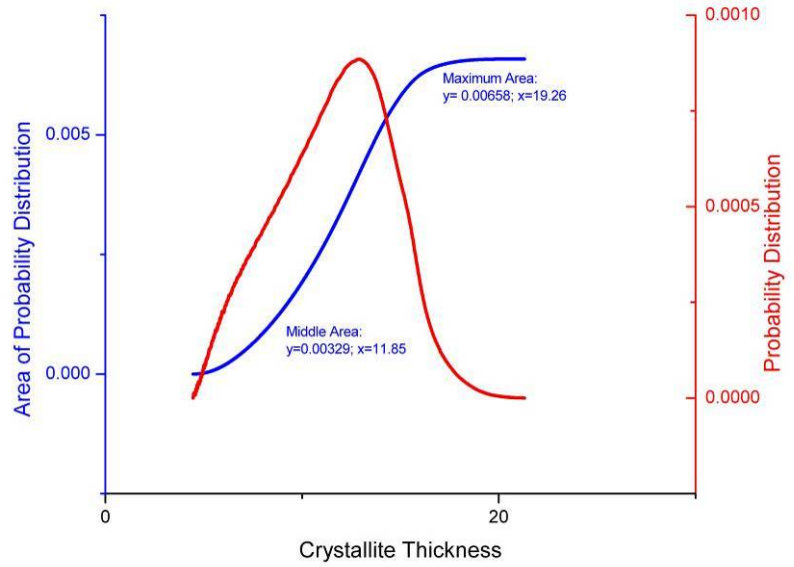

Figure 183: 8.7 kGy Proton Irradiated (Sample 83) Crystallite Thickness Distribution for Run 2 (Area Calculations)

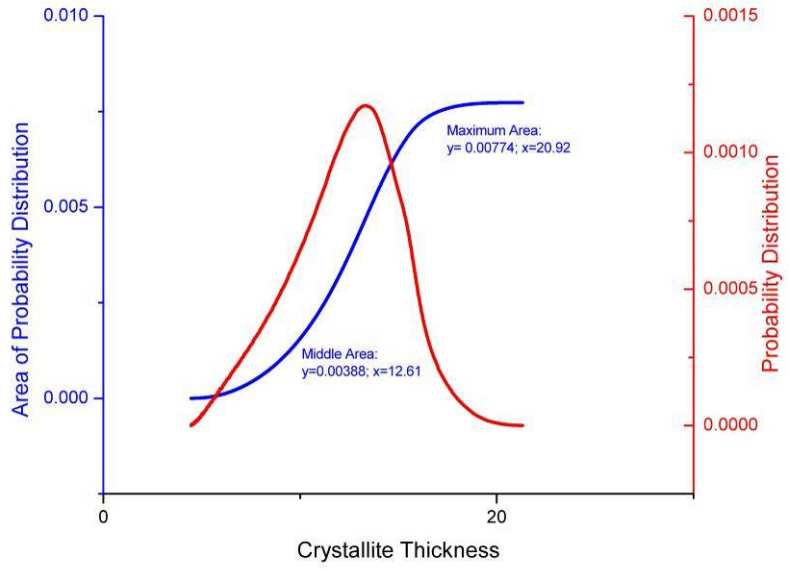

Figure 184: First Moment of 8.7 kGy Proton Irradiated (Sample 83) Crystallite Thickness Distribution for Run 2 (Area Calculations)

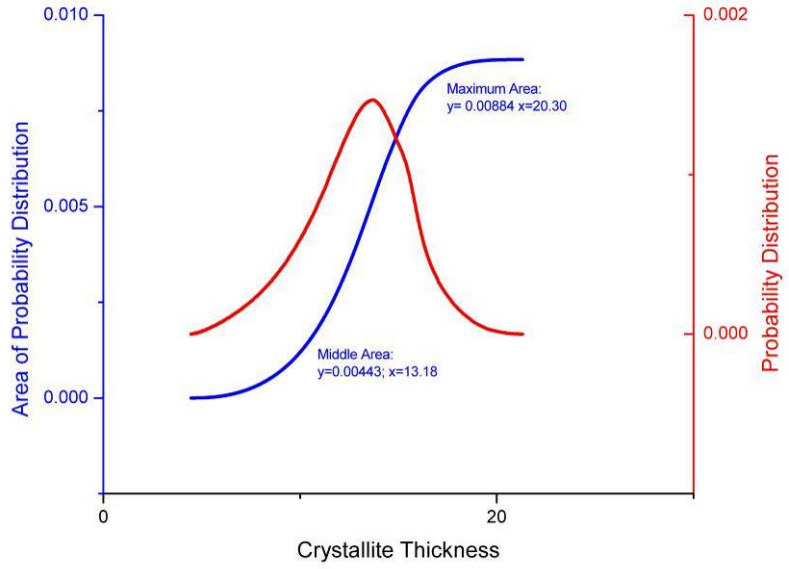

Figure 185: Second Moment of 8.7 kGy Proton Irradiated (Sample 83) Crystallite Thickness Distribution for Run 2 (Area Calculations)

Appendix 3: Gamma Irradiated DSC

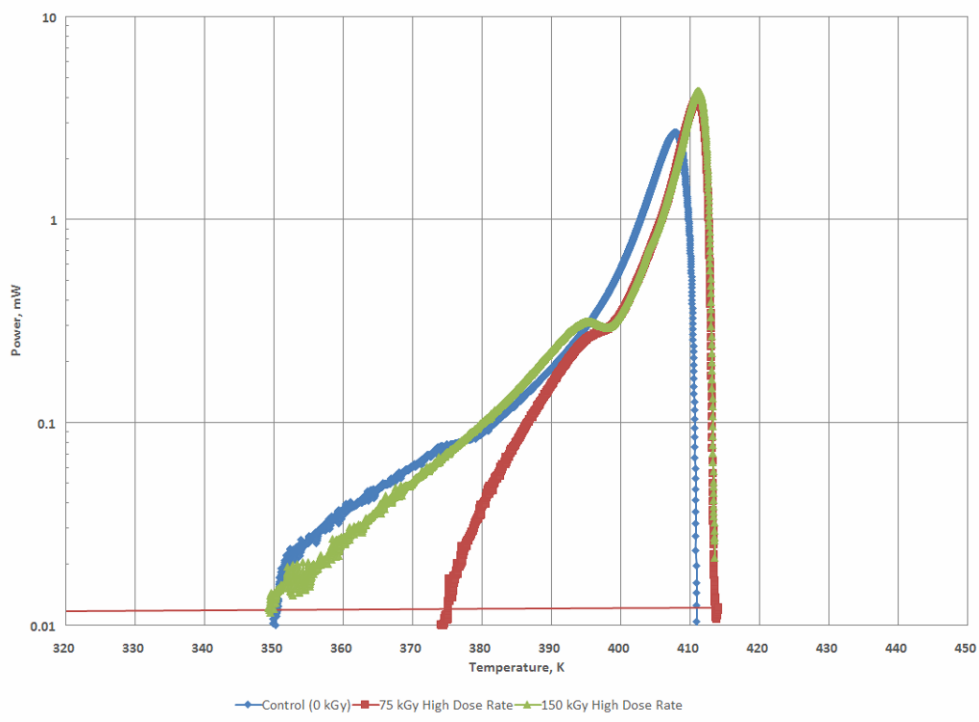

Figure 186: Endotherm for the Surface of High Dose Rate Irradiation

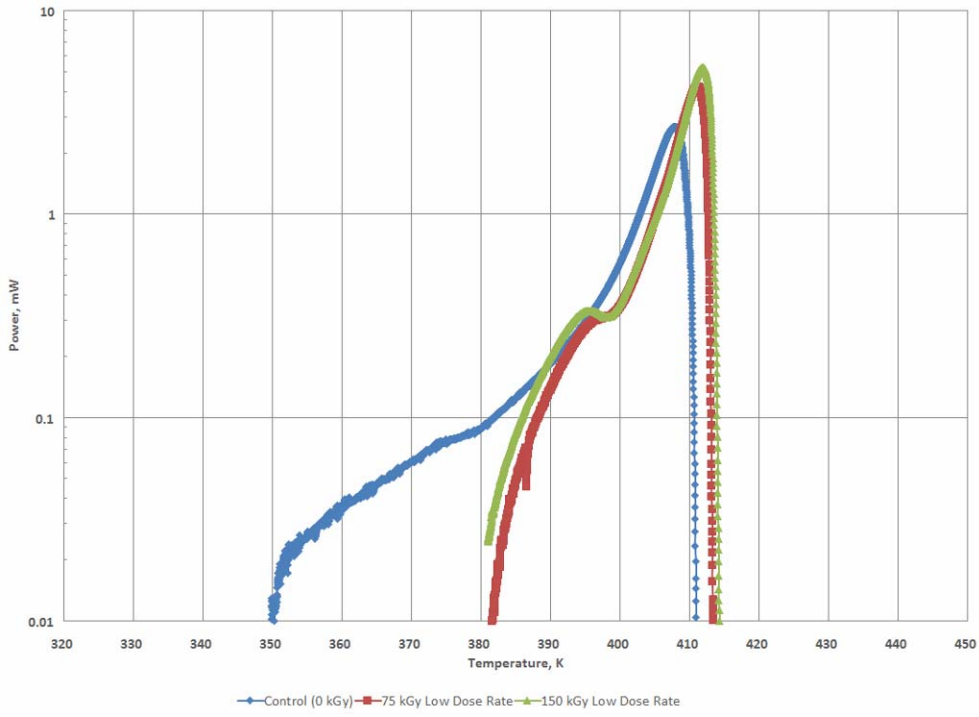

Figure 187: Endotherm for the Surface of Low Dose Rate Irradiation

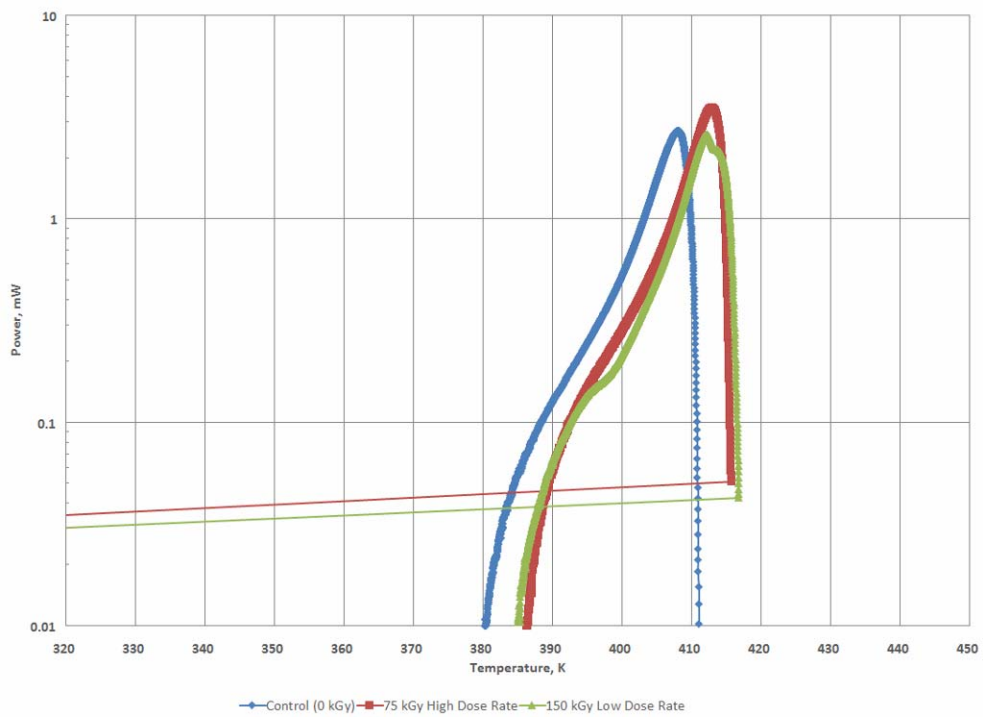

Figure 188: Endotherm for the Center of High Dose Rate Irradiation

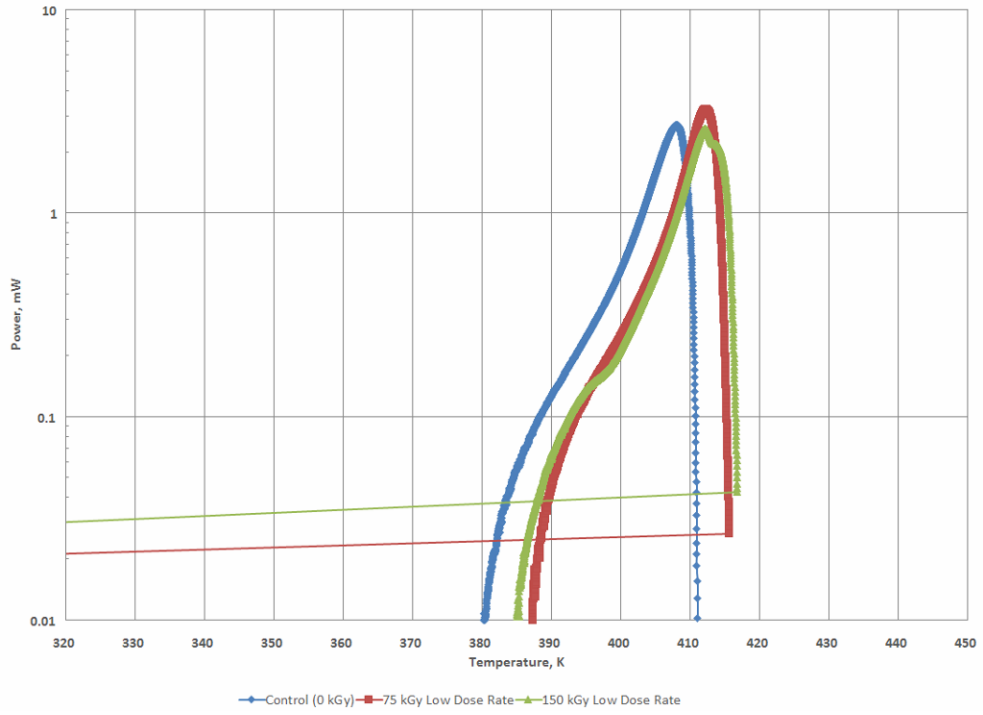

Figure 189: Endotherm for the Center of Low Dose Rate Irradiation

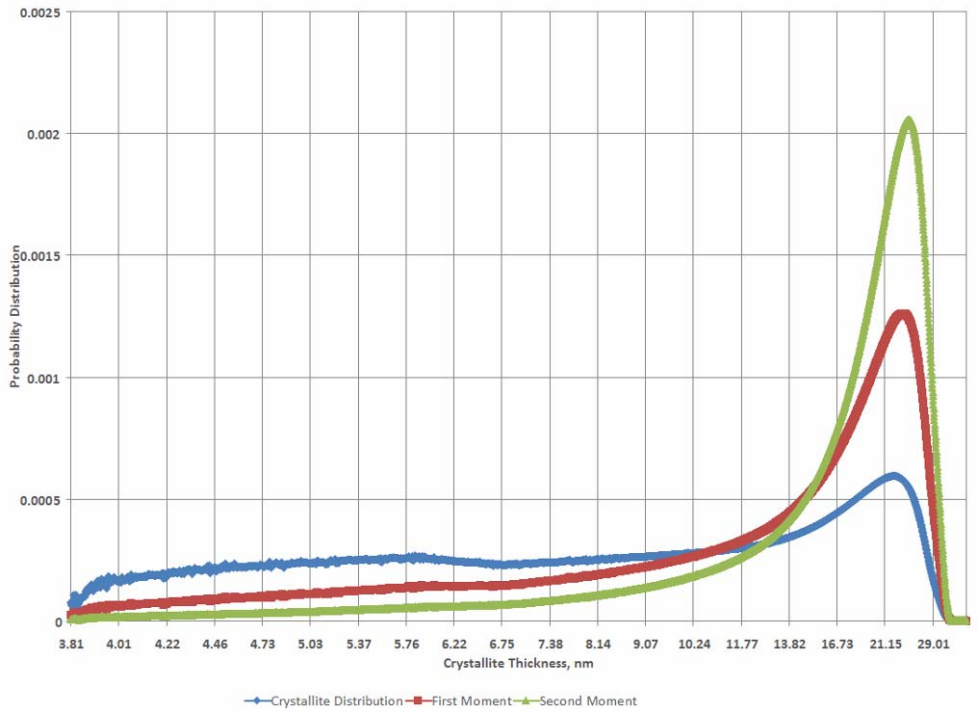

Figure 190: Surface of Control (0 kGy) Gamma Irradiated Sample (1801)

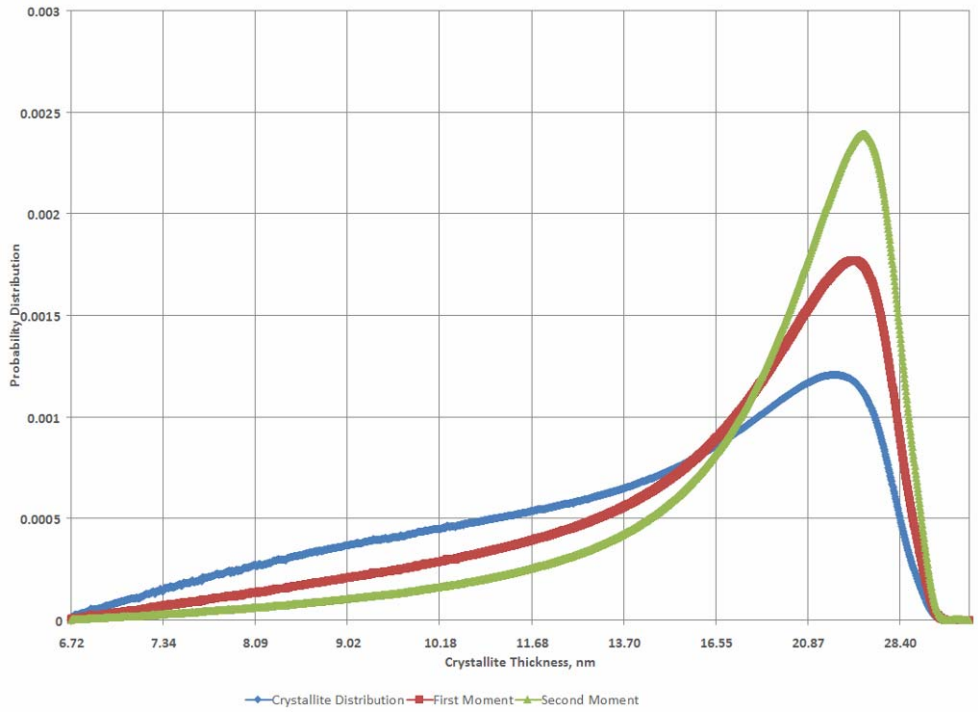

Figure 191: Center of Control (0 kGy) Gamma Irradiated Sample (1803)

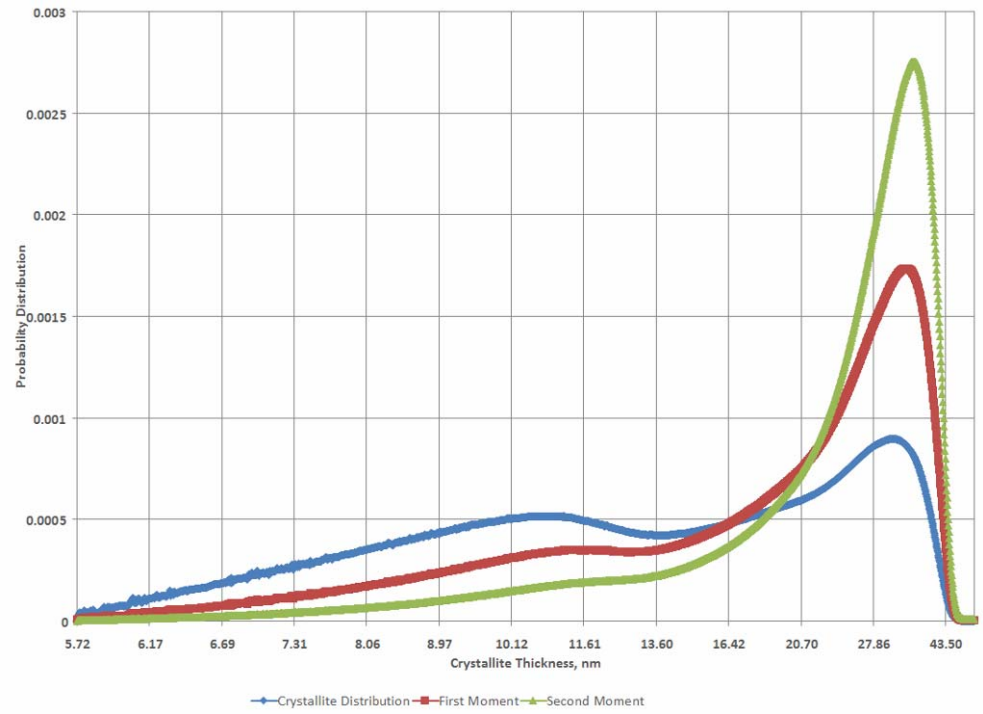

Figure 192: Surface of 75 kGy High Dose Rate Gamma Irradiated Sample (3701)

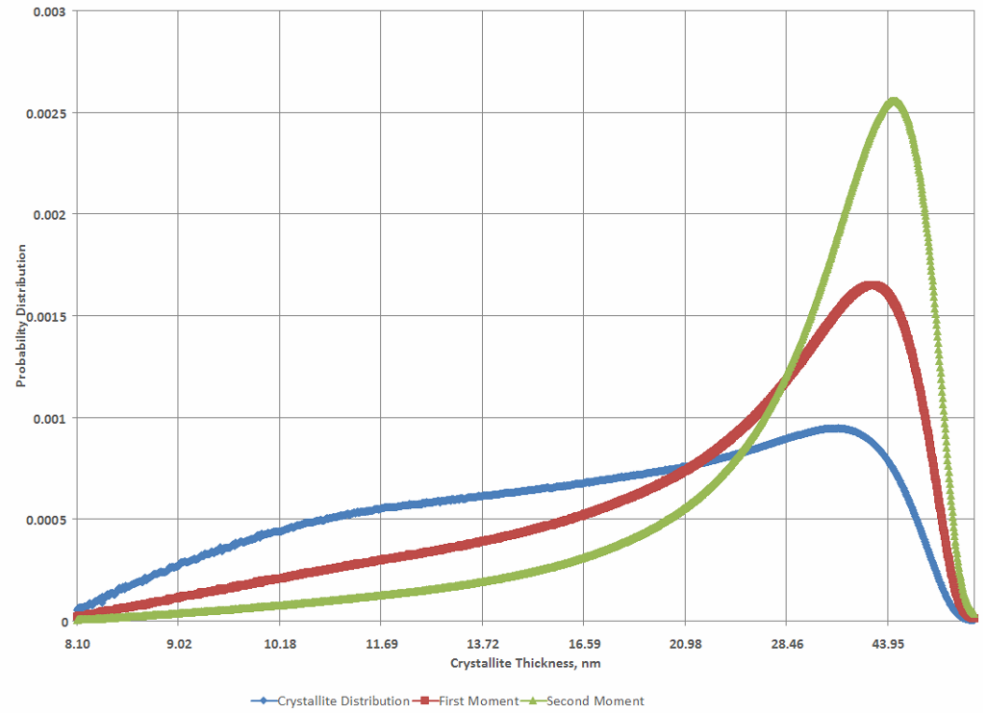

Figure 193: Center of 75 kGy High Dose Rate Gamma Irradiated Sample (3703)

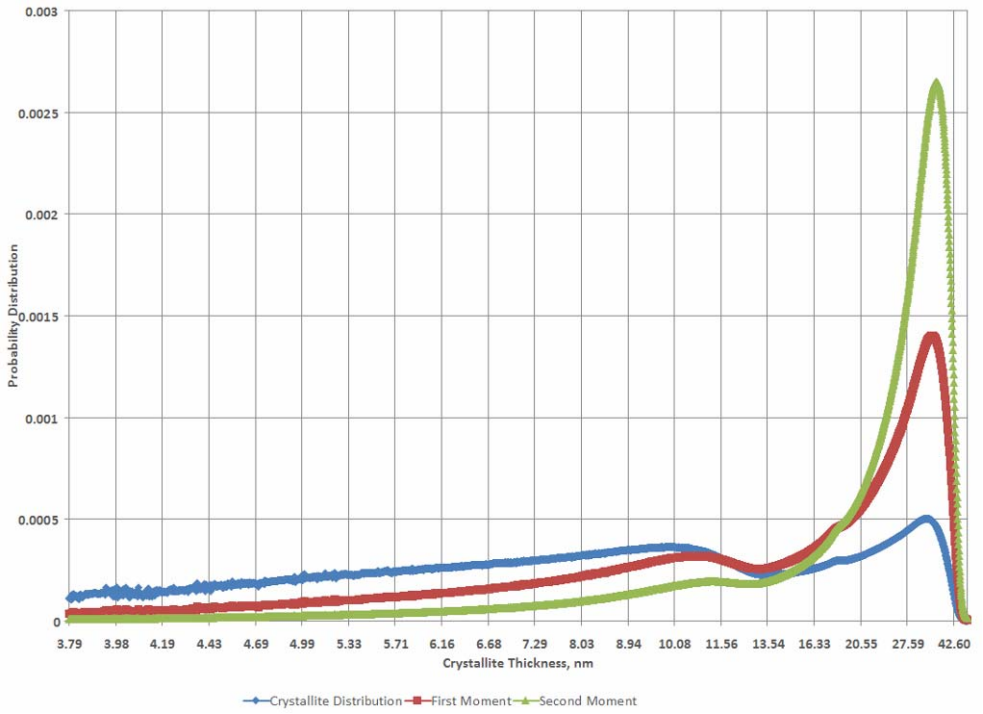

Figure 194: Surface of 150 kGy High Dose Rate Gamma Irradiated Sample (4501)

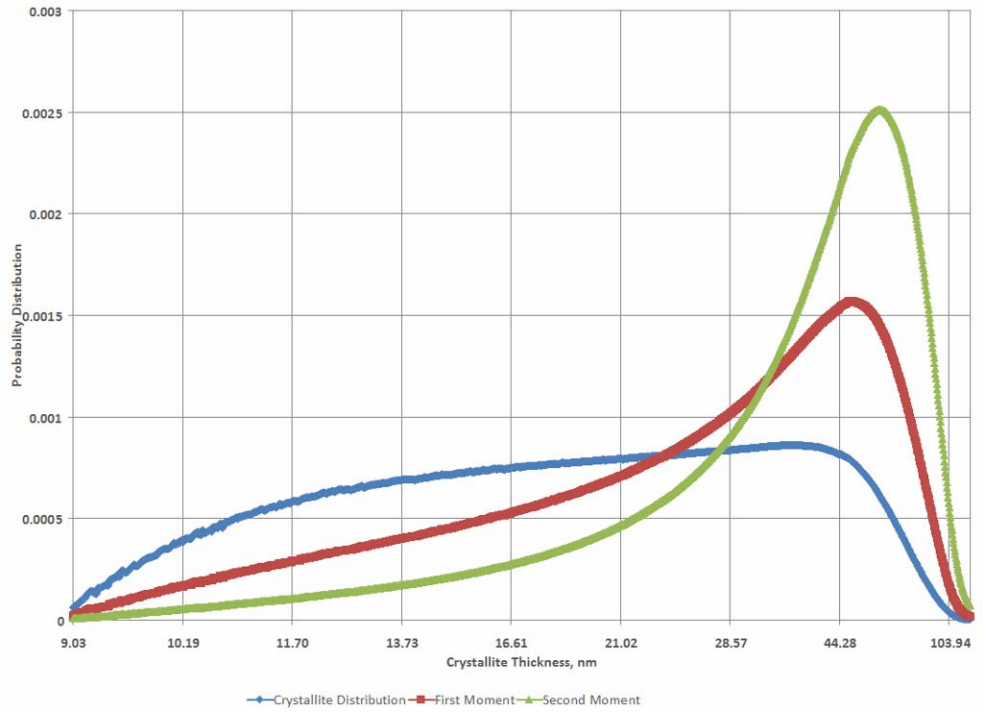

Figure 195: Center of 150 kGy High Dose Rate Gamma Irradiated Sample (4503)

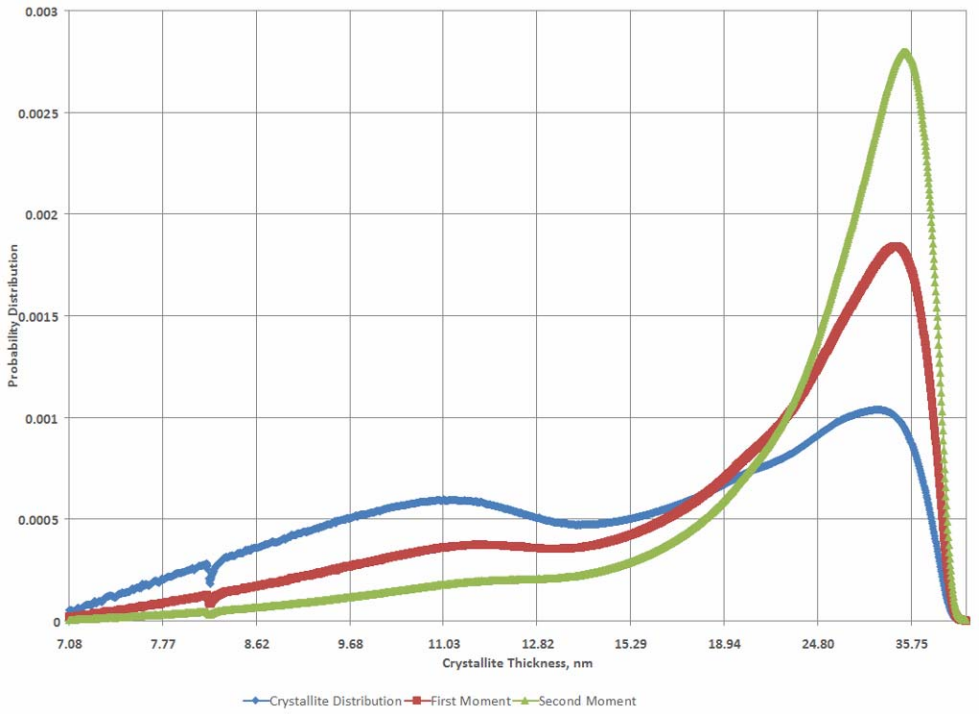

Figure 196: Surface of 75 kGy Low Dose Rate Gamma Irradiated Sample (4701)

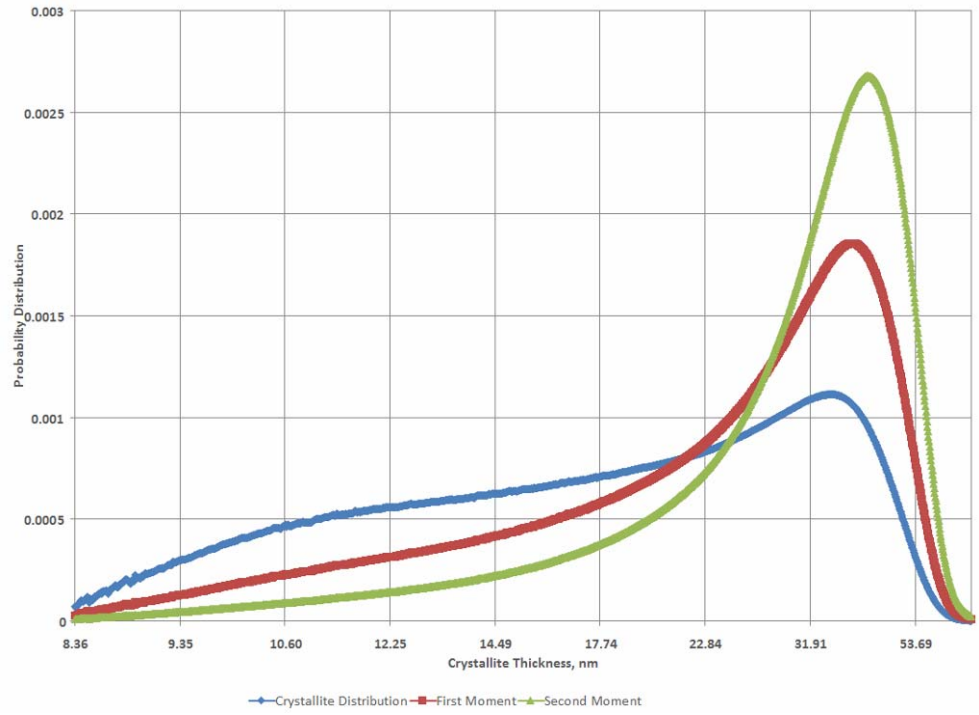

Figure 197: Center of 75 kGy Low Dose Rate Gamma Irradiated Sample (4703)

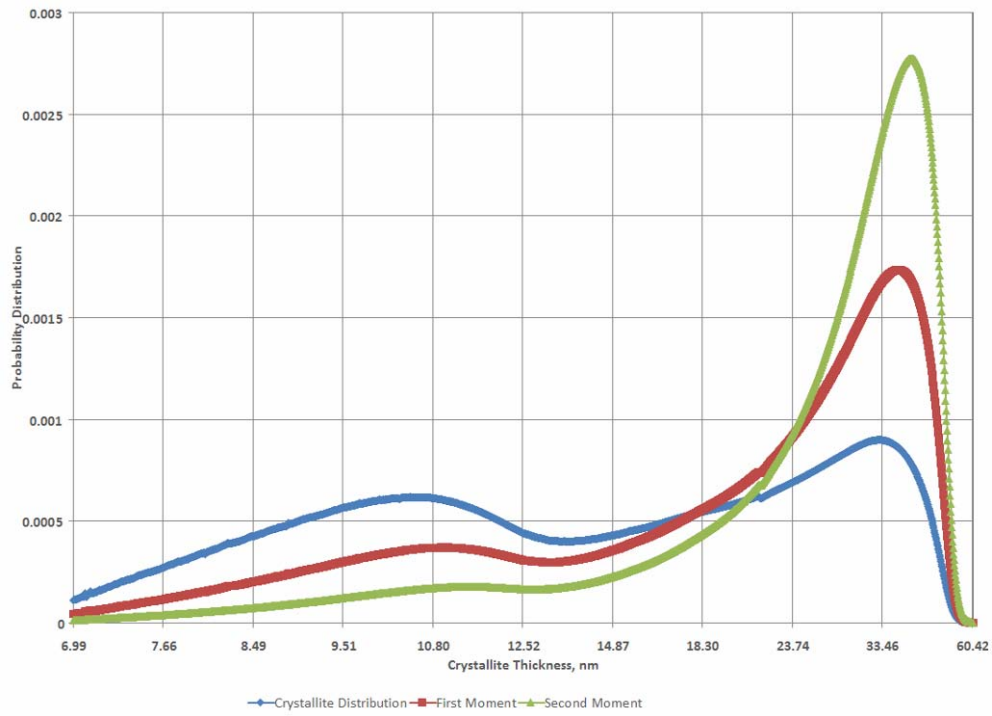

Figure 198: Surface of 150 kGy Low Dose Rate Gamma Irradiated Sample (5301)

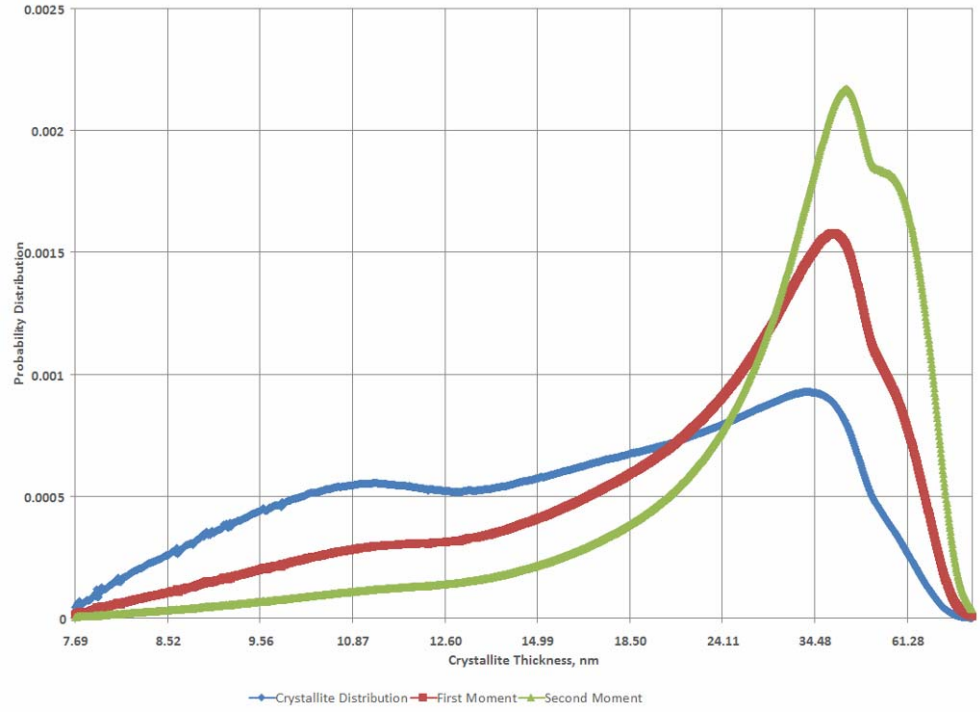

Figure 199: Center of 150 kGy Low Dose Rate Gamma Irradiated Sample (5303)

Appendix 4: Gamma Irradiated Median Crystallite Thickness

Table 28: Median and Maximum Crystallite Thickness for Gamma Irradiation

		Control		75 kGy				150 kGy			
				Low Dose Rate		High Dose Rate		Low Dose Rate		High Dose Rate	
		Surface	Center	Surface	Center	Surface	Center	Surface	Center	Surface	Center
Crystallite Thickness Distribution	Middle	19.16	20.52	27.21	32.81	26.98	30.04	29.67	34.62	26.30	40.01
	Maximum	32.64	33.42	48.00	83.61	47.30	86.65	57.33	138.41	48.65	137.90
First Moment	Middle	21.55	22.19	30.47	37.78	30.46	40.61	33.87	43.05	30.86	51.32
	Maximum	33.34	33.57	48.15	85.43	51.49	86.65	57.97	139.64	49.89	140.40
Second Moment	Middle	23.00	23.42	32.66	41.74	32.66	45.60	36.69	53.33	33.24	61.06
	Maximum	33.77	34.15	50.00	85.89	55.47	87.14	60.42	139.64	51.02	140.40

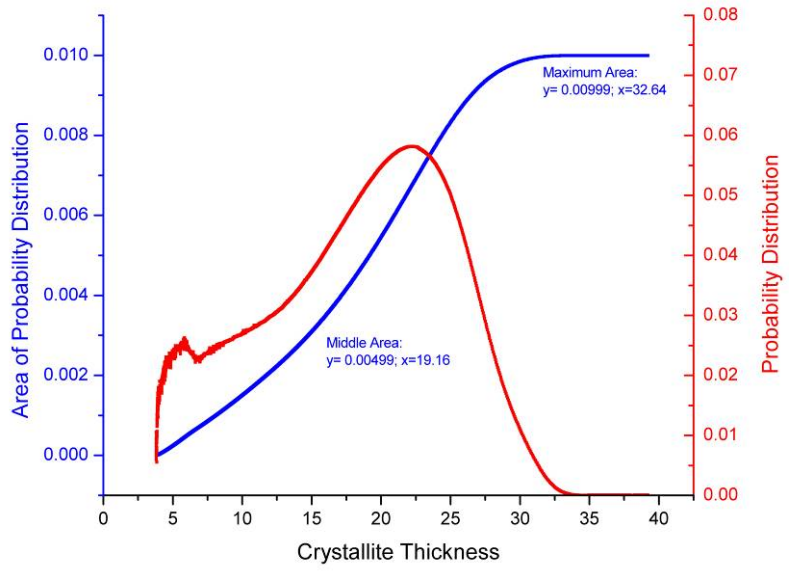

Figure 200: Control (0 kGy) Gamma Irradiated Crystallite Thickness Distribution for the Surface (Area Calculations)

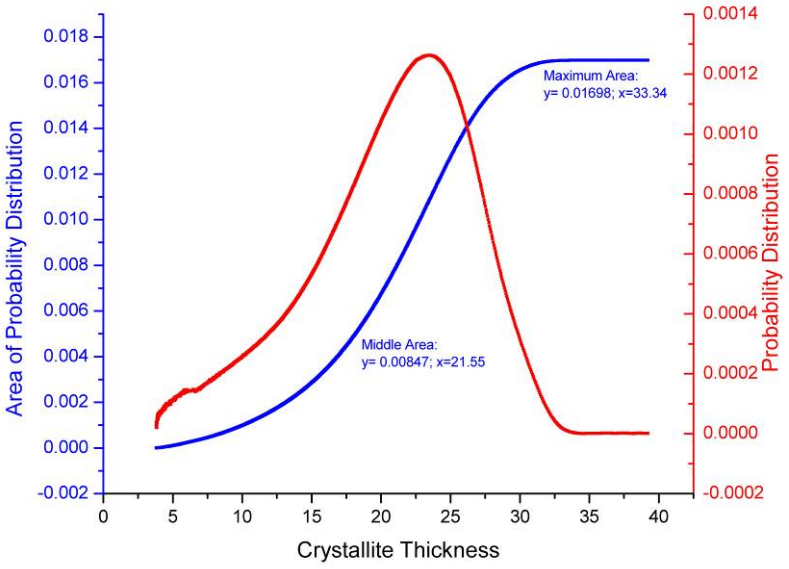

Figure 201: First Moment of Control (0 kGy) Gamma Irradiated Crystallite Thickness Distribution for the Surface (Area Calculations)

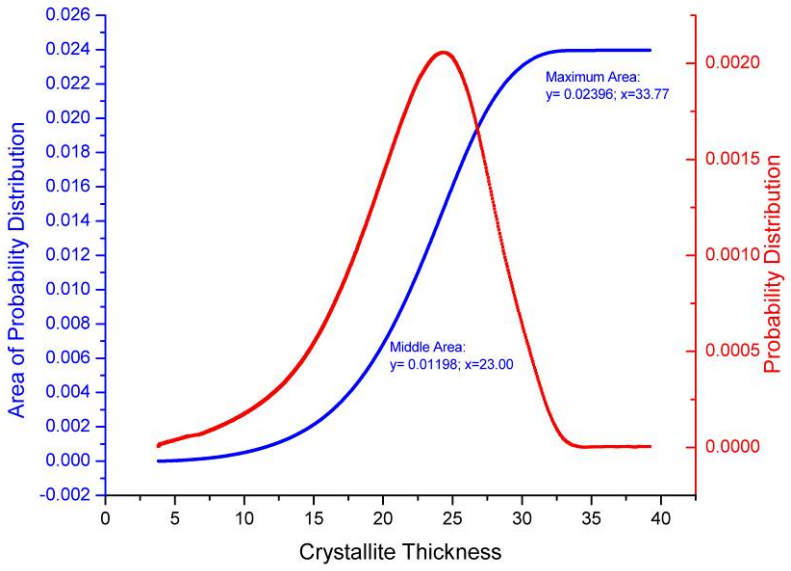

Figure 202: Second Moment of Control (0 kGy) Gamma Irradiated Crystallite Thickness Distribution for the Surface (Area Calculations)

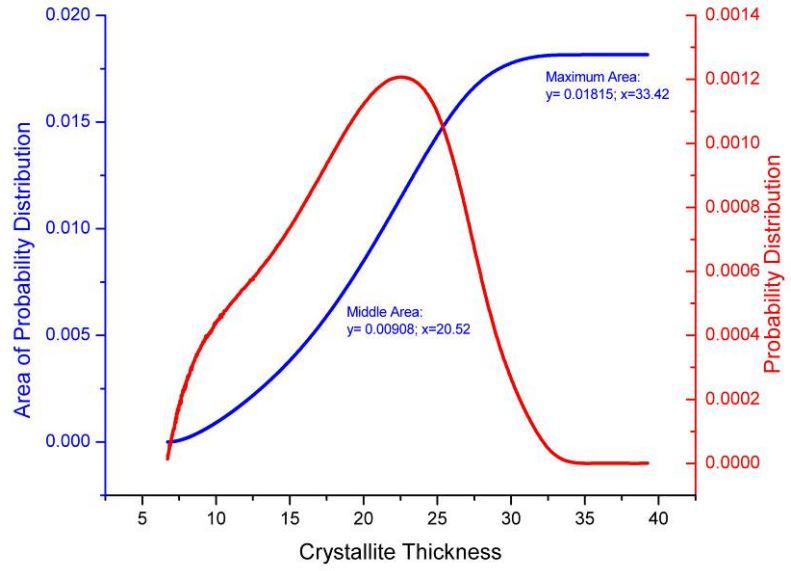

Figure 203: Control (0 kGy) Gamma Irradiated Crystallite Thickness Distribution for the Center (Area Calculations)

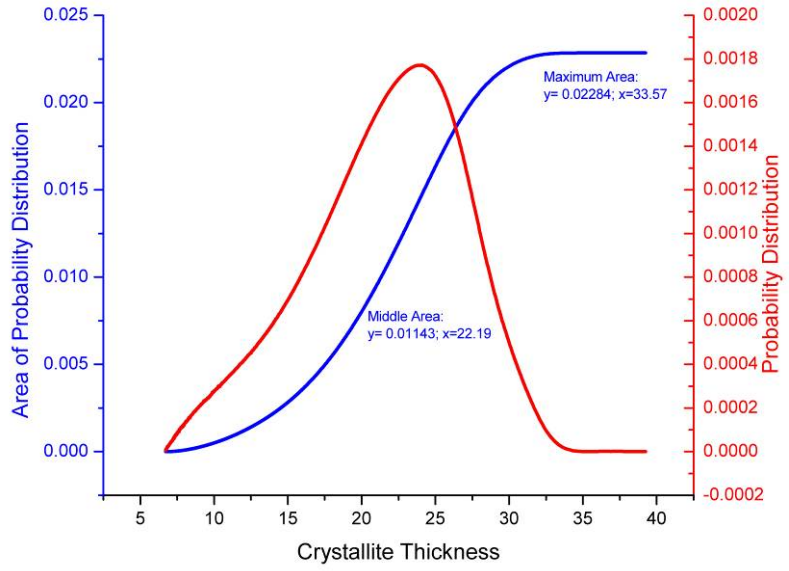

Figure 204: First Moment of Control (0 kGy) Gamma Irradiated Crystallite Thickness Distribution for the Center (Area Calculations)

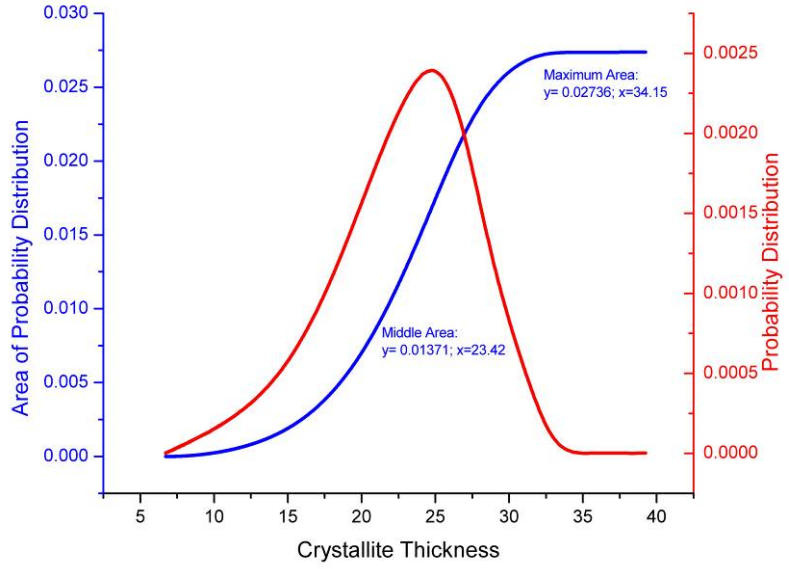

Figure 205: Second Moment of Control (0 kGy) Gamma Irradiated Crystallite Thickness Distribution for the Center (Area Calculations)

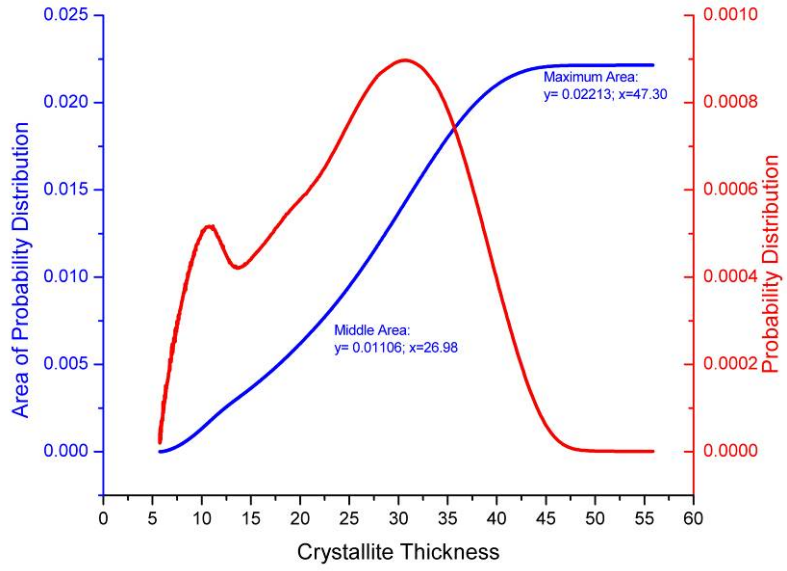

Figure 206: 75 kGy, High Dose Rate, Gamma Irradiated Crystallite Thickness Distribution for the Surface (Area Calculations)

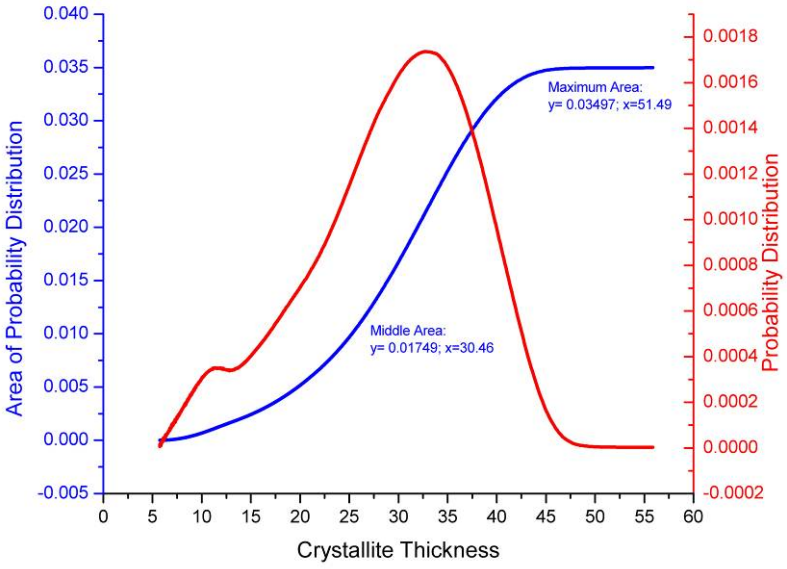

Figure 207: First Moment of 75 kGy, High Dose Rate, Gamma Irradiated Crystallite Thickness Distribution for the Surface (Area Calculations)

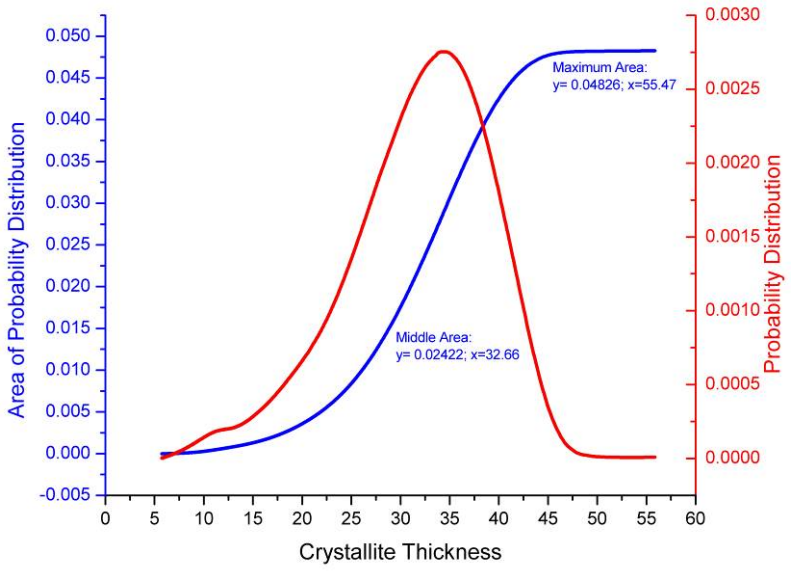

Figure 208: Second Moment of 75 kGy, High Dose Rate, Gamma Irradiated Crystallite Thickness Distribution for the Surface (Area Calculations)

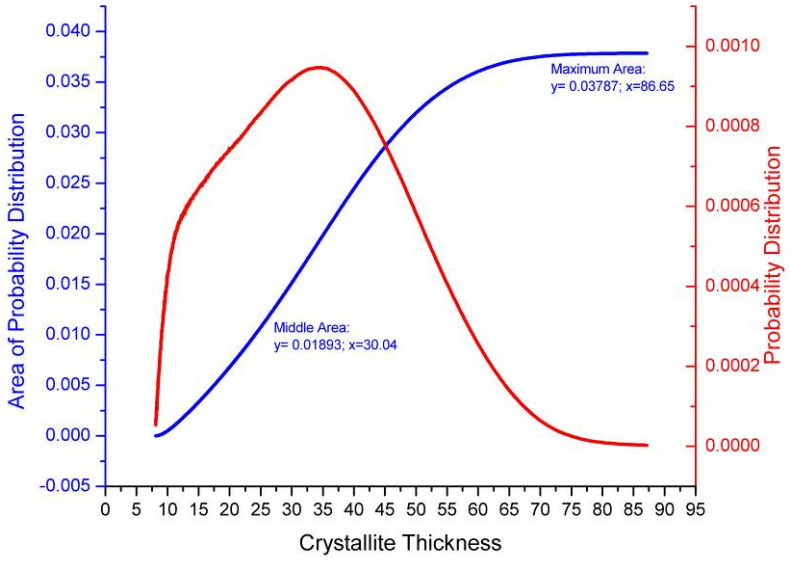

Figure 209: 75 kGy, High Dose Rate, Gamma Irradiated Crystallite Thickness Distribution for the Center (Area Calculations)

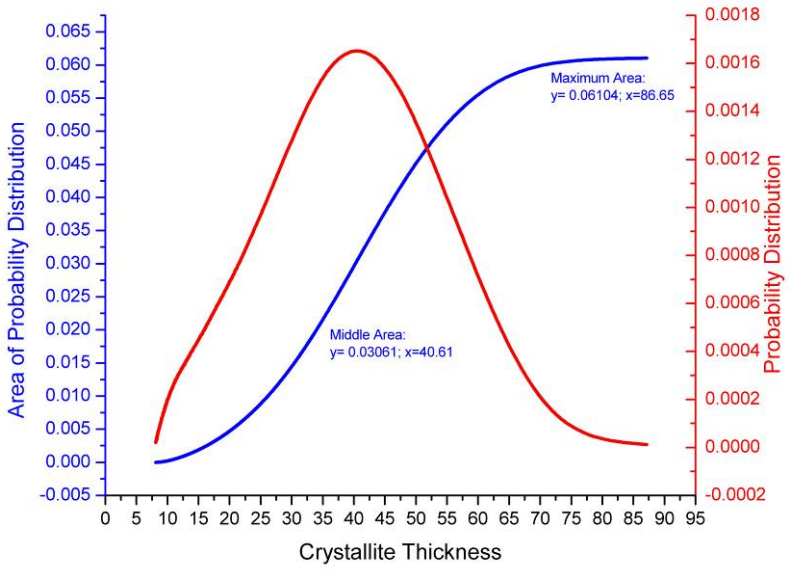

Figure 210: First Moment of 75 kGy, High Dose Rate, Gamma Irradiated Crystallite Thickness Distribution for the Center (Area Calculations)

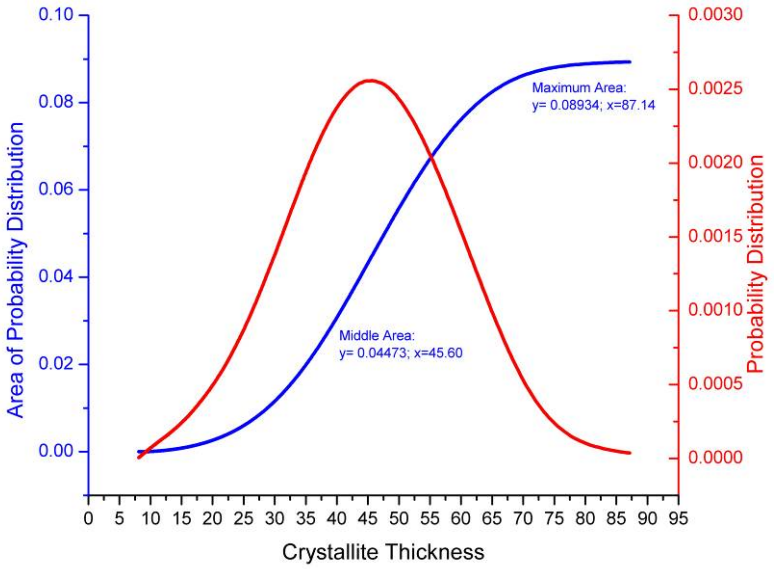

Figure 211: Second Moment of 75 kGy, High Dose Rate, Gamma Irradiated Crystallite Thickness Distribution for the Center (Area Calculations)

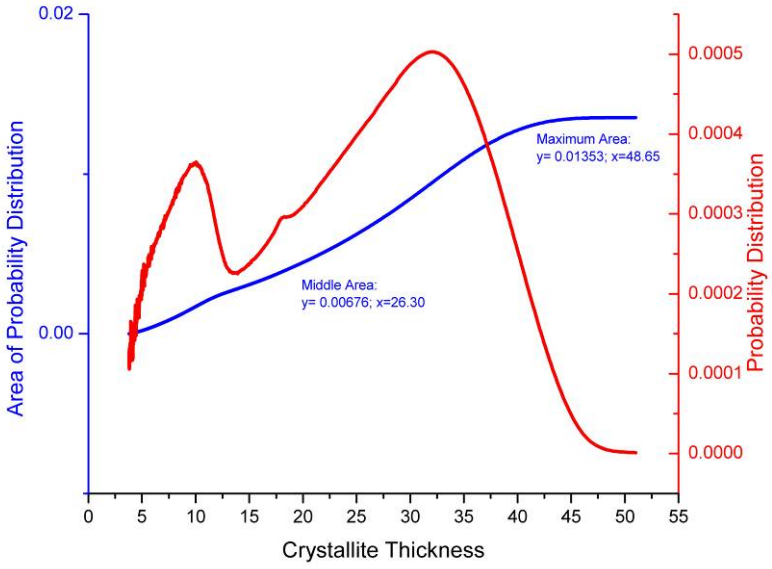

Figure 212: 150 kGy, High Dose Rate, Gamma Irradiated Crystallite Thickness Distribution for the Surface (Area Calculations)

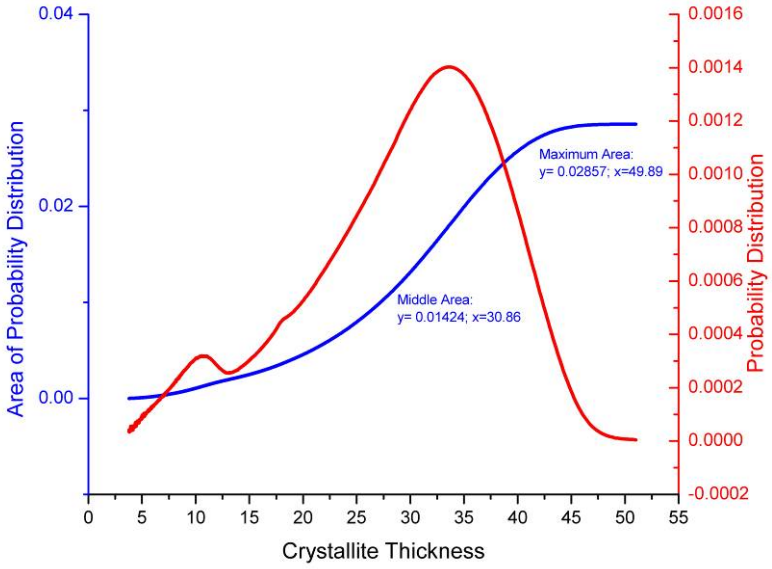

Figure 213: First Moment of 150 kGy, High Dose Rate, Gamma Irradiated Crystallite Thickness Distribution for the Surface (Area Calculations)

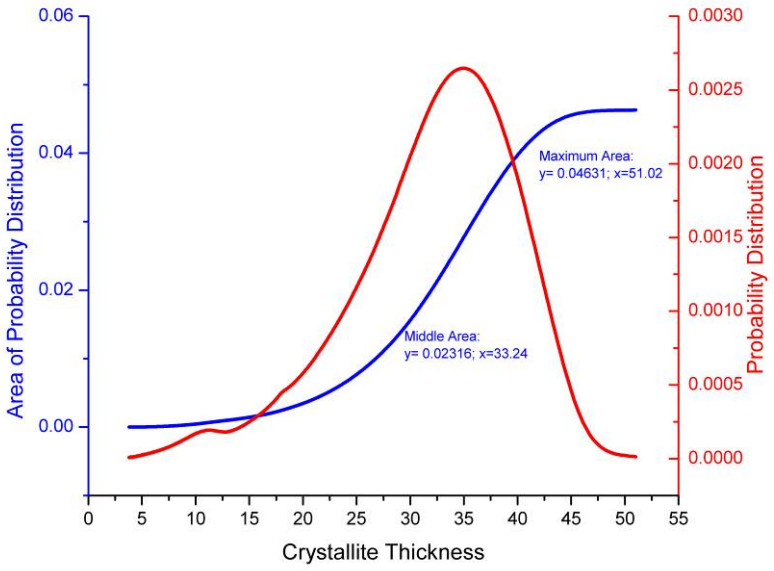

Figure 214: Second Moment of 150 kGy, High Dose Rate, Gamma Irradiated Crystallite Thickness Distribution for the Surface (Area Calculations)

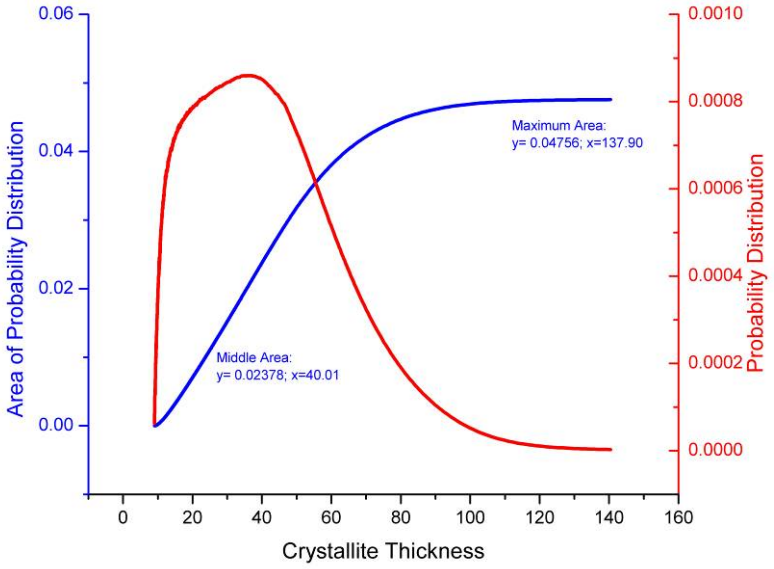

Figure 215: 150 kGy, High Dose Rate, Gamma Irradiated Crystallite Thickness Distribution for the Center (Area Calculations)

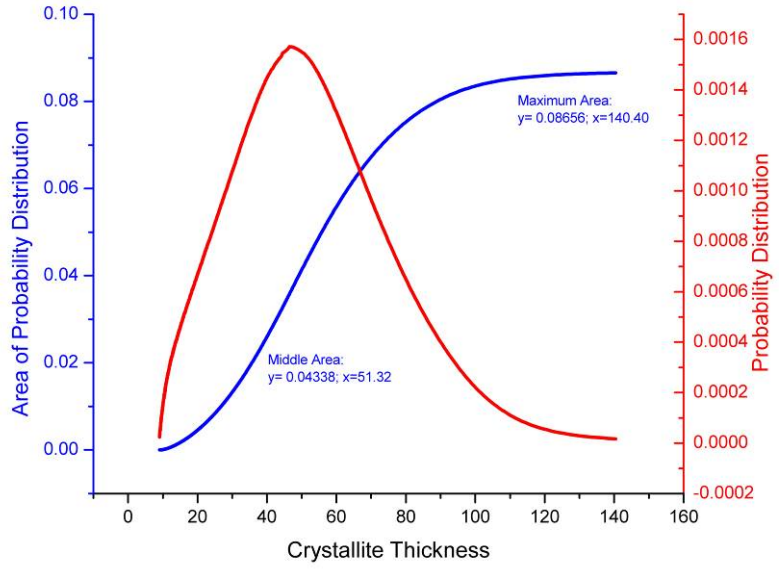

Figure 216: First Moment of 150 kGy, High Dose Rate, Gamma Irradiated Crystallite Thickness Distribution for the Center (Area Calculations)

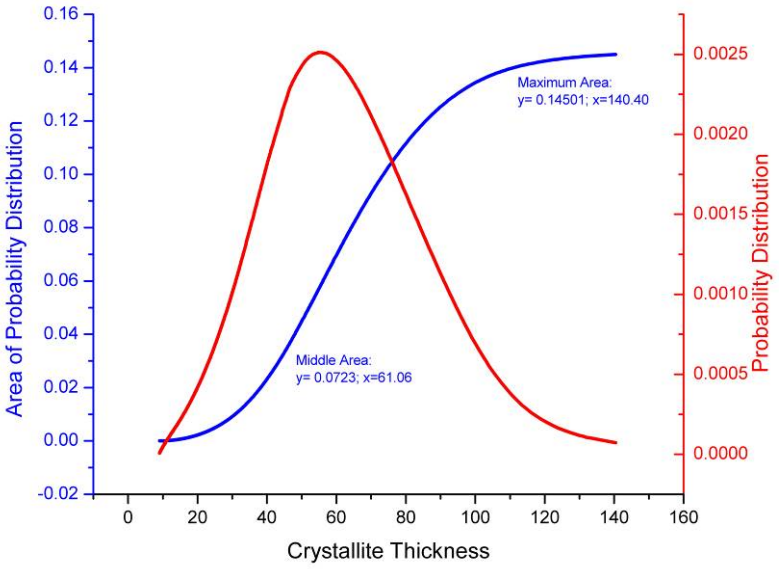

Figure 217: Second Moment of 150 kGy, High Dose Rate, Gamma Irradiated Crystallite Thickness Distribution for the Center (Area Calculations)

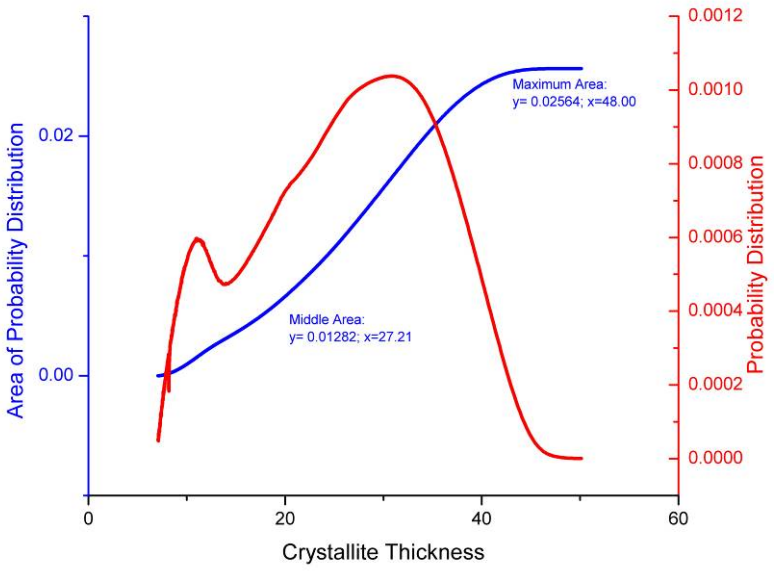

Figure 218: 75 kGy, Low Dose Rate, Gamma Irradiated Crystallite Thickness Distribution for the Surface (Area Calculations)

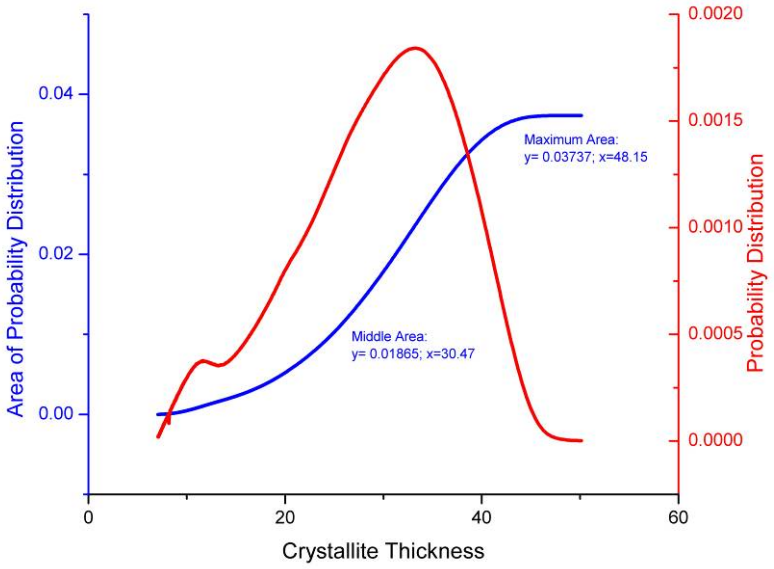

Figure 219: First Moment of 75 kGy, Low Dose Rate, Gamma Irradiated Crystallite Thickness Distribution for the Surface (Area Calculations)

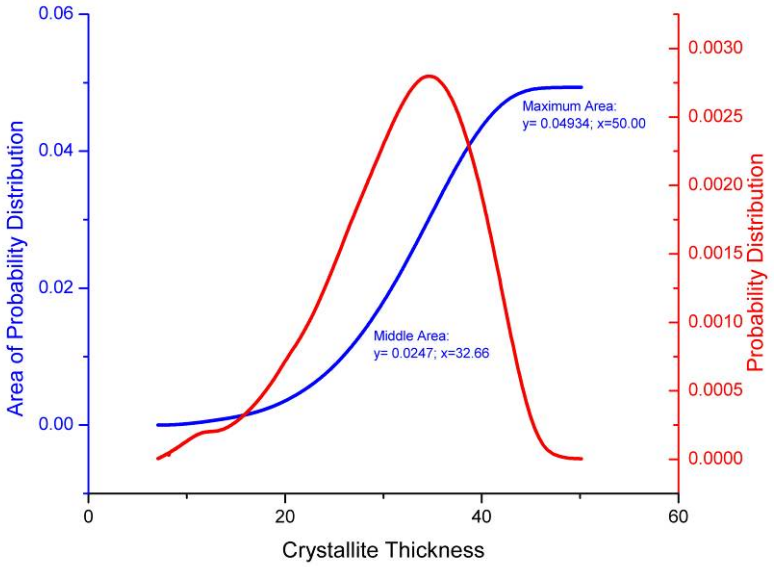

Figure 220: Second Moment of 75 kGy, Low Dose Rate, Gamma Irradiated Crystallite Thickness Distribution for the Surface (Area Calculations)

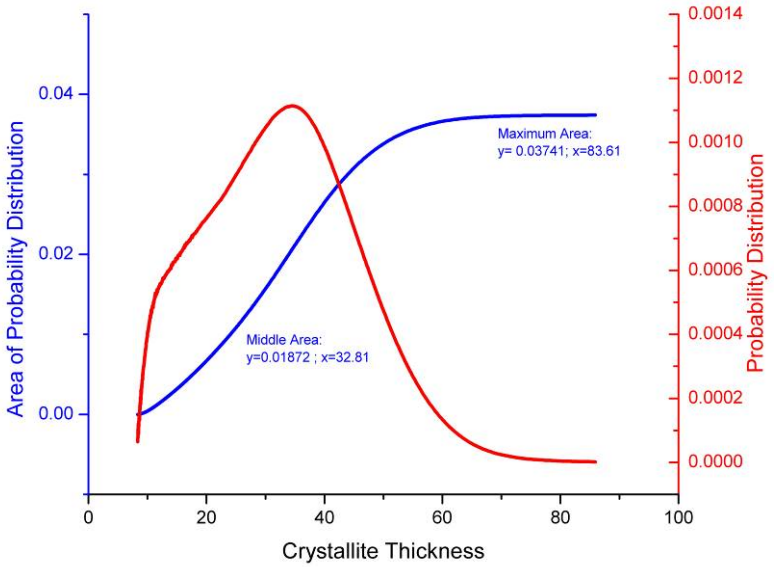

Figure 221: 75 kGy, Low Dose Rate, Gamma Irradiated Crystallite Thickness Distribution for the Center (Area Calculations)

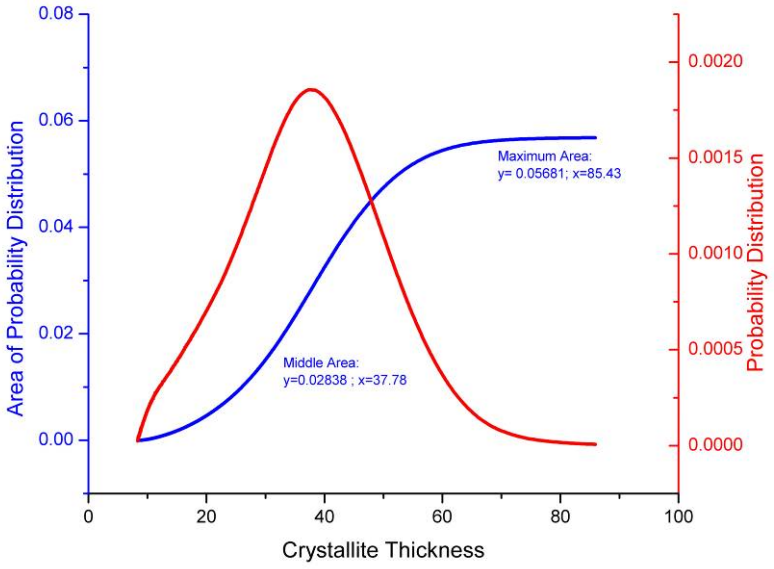

Figure 222: First Moment of 75 kGy, Low Dose Rate, Gamma Irradiated Crystallite Thickness Distribution for the Center (Area Calculations)

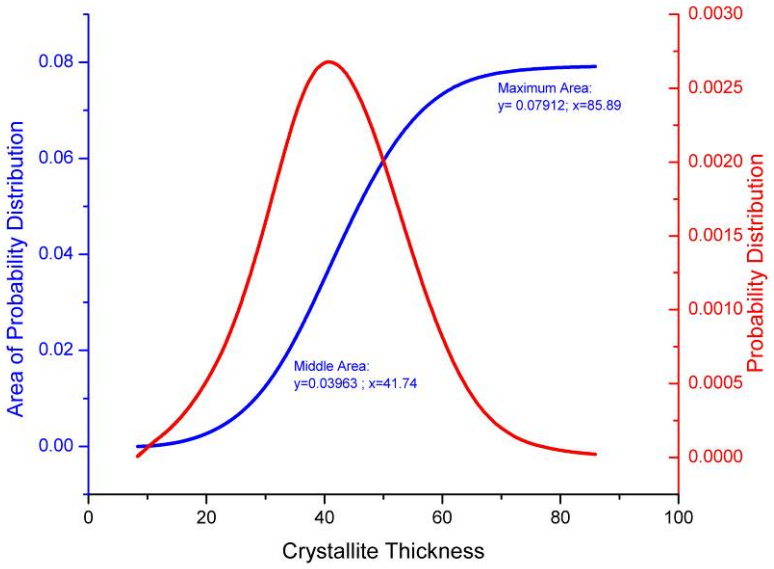

Figure 223: Second Moment of 75 kGy, Low Dose Rate, Gamma Irradiated Crystallite Thickness Distribution for the Center (Area Calculations)

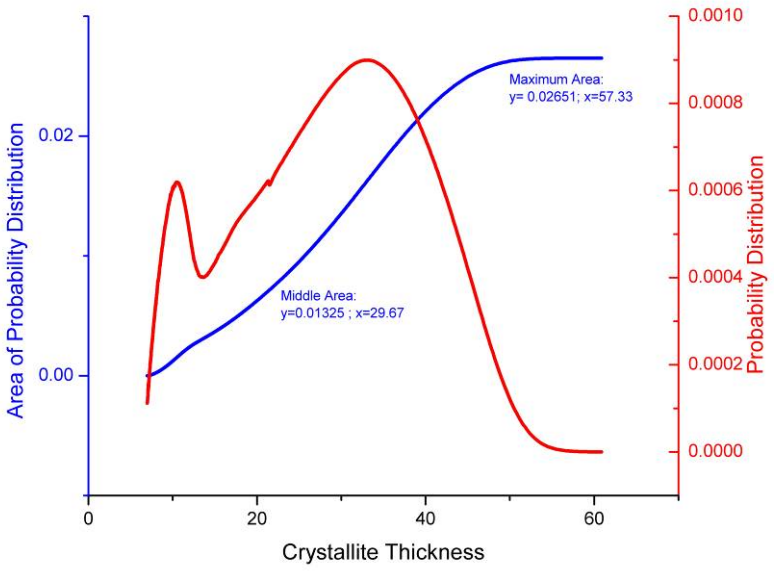

Figure 224: 150 kGy, Low Dose Rate, Gamma Irradiated Crystallite Thickness Distribution for the Surface (Area Calculations)

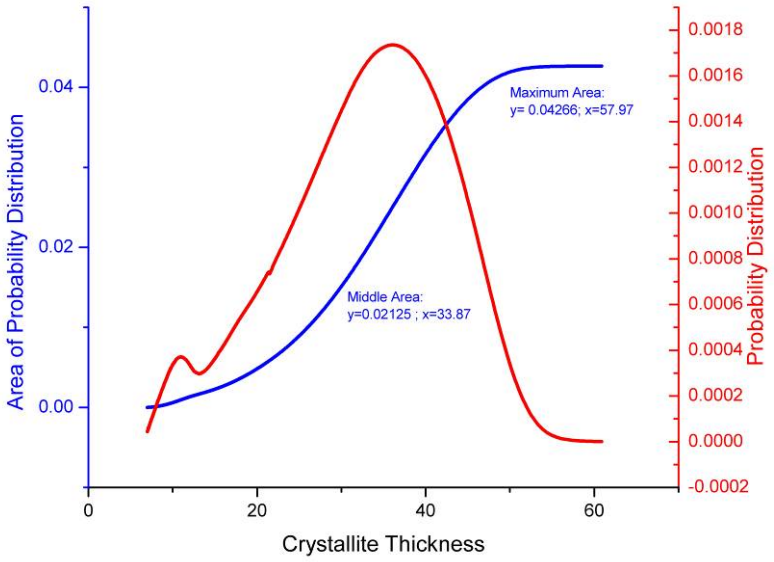

Figure 225: First Moment of 150 kGy, Low Dose Rate, Gamma Irradiated Crystallite Thickness Distribution for the Surface (Area Calculations)

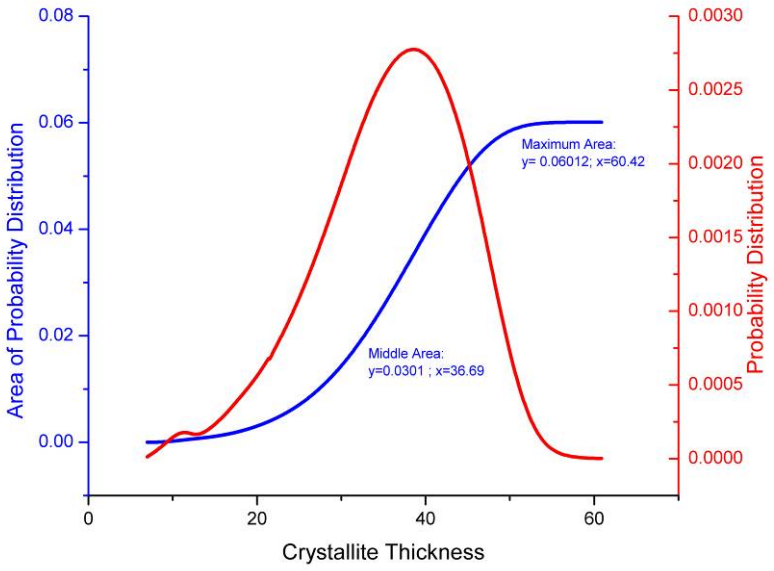

Figure 226: Second Moment of 150 kGy, Low Dose Rate, Gamma Irradiated Crystallite Thickness Distribution for the Surface (Area Calculations)

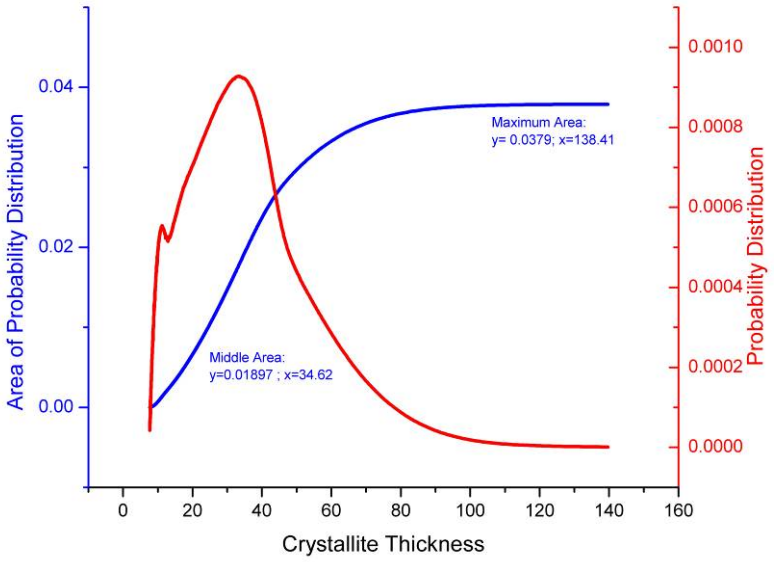

Figure 227: 150 kGy, Low Dose Rate, Gamma Irradiated Crystallite Thickness Distribution for the Center (Area Calculations)

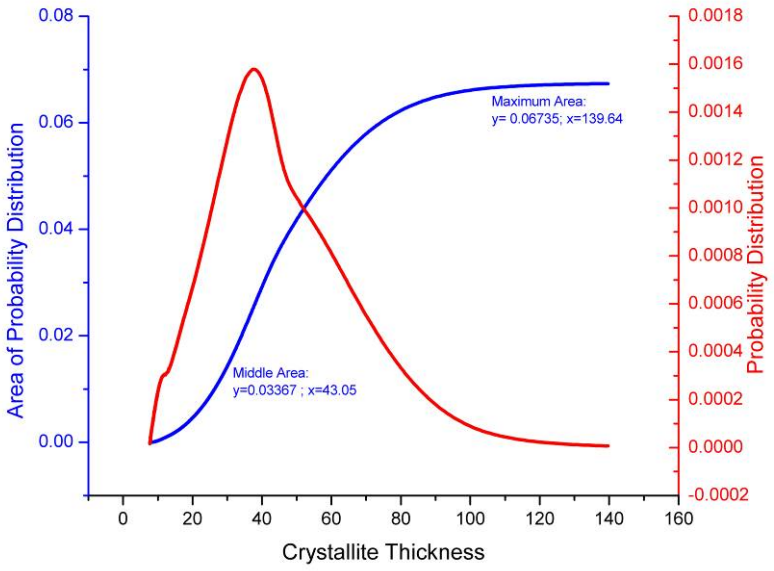

Figure 228: First Moment of 150 kGy, Low Dose Rate, Gamma Irradiated Crystallite Thickness Distribution for the Center (Area Calculations)

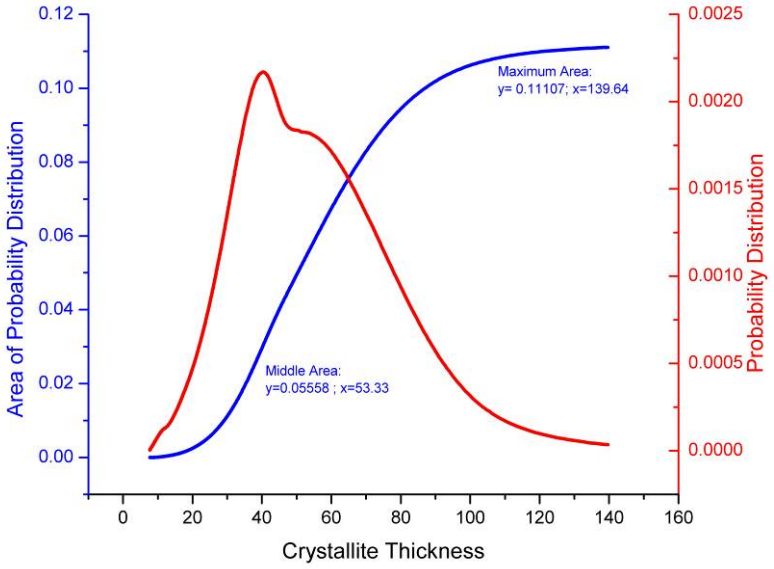

Figure 229: Second Moment of 150 kGy, Low Dose Rate, Gamma Irradiated Crystallite Thickness Distribution for the Center (Area Calculations)

Vita

Christopher P. Stephens was born in Allentown, Pennsylvania, on March 18, 1981. He graduated from Farragut High School in 1999. Chris began his undergraduate education in 1999 at the University of Tennessee at Knoxville and graduated with a B.S. in Materials Science and Engineering in 2004. During Chris's undergraduate studies he interned at Sandia National Laboratories (Livermore, CA) and Johnson Space Center, NASA (Houston, TX). Chris is currently pursuing his doctorate in Polymer Engineering at the University of Tennessee at Knoxville.